Nuclear DFT description of proton-neutron pairing correlations

Betania Camille Tumelero Backes

PhD

University of York
Physics, Engineering and Technology

August 2026

Nuclear DFT description of proton-neutron pairing correlations

Betania Camille Tumelero Backes

PhD

University of York
Physics, Engineering and Technology

August 2026

Abstract

Pairing correlations play a crucial role in nuclear phenomena: their effects range from the odd-even mass staggering in nuclear structure to the phases of matter found in neutron stars. Nuclear Density Functional Theory (DFT) is a framework applicable to different systems, from few-body nuclei to nuclear matter. In this thesis, we describe pairing and its manifestation within nuclear DFT, in both infinite and finite systems.

Starting from a wavefunction combining all spin-isospin channels of a pair condensate in infinite nuclear matter, we obtain the most general density matrix and pairing tensor. Our interaction-independent analysis shows that although the different proton-neutron channels separate in the Thouless matrix, they mix in the pairing tensor and the density matrix, suggesting that the relationship between pairing tensor and pair condensate cannot be taken for granted.

In finite systems, we compute $B(E2; 2_1^+ \rightarrow 0_1^+)$ of $T = 1$ multiplets, as the dependence of $E2$ matrix elements on isospin projection T_z is linked to the conservation of isospin symmetry. We show that $T_z = 0, T = 1$ nuclei should be described by a coherent superposition of blocked $T = 1$ proton-neutron pairs atop the even-even quasiparticle vacua. The computed $B(E2\downarrow)$ in doubly-blocked configurations of the odd-odd $T_z = 0$ nuclei ^{70}Br and ^{78}Y—cases of experimental interest—show that, individually, they do not correspond to isospin-symmetry conservation. We analyse $B(E2)$ rates for even-even $T = 1$ mirror nuclei with $42 \leq A \leq 98$, and demonstrate that collective effects are crucial for describing experimental data near the $N = Z$ line.

We introduce a new algorithm for computing finite-range interactions in nuclear DFT for direct, exchange, and pairing channels. The new technique is based on eigendecomposition truncation and exploits properties specific to Gaussian matrix elements to accelerate DFT calculations of finite-range interactions. This procedure reduces the CPU time by $\approx 60 - 90\%$ without sacrificing numerical precision.

Contents

Abstract ii

List of Figures vii

Acknowledgements xiii

Author's declaration xvi

Abbreviations xviii

I Introduction 1

1 The nuclear many-body problem 2
- 1.1 Why nuclear density functional theory? . . . 3
- 1.2 Why proton-neutron pairing correlations? . . . 5
- 1.3 Thesis structure . . . 7
- 1.4 Reading guide . . . 8

2 Self-consistent methods 9
- 2.1 Hartree-Fock-Bogoliubov method . . . 9
  - 2.1.1 Odd particles: The blocking approximation . . . 12
- 2.2 Constrained calculations . . . 12
- 2.3 Nuclear density functional theory . . . 13
  - 2.3.1 The Gogny EDF . . . 13
  - 2.3.2 The Skyrme EDFs . . . 14
- 2.4 Beyond mean-field: Restoration of broken symmetries . . . 14

3 What is pairing? 15
3.1 What are pairing correlations? . . . 15
3.1.1 The canonical basis . . . 16
3.1.2 Correlations of a single Thouless pair . . . 19
3.2 Pairing correlation factors of mixed states . . . 20

II Proton-neutron pairing correlations 23

4 Homogeneous and isotropic nuclear matter 24
4.1 A general paired wavefunction . . . 26
4.2 The **k**-dependent density matrix and pairing tensor . . . 29
4.3 A simple case: Antisymmetric Thouless sub-matrix . . . 32
4.4 A simple *generalisable* case: z-aligned pairs in the ST basis . . . 35
4.5 The path to the most general pairing tensor of nuclear matter . . . 38
4.5.1 Rotating $\mathscr{Z}_z^+$ in spin and isospin space . . . 38
4.5.2 The rotated Thouless submatrices, $\mathscr{Z}^+_{\mathrm{rot},ST}$ . . . 40
4.5.3 Writing the partial derivatives . . . 41
4.5.4 The pairing tensor . . . 43
4.6 Rotating the pairing tensor . . . 44
4.6.1 Considerations about rotations in the subspace . . . 46
4.7 Conclusions . . . 46

5 Analysis of pairing strengths 48
5.1 Pairing in UNEDF1 . . . 50
5.2 Changing pairing strengths in UNEDF1 . . . 51

6 Odd-odd $N = Z$ nuclei and isospin symmetry-breaking in $T = 1$ multiplets 59
6.1 Isospin symmetry . . . 59
6.2 Isospin symmetry-breaking . . . 63
6.2.1 Tests of isospin symmetry . . . 63
6.2.2 The linearity rule . . . 64
6.3 Is isospin broken at all? . . . 65
6.4 The odd-odd isobaric analog state . . . 67
6.5 Angular momentum projected DFT . . . 70
6.6 The Generalised Bohr Hamiltonian . . . 72
6.7 Global analysis of $T = 1$ mirror nuclei . . . 73

6.8 The $A = 70$ and $A = 78$ isobaric triplets 76
6.9 Conclusions 79

III Other research questions 82

7 Relativistic two-body currents 83

8 The Gaussian Separalisation Method 87
8.1 Computational efficiency 89
8.2 Properties of the Gaussian matrix elements and their eigenvalue decomposition 91
8.3 Simplified structure of the algorithm 94
8.3.1 Traditional approach 95
8.3.2 Simplified Gaussian Separalisation Method (GSM) intermediates . . 95
8.4 Acceleration due to symmetry of the eigenvectors 96
8.5 Acceleration due to eigenvalue cutoffs 99
8.6 Precision 102
8.7 Timing results 105
8.8 Final remarks 108

9 Hybrid neutron stars: equation of state, phase transition, and radial oscillations 109
9.1 A very brief introduction to neutron star equation of state physics 111
9.1.1 Uniting the micro- and macro-physics 114
9.2 The density-dependent equation of state 115
9.2.1 Deconfined quark matter 115
9.2.2 Hadronic matter 117
9.3 Deconfinement phase transition 117
9.4 Some results 118
9.5 Final remarks 120

10 Conclusions and perspectives 122

IV Appendices 124

A The coupled ST representation 125

B Rotated ST states 129

C Rotated Thouless matrix 132

D Partial derivatives of the rotated Thouless matrix 135

E Details of the GSM implementation 138

Bibliography 140

List of Figures

1.1 Segrè chart for nuclei listed in the Atomic Mass Evaluation (Wang et al. 2021a), listed by decay mode. Figure produced with the GitHub package from Karthein 2024. . . 3

1.2 Experimental neutron separation energies from the Atomic Mass Evaluation (Wang et al. 2021a). Magic neutron and proton numbers are marked with dashed vertical lines and bold pink lines, respectively. The inset details Sn isotopes. Figure produced with the GitHub package from Karthein 2024. 6

2.1 Schematic representation of the Hartree-Fock-Bogoliubov (HFB) method. 11

5.1 Comparison between the calculated magnetic dipole μ moments of the $\nu 11/2^-$ configurations in odd-N nuclei and the available experimental data (Stone 2021). The isotopes where the signs of the magnetic dipole moments are experimentally undetermined and determined from the theoretical calculations are marked with the asterisk symbols (*). Reproduced from Wibowo, Backes et al. 2025 49

5.2 Same as in Figure 5.1 for $\pi 7/2^+$ configurations in odd-Z nuclei. Reproduced from Wibowo, Backes et al. 2025. 49

5.3 odd-even staggering (OES) of different isotopes for different pairing strengths, and experimental data (ENSDF 2023). The functional used was UNEDF1 (Kortelainen, McDonnell et al. 2012), and the proton and neutron pairing strengths were modified by summing or subtracting different percentages of the original UNEDF1. 54

5.4 OES of different isotones for different pairing strengths, and experimental data (ENSDF 2023). The functional used was UNEDF1 (Kortelainen, McDonnell et al. 2012), and the proton and neutron pairing strengths were modified by summing or subtracting different percentages of the original UNEDF1. 55

5.5 Residual of all isotopic chains OESs of Figure 5.3. The mean of each pairing strength is indicated by the dashed lines. 56

5.6 Residual of all isotonic chains OESs of Figure 5.4. The mean of each pairing strength is indicated by the dashed lines. 56
5.7 Residual for the individual isotopic chains OESs of Figure 5.3. 57
5.8 Residual for the individual isotonic chains OESs of Figure 5.4. 58

6.1 The proton and neutron as different isospin projections of a nucleon. 60
6.2 Isospin triplets and singlets in the spectra of $A = 10$ isobars, aligning the first $T = 1$ states, i.e., 0^+ (ENSDF 2023). Figure based on Ring and Schuck 1980. 61
6.3 Representation of isospin multiplets. 62
6.4 Data presented by Wimmer et al. 2021 and the linear trend set by ^{70}Br and ^{70}Se. . . . 66
6.5 A helpful representation of how to identify the states closest to the Fermi surface in odd-odd nuclei. Here we display ^{78}Y, and its neighbouring odd nuclei with their respective experimental ground states. 68
6.6 Potential energy curves, obtained with UNEDF1, with constrained quadrupole moments Q_{20} for the mirror pair of $A = 70$ (^{70}Kr,^{70}Se). The energies are normalised to the energy at the spherical shape. 71
6.7 HFB potential energy curves, obtained with UNEDF1, projected on $I = 0$ as functions of quadrupole deformation β (6.5.1) for the even-even $T = 1$ mirror nuclei considered in this study. Solid lines denote $T_z = 1$, and dashed lines $T_z = -1$. The mass numbers are marked explicitly, close to curves of different colours. The energies are normalized to the energy at the spherical shape. 74
6.8 $B(E2)$ values of even-even $T = 1$ mirror nuclei with $42 \leq A \leq 98$ and the available experimental data (Boso et al. 2019; Giles et al. 2019, 2021; Hadyńska-Klęk et al. 2016; Llewellyn et al. 2020; Morse et al. 2018; Pritychenko et al. 2016; Wimmer et al. 2021), in (a) full scale and (b) reduced scale. $T_z = 1$ ($T_z = -1$) nuclei are represented with open (filled) symbols. Stars show experimental values, squares mark the GBH UNEDF1 predictions, and the prolate (oblate) AMP UNEDF1 predictions are shown with up-pointing (down-pointing) triangles. 75
6.9 The Nilsson proton diagrams for ^{70}Br (top) and ^{78}Y (bottom) obtained using the UNEDF1 EDF and plotted as a function of the total intrinsic quadrupole moment Q_{20}. (The neutron diagrams are quite similar; therefore, they are not shown.) Although the wavefunctions are strongly mixed in many cases, the asymptotic quantum numbers $[Nn_x\Lambda]\Omega$ provided match those of Nazarewicz et al. 1985 to simplify the identification of individual levels. The vertical lines mark the false-vacuum equilibrium quadrupole moments of $A = 70$ ($Q_{20}^{\min} \approx -3.2$ b) and $A = 78$ ($Q_{20}^{\min} \approx 7.5$ b) isotriplets. Figure is the same as the one included in Backes, Dobaczewski et al. 2025. 77

6.10 $M_p(E2)$ values computed with HFB+AMP and UNEDF1 for (a) $A = 70$ and (b) $A = 78$ triplets, and the available experimental data (Wimmer et al. 2021). We selected the oblate solutions for the $A = 70$ triplet and the prolate ones for the $A = 78$ triplet. The different points shown for the odd-odd $T_Z = 0$ nuclei correspond to different 2-quasiparticle states near the Fermi level. Even-even results from GBH calculations are shown as squares. 78

8.1 Execution times obtained for Algorithms 1 and 2 shown as a function of N, for a square matrix of dimension $N \times N$. The lines show that the times scale, respectively, as N^4 and N^3. 91

8.2 Schematic representation of the loops for the Harmonic Oscillator (HO) indices for $N_0 = 5$ shells. 97

8.3 Schematic representation of the loops for the HO indices in the new scheme for $N_0 = 5$ shells. Panels (a), (b), and (c) correspond to the innermost loop with HO indices in the x, z, and y direction, respectively. The lighter and patterned indices, always highlighted in the innermost loops, can be omitted in the GSM algorithm. 98

8.4 Ratio between the number of iterations when skipping the symmetric $m \leftrightarrow n$ indices ($O_{\text{sym-skip}}$) and accounting for all HO indices (O_{original}). 100

8.5 Normalised eigenvalue spectra for a product of eigenvalues in one (a,b), two (c,d), and three (e,f) Cartesian directions, for the direct (left) and exchange/pairing (right) channels. Different colors denote the spectra for different basis sizes, and different lines denote the different Gaussian widths for the Gogny DS1 potential. 101

8.6 Precision of the total, direct, exchange, and pairing energies with different eigenvalue cutoffs in 16 HO shells for ^{160}Gd. 103

8.7 Precision of the total, direct, exchange, and pairing energies with different eigenvalue cutoffs in 20 HO shells for ^{160}Gd. 104

8.8 The absolute error as a function of eigenvalue cutoff for 16 (dashed lines) and 20 (full lines) HO shells, for ^{160}Gd. The lines indicate the product between the cutoff and the energy on each channel, $E\lambda_c$. 104

8.9 Precision of the total, direct, and exchange energies with different eigenvalue cutoffs. Results come from Hartree-Fock (HF) calculations in 16 HO shells for ^{208}Pb. 105

8.10 Ratio of the time per iteration with and without use of the GSM, separated between all channels and the total time for 16 HO shells in ^{160}Gd. 106

8.11 Ratio of the time per iteration with and without use of the GSM, separated between all channels and the total time for 20 HO shells in ^{160}Gd. 107

8.12 Ratio of the time per iteration with and without use of the GSM, separated between channels, and the total time, for HF calculations in 16 HO shells for ^{208}Pb. 107

9.1 Conjectured Quantum Chromodynamics phase diagram. Reproduced from Watts et al. 2014. 112
9.2 Illustration of different possible neutron star compositions. 113
9.3 Energy density and pressure variation for the N (solid lines), N+Δ (dotted lines), N+H (dashed lines), and N+H+Δ (dot-dashed lines) DD-RMF EoS for $\alpha_v = 1.0$ with a phase transition to the quark matter at parameter values $(C, D^{1/2}) = (0.90, 125\ \text{MeV})$ for N and N+Δ EoS and $(C, D^{1/2}) = (0.65, 133\ \text{MeV})$ for N+H and N+H+Δ EoS. The inset represents the EoS at low density with constraints from chiral effective field theory (Hebeler et al. 2013). Reproduced from Rather, Marquez, Backes et al. 2024. 119
9.4 Particle population for different hybrid EoS: N (top left), N+Δ (top right), N+H (bottom left), N+H+Δ (bottom right). The solid lines represent baryons while the dashed lines represent the quark fractions. The shaded region (orange) represents the density discontinuity gap between both parts of the EoS. Reproduced from Rather, Marquez, Backes et al. 2024. 120
9.5 Mass-radius profile for DD-RMF parameter set with different compositions of Δ baryons and hyperons along with a phase transition to the quark matter at parameter values $(C, D^{1/2}) = (0.90, 125\ \text{MeV})$ for N and N+Δ EoS and $(C, D^{1/2}) = (0.65, 133\ \text{MeV})$ for N+H and N+H+Δ EoS. The 68% (violet) and 95% (turquoise) credible regions for mass and radius are inferred from the analysis of PSR J0740+6620 (Miller et al. 2021; Riley et al. 2021). For PSR J0030+0451, the indigo dotted region is for 68% credibility while the green dotted region is for 95% credibility (Miller *et al.* 2019). The grey upper (brown lower) shaded region corresponds to the higher (smaller) component of the GW170817 event (Abbott, Abbott et al. 2018). The joint constraints from HIC experiments and multimessenger astrophysics with 68% (orange) and 95% (black) credible ranges are also shown (Huth et al. 2022). Reproduced from Rather, Marquez, Backes et al. 2024. 121

To all those I view as family

"Would you tell me, please, which way I ought to go from here"
"That depends a good deal on where you want to get to," said the Cat.
"I don't much care where—" said Alice.
"Then it doesn't matter which way you go," said the Cat.
"—So long as I get SOMEWHERE" Alice added as an explanation.
"Oh, you're sure to do that," said the Cat, "if you only walk long enough."

Lewis Carroll

To the worm who first gnawed on the cold flesh of my corpse, I dedicate with fond remembrance these Posthumous Memoirs

---

Machado de Assis

Acknowledgements

These acknowledgements are some of the first thoughts I had when creating the files that would become my thesis, and some of the last before it is finally submitted. I feel extremely lucky to have so many wonderful people who shared this journey with me.

First and foremost, I thank Jacek for being a formidable supervisor. Throughout the years, you have continuously inspired me with your physics intuition, work ethic, knowledge, and patience. Years ago, I started this PhD with almost no knowledge of low-energy nuclear physics or many-body methods, and I am forever indebted to you for everything I have learned since. Moreover, you have shown me that you are not only an incredible researcher but also an incredible human being. I am forever grateful for these years, and I hope I continue having the privilege of learning from you for many years to come.

To my colleagues in the theory office, I have a lot to be thankful for. To Adrián and his wisdom and good humour; Herlik and his curiosity and dedication; Xuwei and his focus and hard work: I have learned plenty from all of you. To Anu, my "sister", who was the first to become my family away from my family, I am thankful for all the support and all the laughs over these years. Lastly, to Alejandro, my "theory younger brother", I am grateful for all the discussions and the moments we shared; you never failed to keep my spirit up with your brilliance. As the "dictator of the theory office", I admire all of you immensely, and I could not have asked for better office partners.

To Valentin, Karim, and Michael, I am extremely grateful for welcoming me in Lyon and making me feel at home. I learned a great deal during my brief time there and grew significantly through our exchanges—and an additional thanks to Jacques, who kindly shared his desk with me during my stay.

I would like to thank Kau Marquez (*in memoriam*), who was not only a collaborator but a dear friend and one of my biggest inspirations since I was an undergraduate. Collaborating with Kau during my PhD was an incredible experience, and I am forever shaped by the time we shared on Earth. Another thanks to Mikael Maraschin (*in memoriam*), for being a great friend since our high school years, and whose lengthy phone calls I dearly miss. Our trajectories ran parallel for a

long time, and even though you may not have finished your PhD in DFT, I carry your spirit with me for the rest of the ride (of both my PhD and my life).

It would undoubtedly have been a much more difficult path to walk if not for my collaborators and advisors, some of whom have already been mentioned. To the members of my Thesis Advisory Panel, many thanks to Matt for the continuous support, and to Mike for always believing in me and the years of advice. Thank you so much to P.-G., Bob, Ishfaq, and David for your incredible work and help along the years. A special thanks to Witek, who also welcomed me to FRIB during my visits to East Lansing, and whose infinite knowledge will never cease to amaze me. I am also thankful to the folks from the FiDiPro Zoom meetings for all of your comments throughout the years. I would also like to acknowledge and thank the panel, Marina and Gianluca, for the fruitful discussions and comments on the first version of the thesis.

If I came to the United Kingdom, it is thanks to the wonderful people at UFSC who made me the physicist I am. I thank all the lecturers, supervisors, and staff, but especially Débora and Tiago, who not only helped me move forward, but never stopped keeping up with my work and encouraged me every step of the way.

Despite being an ocean away, I am lucky to have friendships that followed me and never failed to be a reminder of home when I most needed it. I am incredibly thankful to Gustavo, Valéria, Valeria, Cheryl, Eduardo, Vitória, Ivan, Otto, Tiz, Matheus, Bazzo, and Jota for that. In the same category, I am also incredibly thankful for having all AMSG folks in my life to this day. I must thank Jow personally for keeping me sane, being both my anchor and source of entertainment through so many moments over the years. I dearly love all of you.

I am also lucky to have such incredible friendships here, and I am very thankful to Amelie, Charlie, Christina, Luke, Ali, Beatriz, Laura, Josh, Joshua, JJ, Mina, Maha, Alex, Stuart, and Abílio. You all are a big part of why York has become truly my home.

These years also blessed me with meeting some of my favourite people. I am so incredibly thankful to my bestie, Richard, for reminding me that above being a physicist, I must always be a human (turns out I had a horrible tendency to forget that before meeting him); thank you for always believing in me, for the carbonara, for the many adventures and moments we shared. To Mariana, I am thankful for bringing me such happiness and showing me the purest friendship, *te quiero mucho, chica.* Thank you so much to Joey for the great company, the fruits, and the walks. Thank you to Anthony for showing me so much kindness and giving me so much strength. Thank you to Daniel for understanding me so effortlessly, caring for me, and grounding me when I needed it. Thank you to Istvan for all the homecooked meals, for the advice, for sheltering me in moments of stress, and for all the lengthy conversations. Thank you to Aslı, my *gym wife*, for having the biggest heart; there isn't a day on which your strength (both physical and mental) has not amazed me, and the bond we share has been one of my greatest joys over the years. To all of you, thank you

for allowing me to be completely transparent. I can never repay what you have done for me, and I love you from the bottom of my heart.

I thank Patrick for much more than proofreading this document and being by my side. Thank you for taking care of me, not letting me give up, and giving me the strength to follow my dreams even when it wasn't easy. Sharing this journey with you is a privilege, an honour and a pleasure; your brilliance inspires me always.

I can never repay what my family has done for me. Thank you to my brother for being my most constant support, and to my parents for their endless love, patience, and care. The three of you are my biggest example of what strength and dedication actually are. I love and admire you immensely, and could not have gotten to this point without you.

Lastly, I extend my thanks to the Brazilian and British people. With the future of fundamental science now under threat, it is more important than ever to recognise that this work (and many others) relies on public funds. I thank UKRI and STFC for my PhD studentship, CAPES and CNPq for my previous studentships back home, and the public educational system in Brazil. I would not be here if it were not for these opportunities.

Tamo junto,
Betânia Camille Tumelero Backes
York, 2026

Author's declaration

I declare that this thesis is a presentation of original work and I am the sole author. This work has not previously been presented for a degree or other qualification at this University or elsewhere. All sources are acknowledged as references.

Declaration on the use of generative AI tools: No generative AI tools were used in creating the text or material content herein. Generative AI was utilised to assist with the scripts of some Tikz illustrations.

My published works during this degree are

B. C. Backes, J. Dobaczewski, D. Muir, W. Nazarewicz, P.-G. Reinhard, M. A. Bentley, and R. Wadsworth, "Quadrupole Strength in Isobaric Triplets," *Physical Review C* **112**, 064311 (2025). [DOI] [arXiv:2505.15375].

H. Wibowo, **B. C. Backes**, J. Dobaczewski, R. P. de Groote, A. Nagpal, A. Sánchez-Fernández, X. Sun, and J. L. Wood, "Electromagnetic moments in the Sn-Gd region determined within nuclear DFT," *Journal of Physics G: Nuclear and Particle Physics* **52**, 065104 (2025). [DOI] [arXiv:2503.15738].

I. A. Rather, K. D. Marquez, **B. C. Backes**, G. Panotopoulos, and I. Lopes, "Radial Oscillations of Hybrid Stars and Neutron Stars including Delta baryons: The Effect of a Slow Quark Phase Transition," *Journal of Cosmology and Astroparticle Physics* **2024**, 130 (2024). [DOI] [arXiv:2401.07789].

J. Dobaczewski, **B. C. Backes**, R. P. de Groote, A. Restrepo-Giraldo, X. Sun, and H. Wibowo, "Electromagnetic and Exotic Moments in Nuclear DFT," *Annual Review of Nuclear and Particle Science* **76** (2026), in press. [DOI] [arXiv:2511.04632].

The following manuscript is currently under peer review in Physical Review Letters

M. L. Bissell, M. Jankowski, A. Antušek, N. Azaryan, **B. C. Backes**, M. Baranowski, M. Chojnacki, K. M. Dziubińska-Kühn, R. Han, A. Hurajt, B. Karg, I. Michelon, M. Pesek, M. Piersa-Siłkowska, B. M. Roberts, G. Sanamyan, T. P. Treczoks, L. Vasquez Rodriguez, H. Wibowo, D. Zakoucky, M. Žňava, M. Kortelainen, J. Dobaczewski, J. S. M. Ginges, and M. Kowalska, "Interrogating the composition and distribution of nuclear magnetization via the hyperfine anomaly: experiment meets nuclear and atomic theory for short-lived ^{47}K," *arXiv preprint* arXiv:2603.20090 (2026). [arXiv:2603.20090].

Lastly, the following manuscripts are in preparation

B. C. Backes, J. Dobaczewski, V. Guillon, and K. Bennaceur, "The nuclear DFT proton-neutron paired states in homogeneous and isotropic infinite nuclear matter", (2026).

B. C. Backes, J. Dobaczewski, K. Bennaceur, A. M. Romero, and A. Sánchez-Fernandez, "Acceleration of the algorithm to solve the nuclear DFT equations for finite-range interactions", (2026).

H. Wibowo, R. Han, **B. C. Backes**, G. Danneaux, J. Dobaczewski, W. C. Haxton, W. Jiang, and M. Kortelainen, "Nuclear DFT meson-exchange contributions to magnetic dipole moments of atomic nuclei", (2026).

A. Restrepo-Giraldo, **B. C. Backes**, J. Bonnard, J. Cubiss, J. Dobaczewski, A. McFarlane, A. Nagpal, C. Page, X. Sun, B. van den Borne, H. Wibowo, J. Wilson, and Z. Yue, "How to calculate your own nucleus in nuclear DFT: A primer in using the code HFODD", (2026).

J. Dobaczewski, **B. C. Backes**, A. Restrepo-Giraldo, A. Sánchez-Fernandez, X. Sun, H. Wibowo, et al., "Code HFODD, version to be published", (2026).

H. Wibowo, **B. C. Backes**, A. Borschewski, J. Dobaczewski, W. C. Haxton, R. F. Garcia Ruiz, "Anapole moments in nuclear DFT", (2027).

The content from all the references above is cited throughout the thesis and has inspired the chapters of this work.

Abbreviations

χEFT Chiral Effective Field Theory

AMP angular momentum projection

BCS Bardeen–Cooper–Schrieffer

DDQM density-dependent quark mass

DFT density functional theory

EDF energy density functional

EoS equation of state

GSM Gaussian Separalisation Method

HF Hartree-Fock

HFB Hartree-Fock-Bogoliubov

HO Harmonic Oscillator

IAS isobaric analog states

LN Lipkin-Nogami

LQCD lattice quantum chromodynamics

NM nuclear matter

NN nucleon-nucleon

NS neutron star

OES odd-even staggering

PNP particle-number projection

QCD Quantum Chromodynamics

qp quasiparticle

RMF relativistic mean-field

s.p. single-particle

TOV Tolman-Oppenheimer-Volkoff

Note that, following the nuclear physics tradition, we will synonymously use the abbreviations HF and HFB for unpaired and paired DFT, respectively.

Part I

Introduction

One

The nuclear many-body problem

Setting aside technical details, we shall understand some of the difficulties behind the nuclear many-body problem and why density functional theory is a remarkable framework among current theoretical methods. We shall also understand why the problem of proton-neutron pairing is worth investigating, and the structure of this thesis.

> [...] we can see how the whole becomes not only more than but also very different from the sum of its parts.
>
> Anderson 1972

As any physics student eventually comes to know, there is no closed analytical solution for a three-body problem. In fact, many-body problems are analytically unsolvable in general. Nuclear systems are not only quantum many-body problems, but the constituents of a nucleus are not elementary particles themselves. The interaction between nucleons, i.e., protons and neutrons—called *nuclear interaction*—is also not a fundamental one, but what arises after the strong interaction between quarks and gluons confines their constituents into composite particles, which interact with each other. Even the underlying and fundamental strong interaction, described by Quantum Chromodynamics (QCD), cannot be solved exactly apart from the very specific conditions of high temperature and low density, where Lattice QCD is applicable (Greiner, Schramm and Stein 2007). Moreover, the nucleus is not charge neutral, which further complicates the problem. The delicate balance between Pauli blocking, short-range correlations, Coulomb repulsion, the repulsive short-range and attractive medium-range strong interaction, gives rise to a very rich phenomenology. As one would expect from the complexity of the nuclear many-body problem, describing the plethora of phenomena observed in nuclei—such as shell structure, pairing or nuclear superfluidity, collective motion, clustering, the diversity of shapes and transitions between different shapes, and so on—is no trivial task. Over the decades, this gave rise to different theoretical approaches, from different starting points. This chapter motivates the choice of density functional theory (DFT),

the theoretical framework we use throughout most of this thesis, and also introduces pairing, the main theme of our work.

1.1 Why nuclear density functional theory?

When faced with the difficulties of the nuclear many-body problem, one could choose to tackle the problem from different principles. Schunck 2019 lists the reductionist and the emergent viewpoint, which relate to the degrees of freedom you choose. The first argues that all nuclear phenomena can be described from the properties of nucleons, considering protons and neutrons as the fundamental degrees of freedom. The latter argues that understanding the behaviour of such complex systems entails the introduction of new and different degrees of freedom. A second categorisation introduced in Schunck 2019, section 1.1.3, is the vertical and horizontal philosophies, related to how you build many-body correlations. A vertical approach consists of building correlations through a set of particle-hole excitations atop a symmetry-restricted vacuum, preserving all symmetries from the original Hamiltonian. The horizontal, on the other hand, introduces a series of non-orthogonal, symmetry-breaking vacua.

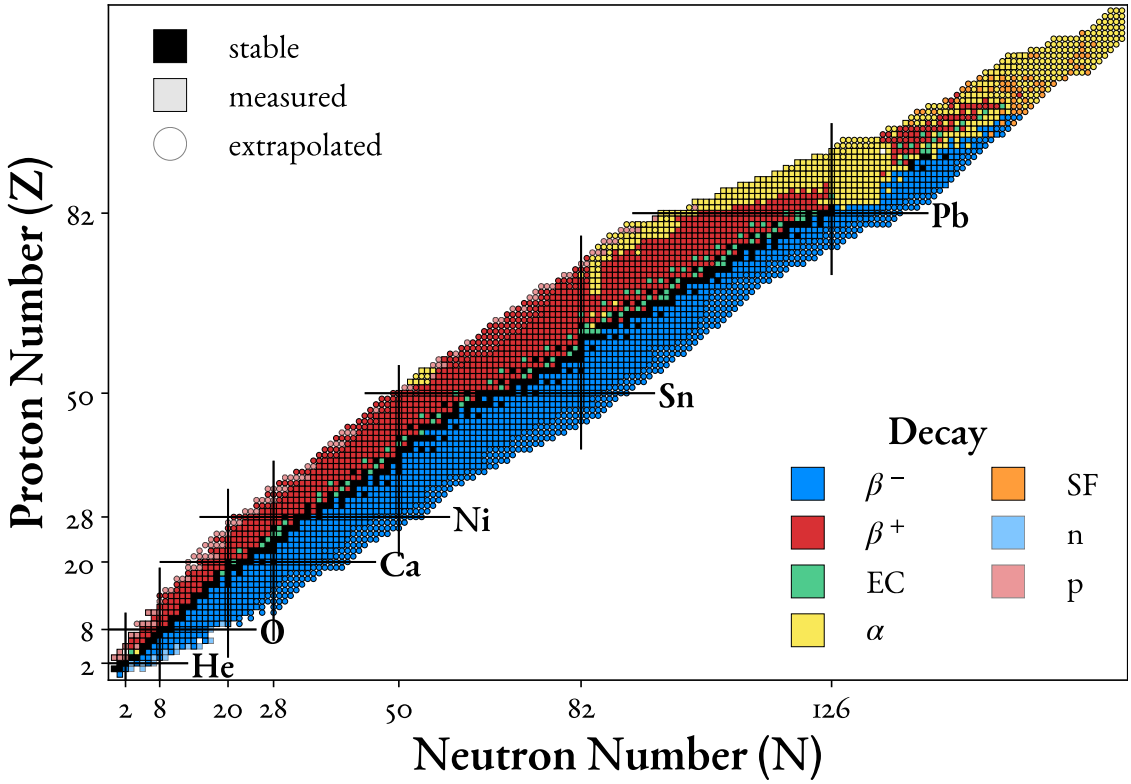


Figure 1.1: Segrè chart for nuclei listed in the Atomic Mass Evaluation (Wang et al. 2021a), listed by decay mode. Figure produced with the GitHub package from Karthein 2024.

Figure 1.1 shows all observed or extrapolated nuclei by 2020. The three major frameworks for nuclear structure are *ab initio*, shell model, and mean-field or density functional theory. *Ab initio* consists mostly of reductionist and vertical methods, based on solving the many-body Hamiltonian from interactions between nucleons, utilising protons and neutrons as the relevant degrees of freedom. The interaction between nucleons for current *ab initio* calculations is derived from Chiral Effective Field Theory (χEFT). As an effective field theory, results coming from χEFT have the advantage of providing a systematic way to quantify theoretical uncertainties associated with the truncation of the chiral expansion (Ekström et al. 2023). The clear downside of having, in general, a reductionist and vertical theory is that the full configuration space grows exponentially with the system size. This hinders the applicability of the method, as computing heavy systems is increasingly demanding. Moreover, describing properties of medium-heavy nuclei, even when computationally possible, remains an outstanding challenge (Machleidt and Sammarruca 2024). Nevertheless, it remains a lively area of research, with various techniques focused on solving the many-body problem—e.g., self-consistent Green's function, coupled cluster, in-medium similarity renormalisation group, no-core shell model, and quantum Monte Carlo (Hergert 2020).

The shell model, which comes from the pioneering work of Goeppert-Mayer 1949, also consists mostly of a vertical approach. It consists of selecting an inert core, typically a doubly-magic nucleus, choosing a configuration space, building an effective Hamiltonian, and diagonalising it within a truncated valence space to solve the many-body Schrödinger equation. Except for the no-core shell model, which falls under the umbrella of an *ab initio* method, shell model approaches typically use phenomenological effective Hamiltonians, which are adapted across the nuclear chart and are dependent on experimental data (Liu and Yuan 2023). Restricting the valence space due to the inert core makes it possible for shell-model calculations to reach higher masses than those of *ab initio*, but a rapidly growing dimensionality still means calculations in the mid-shells remain a known challenge.

Nuclear DFT, on the other hand, is quite different from both *ab initio* and shell model. It is rooted in the Hohenberg-Kohn theorem and Kohn-Sham theory (Hohenberg and Kohn 1964; Kohn and Sham 1965), which formally establishes the existence of a universal energy density functional (EDF) for which the solution of the many-body problem is exact. While the existence of such a functional is guaranteed, the form of the true nuclear EDF is unknown. In practice, EDFs are parametrised and calibrated in a more phenomenological way, where the free parameters are adjusted from nuclear structure data (Bender, Heenen and Reinhard 2003), even though the roots of nuclear DFT are those of an *ab initio*[*] and exact[†] theory (Bartlett 2010). The Kohn-Sham formulation allows us to map an interacting many-body system into an auxiliary many-body system

[*] In the sense of being from first principles.
[†] Which we cannot yet access in practice.

of non-interacting particles moving in a mean field. To this end, we use one-body densities as degrees of freedom, and the energy becomes a functional of these one-body densities. In practice, the auxiliary system from Kohn-Sham is represented by a product state. Consequently, the dynamical equations of the system take the same form as that of Hartree-Fock or Hartree-Fock-Bogoliubov (HFB), which is the reason behind the common use of these terms when referring to unpaired and paired nuclear DFT (Sheikh, Dobaczewski et al. 2021). Nuclear mean field solutions often break the symmetries of the underlying Hamiltonian, such that it constitutes a horizontal philosophy, deeply rooted in spontaneous symmetry-breaking. The restoration of broken symmetries, therefore, is an extension which takes the method beyond the mean field approximation (Sheikh, Dobaczewski et al. 2021). Overall, nuclear DFT is a unified approach capable of computing nuclear properties across the entirety of the nuclear chart. These features make DFT a powerful framework, especially for describing heavy and mid-shell nuclei, as covered in some chapters of this thesis.

1.2 Why proton-neutron pairing correlations?

The concept of pairing emerged from systematic experimental observations (Brink and Broglia 2005; Ring and Schuck 1980). Figure 1.2 represents one of these observations, which is the neutron separation energy. If $B(N,Z)$ is the binding energy of a nucleus with N neutrons and Z protons,

$$S_{1n}(N,Z) = B(N,Z) - B(N-1,Z) \tag{1.2.1}$$

is the energy required to separate the last neutron. As there is an odd-even staggering in nuclear masses/binding energies, the one-neutron separation energy S_{1n} is also observed to be larger for even neutron numbers than for odd ones. This reflects the additional energy associated with forming pairs: removing one neutron from the odd system makes it even; removing a neutron from an even system entails breaking a pair. To describe this phenomenon, early models such as the liquid drop model introduced a pairing term (Bethe and Bacher 1936; Weizsäcker 1935), which accounts for the evenness of the nucleus

$$\delta(N,Z) = \begin{cases} +\delta_0 \text{ if } N \text{ and } Z \text{ even} \\ 0 \text{ if } N+Z \text{ odd} \\ -\delta_0 \text{ if } N \text{ and } Z \text{ odd,} \end{cases} \tag{1.2.2}$$

indicating that a system with an even number of particles (be it N and/or Z) is more bound than one with an odd number of particles. Another example, which also led to the idea of pairing, is the difference in spectra of even-even and odd nuclei. While even-even nuclei have few levels, which can be interpreted as rotational and vibrational bands, odd nuclei have a much larger level density in the same energy interval. This can be understood if one considers that breaking a pair requires

more energy than the simple particle-hole excitations, which are possible at low energy cost in odd nuclei. Moments of inertia of deformed nuclei are another evidence of pairing, as superfluidity generates a departure from what is expected of a rigid body. Moreover, pair transfer reactions are sensitive to the correlations between the particles involved, and are both evidence of nuclear superfluidity and a very useful experimental tool to probe different pairing modes (Sagawa, Bai and Colò 2016).

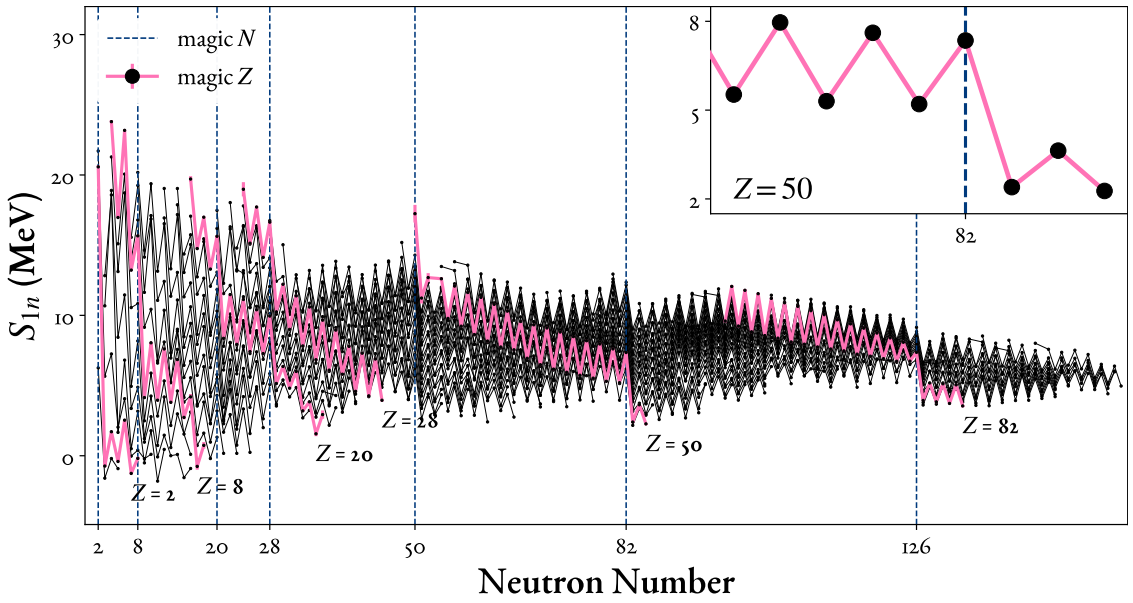


Figure 1.2: Experimental neutron separation energies from the Atomic Mass Evaluation (Wang et al. 2021a). Magic neutron and proton numbers are marked with dashed vertical lines and bold pink lines, respectively. The inset details Sn isotopes. Figure produced with the GitHub package from Karthein 2024.

From early on, pairing correlations started being understood as the result of a short-range attractive force (Goeppert-Mayer 1950). This point of view stands to this day, where the microscopic origin of pairing is largely attributed to the short-range attractive part of the underlying nucleon-nucleon interaction (Dean and Hjorth-Jensen 2003; Rios, Polls and Dickhoff 2017). Shortly after the theory of superconductivity was developed by Bardeen, Cooper and Schrieffer 1957, it was promptly adapted to superfluid nuclear systems (Bohr, Mottelson and Pines 1958; Cooper, Mills and Sessler 1959; Mills et al. 1959). Similarly, after the work of Bogoliubov 1958, HFB became a core feature of nuclear theories (e.g. in Marshalek 1965 and Satpathy, Goss and Banerjee 1969). Like-particle pairing has since become well established as a central aspect of nuclear structure.

On the other hand, the role of unlike-particle proton-neutron (pn) pairing remains an open subject (Frauendorf and Macchiavelli 2014; Qi 2026; Sagawa, Bai and Colò 2016). Close to the

$N = Z$ line, protons and neutrons occupy similar orbitals close to the Fermi surface. The large spatial overlap between the proton and neutron wavefunctions allows for different pairs, where they may couple to a total angular momentum $J = 0$ and total isospin $T = 1$ (called isovector pairing), or to total angular momentum $J = 1$ and total isospin $T = 0$ (called isoscalar pairing). This problem becomes particularly interesting for odd-odd $N = Z$ nuclei. Odd-odd nuclei are notoriously complicated systems for both theory and experiment. While experimentalists face an enormous level density, theorists must address dynamic core polarisation arising from the time-odd fields of unpaired nucleons. In the $N = Z$ line with *pn* pairing, further complications arise from the need to restore multiple broken symmetries (Romero, Dobaczewski and Pastore 2019). Moreover, $N = Z$ nuclei are also key systems in the study of isospin symmetry (Lenzi and Bentley 2009), a subject we shall study in this thesis. As *pn* pairing remains a central question, and experiments continuously access data for heavier nuclei close to the proton drip line, elucidating *pn* pairing from nuclear theory remains an outstanding open question in nuclear structure.

1.3 Thesis structure

This thesis is divided into four parts.

- Part I, to which this chapter belongs, introduces the framework for our research. Chapter 2 briefly introduces self-consistent many-body methods, which are the building blocks of everything that follows. Chapter 3 offers a perspective of what defines a paired state, starting from any many-body wavefunction.

- Part II consists of works within the topic of pairing. Chapter 4 introduces a novel approach to the description of proton-neutron paired states in infinite nuclear matter within nuclear DFT. Chapter 5 turns to the subject of finite nuclei, and discusses the assessment of pairing strengths in a study of electromagnetic moments. Chapter 6 introduces concepts related to isospin symmetry and tests thereof, showcasing the importance of proton-neutron pairing to the accurate description of nuclei close to the $N = Z$ line.

- Part III is devoted to research questions outside the topic of pairing. Chapter 7 introduces the problem of computing two-body magnetic dipole moments within nuclear DFT. Chapter 8 introduces a novel algorithm for computing finite-range interactions in DFT, which is crucial for enabling the progress of this increasingly resource-demanding theoretical framework, including that of pairing correlations. Chapter 9 briefly introduces equation of state studies for neutron stars within hadron effective models, showcasing some results of my work in the area. Lastly, Chapter 10 draws the conclusions from the collection of works presented.

- Part IV consists of the appendices, containing intricate details from the works of the previous chapters.

1.4 Reading guide

This thesis is written for readers with a strong background in quantum mechanics and nuclear physics. To allow for a stronger emphasis on original research, the introduction to the framework of nuclear DFT is a brief review rather than a detailed derivation. Chapters 4, 6, and 8 constitute the three major projects of my PhD, which were led by me. Therefore, the discussion therein is thorough. Chapters 5, 7, and 9 are contributions I made to larger research projects, so their discussion is more succinct.



Two

Self-consistent methods

For completeness, we briefly introduce the techniques we utilise to describe nuclear systems in the following chapters. Due to our focus on pairing, we introduce: (i) the Hartree-Fock-Bogoliubov (HFB) method for even and odd states, (ii) how to constrain calculations to desired expectation values, (iii) the most popular energy density functionals (EDFs), and (iv) the process of symmetry restoration.

> It would, indeed, be remarkable if Nature fortified herself against further advance in knowledge behind the analytical difficulties of the many-body problem.
>
> Max Born

This chapter serves the purpose of providing a summary, as textbooks on the topics discussed here are plentiful. Readers interested in many-body methods are referred to Ring and Schuck 1980 and Shavitt and Bartlett 2009, while those interested specifically in density functional theory are referred to Schunck 2019, Petkov and Stoitsov 1991, Dreizler and Gross 1990, and the introductory material by Colò 2018.

2.1 Hartree-Fock-Bogoliubov method

To account for pairing, we shall use the HFB formalism, and look for *quasiparticle* product states instead of the usual particle product states (Ring and Schuck 1980; Schunck 2019). The Bogoliubov transformation gives the quasiparticle creation and annihilation operators as combinations of particle creation and annihilation operators,

$$\alpha_\alpha^\dagger = \sum_\nu \left(A_{\nu\alpha} a_\nu^\dagger + B_{\nu\alpha} a_\nu\right), \tag{2.1.1}$$

$$\alpha_\alpha = \sum_\nu \left(A_{\nu\alpha}^* a_\nu + B_{\nu\alpha}^* a_\nu^\dagger\right), \tag{2.1.2}$$

respectively. The HFB vacuum is a zero-quasiparticle state

$$|\Psi\rangle = \mathcal{N} \prod_\nu \alpha_\nu |0\rangle, \quad \alpha_\nu |\Psi\rangle = 0, \tag{2.1.3}$$

where the product runs over the so-called essential quasiparticles α_ν, that is, those that do not annihilate the particle vacuum, $\alpha_\nu|0\rangle \neq 0$, and $\mathcal{N}$ is a normalisation constant. We note that: (i) if the number of essential quasiparticles is even (odd), the state $|\Psi\rangle$ is a linear combination of states with even (odd) numbers of particles, and (ii) the phase of state $|\Psi\rangle$ depends on the product of phases of all essential quasiparticles. For an even number of particles, the quasiparticle vacuum can also be expressed as the Thouless state (Thouless 1960), which corresponds to the most general pair condensate

$$|\Psi\rangle_{\text{even}} = \mathcal{N} \exp\left(\frac{1}{2}\sum_{\mu\nu} Z^*_{\mu\nu} a^+_\mu a^+_\nu\right)|0\rangle, \tag{2.1.4}$$

where $Z_{\mu\nu}$ is the anti-symmetric Thouless matrix, which is linked to the Bogoliubov transformation via $Z = BA^{-1}$, and $a^\dagger$ are the particle creation operators. This representation shall be incredibly useful for the work developed in Chapter 4, and is only valid for $\langle 0|\Psi\rangle_{\text{even}} \neq 0$, which is equivalent to A being non-singular. All the information about state $|\Psi\rangle$ is contained in the generalized density matrix

$$\mathscr{R} = \begin{pmatrix} \rho & \kappa \\ -\kappa^* & 1-\rho^* \end{pmatrix} = \begin{pmatrix} B^*B^T & B^*A^T \\ A^*B^T & A^*A^T \end{pmatrix}, \quad \mathscr{R}^2 = \mathscr{R}, \tag{2.1.5}$$

which commutes with the quasiparticle Hamiltonian. We can apply the variational principle using the pair-condensate state of eq. (2.1.4) as a trial wavefunction, which leads to the HFB equations $\mathscr{H}\mathscr{A} = \mathscr{A}\mathscr{E}$, or explicitly

$$\begin{pmatrix} h'-\lambda & \Delta \\ -\Delta^* & -h'^*+\lambda \end{pmatrix}\begin{pmatrix} \chi & \varphi \end{pmatrix} = \begin{pmatrix} \chi & \varphi \end{pmatrix}\begin{pmatrix} E & 0 \\ 0 & -E \end{pmatrix}, \tag{2.1.6}$$

where $\mathscr{A}$ is the Bogoliubov transformation,

$$\mathscr{A} = \begin{pmatrix} A & B^* \\ B & A^* \end{pmatrix}, \tag{2.1.7}$$

E is a diagonal matrix containing the quasiparticle energies, and $\mathscr{H}$ is the HFB matrix. h' is the single-particle (s.p.) Routhian operator, λ is the Fermi energy, and Δ is the pairing (or particle-particle) mean-field. Since h' depends on the density matrix ρ and Δ depends on the pairing tensor κ, defined in eq. 2.1.5, the HFB quasiparticle Hamiltonian $\mathscr{H}$ has to be diagonalised iteratively until the self-consistent solution $[\mathscr{H}, \mathscr{R}] = 0$ is found, that is, the columns of the Bogoliubov transformation $\mathscr{A}$ (the quasiparticle wave functions) become eigenstates of $\mathscr{H}$. For each state α, there is a quasiparticle χ_α with energy E_α and a quasihole φ_α with energy $-E_\alpha$. χ and φ can be written explicitly in terms of the matrices of the Bogoliubov transformation as

$$\chi = \begin{pmatrix} A \\ B \end{pmatrix}, \quad \varphi = \begin{pmatrix} B^* \\ A^* \end{pmatrix}. \tag{2.1.8}$$

χ and φ are eigenvectors of $\mathscr{R}$ with eigenvalues 0 or 1, respectively, so they refer to empty and occupied quasiparticle states. A schematic diagram for the self-consistent loop in the HFB method is given in Figure 2.1

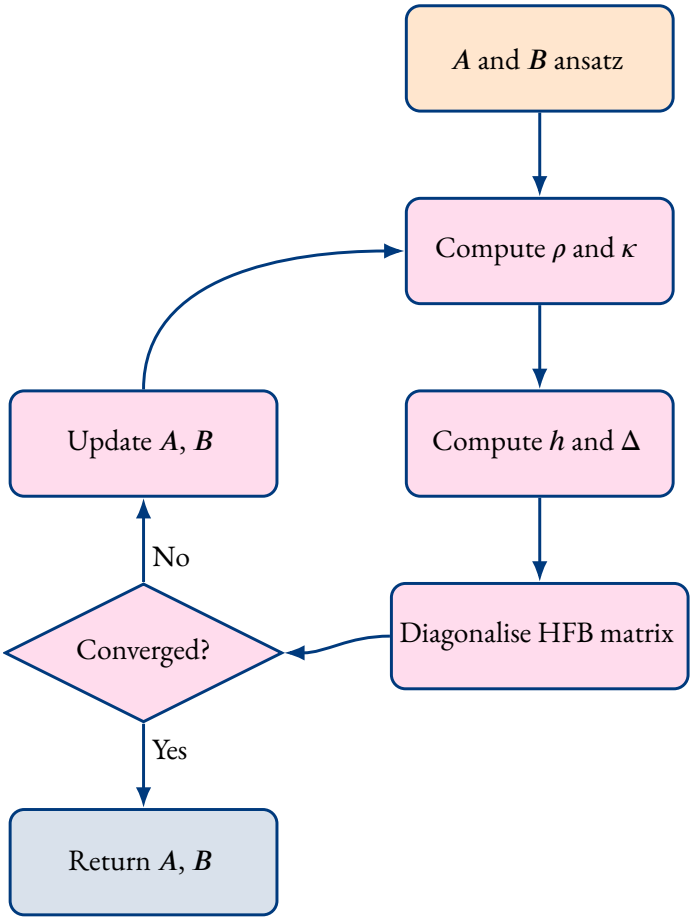


Figure 2.1: Schematic representation of the HFB method.

An important remark is that in the limit of zero pairing, where $\Delta = 0$, the HFB method is equivalent to Hartree-Fock. Moreover, the Bogoliubov transformation of eq. (2.1.2) mixes particle number. This is a canonical example of how breaking a symmetry can introduce new correlations to the system, and the quasiparticle vacuum of eq. (2.1.3) corresponds precisely to the definition of a horizontal approach to building correlations, from the definition given in Chapter 1. To circumvent the downside of this unwanted symmetry-breaking, one can perform a *constrained* calculation, in which Lagrange multipliers are utilised to fix the average value of an observable. A different option is to go from the symmetry-broken state to the symmetry-restored state via particle-number projection. We shall briefly discuss constrained calculations and symmetry restoration in Sections 2.2 and 2.4.

2.1.1 Odd particles: The blocking approximation

The blocking approximation is the standard tool for describing odd-A and odd-odd nuclei. Within this approach, a quasiparticle μ is created atop the even-even state of eq. (2.1.4)

$$|\Psi_\mu\rangle_{\text{odd}} = \mathcal{N}\alpha_\mu^\dagger \exp\left(-\frac{1}{2}\sum_{\mu\nu} Z^*_{\mu\nu} a^+_\mu a^+_\nu\right)|0\rangle. \tag{2.1.9}$$

This corresponds to replacing column χ_μ with the column with opposite energy φ_μ. After the column replacement, one of the s.p. states becomes fully occupied, and thus does not contribute to pairing correlations (see Chapter 3). The effects of blocking include an increase in the total energy of the system by the corresponding pair-breaking contribution and changes in deformation due to polarisation.

Moreover, it is important to select the correct desired blocked state, as it is responsible for the angular momentum of the nucleus, as long as the even subsystem is fully paired and has $J^\pi = 0^+$. One of the difficulties in solving the HFB equations for blocked states lies in accurately following the desired configuration, as the quasiparticle energies shift from one iteration to the next. To address this issue, the blocked configuration should be tagged so that the correct state is blocked in every stage (Dobaczewski, Satuła et al. 2009b; Wibowo, Backes et al. 2025). This relies on the following: In each iteration of the self-consistent loop, we must look for the largest overlap between the fixed-tag s.p. wave function, ϕ_μ, and the quasiparticle states. Scanning the two-component quasiparticle wave functions $\varphi_\nu = \begin{pmatrix} B^*_\nu \\ A^*_\nu \end{pmatrix}$, we determine the overlaps between the upper B^*_ν and the lower time-reversed component $\hat{T}A^*_\nu\hat{T}$, keeping the greater of the two $\mathcal{O}_\nu = \max\left((\phi_\mu|B^*_\nu), (\phi_\mu|\hat{T}A^*_\nu\hat{T})\right)$. The quasiparticle with the greatest overlap with the s.p. state is then chosen to be blocked during that iteration. This procedure is insensitive to whether the quasiparticles are of the particle or hole variety, as it follows the desired state despite of eventual crossing of the Fermi energy.

2.2 Constrained calculations

Notably, self-consistent solutions from the procedure of Section 2.1 only yield results for the (hopefully global) minima of a potential energy surface. To cover different conditions—e.g., to compute the potential energy surface as a function of different electromagnetic moments, or simply to fix the average particle number from an HFB calculation—we must obtain a wavefunction which minimises the energy under a *constrained* expectation value. If an observable $\hat{Q}$ must have the expectation value q,

$$q = \langle\Psi|\,\hat{Q}\,|\Psi\rangle\,, \tag{2.2.1}$$

we can add a Lagrange multiplier to the Hamiltonian $\mathscr{H}$, and minimise the total

$$\langle \mathscr{H}' \rangle = \langle \mathscr{H} \rangle - \lambda \langle \hat{Q} \rangle, \tag{2.2.2}$$

where λ is determined after linking eq. (2.2.1). Procedures such as the Augmented Lagrangian Method are more robust enforcements of constrained self-consistent calculations (Staszczak et al. 2010).

2.3 Nuclear density functional theory

As briefly discussed in Chapter 1, the dynamical equations of paired density functional theory (DFT) take the same form as that of HFB, although with a different interpretation and an interaction carried out in the form of an EDF. The nuclear EDF can be split into different terms: kinetic, potential, pairing, Coulomb, and centre-of-mass correction

$$\mathscr{E}[\rho, \kappa^*, \kappa] = \mathscr{E}_{\text{kin}}[\rho] + \mathscr{E}_{\text{pot}}[\rho] + \mathscr{E}_{\text{pair}}[\rho, \kappa^*, \kappa] + \mathscr{E}_{\text{Cou}}[\rho] + \mathscr{E}_{\text{c.o.m}}[\rho], \tag{2.3.1}$$

where ρ and κ are the normal and anomalous density matrices. The nuclear forces comprise the potential part, which can have many different forms and parametrisations. Note that EDFs are expressed in terms of different densities and derivatives of densities, such as the kinetic density τ, spin density $\mathbf{s}$, and current density $\mathbf{j}$. Further information on this decomposition and different nuclear EDFs can be found in Schunck 2019. Here we briefly list the two most famous types of functional generators, which we utilise throughout this thesis.

2.3.1 The Gogny EDF

Introduced by Dechargé and Gogny 1980, this consists of a finite-range functional generator, based on a sum of two Gaussians of different ranges. The goal behind this generator was to have a unified treatment of particle-hole and particle-particle correlations at the HFB level. The Gogny force reads

$$\begin{aligned} V_{\text{Gogny}}(\vec{r}_1, \vec{r}_2) \quad = \quad & \sum_{j=1}^{2} e^{-\frac{|\vec{r}_1 - \vec{r}_2|^2}{\mu_j^2}} \left(W_j + B_j P_\sigma - H_j P_\tau - M_j P_\sigma P_\tau \right) \\ & + t_3 \left(1 + x_0 P_\sigma\right) \delta(\vec{r}_1 - \vec{r}_2) \rho^\alpha \left(\frac{\vec{r}_1 + \vec{r}_2}{2} \right) \\ & + i W_{ls} \left(\vec{\sigma}_1 + \vec{\sigma}_2\right) \cdot \vec{k}^\dagger \times \delta(\vec{r}_1 - \vec{r}_2) \vec{k}, \end{aligned} \tag{2.3.2}$$

where P_σ and P_τ are the spin and isospin exchange operators, respectively, and $\vec{k}$ is the relative momentum with adjoint $\vec{k}^\dagger$. The first line of eq. (2.3.2) corresponds to the sum of Gaussians, the second line is the density-dependent term, and the third is the spin-orbit interaction.

2.3.2 The Skyrme EDFs

First proposed by Skyrme 1959, the Skyrme family of forces now constitutes a class of zero-range, momentum-dependent forces which typically takes a form similar to

$$\begin{aligned} V_{\text{Skyrme}}(\vec{r}_1,\vec{r}_2) &= t_0\left(1+x_0P_\sigma\right)\delta(\vec{r}_1-\vec{r}_2)+\frac{1}{2}t_1\left(1+x_1P_\sigma\right)\left(\vec{k}^{\dagger 2}\delta(\vec{r}_1-\vec{r}_2)+\delta(\vec{r}_1-\vec{r}_2)\vec{k}^2\right) \\ &\quad +t_2\left(1+x_2P_\sigma\right)\vec{k}^\dagger\cdot\delta(\vec{r}_1-\vec{r}_2)\vec{k}+\frac{1}{6}t_3\left(1+x_3P_\sigma\right)\delta(\vec{r}_1-\vec{r}_2)\rho^\alpha\left(\frac{\vec{r}_1+\vec{r}_2}{2}\right) \\ &\quad +iW_0\left(\vec{\sigma}_1+\vec{\sigma}_2\right)\cdot\vec{k}^\dagger\times\delta(\vec{r}_1-\vec{r}_2)\vec{k}. \end{aligned} \tag{2.3.3}$$

Note that, as there are no finite-range terms, the computational burden associated with Skyrme DFT calculations is considerably less than that of Gogny.

2.4 Beyond mean-field: Restoration of broken symmetries

As we alluded to when first introducing nuclear DFT, and later exemplified by HFB, mean-field solutions may break symmetries of the many-body Hamiltonian. A typical terminology in the literature is that symmetries of a state are broken in the intrinsic frame, whereas the laboratory frame refers to the state after symmetry restoration. The procedure behind restoring broken symmetries is denoted *projection*, and is rooted in group theory. A complete review of projection techniques is given by Sheikh, Dobaczewski et al. 2021. Within the topic of nuclear electromagnetic moments—which is relevant for Chapters 5, 6, and 7—it is imperative to restore rotational symmetry through angular momentum projection. This procedure is detailed in Section 7 of Dobaczewski, Backes et al. 2026.

Three

What is pairing?

Hitherto, we have mentioned or discussed the effects of pairing, such as differences in the spectra of even-even and odd nuclei, and the odd-even staggering. In this chapter, rather than observing the effects or questioning the origin of pairing, we shall understand what constitutes a paired state.

3.1 What are pairing correlations?

The question we pose in the title of this chapter is part of a category of *easily asked* and *hardly answered* questions. One way of understanding pairing is to observe the experimental facts which led to the idea of pairing correlations, and link these facts to the short-range part of the nucleon-nucleon interaction. Here, we approach the title question in a somewhat orthogonal manner to this notion. A common theme throughout this thesis is utilising the many-body wavefunction as a starting point to our understanding of physical properties. Therefore, before considering the consequences of pairing interactions among indistinguishable fermions in many-body systems, we shall analyse the fundamental aspects of *identifying* pairs of fermions within many-body wavefunctions. First, we shall consider the particle number operator $\hat{N}_\mu = a_\mu^+ a_\mu$. This operator is projective, $\hat{N}_\mu^2 = \hat{N}_\mu$, and thus can be seen as a measurement of the probability V_μ^2 of the single-particle (s.p.) state $|\mu\rangle$ being occupied in the fermion state $|\Psi\rangle$, with $V_\mu^2 = \langle\Psi|\hat{N}_\mu|\Psi\rangle$ and $0 \leq V_\mu^2 \leq 1$. Similarly, the projective operator $\hat{N}_\mu\hat{N}_\nu$, for $\mu \neq \nu$, built of two commuting projectors, $[\hat{N}_\mu, \hat{N}_\nu] = 0$, measures the probability $V_{\mu\nu}^2 = \langle\Psi|\hat{N}_\mu\hat{N}_\nu|\Psi\rangle$ that two s.p. states $|\mu\rangle$ and $|\nu\rangle$ are *simultaneously* occupied in the state $|\Psi\rangle$. We can now define the pairing correlation factor $C_{\mu\nu}$ as a surplus probability of finding both fermions simultaneously over the probability of finding them independently, that is,

$$\begin{aligned} C_{\mu\nu} &\equiv V_{\mu\nu}^2 - V_\mu^2 V_\nu^2 \\ &= \langle\Psi|\hat{N}_\mu\hat{N}_\nu|\Psi\rangle - \langle\Psi|\hat{N}_\mu|\Psi\rangle\langle\Psi|\hat{N}_\nu|\Psi\rangle. \end{aligned} \tag{3.1.1}$$

We emphasize that the definition of the pairing correlation factor $C_{\mu\nu}$ applies to any many-fermion wavefunction $|\Psi\rangle$. First, we observe that $C_{\mu\nu} = 0$ whenever the state $|\mu\rangle$ or $|\nu\rangle$ is either fully occupied or completely empty; that is, for $\hat{N}_\mu|\Psi\rangle = |\Psi\rangle$ or $\hat{N}_\mu|\Psi\rangle = 0$, or for $\hat{N}_\nu|\Psi\rangle = |\Psi\rangle$ or $\hat{N}_\nu|\Psi\rangle = 0$. This indicates that only partially occupied states can form correlated fermion pairs. To illustrate this issue, we may use the example of the simplest four-fermion state

$$|\mu\nu\alpha\beta\rangle = a^+_\mu a^+_\nu a^+_\alpha a^+_\beta|0\rangle, \tag{3.1.2}$$

where $a^+_\mu, \ldots, a^+_\beta$ represent the fermion creation operators in normalized and orthogonal s.p. states $|\mu\rangle, \ldots, |\beta\rangle$, with all indices different from one another, $\mu \neq \ldots \neq \beta$, and $|0\rangle$ represents the particle vacuum. We can write this state as different pair creation operators $\hat{P}^+_{\mu\nu} = a^+_\mu a^+_\nu$, $\hat{P}^+_{\mu\alpha} = a^+_\mu a^+_\alpha$,..., such that state (3.1.2) can be seen as six different fermion pairs, arranged in three different ways

$$|\mu\nu\alpha\beta\rangle \quad \equiv \quad \hat{P}^+_{\mu\nu}\hat{P}^+_{\alpha\beta}|0\rangle \equiv -\hat{P}^+_{\mu\alpha}\hat{P}^+_{\nu\beta}|0\rangle \equiv \hat{P}^+_{\mu\beta}\hat{P}^+_{\nu\alpha}|0\rangle, \tag{3.1.3}$$

or of any linear combination of them. We can now note that despite the possible representations of state (3.1.2) in terms of pairs (3.1.3), there are no correlated pairs in $|\mu\nu\alpha\beta\rangle$. If we consider pairing in the context of *correlations*, this state is simply unpaired. Moreover, because state (3.1.3) is invariant under the unitary mixing of the four s.p. states $|\mu\rangle, \ldots, |\beta\rangle$, none of the mixed states can form correlated pairs either. We shall now analyse more intricate examples of how eq. (3.1.1) can help us identify pairing correlations.

3.1.1 The canonical basis

Perhaps one of the most valuable examples comes from what is called the *canonical basis* for product states. This corresponds to the basis on which the density matrix, ρ, is diagonal

$$\tilde{\rho}_{\mu\nu} = v^2_\mu \delta_{\mu\nu}, \qquad \tilde{\rho} = \begin{pmatrix} v^2_1 & & & & & \\ & \ddots & & & & \\ & & v^2_\mu & & & \\ & & & v^2_\mu & & \\ & & & & \ddots & \\ & & & & & v^2_1 \end{pmatrix}, \tag{3.1.4}$$

where the v_μ^2 correspond to the occupation probabilities. In this basis, the pairing tensor is antidiagonal

$$\tilde{\kappa}_{\mu\nu} = s_{\bar{\mu}} u_\mu v_\mu \delta_{\bar{\mu}\nu}, \qquad \tilde{\kappa} = \begin{pmatrix} & & & & & & u_1 v_1 \\ & & & & & \iddots & \\ & & & & u_\mu v_\mu & & \\ & & & -u_\mu v_\mu & & & \\ & & \iddots & & & & \\ -u_1 v_1 & & & & & & \end{pmatrix}. \tag{3.1.5}$$

The barred state, $\bar{\mu}$, corresponds to the "partner" of the μ-th state, and is said to be canonically conjugated or time-reversed. u_μ^2 corresponds to the probability that μ is unoccupied, and is linked to v_μ via the normalisation condition

$$u_\mu^2 + v_\mu^2 = 1, \tag{3.1.6}$$

and $s_{\bar{\mu}} = -s_\mu$ corresponds to a phase factor, $s_\mu^* s_\mu = 1$. On the right side of eq. (3.1.5), we have utilised the convention of $s_\mu = 1$, which is commonly adopted in literature. In the canonical basis, the quasiparticle vacuum corresponds to the simple form of a Bardeen–Cooper–Schrieffer state

$$|\Psi\rangle = e^{i\phi} \prod_{\nu>0} \left(u_\nu + s_\nu v_\nu a_{\bar{\nu}}^+ a_\nu^+\right) |0\rangle, \tag{3.1.7}$$

where the product runs over $\nu > 0$. This indicates that only labels without a bar are present, which suffices to cover all canonically conjugated pairs. Note that eq. (3.1.6) normalises the state (3.1.7). To compute the correlation factor for this state, we may start by separating the product into

$$|\Psi\rangle = e^{i\phi} \left(u_\mu + s_\mu v_\mu a_{\bar{\mu}}^+ a_\mu^+\right) \prod_{\nu>0, \nu\neq\mu} \left(u_\nu + s_\nu v_\nu a_{\bar{\nu}}^+ a_\nu^+\right) |0\rangle = \left(u_\mu + s_\mu v_\mu a_{\bar{\mu}}^+ a_\mu^+\right) |\Psi_{\text{no }\mu}\rangle, \tag{3.1.8}$$

so that the expectation value of the particle-number operator simplifies to

$$\begin{aligned} \langle\Psi|\hat{N}_\mu|\Psi\rangle &= \langle\Psi|a_\mu^+ a_\mu|\Psi\rangle \\ &= \langle\Psi_{\text{no }\mu}|(u_\mu + s_\mu^* v_\mu a_\mu a_{\bar{\mu}}) a_\mu^+ a_\mu (u_\mu + s_\mu v_\mu a_{\bar{\mu}}^+ a_\mu^+)|\Psi_{\text{no }\mu}\rangle \\ &= v_\mu^2, \end{aligned} \tag{3.1.9}$$

where terms containing only u_μ, or mixing v_μ and u_μ, vanish due to an unequal number of creation and annihilation operators. This explicitly verifies the previous statement that the factor v_μ^2 corresponds to the average number of fermions occupying the μ-th state of the canonical basis. As the next step on obtaining the correlation factor, we shall use the following relation for a fermionic system and operators $ABCD$, coming from Wick's theorem (Shavitt and Bartlett 2009):

$$\langle\Psi|ABCD|\Psi\rangle = \langle\Psi|AB|\Psi\rangle\langle\Psi|CD|\Psi\rangle - \langle\Psi|AC|\Psi\rangle\langle\Psi|BD|\Psi\rangle + \langle\Psi|AD|\Psi\rangle\langle\Psi|BC|\Psi\rangle. \tag{3.1.10}$$

This result simplifies the expectation value of states μ and ν being simultaneously occupied

$$\begin{aligned}\langle\Psi|\hat{N}_\mu\hat{N}_\nu|\Psi\rangle &= \langle\Psi|a_\mu^+a_\mu a_\nu^+a_\nu|\Psi\rangle \\ &= \langle\Psi|a_\mu^+a_\mu|\Psi\rangle\langle\Psi|a_\nu^+a_\nu|\Psi\rangle - \langle\Psi|a_\mu^+a_\nu^+|\Psi\rangle\langle\Psi|a_\mu a_\nu|\Psi\rangle + \langle\Psi|a_\mu^+a_\nu|\Psi\rangle\langle\Psi|a_\mu a_\nu^+|\Psi\rangle \\ &= v_\mu^2v_\nu^2 - \langle\Psi|a_\mu^+a_\nu^+|\Psi\rangle\langle\Psi|a_\mu a_\nu|\Psi\rangle + \langle\Psi|a_\mu^+a_\nu|\Psi\rangle\langle\Psi|a_\mu a_\nu^+|\Psi\rangle. \end{aligned} \tag{3.1.11}$$

It is useful to analyse the remaining terms carefully. Explicitly, we have

$$\langle\Psi|a_\mu^+a_\nu^+|\Psi\rangle = \langle 0|\prod_{\alpha>0}(u_\alpha + s_\alpha^*v_\alpha a_\alpha a_{\bar{\alpha}})a_\mu^+a_\nu^+\prod_{\beta>0}(u_\beta + s_\beta v_\beta a_{\bar{\beta}}^+a_\beta^+)|0\rangle. \tag{3.1.12}$$

By looking at the terms coming from the full bra, $\langle\Psi|$, it is easy to see that this term vanishes if μ and ν are not canonically conjugated. We can rewrite (3.1.12) as

$$\begin{aligned}\langle\Psi|a_\mu^+a_\nu^+|\Psi\rangle &= \langle\Psi|a_\mu^+a_{\bar{\mu}}^+|\Psi\rangle\delta_{\bar{\mu}\nu} \\ &= \langle\Psi_{\text{no }\mu}|(u_\mu + s_\mu^*v_\mu a_\mu a_{\bar{\mu}})a_\mu^+a_{\bar{\mu}}^+(u_\mu + s_\mu v_\mu a_{\bar{\mu}}^+a_\mu^+)|\Psi_{\text{no }\mu}\rangle\delta_{\bar{\mu}\nu} \\ &= -s_\mu^*v_\mu u_\mu\delta_{\bar{\mu}\nu}, \end{aligned} \tag{3.1.13}$$

and analogously

$$\begin{aligned}\langle\Psi|a_\mu a_\nu|\Psi\rangle &= \langle\Psi|a_\mu a_{\bar{\mu}}|\Psi\rangle\delta_{\bar{\mu}\nu} \\ &= \langle\Psi_{\text{no }\mu}|(u_\mu + s_\mu^*v_\mu a_\mu a_{\bar{\mu}})a_\mu a_{\bar{\mu}}(u_\mu + s_\mu v_\mu a_{\bar{\mu}}^+a_\mu^+)|\Psi_{\text{no }\mu}\rangle\delta_{\bar{\mu}\nu} \\ &= u_\mu s_\mu v_\mu\delta_{\bar{\mu}\nu}. \end{aligned} \tag{3.1.14}$$

The remaining terms, $\langle\Psi|a_\mu^+a_\nu|\Psi\rangle$ and $\langle\Psi|a_\mu a_\nu^+|\Psi\rangle$, are zero for $\mu \neq \nu$, and hence are irrelevant for evaluating correlated pairs. Finally, the correlation factor reads

$$C_{\mu\nu} = u_\mu^2v_\mu^2\delta_{\nu\bar{\mu}}. \tag{3.1.15}$$

This very interesting result shows that the probability of finding canonically conjugated pairs is *higher* than the product of the probabilities of finding them individually. This is the very core of the concept of pairing in many-body systems. Moreover, we can also see explicitly that if the states are fully occupied ($v_\mu = 1, u_\mu = 0$), the correlation factor is zero. Again, only partly occupied states can be correlated, which comes naturally for states with mixed particle number. This is a beautiful aspect of Hartree-Fock-Bogoliubov theory, where we break a symmetry of the nuclear system (particle number), and in return we obtain an accurate description of pairing correlations, which we know are also a feature of nuclear systems.

3.1.2 Correlations of a single Thouless pair

As another example, which is intrinsically related to Chapter 4, we shall compute the correlation factor for a wavefunction of the form

$$|\Psi\rangle = \frac{1}{2}\sum_{\alpha\beta} Z^*_{\alpha\beta} a^+_\alpha a^+_\beta |0\rangle . \tag{3.1.16}$$

This corresponds to the single-pair term of a Thouless condensate,

$$|Z\rangle = \exp\left\{\frac{1}{2}\sum_{\alpha\beta} Z^*_{\alpha\beta} a^+_\alpha a^+_\beta\right\} |0\rangle . \tag{3.1.17}$$

The probability that the state $|\mu\rangle$ is occupied is given by

$$\begin{aligned} \langle\Psi|\,\hat{N}_\mu\,|\Psi\rangle &= \langle\Psi|\,a^+_\mu a_\mu\,|\Psi\rangle \\ &= \frac{1}{4}\sum_{\alpha\beta}\sum_{\gamma\delta} Z_{\delta\gamma} Z^*_{\alpha\beta}\,\langle 0|\,a_\gamma a_\delta a^+_\mu a_\mu a^+_\alpha a^+_\beta\,|0\rangle . \end{aligned} \tag{3.1.18}$$

The vacuum expectation value of creation and annihilation operators can be obtained via the Wick theorem, and is given by the fully contracted terms*. Given that

$$\overbracket{a_i a^+_j} = \delta_{ij} \quad , \quad \overbracket{a^+_i a_j} = \overbracket{a_i a_j} = \overbracket{a^+_i a^+_j} = 0, \tag{3.1.19}$$

eq. (3.1.18) reduces to

$$\begin{aligned} \langle\Psi|\,\hat{N}_\mu\,|\Psi\rangle &= \frac{1}{4}\sum_{\alpha\beta}\sum_{\gamma\delta} Z_{\delta\gamma} Z^*_{\alpha\beta} \left(\overbracket{a_\gamma a_\delta a^+_\mu a_\mu a^+_\alpha a^+_\beta} + \overbracket{a_\gamma a_\delta a^+_\mu a_\mu a^+_\alpha a^+_\beta} + \overbracket{a_\gamma a_\delta a^+_\mu a_\mu a^+_\alpha a^+_\beta} + \overbracket{a_\gamma a_\delta a^+_\mu a_\mu a^+_\alpha a^+_\beta} \right) \\ &= \frac{1}{4}\sum_{\alpha\beta}\sum_{\gamma\delta} Z_{\delta\gamma} Z^*_{\alpha\beta} \left(\delta_{\gamma\mu}\delta_{\delta\alpha}\delta_{\mu\beta} - \delta_{\gamma\alpha}\delta_{\delta\mu}\delta_{\mu\beta} - \delta_{\gamma\mu}\delta_{\delta\beta}\delta_{\mu\alpha} + \delta_{\gamma\beta}\delta_{\delta\mu}\delta_{\mu\alpha} \right) \\ &= \frac{1}{4}\sum_{\alpha\beta}\sum_{\gamma\delta} \left(Z^*_{\alpha\mu} Z_{\alpha\mu} + Z^*_{\mu\beta} Z_{\mu\beta} - Z^*_{\alpha\mu} Z_{\mu\alpha} - Z^*_{\mu\beta} Z_{\beta\mu} \right) \\ &= \sum_\alpha |Z_{\alpha\mu}|^2 . \end{aligned} \tag{3.1.20}$$

*As a crude "user's guide", the rules for looking at the following diagrammatic expressions are: (i) All creation and annihilation operators must be connected; (ii) Only lines connecting an annihilation operator on the left and a creation operator on the right are allowed; (iii) The final result will be expressed in terms of deltas, following the definition given in eq. (3.1.19); (iv) The sign accompanying the deltas corresponds to $(-1)^c$, where c is the number of line crossings. Readers are referred to Shavitt and Bartlett 2009, Chapter 3, for a formal and detailed introduction to Wick's theorem and its use in computing matrix elements of many-body systems.

Similarly, the probability that both $|\mu\rangle$ and $|\nu\rangle$ are simultaneously occupied is given by the eight Wick contractions

$$\langle\Psi|\,\hat{N}_\mu\hat{N}_\nu\,|\Psi\rangle = \frac{1}{4}\sum_{\alpha\beta}\sum_{\gamma\delta} Z_{\delta\gamma}Z^*_{\alpha\beta}\Big(a_\gamma a_\delta a^+_\mu a_\mu a^+_\nu a_\nu a^+_\alpha a^+_\beta + a_\gamma a_\delta a^+_\mu a_\mu a^+_\nu a_\nu a^+_\alpha a^+_\beta + a_\gamma a_\delta a^+_\mu a_\mu a^+_\nu a_\nu a^+_\alpha a^+_\beta$$
$$+ a_\gamma a_\delta a^+_\mu a_\mu a^+_\nu a_\nu a^+_\alpha a^+_\beta + a_\gamma a_\delta a^+_\mu a_\mu a^+_\nu a_\nu a^+_\alpha a^+_\beta + a_\gamma a_\delta a^+_\mu a_\mu a^+_\nu a_\nu a^+_\alpha a^+_\beta$$
$$+ a_\gamma a_\delta a^+_\mu a_\mu a^+_\nu a_\nu a^+_\alpha a^+_\beta + a_\gamma a_\delta a^+_\mu a_\mu a^+_\nu a_\nu a^+_\alpha a^+_\beta\Big)$$

$$= \frac{1}{4}\sum_{\alpha\beta}\sum_{\gamma\delta} Z_{\delta\gamma}Z^*_{\alpha\beta}\left(-\delta_{\gamma\mu}\delta_{\delta\nu}\delta_{\mu\alpha}\delta_{\nu\beta} - \delta_{\gamma\alpha}\delta_{\delta\mu}\delta_{\mu\nu}\delta_{\nu\beta} + \delta_{\gamma\nu}\delta_{\delta\mu}\delta_{\mu\alpha}\delta_{\nu\beta} + \delta_{\gamma\mu}\delta_{\delta\alpha}\delta_{\mu\nu}\delta_{\nu\beta}\right.$$
$$\left. +\delta_{\gamma\beta}\delta_{\delta\mu}\delta_{\mu\nu}\delta_{\nu\alpha} - \delta_{\gamma\mu}\delta_{\delta\beta}\delta_{\mu\nu}\delta_{\nu\alpha} - \delta_{\gamma\nu}\delta_{\delta\mu}\delta_{\mu\beta}\delta_{\nu\alpha} + \delta_{\gamma\mu}\delta_{\delta\nu}\delta_{\mu\beta}\delta_{\nu\alpha}\right)$$

$$= |Z_{\mu\nu}|^2 + \sum_\alpha Z^*_{\alpha\nu}Z_{\alpha\mu}\underbrace{\delta_{\mu\nu}}_{=0}. \tag{3.1.21}$$

Note that, as eq. (3.1.16) is *not* a product state, we cannot use (3.1.10), and the expressions above for the vacuum expectation value are a compact way of obtaining $V_{\mu\nu}$. As the expectation values should be normalised, we must write

$$\langle\Psi|\Psi\rangle = \frac{1}{4}\sum_{\alpha\beta}\sum_{\gamma\delta} Z_{\delta\gamma}Z^*_{\alpha\beta}\Big(a_\gamma a_\delta a^+_\alpha a^+_\beta + a_\gamma a_\delta a^+_\alpha a^+_\beta\Big)$$
$$= \frac{1}{4}\sum_{\alpha\beta}\sum_{\gamma\delta} Z_{\delta\gamma}Z^*_{\alpha\beta}\left(-\delta_{\gamma\alpha}\delta_{\delta\beta} + \delta_{\gamma\beta}\delta_{\delta\alpha}\right)$$
$$= \frac{1}{2}\sum_{\alpha\beta}|Z_{\alpha\beta}|^2. \tag{3.1.22}$$

Finally, considering the collective pairs of (3.1.16), we obtain the correlation factor

$$C_{\mu\nu} = 2\frac{|Z_{\mu\nu}|^2}{\sum_{\alpha\beta}|Z_{\alpha\beta}|^2} - \frac{4\sum_{\alpha\beta}|Z_{\alpha\mu}|^2|Z_{\beta\nu}|^2}{\sum_{\alpha\beta\gamma\delta}|Z_{\alpha\beta}|^2|Z_{\gamma\delta}|^2}. \tag{3.1.23}$$

Unlike the correlation factor in the canonical basis, eq. (3.1.23) is not strictly positive. This shows that the single-pair term of a Thouless condensate can be correlated, uncorrelated, or anti-correlated, depending on the structure of the Thouless matrix.

3.2 Pairing correlation factors of mixed states

Lastly, we shall derive properties of the pairing correlation factor (3.1.1) under the unitary mixing of the s.p. states $|\mu\rangle$ and $|\nu\rangle$,

$$a^+_{\mu'} = e^{i\psi_{\mu'}}\left(\cos(\delta)a^+_\mu + \sin(\delta)a^+_\nu\right), \tag{3.2.1}$$
$$a^+_{\nu'} = e^{i\psi_{\nu'}}\left(\sin(\delta)a^+_\mu - \cos(\delta)a^+_\nu\right). \tag{3.2.2}$$

The particle number operators are

$$\begin{aligned}
\hat{N}_{\mu'} = a^+_{\mu'}a_{\mu'} &= \left(\cos(\delta)a^+_\mu + \sin(\delta)a^+_\nu\right)\left(\cos(\delta)a_\mu + \sin(\delta)a_\nu\right) \\
&= \cos^2(\delta)\hat{N}_\mu + \sin^2(\delta)\hat{N}_\nu + \cos(\delta)\sin(\delta)\hat{N}_{\mu\nu}, \qquad (3.2.3)\\
\hat{N}_{\nu'} = a^+_{\nu'}a_{\nu'} &= \left(\sin(\delta)a^+_\mu - \cos(\delta)a^+_\nu\right)\left(\sin(\delta)a_\mu - \cos(\delta)a_\nu\right) \\
&= \sin^2(\delta)\hat{N}_\mu + \cos^2(\delta)\hat{N}_\nu - \cos(\delta)\sin(\delta)\hat{N}_{\mu\nu}, \qquad (3.2.4)
\end{aligned}$$

where the hermitian operator $\hat{N}_{\mu\nu}$ reads,

$$\hat{N}_{\mu\nu} = a^+_\mu a_\nu + a^+_\nu a_\mu = \tfrac{1}{2}\left((a^+_\mu + a^+_\nu)(a_\mu + a_\nu) - (a^+_\mu - a^+_\nu)(a_\mu - a_\nu)\right). \qquad (3.2.5)$$

Then we have,

$$\begin{aligned}
\hat{N}_{\mu'}\hat{N}_{\nu'} &= \left(\cos^2(\delta)\hat{N}_\mu + \sin^2(\delta)\hat{N}_\nu + \cos(\delta)\sin(\delta)\hat{N}_{\mu\nu}\right)\left(\sin^2(\delta)\hat{N}_\mu + \cos^2(\delta)\hat{N}_\nu - \cos(\delta)\sin(\delta)\hat{N}_{\mu\nu}\right) \\
&= \cos^2(\delta)\sin^2(\delta)\hat{N}_\mu + \cos^4(\delta)\hat{N}_\mu\hat{N}_\nu - \cos^3(\delta)\sin(\delta)\hat{N}_\mu\hat{N}_{\mu\nu} \\
&\quad + \sin^4(\delta)\hat{N}_\nu\hat{N}_\mu + \sin^2(\delta)\cos^2(\delta)\hat{N}_\nu - \sin^3(\delta)\cos(\delta)\hat{N}_\nu\hat{N}_{\mu\nu} \\
&\quad + \sin^3(\delta)\cos(\delta)\hat{N}_{\mu\nu}\hat{N}_\mu + \cos^3(\delta)\sin(\delta)\hat{N}_{\mu\nu}\hat{N}_\nu - \sin^2(\delta)\cos^2(\delta)\hat{N}^2_{\mu\nu}. \qquad (3.2.6)
\end{aligned}$$

However, it easy to check that

$$\begin{aligned}
\hat{N}_\mu\hat{N}_{\mu\nu} &= a^+_\mu a_\mu(a^+_\mu a_\nu + a^+_\nu a_\mu) = a^+_\mu a_\nu = (a^+_\mu a_\nu + a^+_\nu a_\mu)a^+_\nu a_\nu = \hat{N}_{\mu\nu}\hat{N}_\nu \qquad (3.2.7)\\
\hat{N}_\nu\hat{N}_{\mu\nu} &= a^+_\nu a_\nu(a^+_\mu a_\nu + a^+_\nu a_\mu) = a^+_\nu a_\mu = (a^+_\mu a_\nu + a^+_\nu a_\mu)a^+_\mu a_\mu = \hat{N}_{\mu\nu}\hat{N}_\mu \qquad (3.2.8)\\
\hat{N}^2_{\mu\nu} &= \hat{N}_\mu + \hat{N}_\nu - 2\hat{N}_\mu\hat{N}_\nu, \qquad (3.2.9)
\end{aligned}$$

which gives

$$\begin{aligned}
\hat{N}_{\mu'}\hat{N}_{\nu'} &= \cos^2(\delta)\sin^2(\delta)\hat{N}_\mu + \cos^4(\delta)\hat{N}_\mu\hat{N}_\nu + \sin^4(\delta)\hat{N}_\nu\hat{N}_\mu + \sin^2(\delta)\cos^2(\delta)\hat{N}_\nu \\
&\quad - \sin^2(\delta)\cos^2(\delta)\left(\hat{N}_\mu + \hat{N}_\nu\right) + 2\sin^2(\delta)\cos^2(\delta)\hat{N}_\mu\hat{N}_\nu = \hat{N}_\mu\hat{N}_\nu. \qquad (3.2.10)
\end{aligned}$$

Taking the average values of eqs. (3.2.3) and (3.2.4), for $N_{\mu\nu} \equiv \langle \hat{N}_{\mu\nu} \rangle$ we obtain the pairing correlation factor (3.1.1) of states $|\mu'\rangle$ and $|\nu'\rangle$,

$$\begin{aligned}
C_{\mu'\nu'} &= C_{\mu\nu} + V_\mu^2 V_\nu^2 \\
&\quad - \left(\cos^2(\delta) V_\mu^2 + \sin^2(\delta) V_\nu^2 + \cos(\delta)\sin(\delta) N_{\mu\nu}\right)\left(\sin^2(\delta) V_\mu^2 + \cos^2(\delta) V_\nu^2 - \cos(\delta)\sin(\delta) N_{\mu\nu}\right) \\
&= C_{\mu\nu} + \left(\cos^4(\delta) + 2\cos^2(\delta)\sin^2(\delta) + \sin^4(\delta)\right) V_\mu^2 V_\nu^2 \\
&\quad - \left(\cos^2(\delta) V_\mu^2 + \sin^2(\delta) V_\nu^2 + \cos(\delta)\sin(\delta) N_{\mu\nu}\right)\left(\sin^2(\delta) V_\mu^2 + \cos^2(\delta) V_\nu^2 - \cos(\delta)\sin(\delta) N_{\mu\nu}\right). \\
&= C_{\mu\nu} - \cos^2(\delta)\sin^2(\delta)\left(V_\mu^2 - V_\nu^2\right)^2 \\
&\quad - \left(\sin^2(\delta) V_\mu^2 + \cos^2(\delta) V_\nu^2 - \cos^2(\delta) V_\mu^2 - \sin^2(\delta) V_\nu^2\right)\cos(\delta)\sin(\delta) N_{\mu\nu} + \cos^2(\delta)\sin^2(\delta) N_{\mu\nu}^2. \\
&= C_{\mu\nu} - \cos^2(\delta)\sin^2(\delta)\left(V_\mu^2 - V_\nu^2\right)^2 \\
&\quad + \left(\cos^2(\delta) - \sin^2(\delta)\right)\left(V_\mu^2 - V_\nu^2\right)\cos(\delta)\sin(\delta) N_{\mu\nu} + \cos^2(\delta)\sin^2(\delta) N_{\mu\nu}^2. \\
&= C_{\mu\nu} - \tfrac{1}{4}\left(V_\mu^2 - V_\nu^2\right)^2 + \tfrac{1}{4}\left(\cos(2\delta)\left(V_\mu^2 - V_\nu^2\right) + \sin(2\delta) N_{\mu\nu}\right)^2. \qquad (3.2.11)
\end{aligned}$$

For a pair of states in the canonical basis, for which all off-diagonal matrix elements vanish, $\langle \Psi | a_\mu^+ a_\nu | \Psi \rangle = 0$ for $\mu \neq \nu$, we have $N_{\mu\nu} = 0$, and thus,

$$C_{\mu'\nu'} = C_{\mu\nu} - \tfrac{1}{4}\sin^2(2\delta)\left(V_\mu^2 - V_\nu^2\right)^2, \qquad (3.2.12)$$

that is, the pairing correlation factor of mixed states in the canonical basis is never larger than that of unmixed ones. If, in addition, the pair of states has degenerate occupation probabilities, $V_\mu^2 = V_\nu^2$, the pairing correlation factor becomes independent of the mixing,

$$C_{\mu'\nu'} = C_{\mu\nu}. \qquad (3.2.13)$$

As canonical pairs have degenerate occupation probabilities, this is always valid for states μ and $\bar{\mu}$. This interesting result shows that mixing does not affect the correlation of canonical pairs.

Part II

Proton-neutron pairing correlations

Four

Homogeneous and isotropic nuclear matter

We shall build our understanding of pairing correlations in nuclear matter by constructing the most general paired wavefunction, showing that one can separate the Thouless matrix into two different blocks, corresponding to different linear momentum-dependent subspaces. From the most general Thouless wavefunction, we will build the most general pairing tensor and density matrix through different approaches, and see that the proton-neutron pairing channels are mixed in nuclear matter, whereas the spin-isospin channels are not. As a result of the mixing, the proton-neutron structure of the paired wavefunction does not correspond to that of the pairing tensor.

> Ce qui est simple est toujours faux.
>
> Paul Valéry

After the theory of superconductivity was developed by Bardeen, Cooper and Schrieffer 1957, the idea was promptly adapted to the description of superfluid nuclear matter (NM) (Cooper, Mills and Sessler 1959; Emery and Sessler 1960; Mills et al. 1959). Nuclear superfluidity is analogous to electronic superconductivity, where pairs of time-reversed particles condensate near the Fermi surface. In the nuclear case, the isospin degree of freedom must also be accounted for. Typically, the allowed pairs are scalar-isovector (with total spin $S = 0$, isospin $T = 1$, and isospin projection $T_z = 0, \pm 1$), vector-isoscalar (with total spin $S = 1$, isospin $T = 0$, and spin projection $S_z = 0, \pm 1$), or scalar-isoscalar. Equivalently, neutrons (n) and protons (p) can form the standard nn, np, pn, and pp pairs.

Notably, pairing plays a crucial role on a neutron star's thermal evolution by suppressing the neutrino emission during the cooling stage (Yakovlev, Levenfish and Shibanov 1999), and may suppress exotic phases in the star's interior (Pelicer et al. 2023). Beyond the interests of nuclear astrophysics, models for NM can be used to study general features of the nuclear interaction. As the strong interaction governs both nuclei and astrophysical objects, a universal energy density functional (EDF) should be able to reproduce the properties of both vastly different systems. To

this end, the nucleon pairing gaps in infinite nuclear matter (INM) can be used to adjust new energy density functionals (Da Costa et al. 2024; Grams et al. 2025), which are suitable to describe both astrophysical phenomena and finite systems.

Within a different framework from density functional theory (DFT), the bare nucleon-nucleon (NN) interaction—i.e., a pair of nucleons interacting in free space—is typically expressed in terms of partial waves and phase shifts obtained from NN scattering experiments. The pairing gap is linked to the attractive part of the NN interaction, and an attractive (positive) phase shift corresponds to a positive pairing gap. Due to this relation, the energy dependence of the phase shifts offers valuable insight on which pair condensates are likely to be formed in different regions of a neutron star: the laboratory energy relates to the Fermi energy and momentum via $E_{\text{lab}} = 4\varepsilon_{\text{F}} = 4\hbar^2 k_F / 2M_N$ when considering a non-interacting Fermi gas*, and the Fermi momentum is linked to the density via $k_F = (3\pi^2\rho)^{1/3}$(Bohr and Mottelson 1998). Therefore, assessing the phase shifts for partial waves as a function of the laboratory energy allows us to draw a rough estimate of which pairing channels should appear in different density regimes. As shown in the review by Dean and Hjorth-Jensen 2003, the ${}^1S_0$ channel, following the spectroscopic notation (${}^{2S+1}L_J$), is the most attractive at low densities. Thus, it is also the most prominent in studies of pairing in NM from the NN interaction point of view, especially concerning neutron matter (e.g., Elgaroy and Hjorth-Jensen 1997; Pelicer et al. 2023). Proton-neutron (pn) pairing, on the other hand, is generally mentioned in the context of symmetric nuclear matter (Elgarøy et al. 1998; Yin et al. 2023). In these studies, pn pairing in INM relates to the ${}^3S_1$-${}^3D_1$ channel, which couple the S- and D-waves driven by the tensor part of the NN interaction. It is important to note that this approach relies on the in-medium pairing force being similar to its vacuum counterpart. The reader is referred to the in-depth review of the topic from the *ab initio* point of view by Dean and Hjorth-Jensen 2003.

In this chapter, we focus on the description of homogeneous and isotropic NM from a general perspective of paired DFT, irrespective of the interaction. This is appropriate to the use-case of both equation of state studies and EDF fitting. In all these approaches, one would often assume that building a pairing tensor with non-zero values between the specific desired proton-neutron channels would carry over that same information to the respective Hartree-Fock-Bogoliubov (HFB) wavefunction. However, what is the relationship between the structure of the pairing tensor and the wavefunction itself in nuclear matter? To address this question, we propose a different approach to the problem of proton-neutron pairs in INM. We move the horse before the cart by building a DFT wavefunction with a combination of all different ST channels, and from it we obtain the most general density matrix and pairing tensor of nuclear matter. We emphasize that through this procedure we do not make any assumptions about the interaction, which allows us to focus

*Note that for HFB calculations, the nucleons are in-medium and adopt an effective mass. Further commentary on this can be found in Section 2.3 of the article by Bender, Bennaceur and Guillon 2026.

solely on the relation between the wavefunction and the pairing tensor to obtain a general result applicable to any paired DFT solution of nuclear matter.

The structure of the chapter is as follows. We introduce the general properties of a paired wavefunction in nuclear matter in section 4.1, showing that we can divide the Thouless matrix into two linear-momentum-dependent sub-matrices. We then proceed to analyse the pairing tensor in nuclear matter in different cases: The simplest one is that of an anti-symmetric Thouless sub-matrix, for which we have a full analytic solution presented in section 4.3; The second case corresponds to z-aligned pairs, with zero spin and isospin z projection, presented in section 4.4; Finally, we generalise this approach in section 4.5, and obtain a general pairing tensor for pairs with an arbitrary orientation in spin and isospin space in section 4.6.

4.1 A general paired wavefunction

As discussed in Chapter 2, the core concept of nuclear DFT is to apply the variational principle to a many-body trial wavefunction. In the case of paired states, the trial wavefunction corresponds to the quasiparticle vacuum (Ring and Schuck 1980; Schunck 2019), which can be conveniently presented in the form of the unnormalised Thouless state representing the pair condensate $|Z\rangle$

$$|Z\rangle = \exp\left\{\hat{Z}^\dagger\right\}|0\rangle, \tag{4.1.1}$$

where $\hat{Z}^\dagger$ denotes the fermion pair creation operator, and $|0\rangle$ is the particle vacuum. When describing finite nuclei, the basis utilised in nuclear mean-field or shell-model approaches consists of M single-particle (s.p.) states. Thouless pairs $\hat{Z}^\dagger$ are then defined in terms of the fermion creation operators $a^\dagger_\mu$ for $\mu = 1, \dots M$,

$$\hat{Z}^\dagger = \tfrac{1}{2}\sum_{\mu\nu} Z^*_{\mu\nu} a^\dagger_\mu a^\dagger_\nu, \tag{4.1.2}$$

where $Z_{\mu\nu}$ are the elements of the complex antisymmetric $M \times M$ Thouless matrix, Z. The norms of condensates $\langle Z|Z\rangle$, pairing tensors $\kappa_{\mu\nu}$, and one-body density matrices $\rho_{\mu\nu}$ can be determined as follows (Ring and Schuck 1980; Schunck 2019),

$$\langle Z|Z\rangle = \det(1 + Z^\ddagger Z)^{1/2}, \tag{4.1.3}$$

$$\kappa_{\mu\nu} = \frac{\langle Z|a_\nu a_\mu|Z\rangle}{\langle Z|Z\rangle} = -\left(\left(1 + Z^\ddagger Z\right)^{-1} Z^\ddagger\right)_{\mu\nu}, \tag{4.1.4}$$

$$\rho_{\mu\nu} = \frac{\langle Z|a^\dagger_\nu a_\mu|Z\rangle}{\langle Z|Z\rangle} = \left(\left(1 + Z^\ddagger Z\right)^{-1} Z^\ddagger Z\right)_{\mu\nu}, \tag{4.1.5}$$

where the double dagger ($\ddagger$) represents the Hermitian conjugation of the antisymmetric pair amplitudes, $Z^\ddagger_{\mu\nu} \equiv Z^*_{\nu\mu} = -Z^*_{\mu\nu}$.

In nuclear matter, expressions (4.1.2)–(4.1.5) must be generalised to the relevant case of an infinite and continuous basis of space wavefunctions, combined with finite and discrete bases for spin and isospin. Limiting ourselves to the case of homogeneous (independent of *position*) and isotropic (independent of *direction*) nuclear matter, translational symmetry must be conserved. Hence, the single-particle wavefunctions of the basis should be eigenstates of linear momentum $\mathbf{k}$, forming a continuous and infinite basis, in contrast to the aforementioned finite and discrete basis of M-s.p. states for nuclei. Then, to also account for spin and isospin, the appropriate basis of INM is that of plane waves, spinors, and isospinors

$$\phi_{\mathbf{k}s_z t_z}(\mathbf{r}\sigma\tau) = (2\pi)^{-3/2}\, \mathrm{e}^{i\mathbf{k}\cdot\mathbf{r}} \chi_{s_z}(\sigma)\chi_{t_z}(\tau), \tag{4.1.6}$$

where $\sigma = \pm\frac{1}{2}$ and $\tau = \pm\frac{1}{2}$ are the spin and isospin projections, and $\chi_{s_z}(\sigma) = \delta_{s_z\sigma}$ and $\chi_{t_z}(\tau) = \delta_{t_z\tau}$ are the spinors and isospinors, respectively.

For the sake of clarity, we now omit the sub-indices z of s_z and t_z, and adopt lower case s and t when referring to the z-projection of spin and isospin. The pair-creation operator (4.1.2) in the aforementioned basis can be expressed in the momentum and coordinate representations as, respectively,

$$\hat{Z}^\dagger = \tfrac{1}{2}\int \mathrm{d}\mathbf{k}_1\mathrm{d}\mathbf{k}_2 \sum_{st,s't'} Z^*_{\mathbf{k}_1 st,\mathbf{k}_2 s't'} a^\dagger_{\mathbf{k}_1 st} a^\dagger_{\mathbf{k}_2 s't'}, \tag{4.1.7}$$

$$\hat{Z}^\dagger = \tfrac{1}{2}\int \mathrm{d}\mathbf{r}_1\mathrm{d}\mathbf{r}_2 \sum_{st,s't'} Z^*(\mathbf{r}_1 st,\mathbf{r}_2 s't') a^\dagger_{\mathbf{r}_1 st} a^\dagger_{\mathbf{r}_2 s't'}. \tag{4.1.8}$$

The antisymmetric momentum or position amplitudes, $Z^*_{\mathbf{k}_1 st,\mathbf{k}_2 s't'}$ or $Z^*(\mathbf{r}_1 st,\mathbf{r}_2 s't')$, should be represented by different symbols; for simplicity, we differentiate between them by using the indices or arguments, respectively. A double Fourier transform* relates the corresponding pair amplitudes as follows

$$Z^*(\mathbf{r}_1 st,\mathbf{r}_2 s't') = \int \frac{\mathrm{d}\mathbf{k}_1\mathrm{d}\mathbf{k}_2}{(2\pi)^3}\, \mathrm{e}^{i\mathbf{k}_1\cdot\mathbf{r}_1 + i\mathbf{k}_2\cdot\mathbf{r}_2} Z^*_{\mathbf{k}_1 st,\mathbf{k}_2 s't'}. \tag{4.1.9}$$

To assess translational invariance, it is useful to transform the integrals (4.1.9) to the standard total and relative momenta, $\mathbf{K} = \mathbf{k}_1 + \mathbf{k}_2$ and $\mathbf{k} = \frac{1}{2}(\mathbf{k}_1 - \mathbf{k}_2)$, leading to

$$Z^*(\mathbf{r}_1 st,\mathbf{r}_2 s't') = \int \frac{\mathrm{d}\mathbf{K}\mathrm{d}\mathbf{k}}{(2\pi)^3}\, \mathrm{e}^{i\mathbf{K}\cdot\mathbf{R} + i\mathbf{k}\cdot\mathbf{r}} Z^*_{\left(\frac{\mathbf{K}}{2}+\mathbf{k}\right)st,\left(\frac{\mathbf{K}}{2}-\mathbf{k}\right)s't'}, \tag{4.1.10}$$

where the centre-of-mass and relative coordinates are denoted by $\mathbf{R} = \frac{1}{2}(\mathbf{r}_1 + \mathbf{r}_2)$ and $\mathbf{r} = \mathbf{r}_1 - \mathbf{r}_2$. As we are concerned with homogeneous and isotropic nuclear matter, translational invariance is

*We have employed a unitary convention for the Fourier Transform, under which the transform and the inverse are both preceded by a factor of $\frac{1}{\sqrt{2\pi}}$.

conserved, which requires that the physics remain unchanged if the system is translated in space by **a**. Under such a transformation, we have

$$\begin{aligned} \mathbf{r}_1 &\to \mathbf{r}_1 + \mathbf{a}, & \mathbf{r}_2 &\to \mathbf{r}_2 + \mathbf{a}; \\ \mathbf{R} &\to \mathbf{R} + \mathbf{a}, & \mathbf{r} &\to \mathbf{r}. \end{aligned}$$

Thus, the right-hand side of eq. (4.1.10) cannot depend on the centre-of-mass coordinate **R**. In the momentum representation, this translates into the following pair amplitude

$$Z^*_{\mathbf{k}_1 st, \mathbf{k}_2 s't'} = \delta(\mathbf{K}) Z^*_{\mathbf{k} st, -\mathbf{k} s't'} = \delta(\mathbf{k}_1 + \mathbf{k}_2) Z^*_{\mathbf{k}_1 st, \mathbf{k}_2 s't'}, \tag{4.1.11}$$

where the first equality holds for the variables **K** and **k** in eq. (4.1.10), while the second is valid after using the Dirac delta $\delta(\mathbf{k}_1 + \mathbf{k}_2)$ in eq. (4.1.9). It is now clear that the pair-creation operator (4.1.7) depends only on the relative momentum. This allows us to introduce 4×4 **k**-dependent spin-isospin matrices defined by $Z^*(\mathbf{k})_{st,s't'} \equiv Z^*_{\mathbf{k}st,-\mathbf{k}s't'}$. For these, we have $Z^*(\mathbf{k}) = -Z^+(-\mathbf{k})$, where we use the $(+)$ and (T) symbols to represent the matrix spin-isospin Hermitian conjugation and transposition, respectively, of **k**-dependent functions (e.g., $Z^+(\mathbf{k})_{s't',st} \equiv Z^*(\mathbf{k})_{st,s't'}$ and $Z^T(\mathbf{k})_{s't',st} \equiv Z(\mathbf{k})_{st,s't'}$). With this, we have

$$\hat{Z}^\dagger = \tfrac{1}{2} \int \mathrm{d}\mathbf{k} \sum_{st,s't'} Z^*(\mathbf{k})_{st,s't'} a^\dagger_{\mathbf{k}st} a^\dagger_{-\mathbf{k}s't'} \tag{4.1.12}$$

$$= -\tfrac{1}{2} \int \mathrm{d}\mathbf{k} \sum_{st,s't'} Z^+(\mathbf{k})_{st,s't'} a^\dagger_{-\mathbf{k}st} a^\dagger_{\mathbf{k}s't'}. \tag{4.1.13}$$

Note that the minus sign of the **k**-dependence above, which is in the identity $Z^*(\mathbf{k}) = -Z^+(-\mathbf{k})$, does not appear in (4.1.13) as the sign of **k** is exchanged in the creation operators. This notation allows us to separate the integration over momentum **k** in eq. (4.1.12) into two arbitrary halves of momentum space, $\mathbf{k} > 0$ and $\mathbf{k} < 0$. By defining a **k**-dependent 4×4 Thouless *submatrix* as $\mathcal{Z}(\mathbf{k}) \equiv Z^T(\mathbf{k})$, we have,

$$\hat{Z}^\dagger = \tfrac{1}{2} \int_{\mathbf{k}>0} \mathrm{d}\mathbf{k} \sum_{st,s't'} \left(\mathcal{Z}^+(\mathbf{k})_{st,s't'} a^\dagger_{\mathbf{k}st} a^\dagger_{-\mathbf{k}s't'} - \mathcal{Z}^*(\mathbf{k})_{st,s't'} a^\dagger_{-\mathbf{k}st} a^\dagger_{\mathbf{k}s't'} \right). \tag{4.1.14}$$

Explicitly, at every momentum $\mathbf{k} > 0$, the integrand in eq. (4.1.14) can be defined in terms of the following eight spin-isospin states,

$$\begin{aligned} |1\rangle &\equiv |+\,\mathbf{k}\uparrow n\rangle\,, & |5\rangle &\equiv |-\,\mathbf{k}\uparrow n\rangle, \\ |2\rangle &\equiv |+\,\mathbf{k}\downarrow n\rangle\,, & |6\rangle &\equiv |-\,\mathbf{k}\downarrow n\rangle, \\ |3\rangle &\equiv |+\,\mathbf{k}\uparrow p\rangle\,, & |7\rangle &\equiv |-\,\mathbf{k}\uparrow p\rangle, \\ |4\rangle &\equiv |+\,\mathbf{k}\downarrow p\rangle\,, & |8\rangle &\equiv |-\,\mathbf{k}\downarrow p\rangle. \end{aligned} \tag{4.1.15}$$

In this representation, the two terms in eq. (4.1.14) appear as two off-diagonal 4×4 blocks of the 8×8 antisymmetric Thouless matrix $\tilde{Z}^*(\mathbf{k})$ defined as,

$$\tilde{Z}^*(\mathbf{k}) = \begin{pmatrix} 0 & Z^*(\mathbf{k}) \\ -Z^+(\mathbf{k}) & 0 \end{pmatrix} = \begin{pmatrix} 0 & \mathscr{Z}^+(\mathbf{k}) \\ -\mathscr{Z}^*(\mathbf{k}) & 0 \end{pmatrix}. \tag{4.1.16}$$

We note that the Thouless matrix $\tilde{Z}^*(\mathbf{k})$ must be antisymmetric, and this is fulfilled regardless of the symmetry of $\mathscr{Z}$. Here and below, we utilise the tilde to represent 8×8 **k**-dependent matrices.

4.2 The **k**-dependent density matrix and pairing tensor

In agreement with eqs. (4.1.3)–(4.1.5), here and below, we use the double dagger (‡) to represent the Hermitian conjugation of the antisymmetric momentum amplitudes defined in eq. (4.1.7), $Z^{\ddagger}_{\mathbf{k}_2 s't',\mathbf{k}_1 st} \equiv Z^*_{\mathbf{k}_1 st,\mathbf{k}_2 s't'} = -Z^*_{\mathbf{k}_2 s't',\mathbf{k}_1 st}$. The representation off-diagonal in **k**, eq. (4.1.12), is inconvenient for generalizing products of matrices $Z^{\ddagger}Z$, eqs. (4.1.3)–(4.1.5) to the infinite and continuous basis. For that, we must start with the original representation of eq. (4.1.7). In this representation, we get

$$\begin{aligned} Q_{\mathbf{k}_1 st,\mathbf{k}_2 s't'} &\equiv \left[Z^{\ddagger}Z\right]_{\mathbf{k}_1 st,\mathbf{k}_2 s't'} = \int \mathrm{d}\mathbf{k}'' \sum_{s''t''} Z^{\ddagger}_{\mathbf{k}_1 st,\mathbf{k}'' s''t''} Z_{\mathbf{k}'' s''t'',\mathbf{k}_2 s't'} = \int \mathrm{d}\mathbf{k}'' \sum_{s''t''} Z^*_{\mathbf{k}'' s''t'',\mathbf{k}_1 st} Z_{\mathbf{k}'' s''t'',\mathbf{k}_2 s't'} \\ &= \int \mathrm{d}\mathbf{k}'' \sum_{s''t''} \left\{\delta(\mathbf{k}_1 + \mathbf{k}'') Z^*_{\mathbf{k}'' s''t'',\mathbf{k}_1 st}\right\}\left\{\delta(\mathbf{k}'' + \mathbf{k}_2) Z_{\mathbf{k}'' s''t'',\mathbf{k}_2 s't'}\right\} \\ &= \delta(\mathbf{k}_1 - \mathbf{k}_2) \sum_{s''t''} Z^*_{-\mathbf{k}_1 s''t'',\mathbf{k}_1 st} Z_{-\mathbf{k}_2 s''t'',\mathbf{k}_2 s't'} = \delta(\mathbf{k}_1 - \mathbf{k}_2) \sum_{s''t''} Z^*_{\mathbf{k}_1 st,-\mathbf{k}_1 s''t''} Z_{\mathbf{k}_2 s't',-\mathbf{k}_2 s''t''} \\ &= \delta(\mathbf{k}_1 - \mathbf{k}_2) \sum_{s''t''} \tilde{Z}^*(\mathbf{k}_1)_{st,s''t''} \tilde{Z}(\mathbf{k}_2)_{s't',s''t''} = \delta(\mathbf{k}_1 - \mathbf{k}_2) \left[\tilde{Z}^*(\mathbf{k}_1)\tilde{Z}^T(\mathbf{k}_2)\right]_{st,s't'}. \end{aligned} \tag{4.2.1}$$

Hence, the Hermitian matrix $Q_{\mathbf{k}_1 st,\mathbf{k}_2 s't'}$, $Q^{\ddagger} = Q$, is diagonal in linear momenta $\mathbf{k}_1 = \mathbf{k}_2$ and at each relative linear momentum $\mathbf{k} \equiv \mathbf{k}_1 = \mathbf{k}_2$ is equal to the Hermitian product of **k**-dependent matrices defining the diagonal representation of the Thouless pair (4.1.16),

$$\tilde{Q}(\mathbf{k}) \equiv \tilde{Z}^*(\mathbf{k})\tilde{Z}^T(\mathbf{k}) = \begin{pmatrix} \mathscr{Z}^+(\mathbf{k})\mathscr{Z}(\mathbf{k}) & 0 \\ 0 & \mathscr{Z}^*(\mathbf{k})\mathscr{Z}^T(\mathbf{k}) \end{pmatrix},$$

for $\tilde{Q}^+(\mathbf{k}) = \tilde{Q}(\mathbf{k})$.

The overlap and density matrix of eqs. (4.1.3) and (4.1.5) can then be clearly expressed as

$$\langle Z|Z\rangle = \det\left(1 + \tilde{Q}(\mathbf{k})\right)^{1/2}, \tag{4.2.2}$$

$$\rho = \left(1 + \tilde{Q}(\mathbf{k})\right)^{-1} \tilde{Q}(\mathbf{k}). \tag{4.2.3}$$

We may also explicitly obtain the pairing tensor from the original representation via a similar procedure. Writing

$$S_{\mathbf{k}_1 st,\mathbf{k}_2 s't'} = \left(1 + Q\right)^{-1}_{\mathbf{k}_1 st,\mathbf{k}_2 s't'}, \tag{4.2.4}$$

and noting that $\kappa = -SZ^{\ddagger}$, we obtain

$$\begin{aligned}
\kappa_{\mathbf{k}_1 st, \mathbf{k}_2 s't'} &\equiv \left[-SZ^{\ddagger}\right]_{\mathbf{k}_1 st, \mathbf{k}_2 s't'} = -\int \mathrm{d}\mathbf{k}'' \sum_{s''t''} S_{\mathbf{k}_1 st, \mathbf{k}'' s''t''} Z^{\ddagger}_{\mathbf{k}'' s''t'', \mathbf{k}_2 s't'} \\
&= -\int \mathrm{d}\mathbf{k}'' \sum_{s''t''} \left\{\delta\left(\mathbf{k}_1 + \mathbf{k}''\right) S_{\mathbf{k}_1 st, \mathbf{k}'' s''t''}\right\} \left\{\delta\left(\mathbf{k}'' + \mathbf{k}_2\right) Z^{*}_{\mathbf{k}_2 s't', \mathbf{k}'' s''t''}\right\} \\
&= -\delta\left(\mathbf{k}_1 - \mathbf{k}_2\right) \sum_{s''t''} S_{\mathbf{k}_1 st, -\mathbf{k}_1 s''t''} Z^{*}_{\mathbf{k}_2 s't', -\mathbf{k}_2 s''t''} \\
&= -\delta\left(\mathbf{k}_1 - \mathbf{k}_2\right) \sum_{s''t''} \tilde{S}(\mathbf{k}_1)_{st, s''t''} \tilde{Z}^{*}(\mathbf{k}_2)_{s't', s''t''} = -\delta\left(\mathbf{k}_1 - \mathbf{k}_2\right) \left[\tilde{S}(\mathbf{k}_1) \tilde{Z}^{+}(\mathbf{k}_2)\right]_{st, s't'}. \qquad (4.2.5)
\end{aligned}$$

From eq. (4.1.16) we can write

$$\tilde{Z}^{+}(\mathbf{k}) = \begin{pmatrix} 0 & -\mathscr{Z}^{+}(\mathbf{k}) \\ \mathscr{Z}^{*}(\mathbf{k}) & 0 \end{pmatrix}, \qquad (4.2.6)$$

so that the pairing tensor can be expressed as

$$\kappa = -\left(1 + \tilde{Q}(\mathbf{k})\right)^{-1} \tilde{Z}^{+}(\mathbf{k}). \qquad (4.2.7)$$

Writing the density matrix explicitly in terms of the Thouless submatrices gives

$$\begin{aligned}
\rho &= \left(1 + Z^{\ddagger} Z\right)^{-1} Z^{\ddagger} Z = \left(1 + \tilde{Q}(\mathbf{k})\right)^{-1} \tilde{Q}(\mathbf{k}) \\
&= \begin{pmatrix} \left(1 + \mathscr{Z}^{+}(\mathbf{k}) \mathscr{Z}(\mathbf{k})\right)^{-1} \mathscr{Z}^{+}(\mathbf{k}) \mathscr{Z}(\mathbf{k}) & 0 \\ 0 & \left(1 + \mathscr{Z}^{*}(\mathbf{k}) \mathscr{Z}^{T}(\mathbf{k})\right)^{-1} \mathscr{Z}^{*}(\mathbf{k}) \mathscr{Z}^{T}(\mathbf{k}) \end{pmatrix}, \qquad (4.2.8)
\end{aligned}$$

and the pairing tensor

$$\begin{aligned}
\kappa &= -\left(1 + Z^{\ddagger} Z\right)^{-1} Z^{\ddagger} = -\left(1 + \tilde{Q}(\mathbf{k})\right)^{-1} \tilde{Z}^{+}(\mathbf{k}) \\
&= \begin{pmatrix} 0 & -\left(1 + \mathscr{Z}^{+}(\mathbf{k}) \mathscr{Z}(\mathbf{k})\right)^{-1} \mathscr{Z}^{+}(\mathbf{k}) \\ \left(1 + \mathscr{Z}^{*}(\mathbf{k}) \mathscr{Z}^{T}(\mathbf{k})\right)^{-1} \mathscr{Z}^{*}(\mathbf{k}) & 0 \end{pmatrix}. \qquad (4.2.9)
\end{aligned}$$

Note that we have used the explicit product of matrices in the original representation, eqs. (4.2.1) and (4.2.5), to obtain the expressions above for κ and ρ. The $\mathbf{k}$-dependent blocks can be further simplified. Defining the 4×4 matrix $\mathscr{K}(\mathbf{k}) \equiv -\left(1 + \mathscr{Z}^{+}(\mathbf{k}) \mathscr{Z}(\mathbf{k})\right)^{-1} \mathscr{Z}^{+}(\mathbf{k})$, which corresponds to one of the two blocks of the pairing tensor, we can write the other off-diagonal block as

$$\begin{aligned}
\left(1 + \mathscr{Z}^{*}(\mathbf{k}) \mathscr{Z}^{T}(\mathbf{k})\right)^{-1} \mathscr{Z}^{*}(\mathbf{k}) &= \left[\left(1 + \mathscr{Z}(\mathbf{k}) \mathscr{Z}^{+}(\mathbf{k})\right)^{T}\right]^{-1} \left(\mathscr{Z}^{+}(\mathbf{k})\right)^{T} \\
&= \left[\left(1 + \mathscr{Z}(\mathbf{k}) \mathscr{Z}^{+}(\mathbf{k})\right)^{-1}\right]^{T} \left(\mathscr{Z}^{+}(\mathbf{k})\right)^{T} \\
&= \left[\mathscr{Z}^{+}(\mathbf{k}) \left(1 + \mathscr{Z}(\mathbf{k}) \mathscr{Z}^{+}(\mathbf{k})\right)^{-1}\right]^{T} \\
&= -\mathscr{K}^{T}(\mathbf{k}), \qquad (4.2.10)
\end{aligned}$$

where we have used the identity $\mathscr{Z}^+(\mathbf{k})\left(1+\mathscr{Z}(\mathbf{k})\mathscr{Z}^+(\mathbf{k})\right)^{-1} = \left(1+\mathscr{Z}^+(\mathbf{k})\mathscr{Z}(\mathbf{k})\right)^{-1}\mathscr{Z}^+(\mathbf{k})$, which can be proved via

$$\begin{aligned} X &= \mathscr{Z}^+(\mathbf{k})\left(1+\mathscr{Z}(\mathbf{k})\mathscr{Z}^+(\mathbf{k})\right)^{-1}, \\ (1+\mathscr{Z}^+(\mathbf{k})\mathscr{Z}(\mathbf{k}))X &= (1+\mathscr{Z}^+(\mathbf{k})\mathscr{Z}(\mathbf{k}))\mathscr{Z}^+(\mathbf{k})\left(1+\mathscr{Z}(\mathbf{k})\mathscr{Z}^+(\mathbf{k})\right)^{-1} \\ &= \mathscr{Z}^+(\mathbf{k})\left(1+\mathscr{Z}(\mathbf{k})\mathscr{Z}^+(\mathbf{k})\right)\left(1+\mathscr{Z}(\mathbf{k})\mathscr{Z}^+(\mathbf{k})\right)^{-1} = \mathscr{Z}^+(\mathbf{k}), \\ X = \mathscr{Z}^+(\mathbf{k})\left(1+\mathscr{Z}(\mathbf{k})\mathscr{Z}^+(\mathbf{k})\right)^{-1} &= \left(1+\mathscr{Z}^+(\mathbf{k})\mathscr{Z}(\mathbf{k})\right)^{-1}\mathscr{Z}^+(\mathbf{k}). \end{aligned}$$

Henceforth, the pairing tensor and density matrix can also be defined in term of the submatrices

$$\kappa = \begin{pmatrix} 0 & \mathscr{K}(\mathbf{k}) \\ -\mathscr{K}^T(\mathbf{k}) & 0 \end{pmatrix}, \qquad \rho = \begin{pmatrix} -\mathscr{K}(\mathbf{k})\mathscr{Z}(\mathbf{k}) & 0 \\ 0 & -\mathscr{K}^T(\mathbf{k})\mathscr{Z}^T(\mathbf{k}) \end{pmatrix}. \tag{4.2.11}$$

Lastly, the overlap, eq. (4.1.4), can also be expressed in terms of the **k**-dependent submatrices as

$$\begin{aligned} \langle Z|Z\rangle &= \det\left(1+Z^\dagger Z\right)^{1/2} \\ &= \det\left(1+\mathscr{Z}^+(\mathbf{k})\mathscr{Z}(\mathbf{k})\right)^{1/2}\det\left(1+\mathscr{Z}^*(\mathbf{k})\mathscr{Z}^T(\mathbf{k})\right)^{1/2}. \end{aligned} \tag{4.2.12}$$

Using the fact that transposing does not change the determinant, we have

$$\det\left(1+\mathscr{Z}^*(\mathbf{k})\mathscr{Z}^T(\mathbf{k})\right)^{1/2} = \det\left(1+\mathscr{Z}(\mathbf{k})\mathscr{Z}^+(\mathbf{k})\right)^{1/2} \tag{4.2.13}$$

and further for non-singular matrices

$$\begin{aligned} \det\left(1+\mathscr{Z}^+(\mathbf{k})\mathscr{Z}(\mathbf{k})\right)^{1/2} &= \left(\det\left(\mathscr{Z}^{-1}(\mathbf{k})+\mathscr{Z}^+(\mathbf{k})\right)\det(\mathscr{Z}(\mathbf{k}))\right)^{1/2} \\ &= \left(\det(\mathscr{Z}(\mathbf{k}))\det\left(\mathscr{Z}^{-1}(\mathbf{k})+\mathscr{Z}^+(\mathbf{k})\right)\right)^{1/2} \\ &= \det\left(1+\mathscr{Z}(\mathbf{k})\mathscr{Z}^+(\mathbf{k})\right)^{1/2}, \end{aligned} \tag{4.2.14}$$

such that

$$\langle Z|Z\rangle \equiv \langle\mathscr{Z}(\mathbf{k})|\mathscr{Z}(\mathbf{k})\rangle^2 = \det\left(1+\mathscr{Z}^+(\mathbf{k})\mathscr{Z}(\mathbf{k})\right). \tag{4.2.15}$$

Finally, the pairing tensor may also be expressed via the Onishi theorem (Onishi and Yoshida 1966; Ring and Schuck 1980) as

$$\kappa_{\mu\nu} = \frac{\partial}{\partial Z_{\mu\nu}}\log\langle Z|Z\rangle \tag{4.2.16}$$

$$= \frac{\partial}{\partial Z_{\mu\nu}}\log\det\left(1+\mathscr{Z}^+(\mathbf{k})\mathscr{Z}(\mathbf{k})\right). \tag{4.2.17}$$

This form is crucial for the results that follow over the next sections. From now on, we shall drop the explicit **k** dependence and write the submatrices purely as $\mathscr{Z}$ and $\mathscr{K}$. We will now go through an example, and later derive the most general pairing tensor for infinite nuclear matter.

4.3 A simple case: Antisymmetric Thouless sub-matrix

As defined in eq. (4.1.16), the 8×8 Thouless matrix $\tilde{Z}^*$ is antisymmetric by construction, regardless of any structure of $\mathscr{Z}$. Henceforth, when dealing with the Thouless submatrices, not only do they not need to be antisymmetric (as the 8×8 matrix is antisymmetric by construction), but they also do not have to be symmetric at all. In particular, the different linear momenta allow for like-particle pairs with the same spin orientation, which is unusual in describing nuclear matter. The freedom in the structure of $\mathscr{Z}$ presents difficulties in obtaining the most general pairing tensor for nuclear matter, which shall be discussed over the next sections. Firstly, we limit ourselves to the familiar case of an antisymmetric Thouless submatrix with different ST channels. In particular, we begin by considering the space-symmetric components, and thus channels $ST = 01$ and 10 only. Omitting the linear-momentum arguments of $\mathbf{k}$, everything relies only on the Thouless submatrix $\mathscr{Z}^+$ (i.e. the off-diagonal part of Z). In the basis of four spin-isospin states ordered as $|1\rangle \equiv |\uparrow n\rangle$, $|2\rangle \equiv |\downarrow n\rangle$, $|3\rangle \equiv |\uparrow p\rangle$, and $|4\rangle \equiv |\downarrow p\rangle$, we can write

$$\hat{\mathscr{Z}}^+ = z^*_n a^+_{\uparrow n} a^+_{\downarrow n} + z^*_p a^+_{\uparrow p} a^+_{\downarrow p} + z^*_\uparrow a^+_{\uparrow n} a^+_{\uparrow p} + z^*_\downarrow a^+_{\downarrow n} a^+_{\downarrow p} + z^*_+ a^+_{\uparrow n} a^+_{\downarrow p} + z^*_- a^+_{\downarrow n} a^+_{\uparrow p}. \tag{4.3.1}$$

The first two pairs are scalar-isovector with projections of $T_z = \pm 1$, the next two are vector-isoscalar with projections of $S_z = \pm 1$, and the last two pairs are those with $S_z = T_z = 0$.

For a scalar and isoscalar interaction, we have the liberty of choosing an arbitrary orientation of the pair's spin and isospin. For example, Romero, Dobaczewski and Pastore 2019 chose the orientation along the spin and isospin z axes, which in the spherical tensor representation corresponds to $S_z = T_z = 0$, and thus utilised only the last two pairs of eq. (4.3.1). Here, we seek a general understanding of spin and/or isospin-polarized systems, for which the complete wavefunction is required. We choose the pair's orientation in the planes perpendicular to the spin and isospin z axes, which in the spherical tensor representation corresponds to $S_z = \pm 1$ and $T_z = \pm 1$. By keeping all pairs, and assuming an antisymmetric Thouless submatrix, we have

$$\mathscr{Z}^+ = \begin{pmatrix} 0 & z^*_n & z^*_\uparrow & z^*_+ \\ -z^*_n & 0 & z^*_- & z^*_\downarrow \\ -z^*_\uparrow & -z^*_- & 0 & z^*_p \\ -z^*_+ & -z^*_\downarrow & -z^*_p & 0 \end{pmatrix}, \tag{4.3.2}$$

and the product $\mathscr{Z}^+\mathscr{Z}$

$$\mathscr{Z}^+\mathscr{Z} = \begin{pmatrix} |z_n|^2 + |z_\uparrow|^2 + |z_+|^2 & z^*_\uparrow z_- + z^*_+ z_\downarrow & -z^*_n z_- + z^*_+ z_p & -z^*_n z_\downarrow - z^*_\uparrow z_p \\ z^*_- z_\uparrow + z^*_\downarrow z_+ & |z_n|^2 + |z_\downarrow|^2 + |z_-|^2 & z^*_n z_\uparrow + z^*_\downarrow z_p & z^*_n z_+ - z^*_- z_p \\ -z^*_- z_n + z^*_p z_+ & z^*_\uparrow z_n + z^*_p z_\downarrow & |z_p|^2 + |z_\uparrow|^2 + |z_-|^2 & z^*_\uparrow z_+ + z^*_- z_\downarrow \\ -z^*_\downarrow z_n - z^*_p z_\uparrow & z^*_+ z_n - z^*_p z_- & z^*_+ z_\uparrow + z^*_\downarrow z_- & |z_p|^2 + |z_\downarrow|^2 + |z_+|^2 \end{pmatrix}.$$

This product of Thouless submatrices has two doubly degenerate eigenvalues

$$\begin{aligned} z_{1,2} = \; & \tfrac{1}{2} \quad (|z_\uparrow|^2 + |z_\downarrow|^2 + |z_p|^2 + |z_n|^2 + |z_+|^2 + |z_-|^2 \\ & \pm \quad \{(|z_\uparrow|^2 + |z_\downarrow|^2 + |z_p|^2 + |z_n|^2 + |z_+|^2 + |z_-|^2)^2 - 4|z_- z_+ + z_n z_p - z_\uparrow z_\downarrow|^2\}^{1/2}), \end{aligned} \tag{4.3.3}$$

which can be expressed as

$$z_{1,2} = \eta(1 \pm \cos\alpha), \tag{4.3.4}$$

where

$$\begin{aligned} \eta &= \tfrac{1}{2}(|z_n|^2 + |z_p|^2 + |z_\uparrow|^2 + |z_\downarrow|^2 + |z_+|^2 + |z_-|^2), \\ \sin(\alpha) &= |z_+ z_- + z_n z_p - z_\downarrow z_\uparrow|/\eta. \end{aligned}$$

The spectrum of $Z^\dagger Z$ is directly linked to the occupation probabilities. We have previously established that this product can be represented by the block diagonal matrix of eq. (4.2.2), and since the eigenvalues of the diagonal blocks of a matrix are also eigenvalues of the full block matrix, the spectra of $\mathscr{Z}^+\mathscr{Z}$ also lead to the following doubly degenerate occupation factors

$$v^2_{1,2} = \frac{z_{1,2}}{1 + z_{1,2}} = \frac{\eta(1 \pm \cos\alpha)}{1 + \eta(1 \pm \cos\alpha)}. \tag{4.3.5}$$

Obtaining the pairing tensor and density matrix analytically from this product, however, becomes a nontrivial task, as the eigenvectors have a complicated structure that depends on all six parameters. In this case, the aforementioned derivation following from the Onishi theorem becomes hugely beneficial. The overlap is obtained from the submatrices following eq. (4.2.15), and reads

$$\langle Z|Z\rangle = (1 + |z_\uparrow|^2 + |z_\downarrow|^2 + |z_+|^2 + |z_-|^2 + |z_p|^2 + |z_n|^2 + |z_+ z_- + z_n z_p - z_\uparrow z_\downarrow|^2)^2. \tag{4.3.6}$$

Obtaining the pairing tensor then requires following eq. (4.2.17), where we shall find the components of $\mathscr{K}$ by computing derivatives of the overlap of eq. (4.3.6) respective to the components of the Thouless submatrix (4.3.2). To this end, we shall utilise the often called Wirtinger calculus for complex-valued functions. If we suppose a complex number $z = x + iy$, with x and y being real numbers, and a complex function $f(x,y) : \mathbb{C} \longrightarrow \mathbb{C}$ which is *real*-differentiable*, this function can also be expressed as $f(x,y) \equiv \bar{f}\left(z(x,y), z^*(x,y)\right) = \bar{f}(x + iy, x - iy)$. By applying the chain rule, we can easily obtain that

$$\frac{\partial \bar{f}}{\partial z} = \frac{1}{2}\left(\frac{\partial \bar{f}}{\partial x} - i\frac{\partial \bar{f}}{\partial y}\right), \qquad \frac{\partial \bar{f}}{\partial z^*} = \frac{1}{2}\left(\frac{\partial \bar{f}}{\partial x} + i\frac{\partial \bar{f}}{\partial y}\right), \tag{4.3.7}$$

which allows us to introduce the Wirtinger derivatives

$$\frac{\partial}{\partial z} \equiv \frac{1}{2}\left(\frac{\partial}{\partial x} - i\frac{\partial}{\partial y}\right), \qquad \frac{\partial}{\partial z^*} \equiv \frac{1}{2}\left(\frac{\partial}{\partial x} + i\frac{\partial}{\partial y}\right). \tag{4.3.8}$$

*Note that f need not be complex differentiable.

The fundamental inputs continue to be the real numbers x and y, although in practice one can simply proceed with the $\bar{f}$ notation of a complex function and merely treat z and z^* as two independent variables. The introduction of the complex differential operators (4.3.8) is crucial, as we wish to compute derivatives of the overlap of paired wave-functions which is written in terms of the absolute values $|z_i|$, which is not complex differentiable. For a detailed overview of complex-differentiable calculus, the reader is referred to Remmert 1991, chapter 1, section 4. As a practical example, the 21 component of $\mathscr{K}$ is obtained from

$$\mathscr{K}_{21} = \frac{\partial}{\partial z_n} \log\langle Z|Z\rangle \tag{4.3.9}$$

$$= \frac{1}{\langle Z|Z\rangle} \frac{\partial}{\partial z_n} \langle Z|Z\rangle. \tag{4.3.10}$$

The derivative involved in computing the 21 component of the pairing tensor is, explicitly,

$$\begin{aligned} \frac{\partial}{\partial z_n}\langle Z|Z\rangle &= \frac{\partial}{\partial z_n}(1 + |z_\uparrow|^2 + |z_\downarrow|^2 + |z_+|^2 + |z_-|^2 + |z_p|^2 + |z_n|^2 + |z_+z_- + z_nz_p - z_\uparrow z_\downarrow|^2)^2 \\ &= 2[z_n^* + z_p(z_+^*z_-^* + z_n^*z_p^* - z_\uparrow^* z_\downarrow^*)]\sqrt{\langle Z|Z\rangle}. \end{aligned}$$

Similarly, all other derivatives of components of $\mathscr{Z}$ read

$$\begin{aligned} \frac{\partial}{\partial z_p}\langle Z|Z\rangle &= 2[z_p^* + z_n(z_+^*z_-^* + z_n^*z_p^* - z_\uparrow^* z_\downarrow^*)]\sqrt{\langle Z|Z\rangle}, \\ \frac{\partial}{\partial z_+}\langle Z|Z\rangle &= 2[z_+^* + z_-(z_+^*z_-^* + z_n^*z_p^* - z_\uparrow^* z_\downarrow^*)]\sqrt{\langle Z|Z\rangle}, \\ \frac{\partial}{\partial z_-}\langle Z|Z\rangle &= 2[z_-^* + z_+(z_+^*z_-^* + z_n^*z_p^* - z_\uparrow^* z_\downarrow^*)]\sqrt{\langle Z|Z\rangle}, \\ \frac{\partial}{\partial z_\uparrow}\langle Z|Z\rangle &= 2[z_\uparrow^* - z_\downarrow(z_+^*z_-^* + z_n^*z_p^* - z_\uparrow^* z_\downarrow^*)]\sqrt{\langle Z|Z\rangle}, \\ \frac{\partial}{\partial z_\downarrow}\langle Z|Z\rangle &= 2[z_\downarrow^* - z_\uparrow(z_+^*z_-^* + z_n^*z_p^* - z_\uparrow^* z_\downarrow^*)]\sqrt{\langle Z|Z\rangle}. \end{aligned}$$

Noting that the inverse of the Thouless submatrix is

$$\mathscr{Z}^{-1} = \frac{1}{z_nz_p + z_+z_- - z_\uparrow z_\downarrow} \begin{pmatrix} 0 & z_p & -z_\downarrow & z_- \\ -z_p & 0 & z_+ & -z_\uparrow \\ z_\downarrow & -z_+ & 0 & z_n \\ -z_- & z_\uparrow & -z_n & 0 \end{pmatrix},$$

we can see that the pairing tensor can be written as

$$\mathscr{K} = \frac{-2(\mathscr{Z}^+ + |z_nz_p + z_+z_- - z_\uparrow z_\downarrow|^2\mathscr{Z}^{-1})}{\sqrt{\langle Z|Z\rangle}}, \tag{4.3.11}$$

such that when we have

$$z_n z_p + z_+ z_- = z_\uparrow z_\downarrow \tag{4.3.12}$$

the Thouless submatrix and the pairing tensor are equivalent. The first block in the diagonal of the density matrix is

$$\mathscr{R} = -\mathscr{K}\mathscr{Z}, \tag{4.3.13}$$

so that we can also immediately write the density matrix from the pairing tensor and the Thouless submatrix

$$\mathscr{R} = \frac{2(\mathscr{Z}^+\mathscr{Z} + \mathbb{I}|z_n z_p + z_+ z_- - z_\uparrow z_\downarrow|^2)}{\sqrt{\langle Z|Z\rangle}}. \tag{4.3.14}$$

These results show explicitly that even in the simple case of an antisymmetric Thouless submatrix, the different proton-neutron channels do not easily separate in nuclear matter: although they may appear separately in the wavefunction, they are strongly mixed in the pairing tensor and density matrix. Specifically, a strong proton-neutron mixing appears in the pairing tensor of nuclear matter, which could not be inferred solely from the wavefunction. This intriguing result, however, does not paint the full picture: some of the proton-neutron channels were not present in this derivation, and a general result would require $\mathscr{Z}$ to have an arbitrary structure, and thus, 16 free parameters. Obtaining the overlap for such a system analytically does not provide any clarity, as the expressions become extremely complicated, so the next sections outline a different approach that enables us to access the full pairing tensor.

4.4 A simple *generalisable* case: z-aligned pairs in the ST basis

It has now become clear that proceeding with the basis of four spin-isospin states, as discussed in the previous section, is unfeasible in the case of general proton-neutron pairs in NM. In the following sections, we switch to the coupled ST representation $|SS_zTT_z\rangle$, for which all transformations are detailed in Appendix A. We shall start in the simplest way possible: including only pairs with zero spin and isospin projections. This choice includes all proton-neutron channels, for which the new basis states read

$$|0000\rangle = \tfrac{1}{2}(|\uparrow n\rangle|\downarrow p\rangle - |\uparrow p\rangle|\downarrow n\rangle + |\downarrow p\rangle|\uparrow n\rangle - |\downarrow n\rangle|\uparrow p\rangle), \tag{4.4.1}$$

$$|1000\rangle = \tfrac{1}{2}(|\uparrow n\rangle|\downarrow p\rangle - |\uparrow p\rangle|\downarrow n\rangle - |\downarrow p\rangle|\uparrow n\rangle + |\downarrow n\rangle|\uparrow p\rangle), \tag{4.4.2}$$

$$|0010\rangle = \tfrac{1}{2}(|\uparrow n\rangle|\downarrow p\rangle + |\uparrow p\rangle|\downarrow n\rangle - |\downarrow p\rangle|\uparrow n\rangle - |\downarrow n\rangle|\uparrow p\rangle), \tag{4.4.3}$$

$$|1010\rangle = \tfrac{1}{2}(|\uparrow n\rangle|\downarrow p\rangle + |\uparrow p\rangle|\downarrow n\rangle + |\downarrow p\rangle|\uparrow n\rangle + |\downarrow n\rangle|\uparrow p\rangle), \tag{4.4.4}$$

and correspond to the following Thouless submatrices, denoted by the ST quantum numbers:

$$\mathscr{Z}^{+}_{00} = \begin{pmatrix} 0 & 0 & 0 & +1 \\ 0 & 0 & -1 & 0 \\ 0 & -1 & 0 & 0 \\ +1 & 0 & 0 & 0 \end{pmatrix}, \qquad \mathscr{Z}^{+}_{10} = \begin{pmatrix} 0 & 0 & 0 & +1 \\ 0 & 0 & +1 & 0 \\ 0 & -1 & 0 & 0 \\ -1 & 0 & 0 & 0 \end{pmatrix},$$

$$\mathscr{Z}^{+}_{01} = \begin{pmatrix} 0 & 0 & 0 & +1 \\ 0 & 0 & -1 & 0 \\ 0 & +1 & 0 & 0 \\ -1 & 0 & 0 & 0 \end{pmatrix}, \qquad \mathscr{Z}^{+}_{11} = \begin{pmatrix} 0 & 0 & 0 & +1 \\ 0 & 0 & +1 & 0 \\ 0 & +1 & 0 & 0 \\ +1 & 0 & 0 & 0 \end{pmatrix}.$$

Therefore, the linear combination of the aligned pairs,

$$\mathscr{Z}^{+}_{z} = z^{*}_{00}|0000\rangle + z^{*}_{10}|1000\rangle + z^{*}_{01}|0010\rangle + z^{*}_{11}|1010\rangle, \tag{4.4.5}$$

corresponds to the following Thouless submatrix, which is neither symmetric nor antisymmetric,

$$\mathscr{Z}^{+}_{z} = \begin{pmatrix} 0 & 0 & 0 & z^{*}_{+} \\ 0 & 0 & z^{*}_{-} & 0 \\ 0 & \bar{z}^{*}_{-} & 0 & 0 \\ \bar{z}^{*}_{+} & 0 & 0 & 0 \end{pmatrix}, \tag{4.4.6}$$

for

$$z^{*}_{+} = z^{*}_{00} + z^{*}_{10} + z^{*}_{01} + z^{*}_{11}, \tag{4.4.7}$$

$$z^{*}_{-} = -z^{*}_{00} + z^{*}_{10} - z^{*}_{01} + z^{*}_{11}, \tag{4.4.8}$$

$$\bar{z}^{*}_{-} = -z^{*}_{00} - z^{*}_{10} + z^{*}_{01} + z^{*}_{11}, \tag{4.4.9}$$

$$\bar{z}^{*}_{+} = z^{*}_{00} - z^{*}_{10} - z^{*}_{01} + z^{*}_{11}. \tag{4.4.10}$$

However, its symmetric and antisymmetric channels separate and the eigenvalues and eigenvectors read

$$\sqrt{z^{*}_{+}\bar{z}^{*}_{+}}, \begin{pmatrix} \sqrt{z^{*}_{+}} \\ 0 \\ 0 \\ \sqrt{\bar{z}^{*}_{+}} \end{pmatrix}; \quad -\sqrt{z^{*}_{+}\bar{z}^{*}_{+}}, \begin{pmatrix} \sqrt{z^{*}_{+}} \\ 0 \\ 0 \\ -\sqrt{\bar{z}^{*}_{+}} \end{pmatrix}; \quad \sqrt{z^{*}_{-}\bar{z}^{*}_{-}}, \begin{pmatrix} 0 \\ \sqrt{z^{*}_{-}} \\ \sqrt{\bar{z}^{*}_{-}} \\ 0 \end{pmatrix}; \quad -\sqrt{z^{*}_{-}\bar{z}^{*}_{-}}, \begin{pmatrix} 0 \\ \sqrt{z^{*}_{-}} \\ -\sqrt{\bar{z}^{*}_{-}} \\ 0 \end{pmatrix}. \tag{4.4.11}$$

If we decide to proceed via the route of computing κ and ρ via Onishi theorem, we must start from the overlap

$$\langle Z_{z}|Z_{z}\rangle = (1 + |z_{+}|^{2})(1 + |z_{-}|^{2})(1 + |\bar{z}_{+}|^{2})(1 + |\bar{z}_{+}|^{2}), \tag{4.4.12}$$

from which we easily obtain the pairing tensor as in eq. (4.2.17). For $i, j = z_+, z_-, \bar{z}_+$ and $\bar{z}_-$, we have

$$\frac{1}{\langle Z_z|Z_z\rangle}\frac{\partial}{\partial z_i}\langle Z_z|Z_z\rangle = \frac{1}{\langle Z_z|Z_z\rangle} z_i^* \prod_{j\neq i}(1+|z_j|^2), \tag{4.4.13}$$

which can also be expressed as

$$\frac{1}{\langle Z_z|Z_z\rangle}\frac{\partial}{\partial z_i}\langle Z_z|Z_z\rangle \quad = \quad \frac{\langle Z_z|Z_z\rangle}{\langle Z_z|Z_z\rangle}\frac{z_i^*}{(1+|z_i|^2)} = \frac{z_i^*}{(1+|z_i|^2)}, \tag{4.4.14}$$

so that the (subspace) pairing tensor reads

$$\mathscr{K}_{\mu\nu} = \frac{\mathscr{Z}^*_{\mu\nu}}{(1+|\mathscr{Z}_{\mu\nu}|^2)}. \tag{4.4.15}$$

Due to the simplicity of the z-aligned wavefunction, we can also obtain κ and ρ directly from (4.1.4)-(4.1.5), as well as from the definitions given from the subspace Thouless matrices (4.2.11). Naturally, all definitions yield the same density matrix

$$\rho \quad = \quad \begin{pmatrix} \frac{|z_+|^2}{1+|z_+|^2} & 0 & 0 & 0 & 0 & 0 & 0 & 0 \\ 0 & \frac{|z_-|^2}{1+|z_-|^2} & 0 & 0 & 0 & 0 & 0 & 0 \\ 0 & 0 & \frac{|\tilde{z}_-|^2}{1+|\tilde{z}_-|^2} & 0 & 0 & 0 & 0 & 0 \\ 0 & 0 & 0 & \frac{|\tilde{z}_+|^2}{1+|\tilde{z}_+|^2} & 0 & 0 & 0 & 0 \\ 0 & 0 & 0 & 0 & \frac{|\tilde{z}_+|^2}{1+|\tilde{z}_+|^2} & 0 & 0 & 0 \\ 0 & 0 & 0 & 0 & 0 & \frac{|\tilde{z}_-|^2}{1+|\tilde{z}_-|^2} & 0 & 0 \\ 0 & 0 & 0 & 0 & 0 & 0 & \frac{|z_-|^2}{1+|z_-|^2} & 0 \\ 0 & 0 & 0 & 0 & 0 & 0 & 0 & \frac{|z_+|^2}{1+|z_+|^2} \end{pmatrix}, \tag{4.4.16}$$

and pairing tensor

$$\kappa \quad = \quad \begin{pmatrix} 0 & 0 & 0 & 0 & 0 & 0 & 0 & -\frac{z_+^*}{1+|z_+|^2} \\ 0 & 0 & 0 & 0 & 0 & 0 & -\frac{z_-^*}{1+|z_-|^2} & 0 \\ 0 & 0 & 0 & 0 & 0 & -\frac{\tilde{z}_-^*}{1+|\tilde{z}_-|^2} & 0 & 0 \\ 0 & 0 & 0 & 0 & -\frac{\tilde{z}_+^*}{1+|\tilde{z}_+|^2} & 0 & 0 & 0 \\ 0 & 0 & 0 & \frac{\tilde{z}_+^*}{1+|\tilde{z}_+|^2} & 0 & 0 & 0 & 0 \\ 0 & 0 & \frac{\tilde{z}_-^*}{1+|\tilde{z}_-|^2} & 0 & 0 & 0 & 0 & 0 \\ 0 & \frac{z_-^*}{1+|z_-|^2} & 0 & 0 & 0 & 0 & 0 & 0 \\ \frac{z_+^*}{1+|z_+|^2} & 0 & 0 & 0 & 0 & 0 & 0 & 0 \end{pmatrix}. \tag{4.4.17}$$

Note that, as these states produce a diagonal density matrix, this corresponds to the canonical basis. Differently from the previous section, we note that the different spin and isospin channels

are *not* mixed in the case of z-aligned pairs. If one of the different ST channels is omitted in the wavefunction, it also disappears in the pairing tensor and density matrix. This result completes the derivation of our main conclusion: the general intuition of assuming decoupled proton-neutron channels is not correct; only the ST channels of the paired DFT wavefunction decouple. The next section deals with generalising these results such that we may have pn pairs with an arbitrary orientation in both space and isospin space.

4.5 The path to the most general pairing tensor of nuclear matter

The Onishi formalism for deriving the pairing tensor presents us with a unique opportunity. Analytic expressions for the overlap of a general paired wavefunction are complicated, and even the general Thouless matrix has a rich structure, which makes obtaining the pairing tensor appear unfeasible. However, eq. (4.2.15) makes it clear that the overlap can be determined from the determinant of $\mathbf{k}$-dependent Thouless submatrices. Since the determinant is invariant under rotations—as the determinant of any rotation matrix is always equal to 1, and also due to multiplicativity, i.e. $\det(AB) = \det(A)\det(B)$—*any* overlap can be utilised to determine κ. Henceforth, the very simple expression for the z-aligned overlap (4.4.12) can be used directly to cover the entirety of space and isospin space and determine the pairing tensor via

$$\mathscr{K}^{\text{rot}}_{\mu\nu} = \frac{1}{\langle Z_z|Z_z\rangle}\frac{\partial}{\partial \mathscr{Z}^{\text{rot}}_{\mu\nu}}\langle Z_z|Z_z\rangle, \tag{4.5.1}$$

provided we also obtain the rotated Thouless submatrix $\mathscr{Z}^{\text{rot}}$.

4.5.1 Rotating $\mathscr{Z}^{+}_{z}$ in spin and isospin space

The starting point for obtaining a general paired wavefunction consists of the z-aligned pairs given in eq. (4.4.5). We must then define the spin and isospin rotation operators, $\hat{R}_S$ and $\hat{R}_T$, respectively

$$\hat{R}_S(\alpha_S,\beta_S,\gamma_S) = e^{-i\alpha_S\hat{S}_z}e^{-i\beta_S\hat{S}_y}e^{-i\gamma_S\hat{S}_z}, \tag{4.5.2}$$
$$\hat{R}_T(\alpha_T,\beta_T,\gamma_T) = e^{-i\alpha_T\hat{T}_z}e^{-i\beta_T\hat{T}_y}e^{-i\gamma_T\hat{T}_z}, \tag{4.5.3}$$

where the corresponding α,β and γ correspond to the Euler angles, characterised by an active rotation over the z, y, and z axes. As a simple example, a rotated state in spin is given by

$$|SS_z\rangle = \hat{R}_S(\alpha_S,\beta_S,\gamma_S)\,|S0\rangle \tag{4.5.4}$$
$$= \sum_{S'_z}|SS'_z\rangle\langle SS'_z|\,\hat{R}_S(\alpha_S,\beta_S,\gamma_S)\,|S0\rangle\,, \tag{4.5.5}$$

where the matrix elements correspond to one of the Wigner D-functions (Varshalovich, Moskalev and Khersonskii 1988), defined as

$$D^S_{s's}(\alpha_S,\beta_S,\gamma_S) \equiv \langle Ss'|\,\hat{R}_S(\alpha_S,\beta_S,\gamma_S)\,|Ss\rangle \tag{4.5.6}$$
$$= e^{-is'\alpha_S} d^S_{s's}(\beta_S) e^{-is\gamma_S}, \tag{4.5.7}$$

and similarly for isospin

$$D^T_{t't}(\alpha_T,\beta_T,\gamma_T) \equiv \langle Tt'|\,\hat{R}_T(\alpha_T,\beta_T,\gamma_T)\,|Tt\rangle \tag{4.5.8}$$
$$= e^{-it'\alpha_T} d^T_{t't}(\beta_T) e^{-it\gamma_T}. \tag{4.5.9}$$

Following the notation of Appendix A for the ST basis, i.e.,

$$|SS_zTT_z\rangle = \sum_{s'st't=\pm1/2} C^{SS_z}_{\frac{1}{2}s'\frac{1}{2}s} C^{TT_z}_{\frac{1}{2}t'\frac{1}{2}t} |\tfrac{1}{2}s'\tfrac{1}{2}t'\rangle|\tfrac{1}{2}s\tfrac{1}{2}t\rangle, \tag{4.5.10}$$

we can write the $ST = 00, 10, 01, 11$ parts of $\mathcal{Z}^+_z$, respectively, as

$$z^*_{00}\,|0000\rangle = z^*_{00} \sum_{s'st't=\pm1/2} C^{00}_{\frac{1}{2}s'\frac{1}{2}s} C^{00}_{\frac{1}{2}t'\frac{1}{2}t} |\tfrac{1}{2}s'\tfrac{1}{2}t'\rangle|\tfrac{1}{2}s\tfrac{1}{2}t\rangle, \tag{4.5.11}$$
$$z^*_{10}\,|1000\rangle = z^*_{10} \sum_{s'st't=\pm1/2} C^{10}_{\frac{1}{2}s'\frac{1}{2}s} C^{00}_{\frac{1}{2}t'\frac{1}{2}t} |\tfrac{1}{2}s'\tfrac{1}{2}t'\rangle|\tfrac{1}{2}s\tfrac{1}{2}t\rangle, \tag{4.5.12}$$
$$z^*_{01}\,|0010\rangle = z^*_{01} \sum_{s'st't=\pm1/2} C^{00}_{\frac{1}{2}s'\frac{1}{2}s} C^{10}_{\frac{1}{2}t'\frac{1}{2}t} |\tfrac{1}{2}s'\tfrac{1}{2}t'\rangle|\tfrac{1}{2}s\tfrac{1}{2}t\rangle, \tag{4.5.13}$$
$$z^*_{11}\,|1010\rangle = z^*_{11} \sum_{s'st't=\pm1/2} C^{10}_{\frac{1}{2}s'\frac{1}{2}s} C^{10}_{\frac{1}{2}t'\frac{1}{2}t} |\tfrac{1}{2}s'\tfrac{1}{2}t'\rangle|\tfrac{1}{2}s\tfrac{1}{2}t\rangle. \tag{4.5.14}$$

We shall now apply the rotations (4.5.2) and (4.5.3) to all ST channels. From now on, we shall adopt Ω_S and Ω_T as the notation for the Euler angles for compactness. The scalar-isoscalar proton-neutron pairs are naturally invariant under S and T rotations, and thus, we shall start from the vector-isoscalar pairs, i.e. $ST = 10$, which read

$$|1S_z(\Omega_S)00\rangle = \hat{R}_{s'}(\Omega_S)\hat{R}_s(\Omega_S)\hat{R}_{t'}(\Omega_T)\hat{R}_t(\Omega_T)\left(z^*_{10}\sum_{s'st't=\pm1/2} C^{10}_{\frac{1}{2}s'\frac{1}{2}s} C^{00}_{\frac{1}{2}t'\frac{1}{2}t} |\tfrac{1}{2}s'\tfrac{1}{2}t'\rangle|\tfrac{1}{2}s\tfrac{1}{2}t\rangle\right).$$

Since this state is a scalar in isospin space, it is invariant under rotations, and we can rewrite it as

$$|1S_z(\Omega_S)00\rangle = \hat{R}_{s'}(\Omega_S)\hat{R}_s(\Omega_S)\left(z^*_{10}\sum_{s'st't=\pm1/2} C^{10}_{\frac{1}{2}s'\frac{1}{2}s} C^{00}_{\frac{1}{2}t'\frac{1}{2}t} |\tfrac{1}{2}s'\tfrac{1}{2}t'\rangle|\tfrac{1}{2}s\tfrac{1}{2}t\rangle\right)$$
$$= z^*_{10}\sum_{t't=\pm1/2} C^{00}_{\frac{1}{2}t'\frac{1}{2}t} \sum_{ss'\tilde{s}\tilde{s}=\pm1/2} C^{10}_{\frac{1}{2}s'\frac{1}{2}s} D^{\frac{1}{2}}_{\tilde{s}s'} D^{\frac{1}{2}}_{\tilde{s}s} |\tfrac{1}{2}\tilde{s}\tfrac{1}{2}t'\rangle|\tfrac{1}{2}\tilde{s}\tfrac{1}{2}t\rangle. \tag{4.5.15}$$

As the Wigner D-functions have the same arguments, i.e., as these rotations are coupled, we may expand them as a series of Clebsch-Gordan coefficients (Varshalovich, Moskalev and Khersonskii 1988)

$$D^{\frac{1}{2}}_{\tilde{s}s'}(\Omega_S)D^{\frac{1}{2}}_{\tilde{s}s}(\Omega_S) = \sum_{ss'\tilde{s}\tilde{s}=\pm 1/2} C^{SS'_z}_{\frac{1}{2}\tilde{s}\frac{1}{2}\tilde{s}} D^{S}_{S'_zS_z} C^{SS_z}_{\frac{1}{2}s'\frac{1}{2}s}, \tag{4.5.16}$$

which after substituting in eq. (4.5.15) gives

$$\begin{aligned}
|1S_z(\Omega_S)00\rangle &= z^*_{10}\sum_{t't=\pm 1/2} C^{00}_{\frac{1}{2}t'\frac{1}{2}t}\sum_{ss'\tilde{s}\tilde{s}=\pm 1/2}\underbrace{C^{10}_{\frac{1}{2}s'\frac{1}{2}s}C^{SS_z}_{\frac{1}{2}s'\frac{1}{2}s}}_{\delta_{S1}\delta_{S_z0}} D^{S}_{S'_zS_z}C^{SS'_z}_{\frac{1}{2}\tilde{s}\frac{1}{2}\tilde{s}}|\tfrac{1}{2}\tilde{s}\tfrac{1}{2}t'\rangle|\tfrac{1}{2}\tilde{s}\tfrac{1}{2}t\rangle \\
&= z^*_{10}\sum_{t't=\pm 1/2} C^{00}_{\frac{1}{2}t'\frac{1}{2}t}\sum_{\tilde{s}\tilde{s}=\pm 1/2} D^{1}_{S'_z0}C^{1S'_z}_{\frac{1}{2}\tilde{s}\frac{1}{2}\tilde{s}}|\tfrac{1}{2}\tilde{s}\tfrac{1}{2}t'\rangle|\tfrac{1}{2}\tilde{s}\tfrac{1}{2}t\rangle \\
&= z^*_{10}\sum_{t't=\pm 1/2} C^{00}_{\frac{1}{2}t'\frac{1}{2}t}\sum_{s's=\pm 1/2} D^{1}_{S'_z0}C^{1S'_z}_{\frac{1}{2}s'\frac{1}{2}s}|\tfrac{1}{2}s'\tfrac{1}{2}t'\rangle|\tfrac{1}{2}s\tfrac{1}{2}t\rangle.
\end{aligned} \tag{4.5.17}$$

Note that we have chosen to rotate $|st\rangle$ states in the expressions above, for clarity. This is equivalent to utilising the Wigner D-functions directly into $|ST\rangle$ states.

Analogously, the $ST = 01$ pairs are invariant under spin rotation, and we can write

$$\begin{aligned}
|001T_z(\Omega_T)\rangle &= \hat{R}_{t'}(\Omega_T)\hat{R}_t(\Omega_T)\left(z^*_{01}\sum_{s'st't=\pm 1/2} C^{00}_{\frac{1}{2}s'\frac{1}{2}s}C^{10}_{\frac{1}{2}t'\frac{1}{2}t}|\tfrac{1}{2}s'\tfrac{1}{2}t'\rangle|\tfrac{1}{2}s\tfrac{1}{2}t\rangle\right) \\
&= z^*_{01}\sum_{s's=\pm 1/2} C^{00}_{\frac{1}{2}s'\frac{1}{2}s}\sum_{t't=\pm 1/2} D^{1}_{T'_z0}C^{1T'_z}_{\frac{1}{2}t'\frac{1}{2}t}|\tfrac{1}{2}s'\tfrac{1}{2}t'\rangle|\tfrac{1}{2}s\tfrac{1}{2}t\rangle.
\end{aligned} \tag{4.5.18}$$

Lastly, for the $ST = 11$ channel, both rotations in spin and isospin space are allowed, which gives

$$|1S_z(\Omega_S)1T_z(\Omega_T)\rangle = \sum_{s's=\pm 1/2} D^{1}_{S'_z0}C^{1S'_z}_{\frac{1}{2}s'\frac{1}{2}s}\sum_{t't=\pm 1/2} D^{1}_{T'_z0}C^{1T'_z}_{\frac{1}{2}t'\frac{1}{2}t}|\tfrac{1}{2}s'\tfrac{1}{2}t'\rangle|\tfrac{1}{2}s\tfrac{1}{2}t\rangle. \tag{4.5.19}$$

The Wigner D-functions which appear in the rotated wavefunctions are

$$D^1_{10}(\Omega) = -\frac{\sin\beta}{\sqrt{2}}e^{-i\alpha}, \qquad D^1_{-10}(\Omega) = \frac{\sin\beta}{\sqrt{2}}e^{+i\alpha}, \qquad D^1_{00}(\Omega) = \cos\beta. \tag{4.5.20}$$

Note that as we start from pairs which are aligned to the z direction, the dependence on γ—which comes from rotating the system around the z axis—naturally disappears. The explicit expressions for the rotated states are written in Appendix B.

4.5.2 The rotated Thouless submatrices, $\mathscr{Z}^+_{\text{rot},ST}$

The expressions shown in Appendix B make it possible to write the rotated Thouless submatrices, $\mathscr{Z}^+_{\text{rot},ST}$:

$$\mathscr{Z}^{+}_{\mathrm{rot},00} = \frac{z^{*}_{00}}{2}\begin{pmatrix} 0 & 0 & 0 & +1 \\ 0 & 0 & -1 & 0 \\ 0 & -1 & 0 & 0 \\ +1 & 0 & 0 & 0 \end{pmatrix},$$

$$\mathscr{Z}^{+}_{\mathrm{rot},10} = \frac{z^{*}_{10}}{2}\begin{pmatrix} 0 & 0 & -\sin\beta_S e^{-i\alpha_S} & \cos\beta_S \\ 0 & 0 & \cos\beta_S & +\sin\beta_S e^{+i\alpha_S} \\ +\sin\beta_S e^{-i\alpha_S} & -\cos\beta_S & 0 & 0 \\ -\cos\beta_S & -\sin\beta_S e^{+i\alpha_S} & 0 & 0 \end{pmatrix},$$

$$\mathscr{Z}^{+}_{\mathrm{rot},01} = \frac{z^{*}_{01}}{2}\begin{pmatrix} 0 & -\sin\beta_T e^{-i\alpha_T} & 0 & \cos\beta_T \\ +\sin\beta_T e^{-i\alpha_T} & 0 & -\cos\beta_T & 0 \\ 0 & \cos\beta_T & 0 & +\sin\beta_T e^{+i\alpha_T} \\ -\cos\beta_T & 0 & -\sin\beta_T e^{+i\alpha_T} & 0 \end{pmatrix},$$

$$\mathscr{Z}^{+}_{\mathrm{rot},11} = \frac{z^{*}_{11}}{2}\begin{pmatrix} \sin\beta_T e^{-i\alpha_T}\sin\beta_S e^{-i\alpha_S} & -\sin\beta_T e^{-i\alpha_T}\cos\beta_S & -\cos\beta_T\sin\beta_S e^{-i\alpha_S} & \cos\beta_T\cos\beta_S \\ -\sin\beta_T e^{-i\alpha_T}\cos\beta_S & -\sin\beta_T e^{-i\alpha_T}\sin\beta_S e^{+i\alpha_S} & \cos\beta_T\cos\beta_S & \cos\beta_T\sin\beta_S e^{+i\alpha_S} \\ -\cos\beta_T\sin\beta_S e^{-i\alpha_S} & \cos\beta_T\cos\beta_S & -\sin\beta_T e^{+i\alpha_T}\sin\beta_S e^{-i\alpha_S} & \sin\beta_T e^{+i\alpha_T}\cos\beta_S \\ \cos\beta_T\cos\beta_S & \cos\beta_T\sin\beta_S e^{+i\alpha_S} & \sin\beta_T e^{+i\alpha_T}\cos\beta_S & \sin\beta_T e^{+i\alpha_T}\sin\beta_S e^{+i\alpha_S} \end{pmatrix},$$

where the first and last two columns of $\mathscr{Z}^{+}_{\mathrm{rot},11}$ are written separately due to space. The complete rotated Thouless submatrix consists of the addition of all ST channels. For the sake of clarity, it is useful to write the full $\mathscr{Z}^{+}_{\mathrm{rot}}$ element-wise. This is shown in Appendix C.

4.5.3 Writing the partial derivatives

Having the expressions for the rotated Thouless matrix, $\mathscr{Z}_{\mathrm{rot}}$, we must compute the partial derivatives $\partial/\partial(\mathscr{Z}_{\mathrm{rot}})_{\mu\nu}$ to compute the pairing tensor

$$(\mathscr{H}_{\mathrm{rot}})_{\mu\nu} = \frac{1}{\langle Z_z|Z_z\rangle}\frac{\partial}{\partial(\mathscr{Z}_{\mathrm{rot}})_{\mu\nu}}\langle Z_z|Z_z\rangle. \tag{4.5.21}$$

Noting that the overlap, $\langle Z_z|Z_z\rangle$, does not depend on the Euler angles, we have that

$$\frac{\partial}{\partial\beta_{S,T}}\langle Z_z|Z_z\rangle = \frac{\partial}{\partial\alpha_{S,T}}\langle Z_z|Z_z\rangle = 0. \tag{4.5.22}$$

This simplifies the final expressions for the pairing tensor. Hence, as terms dependent on (4.5.22) will vanish in the pairing tensor, we shall simply denote all terms dependent on the partial derivatives of the Euler angles as $\partial(\alpha\beta)_{\mu\nu}$ instead of explicitly writing them below. Explicitly, they would read

$$\partial(\alpha\beta)_{\mu\nu} \equiv \frac{\partial\alpha_S}{\partial(\mathscr{Z}_{\text{rot}})_{\mu\nu}}\frac{\partial}{\partial\alpha_S} + \frac{\partial\beta_S}{\partial(\mathscr{Z}_{\text{rot}})_{\mu\nu}}\frac{\partial}{\partial\beta_S} + \frac{\partial\alpha_T}{\partial(\mathscr{Z}_{\text{rot}})_{\mu\nu}}\frac{\partial}{\partial\alpha_T} + \frac{\partial\beta_T}{\partial(\mathscr{Z}_{\text{rot}})_{\mu\nu}}\frac{\partial}{\partial\beta_T}. \tag{4.5.23}$$

The full partial derivatives are obtained via the chain rule. The simplest case is that of the diagonal elements of $\mathscr{Z}_{\text{rot}}$, which depend only on z_{11}, $\beta_{T,S}$, and $\alpha_{T,S}$. Omitting the partial derivatives over the Euler angles, which vanish when we compute the derivatives of the z-aligned overlap, we can write

$$\begin{aligned}
\frac{\partial}{\partial(\mathscr{Z}_{\text{rot}})_{11}} &= \frac{\partial z_{11}}{\partial(\mathscr{Z}_{\text{rot}})_{11}}\frac{\partial}{\partial z_{11}} + \partial(\alpha\beta)_{11} = 1/\frac{\partial(\mathscr{Z}_{\text{rot}})_{11}}{\partial z_{11}}\frac{\partial}{\partial z_{11}} + \partial(\alpha\beta)_{11} \\
&= \frac{2}{\sin\beta_T e^{+i\alpha_T}\sin\beta_S e^{+i\alpha_S}}\frac{\partial}{\partial z_{11}} + \partial(\alpha\beta)_{11}, && (4.5.24) \\
\frac{\partial}{\partial(\mathscr{Z}_{\text{rot}})_{22}} &= \frac{\partial z_{11}}{\partial(\mathscr{Z}_{\text{rot}})_{22}}\frac{\partial}{\partial z_{11}} + \partial(\alpha\beta)_{22} = 1/\frac{\partial(\mathscr{Z}_{\text{rot}})_{22}}{\partial z_{11}}\frac{\partial}{\partial z_{11}} + \partial(\alpha\beta)_{22} \\
&= -\frac{2}{\sin\beta_T e^{+i\alpha_T}\sin\beta_S e^{-i\alpha_S}}\frac{\partial}{\partial z_{11}} + \partial(\alpha\beta)_{22}, && (4.5.25) \\
\frac{\partial}{\partial(\mathscr{Z}_{\text{rot}})_{33}} &= \frac{\partial z_{11}}{\partial(\mathscr{Z}_{\text{rot}})_{33}}\frac{\partial}{\partial z_{11}} + \partial(\alpha\beta)_{33} = 1/\frac{\partial(\mathscr{Z}_{\text{rot}})_{33}}{\partial z_{11}}\frac{\partial}{\partial z_{11}} + \partial(\alpha\beta)_{33} \\
&= -\frac{2}{\sin\beta_T e^{-i\alpha_T}\sin\beta_S e^{+i\alpha_S}}\frac{\partial}{\partial z_{11}} + \partial(\alpha\beta)_{33}, && (4.5.26) \\
\frac{\partial}{\partial(\mathscr{Z}_{\text{rot}})_{44}} &= \frac{\partial z_{11}}{\partial(\mathscr{Z}_{\text{rot}})_{44}}\frac{\partial}{\partial z_{11}} + \partial(\alpha\beta)_{44} = 1/\frac{\partial(\mathscr{Z}_{\text{rot}})_{44}}{\partial z_{11}}\frac{\partial}{\partial z_{11}} + \partial(\alpha\beta)_{44} \\
&= \frac{2}{\sin\beta_T e^{-i\alpha_T}\sin\beta_S e^{-i\alpha_S}}\frac{\partial}{\partial z_{11}} + \partial(\alpha\beta)_{44}, && (4.5.27)
\end{aligned}$$

which reduces to

$$\frac{\partial}{\partial(\mathscr{Z}_{\text{rot}})_{\mu\mu}} = \frac{z_{11}}{(\mathscr{Z}_{\text{rot}})_{\mu\mu}}\frac{\partial}{\partial z_{11}} + \partial(\alpha\beta)_{\mu\mu}. \tag{4.5.28}$$

It is important to note that the inversion

$$\frac{\partial z_{11}}{\partial(\mathscr{Z}_{\text{rot}})_{\mu\mu}} = \frac{1}{\frac{\partial(\mathscr{Z}_{\text{rot}})_{\mu\mu}}{\partial z_{11}}}$$

is only valid as long as the denominator is not equal to zero. In all expressions we computed, the denominator would only be zero for the case on which the entire $(\mathscr{Z}_{\text{rot}})_{\mu\mu}$ is zero, on which the corresponding $(\mathscr{K}_{\text{rot}})_{\mu\mu}$ is also zero. Hence, the cases on which z_{11}, $\sin\beta_{S,T}$, or $\cos\beta_{S,T} = 0$ should have the values for the angles plugged in before evaluating the expressions for the partial derivatives. This is also valid for analogous terms in the anti-diagonal and off-diagonal. As our analysis of mixing in the pairing tensor stems from the diagonal terms, we include the remaining derivatives in Appendix D. Although the rotated pairing tensor is written in terms of z_{ST}, the z-aligned overlap

is written in terms of the symmetric and antisymmetric parameters, $z_+, \bar{z}_+, z_-, \bar{z}_-$. Henceforth, we must write the inverse to the transformation of eqs. (4.4.7)-(4.4.10),

$$z_{00} = \frac{1}{4}(z_+ + \bar{z}_+ - z_- - \bar{z}_-), \tag{4.5.29}$$

$$z_{11} = \frac{1}{4}(z_+ + \bar{z}_+ + z_- + \bar{z}_-), \tag{4.5.30}$$

$$z_{10} = \frac{1}{4}(z_+ - \bar{z}_+ + z_- - \bar{z}_-), \tag{4.5.31}$$

$$z_{01} = \frac{1}{4}(z_+ - \bar{z}_+ - z_- + \bar{z}_-). \tag{4.5.32}$$

The respective partial derivatives are, then

$$\begin{aligned}\frac{\partial}{\partial z_{00}} &= \frac{1}{4}\left(\frac{\partial z_+}{\partial z_{00}}\frac{\partial}{\partial z_+} + \frac{\partial \bar{z}_+}{\partial z_{00}}\frac{\partial}{\partial \bar{z}_+} + \frac{\partial z_-}{\partial z_{00}}\frac{\partial}{\partial z_-} + \frac{\partial \bar{z}_-}{\partial z_{00}}\frac{\partial}{\partial \bar{z}_-}\right) \\ &= \frac{1}{4}\left(\frac{\partial}{\partial z_+} + \frac{\partial}{\partial \bar{z}_+} - \frac{\partial}{\partial z_-} - \frac{\partial}{\partial \bar{z}_-}\right), \end{aligned} \tag{4.5.33}$$

$$\frac{\partial}{\partial z_{10}} = \frac{1}{4}\left(\frac{\partial}{\partial z_+} - \frac{\partial}{\partial \bar{z}_+} + \frac{\partial}{\partial z_-} - \frac{\partial}{\partial \bar{z}_-}\right), \tag{4.5.34}$$

$$\frac{\partial}{\partial z_{01}} = \frac{1}{4}\left(\frac{\partial}{\partial z_+} - \frac{\partial}{\partial \bar{z}_+} - \frac{\partial}{\partial z_-} + \frac{\partial}{\partial \bar{z}_-}\right), \tag{4.5.35}$$

$$\frac{\partial}{\partial z_{11}} = \frac{1}{4}\left(\frac{\partial}{\partial z_+} + \frac{\partial}{\partial \bar{z}_+} + \frac{\partial}{\partial z_-} + \frac{\partial}{\partial \bar{z}_-}\right). \tag{4.5.36}$$

4.5.4 The pairing tensor

The simplest case to evaluate the full pairing tensor is that of the diagonal, which is fully expressed in terms of the Euler angles and the vector-isovector parameter z_{11} in the Thouless submatrix (see eqs. (C.0.1)-(C.0.4)). As a reminder, the pairing tensor is written as

$$(\mathscr{K}_{\rm rot})_{\mu\nu} = \frac{1}{\langle \mathscr{Z}_z | \mathscr{Z}_z \rangle} \frac{\partial}{\partial (\mathscr{Z}_{\rm rot})_{\mu\nu}} \langle \mathscr{Z}_z | \mathscr{Z}_z \rangle.$$

In the diagonal, denoting different pre-factors dependent solely on the Euler angles as $C(\alpha_{S,T}, \beta_{S,T})$, the Thouless submatrix is

$$(\mathscr{Z}_{\rm rot})_{\mu\mu} = z_{11} C(\alpha_{S,T}, \beta_{S,T})_{\mu\mu}. \tag{4.5.37}$$

As we have that

$$\frac{\partial}{\partial (\mathscr{Z}_{\rm rot})_{\mu\mu}} = \frac{z_{11}}{(\mathscr{Z}_{\rm rot})_{\mu\mu}} \frac{\partial}{\partial z_{11}} + \partial(\alpha\beta)_{\mu\mu},$$

the diagonal of the pairing tensor can be written as

$$(\mathscr{K}_{\rm rot})_{\mu\mu} = \frac{C(\alpha_{S,T}, \beta_{S,T})^{-1}_{\mu\mu}}{\langle \mathscr{Z}_z | \mathscr{Z}_z \rangle} \frac{\partial}{\partial z_{11}} \langle \mathscr{Z}_z | \mathscr{Z}_z \rangle \tag{4.5.38}$$

$$= \frac{C(\alpha_{S,T}, \beta_{S,T})^{-1}_{\mu\mu}}{\langle \mathscr{Z}_z | \mathscr{Z}_z \rangle} \sum_i \frac{\partial}{\partial z_i} \langle \mathscr{Z}_z | \mathscr{Z}_z \rangle, \tag{4.5.39}$$

where $z_i = z_+, \bar{z}_+, z_-, \bar{z}_-$ appear after applying eq. 4.5.36. Finally, we get the compact expression

$$\mathscr{K}^{\text{rot}}_{\mu\mu} = C(\alpha_{S,T}, \beta_{S,T})^{-1}_{\mu\mu} \left[\frac{z_+^*}{1+|z_+|^2} + \frac{\bar{z}_+^*}{1+|\bar{z}_+|^2} + \frac{z_-^*}{1+|z_-|^2} + \frac{\bar{z}_-^*}{1+|\bar{z}_-|^2} \right]. \tag{4.5.40}$$

Although the diagonal entries of the Thouless submatrix depend only on the vector-isovector constant, $z_{11}^* = z_+^* + \bar{z}_+^* + z_-^* + \bar{z}_-^*$, and the Euler angles, the same entries in the subspace pairing tensor cannot be written solely as a function of $\alpha_{S,T}, \beta_{S,T}, z_{11}$. Therefore, different spin-isospin channels are mixed in the pairing tensor, even though they separate in the Thouless matrix $\mathscr{X}^+_{\text{rot}}$. Although the diagonal is the easiest way to visualise such mixing, it is important to notice that this is also true for the anti-diagonal and off-diagonal elements. However, the expressions become less clear, as each partial derivative $\partial/\partial z_i$ has a different pre-factor dependent on $\alpha_{S,T}, \beta_{S,T}$ (see appendix D).

4.6 Rotating the pairing tensor

Although we have accomplished our goal of obtaining an expression for the pairing tensor of nuclear matter from a general HFB wavefunction, there is one more approach we could follow as a different check to our peculiar conclusion of mixing in the ST channels. In principle, we could rotate the z-aligned pairing tensor over the same Euler angles to obtain a pairing tensor with an arbitrary orientation in space and isospin space, albeit not obtained directly from a general wavefunction. This result could be compared with the Thouless submatrix obtained in the previous section, $\mathscr{X}^+_{\text{rot}}$, to analyse spin and isospin mixing. To perform such rotation in spin and isospin space, the rotation matrix $U(R)$ should be given by

$$U(R) = U_T(\Omega_T) \otimes U_S(\Omega_S), \tag{4.6.1}$$

i.e.,

$$U(R) = \begin{pmatrix} U_T^{11}(\Omega_T)U_S(\Omega_S) & U_T^{12}(\Omega_T)U_S(\Omega_S) \\ U_T^{21}(\Omega_T)U_S(\Omega_S) & U_T^{22}(\Omega_T)U_S(\Omega_S) \end{pmatrix}, \tag{4.6.2}$$

where each entry is a 2×2 block matrix. We can explicitly write these rotation matrices for spin and isospin as

$$U_S(\Omega_S) = \begin{pmatrix} e^{-i\alpha_S/2} & 0 \\ 0 & e^{+i\alpha_S/2} \end{pmatrix} \begin{pmatrix} \cos\frac{\beta_S}{2} & -\sin\frac{\beta_S}{2} \\ \sin\frac{\beta_S}{2} & \cos\frac{\beta_S}{2} \end{pmatrix} \begin{pmatrix} e^{-i\gamma_S/2} & 0 \\ 0 & e^{+i\gamma_S/2} \end{pmatrix}, \tag{4.6.3}$$

$$= \begin{pmatrix} e^{-i(\alpha_S+\gamma_S)/2}\cos\frac{\beta_S}{2} & -e^{-i(\alpha_S-\gamma_S)/2}\sin\frac{\beta_S}{2} \\ e^{i(\alpha_S-\gamma_S)/2}\sin\frac{\beta_S}{2} & e^{i(\alpha_S+\gamma_S)/2}\cos\frac{\beta_S}{2} \end{pmatrix}. \tag{4.6.4}$$

Therefore, the full rotation matrix is then given by

$$U(R) = \begin{pmatrix} e^{-i(\alpha_T+\gamma_T)/2}\cos\frac{\beta_T}{2}U_S(\Omega_S) & -e^{-i(\alpha_T-\gamma_T)/2}\sin\frac{\beta_T}{2}U_S(\Omega_S) \\ e^{i(\alpha_T-\gamma_T)/2}\sin\frac{\beta_T}{2}U_S(\Omega_S) & e^{i(\alpha_T+\gamma_T)/2}\cos\frac{\beta_T}{2}U_S(\Omega_S) \end{pmatrix}, \tag{4.6.5}$$

and explicitly

$$U(R) = \begin{pmatrix} e^{-i(\alpha_T+\gamma_T)/2}\cos\frac{\beta_T}{2}e^{-i(\alpha_S+\gamma_S)/2}\cos\frac{\beta_S}{2} & -e^{-i(\alpha_T+\gamma_T)/2}\cos\frac{\beta_T}{2}e^{-i(\alpha_S-\gamma_S)/2}\sin\frac{\beta_S}{2} \\ e^{-i(\alpha_T+\gamma_T)/2}\cos\frac{\beta_T}{2}e^{i(\alpha_S-\gamma_S)/2}\sin\frac{\beta_S}{2} & e^{-i(\alpha_T+\gamma_T)/2}\cos\frac{\beta_T}{2}e^{i(\alpha_S+\gamma_S)/2}\cos\frac{\beta_S}{2} \\ e^{i(\alpha_T-\gamma_T)/2}\sin\frac{\beta_T}{2}e^{-i(\alpha_S+\gamma_S)/2}\cos\frac{\beta_S}{2} & -e^{i(\alpha_T-\gamma_T)/2}\sin\frac{\beta_T}{2}e^{-i(\alpha_S-\gamma_S)/2}\sin\frac{\beta_S}{2} \\ e^{i(\alpha_T-\gamma_T)/2}\sin\frac{\beta_T}{2}e^{i(\alpha_S-\gamma_S)/2}\sin\frac{\beta_S}{2} & e^{i(\alpha_T-\gamma_T)/2}\sin\frac{\beta_T}{2}e^{i(\alpha_S+\gamma_S)/2}\cos\frac{\beta_S}{2} \end{pmatrix} \tag{4.6.6}$$

$$\begin{pmatrix} -e^{-i(\alpha_T-\gamma_T)/2}\sin\frac{\beta_T}{2}e^{-i(\alpha_S+\gamma_S)/2}\cos\frac{\beta_S}{2} & e^{-i(\alpha_T-\gamma_T)/2}\sin\frac{\beta_T}{2}e^{-i(\alpha_S-\gamma_S)/2}\sin\frac{\beta_S}{2} \\ -e^{-i(\alpha_T-\gamma_T)/2}\sin\frac{\beta_T}{2}e^{i(\alpha_S-\gamma_S)/2}\sin\frac{\beta_S}{2} & -e^{-i(\alpha_T-\gamma_T)/2}\sin\frac{\beta_T}{2}e^{i(\alpha_S+\gamma_S)/2}\cos\frac{\beta_S}{2} \\ e^{i(\alpha_T+\gamma_T)/2}\cos\frac{\beta_T}{2}e^{-i(\alpha_S+\gamma_S)/2}\cos\frac{\beta_S}{2} & -e^{i(\alpha_T+\gamma_T)/2}\cos\frac{\beta_T}{2}e^{-i(\alpha_S-\gamma_S)/2}\sin\frac{\beta_S}{2} \\ e^{i(\alpha_T+\gamma_T)/2}\cos\frac{\beta_T}{2}e^{i(\alpha_S-\gamma_S)/2}\sin\frac{\beta_S}{2} & e^{i(\alpha_T+\gamma_T)/2}\cos\frac{\beta_T}{2}e^{i(\alpha_S+\gamma_S)/2}\cos\frac{\beta_S}{2} \end{pmatrix}.$$

From $U(R)$, we have the rotated pairing tensor as

$$\mathcal{K}^{\text{rot}} = U(R)\mathcal{K}_z U^+(R). \tag{4.6.7}$$

As the expressions are convoluted, we can look at the rotated pairing tensor element by element

$$\mathcal{K}^{\text{rot}}_{\mu\nu} = \sum_{\delta\rho} U_{\mu\delta}\mathcal{K}^z_{\delta\rho}U^*_{\nu\rho}. \tag{4.6.8}$$

For the diagonal, we can write explicitly

$$\begin{aligned}
\mathcal{K}^{\text{rot}}_{11} &= U_{11}\mathcal{K}^z_{14}U^*_{14} + U_{12}\mathcal{K}^z_{23}U^*_{13} + U_{13}\mathcal{K}^z_{32}U^*_{12} + U_{14}\mathcal{K}^z_{41}U^*_{11} \\
&= -e^{-i(\alpha_T+\gamma_T)/2}\cos\frac{\beta_T}{2}e^{-i(\alpha_S+\gamma_S)/2}\cos\frac{\beta_S}{2}e^{i(\alpha_T-\gamma_T)/2}\sin\frac{\beta_T}{2}e^{i(\alpha_S-\gamma_S)/2}\sin\frac{\beta_S}{2}\frac{z^*_+}{1+|z_+|^2} \\
&\quad -e^{-i(\alpha_T+\gamma_T)/2}\cos\frac{\beta_T}{2}e^{-i(\alpha_S-\gamma_S)/2}\sin\frac{\beta_S}{2}e^{i(\alpha_T-\gamma_T)/2}\sin\frac{\beta_T}{2}e^{i(\alpha_S+\gamma_S)/2}\cos\frac{\beta_S}{2}\frac{\bar{z}^*_+}{1+|\bar{z}_+|^2} \\
&\quad -e^{-i(\alpha_T-\gamma_T)/2}\sin\frac{\beta_T}{2}e^{-i(\alpha_S+\gamma_S)/2}\cos\frac{\beta_S}{2}e^{i(\alpha_T+\gamma_T)/2}\cos\frac{\beta_T}{2}e^{i(\alpha_S-\gamma_S)/2}\sin\frac{\beta_S}{2}\frac{z^*_-}{1+|z_-|^2} \\
&\quad -e^{-i(\alpha_T-\gamma_T)/2}\sin\frac{\beta_T}{2}e^{-i(\alpha_S-\gamma_S)/2}\sin\frac{\beta_S}{2}e^{i(\alpha_T+\gamma_T)/2}\cos\frac{\beta_T}{2}e^{i(\alpha_S+\gamma_S)/2}\cos\frac{\beta_S}{2}\frac{\bar{z}^*_-}{1+|\bar{z}_-|^2} \\
&= -\frac{1}{4}e^{-i\gamma_S}\sin\beta_S e^{-i\gamma_T}\sin\beta_T\frac{z^*_+}{1+|z_+|^2} - \frac{1}{4}e^{+i\gamma_S}\sin\beta_S e^{-i\gamma_T}\sin\beta_T\frac{\bar{z}^*_+}{1+|\bar{z}_+|^2} \\
&\quad -\frac{1}{4}e^{-i\gamma_S}\sin\beta_S e^{+i\gamma_T}\sin\beta_T\frac{z^*_-}{1+|z_-|^2} - \frac{1}{4}e^{+i\gamma_S}\sin\beta_S e^{+i\gamma_T}\sin\beta_T\frac{\bar{z}^*_-}{1+|\bar{z}_-|^2},
\end{aligned}$$

which once again cannot be expressed purely as a function of z_{11} and the rotation angles, indicating mixing of the ST channels compared to the rotated Thouless matrix, which isolates the vector-isovector parameter in the diagonal.

4.6.1 Considerations about rotations in the subspace

It is worth noting that a full rotation in space would also include the linear momentum

$$\tilde{U}(R) = U_{\mathbf{k}}(\Omega) \otimes U_T(\Omega_T) \otimes U_S(\Omega), \tag{4.6.9}$$

and should be applied to the full pairing tensor, κ, instead of the subspace variant, $\mathscr{K}$. In principle, this could mix blocks of different linear momenta, such that the final result is no longer diagonal in $\mathbf{k}$. We can argue, however, that the pairing tensor is *always* diagonal in $\mathbf{k}$ by construction, as shown in eq. (4.2.5), such that the rotation given in eq. (4.6.1), applied to the subspace pairing tensor, $\mathscr{K}$, suffices to obtain the most general system.

4.7 Conclusions

Our theoretical work sets a formal background for how the wavefunction of NM is linked to the pairing tensor and density matrix. We go from simple to general examples and see that the different proton-neutron channels do not separate in the pairing tensor. This curious conclusion tells us that approaches assuming the inclusion of only selected pairing channels can be misleading, as the behaviour of nuclear matter is different from that of a finite many-body system. The quantitative question of how much this mixing impacts the pairing gap in nuclear matter remains open. As our analysis focuses solely on facets of HFB theory, this result is completely interaction-independent.

To quantify any effect, one must apply this study to a desired energy density functional (EDF) and obtain the pairing gap, comparing it to the usual procedure available in the literature, to understand at which point proton-neutron mixing and pairing manifest in practice. Concretely, future work would entail selecting an EDF, solving the gap equation from the starting point of a fully separated pairing tensor, and of the mixed pairing tensor discussed in this chapter. This would allow us to quantify the differences between the two and establish the impact of mixing in the proton-neutron pairing channels. Another significant work worth exploring is understanding *how* the mixed pairing gap can be utilised to fit new functionals, as the pairing gap typically utilised in EDF fittings comes from *ab initio* calculations of either pure neutron matter or symmetric nuclear matter, with an identical proportion of protons and neutrons. Only after this connection has been established can we understand the impact of this work on finite nuclei. For now, the message is that utilising EDFs fitted with paired nuclear matter—which do not account for the intrinsic mixing in infinite systems here discussed—introduces formal mistakes within HFB theory. Applying these functionals to finite nuclei, especially in the pairing channel, could be misleading. A full fitting of an EDF which accounts for both properties of finite nuclei *and* mixed pairing channels on nuclear matter is a complicated subject, but necessary to fully bridge finite and infinite systems. Until this

work is done, this result remains a reminder that more is different, even when the starting point is a theory formulated for a *many*-body system.



Five

Analysis of pairing strengths

We analyse pairing strengths as a source of the discrepancy between theoretical calculations and experimental measurements of magnetic dipole moments within the Sn-Gd region. To that end, we analyse the odd-even staggering (OES) for different pairing strengths.

Electromagnetic moments have long been a powerful source of information on the structure of atomic nuclei (Kopfermann 1958). Electric quadrupole moments tell us about nuclear shapes, being highly sensitive to the collective degrees of freedom (a theme which will be further explored in Chapter 6). On the other hand, single-particle aspects, such as shell properties of the valence unpaired nucleon, heavily influence the magnetic dipole moment (Castel and Towner 1990).

Providing a global description of electromagnetic moments is a challenge for nuclear theory. Traditional shell-model calculations succeed in describing experimental data, but often resort to effective g–factors or effective charges (Klose et al. 2019; Neyens 2003; Papuga et al. 2013; Rodríguez et al. 2020). These vary according to the region of the nuclear chart considered, leading to targeted instead of general results. The more robust *ab initio* approaches still face difficulties tackling heavier systems. These difficulties are due to computational costs and technical challenges, mainly on accounting for extensive many-body correlations (Henderson et al. 2018), or dealing with unmanageably large phase spaces (Stroberg et al. 2022). While achieving results for heavier systems from *ab initio* approaches is still not feasible, nuclear density functional theory (DFT) has been a reliable method, achieving good results throughout the nuclear chart without requiring any specification for different regions.

Sassarini et al. 2022 studied one-particle and one-hole neighbours of doubly magic nuclei, achieving a global description of electric quadrupole and magnetic dipole moments without the need for effective g factors. Subsequently, Bonnard et al. 2023 extended the applicability of current nuclear DFT calculations of electromagnetic moments by including pairing, making the method suitable for describing all nuclei. This major development laid the groundwork for analysing heavy, open-shell, deformed, and paired odd-nuclei within the nuclear DFT approach. In Wibowo, Backes et al. 2025, we performed nuclear DFT calculations to determine the spectroscopic

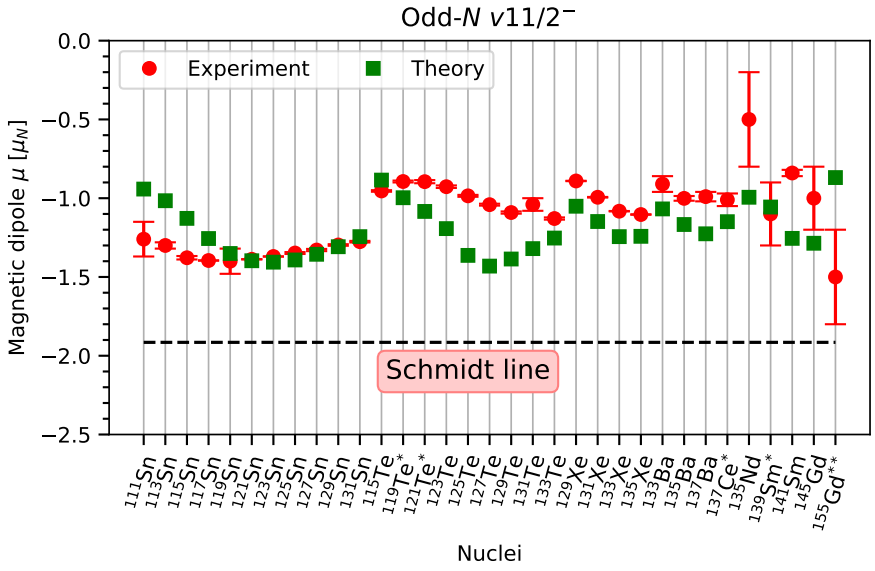


Figure 5.1: Comparison between the calculated magnetic dipole μ moments of the $\nu 11/2^-$ configurations in odd-N nuclei and the available experimental data (Stone 2021). The isotopes where the signs of the magnetic dipole moments are experimentally undetermined and determined from the theoretical calculations are marked with the asterisk symbols (*). Reproduced from Wibowo, Backes et al. 2025

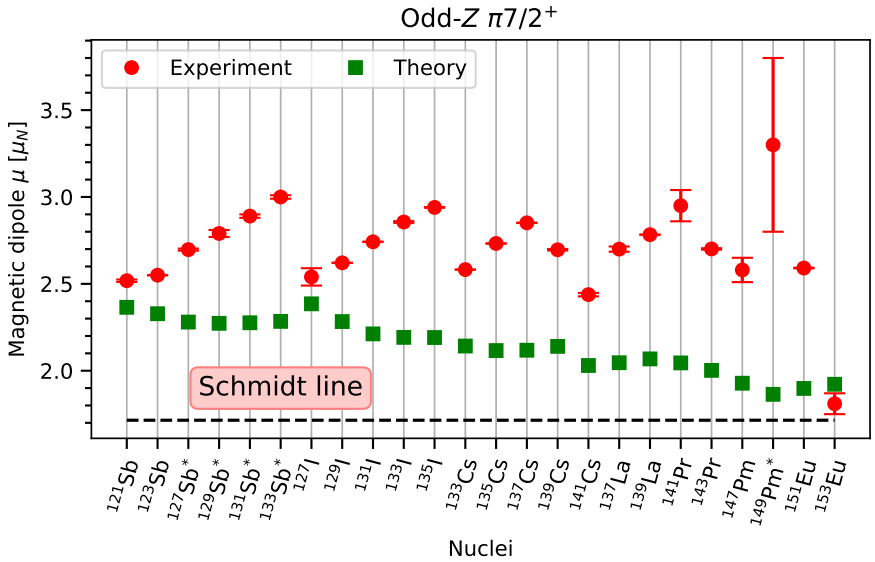


Figure 5.2: Same as in Figure 5.1 for $\pi 7/2^+$ configurations in odd-Z nuclei. Reproduced from Wibowo, Backes et al. 2025.

electric quadrupole and magnetic dipole moments in heavily deformed open-shell paired odd-nuclei. Specifically, we obtained spectroscopic moments of paired nuclear states associated with the blocked proton (neutron) $7/2^+$ ($11/2^-$) configurations within the Sn-Gd region. In this work, we observed a reasonable agreement with experimental data for the electric quadrupole moment. However, the calculated spectroscopic magnetic dipole moments fail to reproduce experimental data in either the $\nu 11/2^-$ or the $\pi 7/2^+$ configuration, as shown in Figures 5.1 and 5.2, respectively. These results suggest that the currently employed spin-spin interactions are insufficient, and that the inclusion of more intricate time-odd interactions, or accounting for many-body contributions, is crucial for accurately describing magnetic dipole moments. To further assess the issue, we first analysed potential sources of discrepancy in our results. Since the magnetic dipole moments heavily depend on the single-particle properties, especially those of the unpaired nucleon, this difference could be due to a poor adjustment of the pairing strengths for our region of interest in the nuclear chart. In this short chapter, we present an extended version of the results from Section 4.2 of Wibowo, Backes et al. 2025.

5.1 Pairing in UNEDF1

The energy density functional (EDF) of choice for this work is a Skyrme functional with the UNEDF1 parametrisation (Kortelainen, McDonnell et al. 2012). The pairing energy density is a mixture of surface and volume pairing (Dobaczewski, Nazarewicz and Stoitsov 2002), given by

$$\tilde{\chi}(\mathbf{r}) = \sum_{q=p,n} \frac{V_{0q}}{2} \left[1 - \frac{\rho_0(\mathbf{r})}{\rho_c}\right] \tilde{\rho}_q^2(\mathbf{r}), \tag{5.1.1}$$

where $\tilde{\rho}_q(\mathbf{r})$ for neutrons ($q = n$) or protons ($q = p$) is the local pairing density, $\rho_c = 0.16$ fm^{-3}, and V_{0n} and V_{0p} are the neutron and proton pairing strengths, which may differ. To prevent the collapse of pairing and restore good particle number, this functional was adjusted while utilising the Lipkin-Nogami (LN) prescription, which is an approximate particle-number projection (PNP) technique (Dobaczewski and Nazarewicz 1993; Dobaczewski 2009; Lipkin 1960; Nogami 1964). In both Wibowo, Backes et al. 2025 and Bonnard et al. 2023, the same mixed pairing was utilised, but the Hartree-Fock-Bogoliubov (HFB) approach was utilised without LN. Bender, Rutz et al. 2000 shows that within the LN with Bardeen–Cooper–Schrieffer (BCS) approach, the particle-number-projected spectral gaps are larger than those of the BCS by the LN second-order coefficient. Despite the difference between BCS and HFB, the same conclusion of Bender, Rutz et al. 2000 holds for HFB, as the canonical HFB basis coincides with the BCS approximation. To compensate for the discrepancies in the pairing gap due to not utilising LN, one can increase the pairing strengths. This automatically leads to an increase in the pairing gaps. In both Bonnard et al. 2023 and Wibowo,

Backes et al. 2025, the increase utilised was that of 20%, which should be, on average, compatible with experimental data. The effect of not utilising exact PNP has also been analysed in Wibowo, Backes et al. 2025, Section 4.3, where it is shown that spectroscopic moments vary only about 1% when computed with and without PNP.

5.2 Changing pairing strengths in UNEDF1

As magnetic dipole moments strongly depend on both the single-particle properties and the polarisation of the paired core, in this section we critically evaluate the adjustment of the pairing strengths in the studied nuclei. To that end, we determined the proton and neutron OES, i.e., the difference in binding energy between a given odd nucleus and the average of its even-even neighbours

$$\mathrm{OES} = B(N_{\mathrm{even}}, Z_{\mathrm{odd}}) - \frac{1}{2}\left(B(N, Z+1) + B(N, Z-1)\right), \tag{5.2.1}$$

$$\mathrm{OES} = B(N_{\mathrm{odd}}, Z_{\mathrm{even}}) - \frac{1}{2}\left(B(N+1, Z) + B(N-1, Z)\right), \tag{5.2.2}$$

respectively. When fitting EDFs, OES are typically the experimental data linked to pairing utilised for the fit. To assess whether the pairing strengths are well adjusted, it is then natural to obtain the OES, which can be compared to experimental data. The binding energies of odd nuclei in the Sn-Gd region were computed and compared with data in Wibowo, Backes et al. 2025, and were utilised as a starting point for the calculations with different pairing strengths detailed in this chapter. In Wibowo, Backes et al. 2025 we utilised the UNEDF1 pairing strength parameters increased by 20% to account for not utilising LN, so for this analysis we experimented with different percentages of the original UNEDF1 parametrisation (Kortelainen, McDonnell et al. 2012), including UNEDF1+20%. Specifically, we chose to investigate the following sets of pairing strength parameters: UNEDF1-20%, UNEDF1, UNEDF1+20%, and UNEDF1+40%. For these sets of parameters, we also computed the ground-state energy of even-even neighbours of odd nuclei in the Sn-Gd region. It is worth noting that the OES values obtained in this manner are not identical to those typically calculated to evaluate the ground-state pairing energies. By analysing the binding energies of specific configurations, regardless of their positions in the spectra of odd nuclei, we assess the combined effects of the pairing strengths and isomer excitation energies. In contrast, the standard ground-state values mix the effects of the pairing strengths and configuration changes.

For a detailed guide on the calculations of odd nuclei, one is referred to the original publication (Wibowo, Backes et al. 2025). For this analysis, we have chosen the lowest energy, i.e., the global minima of the potential energy surface. These minima may be prolate or oblate, so that for consistency, we have selected (i) identical shapes for the two even-even neighbours and (ii) either

the same or opposite shapes for the odd nuclei and their even-even neighbours. We have subtracted the isomer excitation energies from the experimental data (ENSDF 2023) from the corresponding ground-state binding energies (Wang et al. 2021b) of odd nuclei. The neutron and proton OES are shown in Figures 5.3 and 5.4, respectively. Different colours denote different pairing strengths, where percentages of UNEDF1's were either added or subtracted from the original. For completeness, we also show the histograms of the total residuals of the neutron and proton OES in Figures 5.5 and 5.6, and separated by the different isotopic/isotonic chains in Figures 5.7 and 5.8. The histograms of residuals also list the mean and standard deviation for each parameter set.

By inspecting Figures 5.3 and 5.4, it is clear that changing the pairing strength affects the OES. Specifically, the more strongly bound pairs (set UNEDF1+40%) tend to have a larger OES, which decreases for the other parameter sets, and is minimised for UNEDF1-20%. One important aspect in the neutron OES is that, regardless of pairing strength, we are able to replicate the jumps around $N = 82$, which are associated with the shell closure. These experimental jumps are less pronounced than the theoretical values, with the exception of Sn isotopes ($Z = 50$). For heavier isotopic chains, the shape of the OES curve is not entirely reproduced, but this issue is irrespective of the choice of pairing strength. Our results show a better agreement with data for the proton OES, which can be verified in the histograms of the residuals, as the mean is significantly smaller for the proton compared to the neutron OES residuals.

For both the proton and neutron OES, the original set of OES is, on average, the closest to the experimental data. However, it does show a higher standard deviation when compared to the UNEDF1+20% set. It is important to notice, however, that the UNEDF1+20% pairing strength parameter set is the one for which the most calculations converged. For other sets, many of the even and odd nuclei did not converge, mostly due to the collapse of pairing. We also note that for Sn isotopes, which are part of the calibration set of UNEDF1—although Sn OES data is not included in the calibration (Kortelainen, Lesinski et al. 2010)—utilising the pairing strengths increased by 20% yields an almost perfect agreement with experimental data.

Overall, it is easy to note that changing the pairing strengths shifts the theoretical lines toward higher or lower values, and does not address the inconsistencies with experimental values. Increasing the pairing strengths by 20% simultaneously yields the most stable results and a good agreement with experimental data. Henceforth, this approach is viable for calculations with this functional when utilising the LN method for approximate particle number projection. In all other cases, the best approach is to follow the prescription from the original publication and utilise the original pairing strengths *with* the LN method (Kortelainen, McDonnell et al. 2012). Even though the OES analysis does not clarify the inconsistencies in our results for the magnetic dipole moments μ, it eliminates the pairing strengths as a potential factor. Regarding this issue, Chapter 7 introduces a different approach for reconciling density functional theory-calculated magnetic dipole moments

and experimental data. Additionally, keeping a single value for the pairing strengths maintains the generality of DFT calculations, without necessitating parameter adjustments for specific regions of the nuclear chart, which is one of the commendable features of the theory for research on electromagnetic moments.



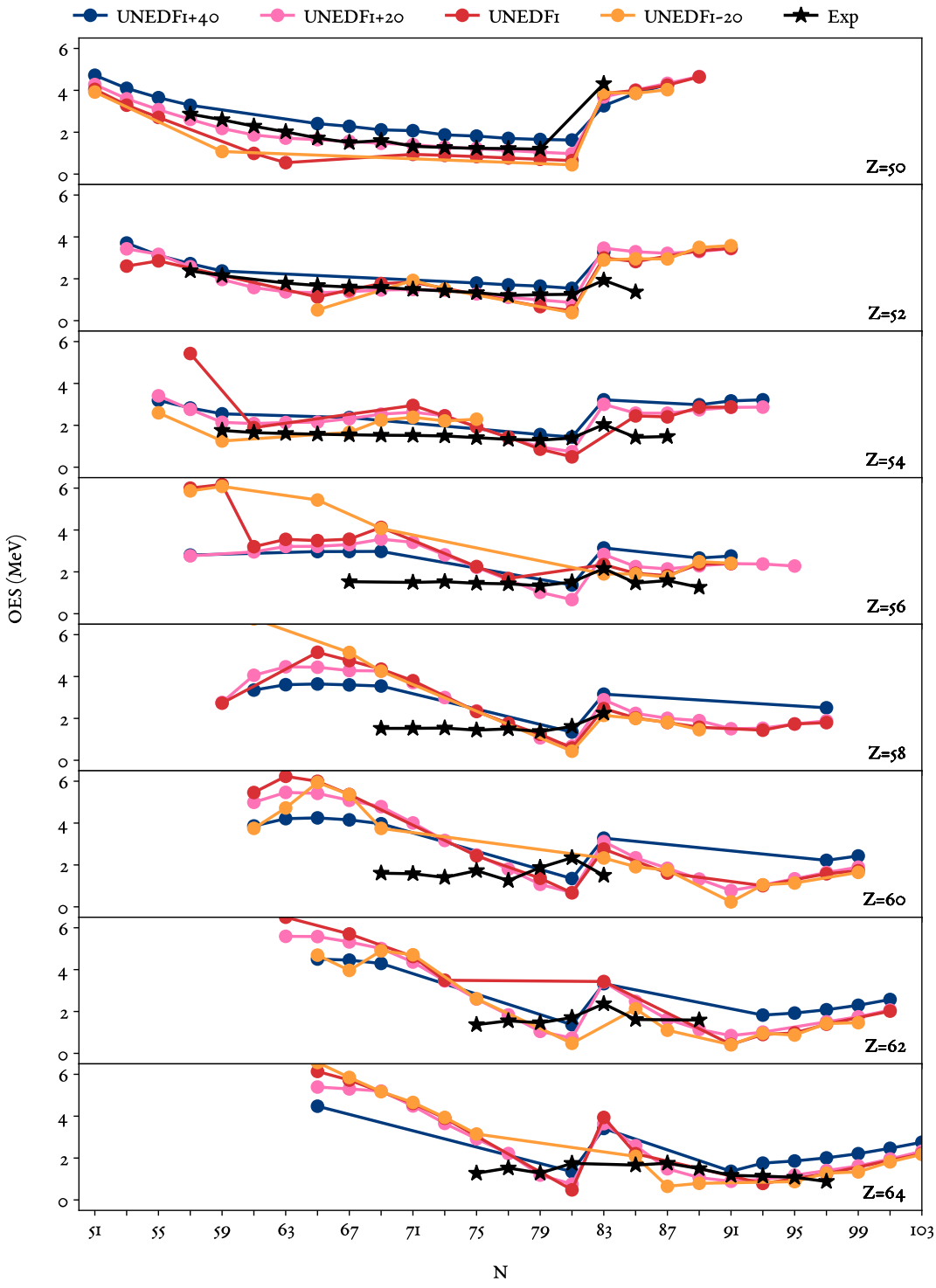


Figure 5.3: OES of different isotopes for different pairing strengths, and experimental data (ENSDF 2023). The functional used was UNEDF1 (Kortelainen, McDonnell et al. 2012), and the proton and neutron pairing strengths were modified by summing or subtracting different percentages of the original UNEDF1.

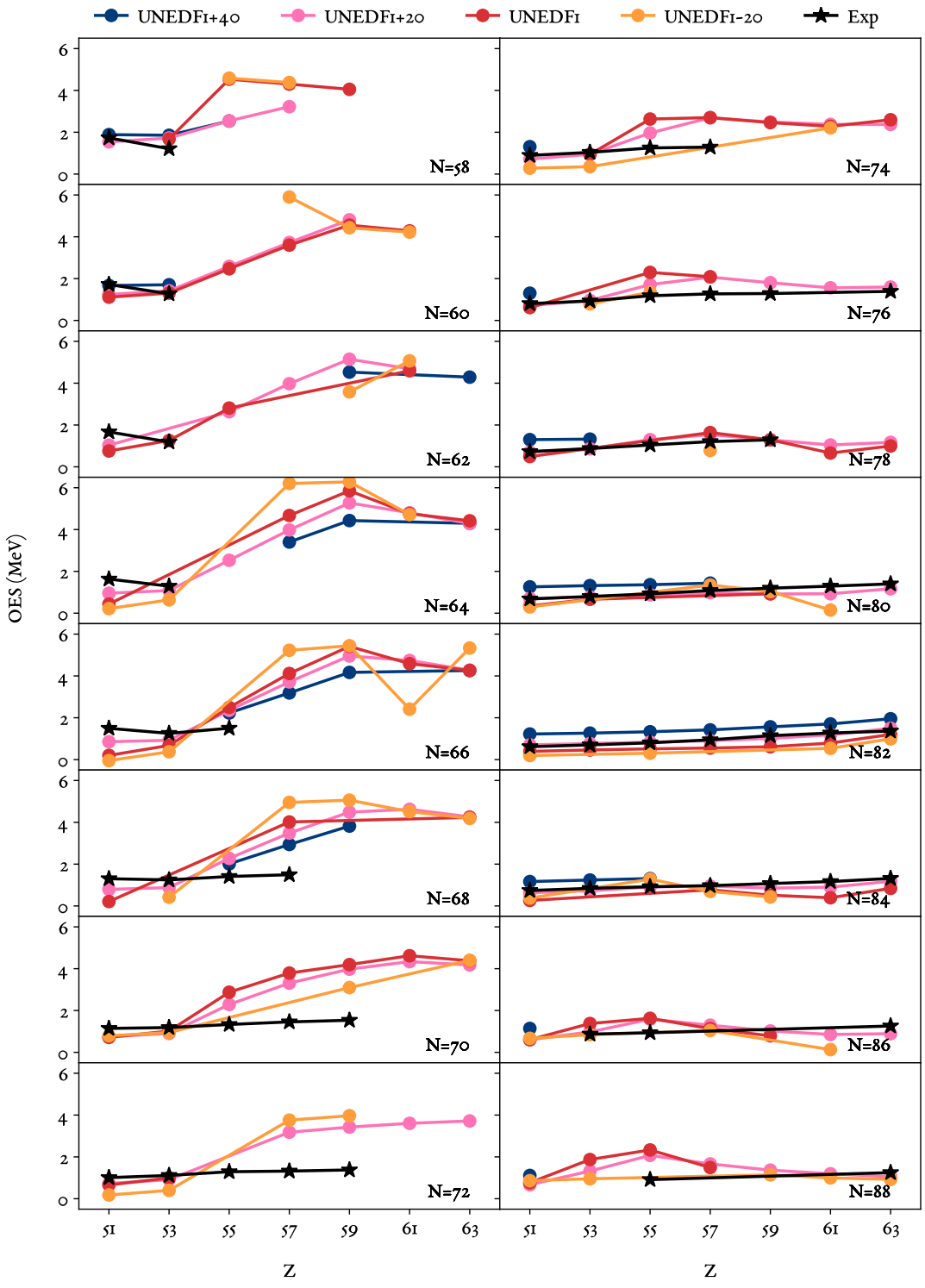


Figure 5.4: OES of different isotones for different pairing strengths, and experimental data (ENSDF 2023). The functional used was UNEDF1 (Kortelainen, McDonnell et al. 2012), and the proton and neutron pairing strengths were modified by summing or subtracting different percentages of the original UNEDF1.

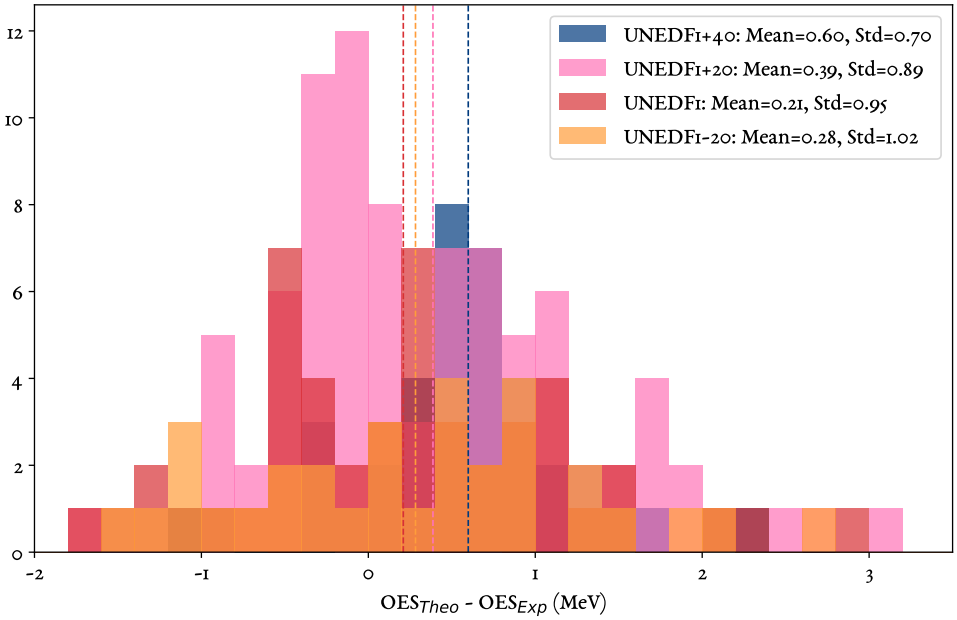


Figure 5.5: Residual of all isotopic chains OESs of Figure 5.3. The mean of each pairing strength is indicated by the dashed lines.

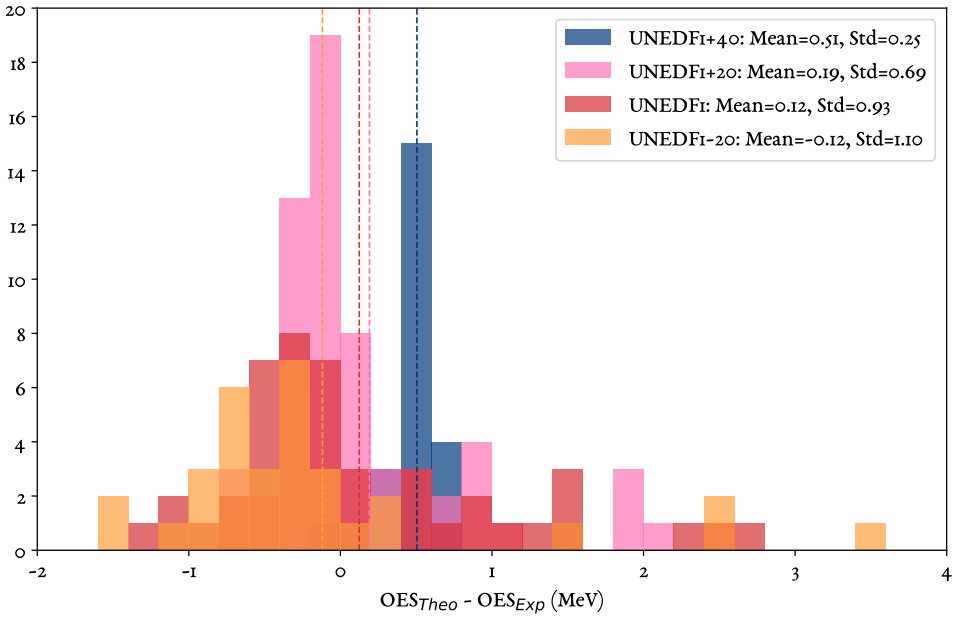


Figure 5.6: Residual of all isotonic chains OESs of Figure 5.4. The mean of each pairing strength is indicated by the dashed lines.

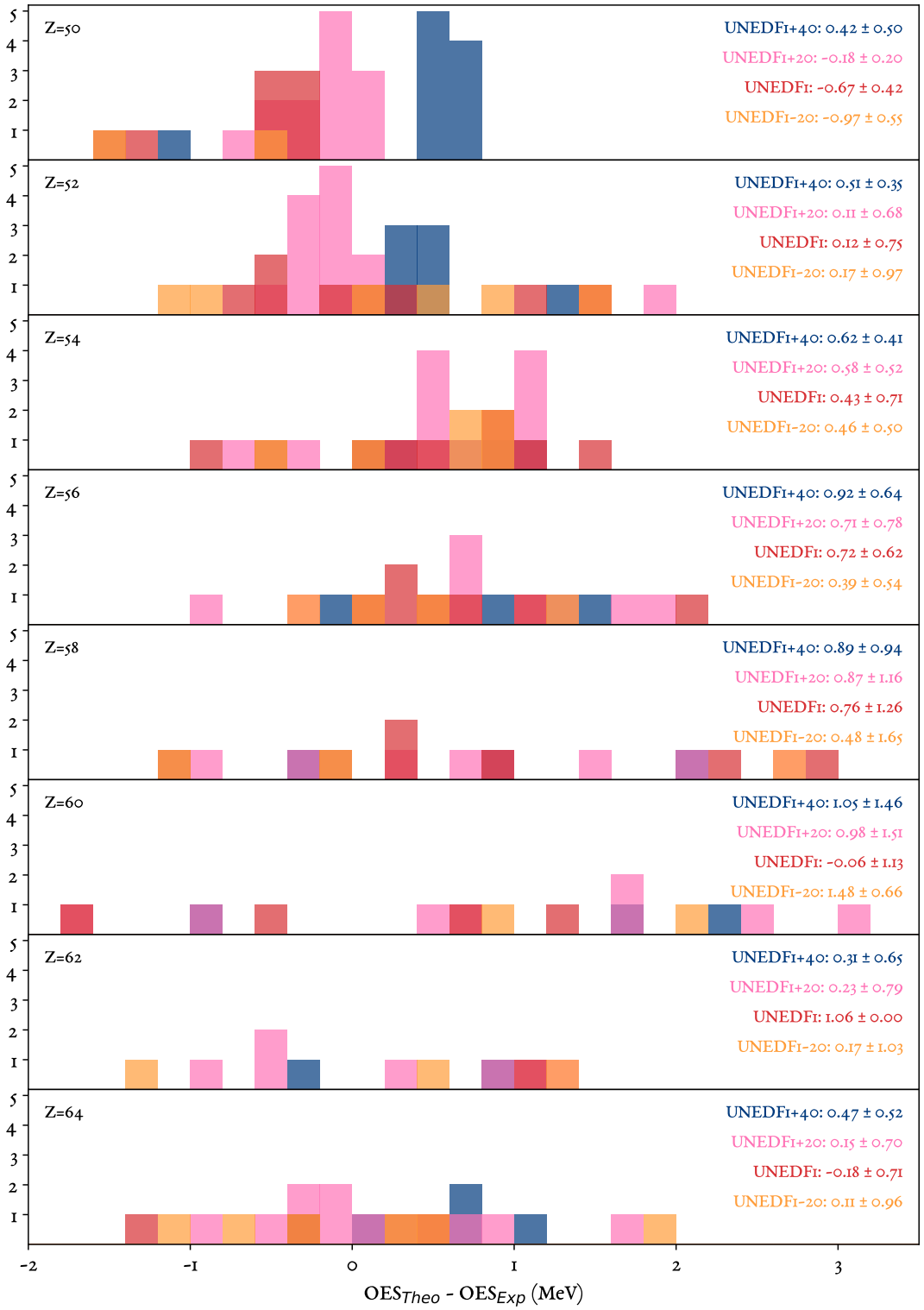


Figure 5.7: Residual for the individual isotopic chains OESs of Figure 5.3.

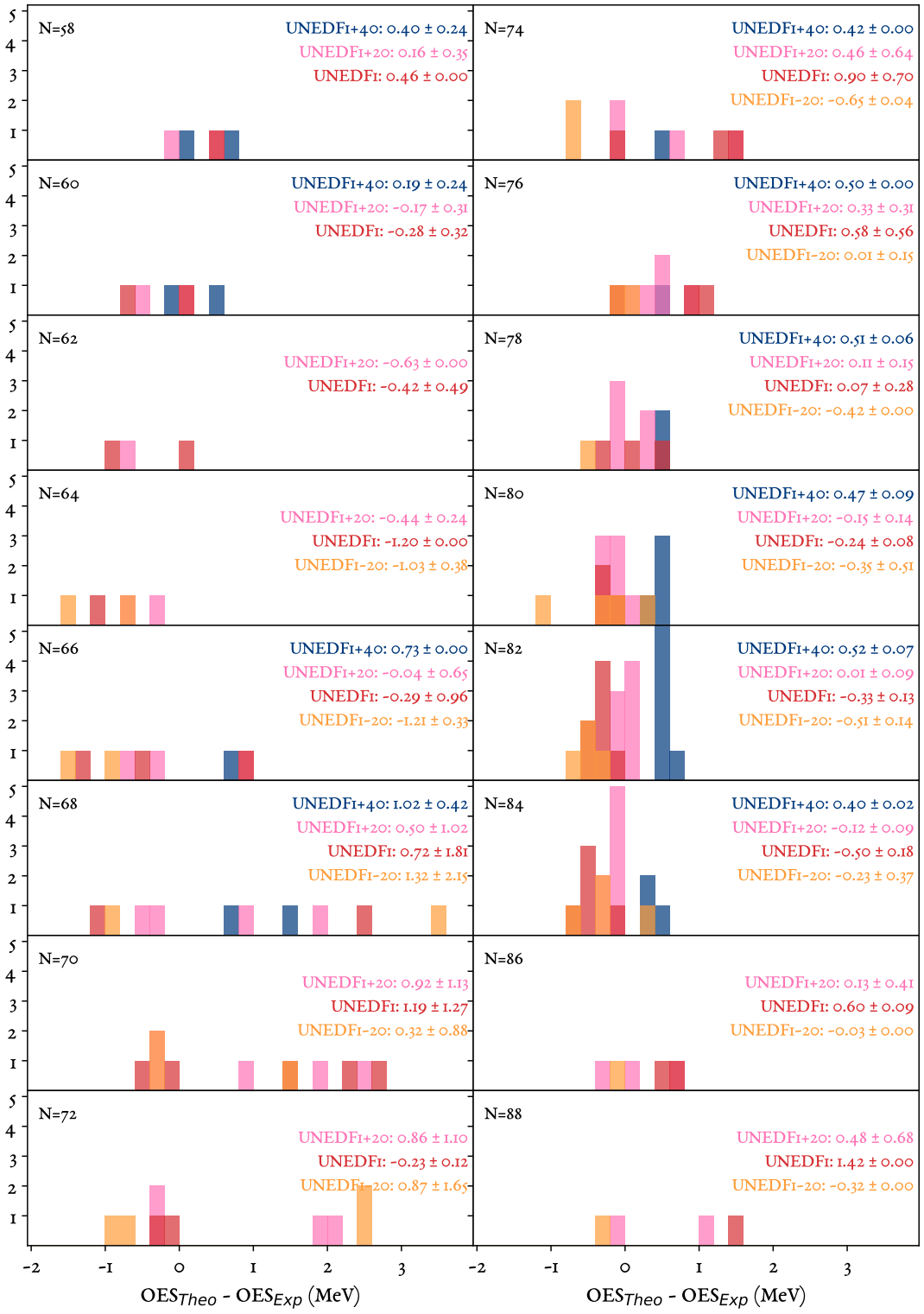


Figure 5.8: Residual for the individual isotonic chains OESs of Figure 5.4.

Six

Odd-odd $N = Z$ nuclei and isospin symmetry-breaking in $T = 1$ multiplets

In this chapter, we shall understand the importance of isospin symmetry for experimental and theoretical analyses, and discuss which observables can be measured experimentally to test isospin symmetry. We shall then focus on one key aspect: that the dependence of the $E2$ matrix elements on isospin projection T_z is linked to the conservation of the isospin symmetry in isobaric nuclei. To study this conjecture, we calculated the $B(E2 : 2^+ \rightarrow 0^+)$ rates for the even-even $T = 1$ mirror nuclei with $42 \leq A \leq 98$ by carrying out angular momentum projection (AMP). Analysing the AMP results against the collective generalised Bohr Hamiltonian calculations showcases that collective effects are crucial for describing experimental data near the $N = Z$ line without invoking explicit beyond-Coulomb isospin symmetry-breaking corrections. With a focus on $N = Z$ nuclei, we discuss the requirements for accurately describing isobaric analog states (IAS), showing that doubly-blocked configurations do not suffice, as the IAS should instead be described via a superposition of proton-neutron pairs atop the quasiparticle vacua. To illustrate this, we go through the $B(E2 \downarrow)$ values for odd-odd $T_z = 0$ nuclei ^{70}Br and ^{78}Y in doubly-blocked configurations, and observe that none of them individually corresponds to the linear trend set by isobar $T = 1$ even-even mirror nuclei.

> Mirror, mirror on the wall, is isospin broken at all?
>
> Jacek Dobaczewski

6.1 Isospin symmetry

The discovery of the neutron by Chadwick 1932 marked a new era for studies of nuclear theory. With a mass very similar to that of the proton, it was clear that the nuclear force acted similarly on both particles. In this scenario, Heisenberg 1932 introduced the notion that the particles in the nucleus should be characterised by their positions, their spin projection, and the projection of a new quantum number, T, which would indicate whether the particle is a proton or a neutron. This concept was later refined by Wigner 1937, who introduced the name of *isotopic spin* for the

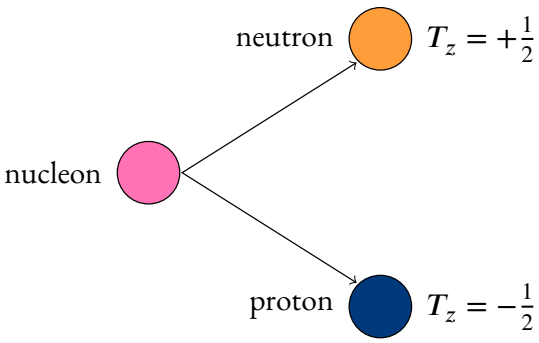


Figure 6.1: The proton and neutron as different isospin projections of a nucleon.

new quantum number which we now call simply *isospin*. Under this picture, protons and neutrons are simply different manifestations of a nucleon, illustrated in Figure 6.1.

As the name suggests, isospin follows the same algebra as spin. This allows us to set the usual z–projection operators[*†], where the projection is not on real space, but in the abstract isospin space

$$\begin{aligned} \hat{t}_z \left|n\right\rangle &= +\tfrac{1}{2} \left|n\right\rangle, \\ \hat{t}_z \left|p\right\rangle &= -\tfrac{1}{2} \left|p\right\rangle, \end{aligned} \qquad \hat{t}_z = \frac{1}{2}\begin{pmatrix} 1 & 0 \\ 0 & -1 \end{pmatrix},$$

and the isospin ladder operators, which are responsible for changing a proton into a neutron or vice-versa

$$\begin{aligned} \hat{t}_- \left|n\right\rangle &= \left|p\right\rangle, & \hat{t}_- \left|p\right\rangle &= 0, \\ \hat{t}_+ \left|n\right\rangle &= 0, & \hat{t}_+ \left|p\right\rangle &= \left|n\right\rangle, \end{aligned} \qquad \hat{t}_+ = \begin{pmatrix} 0 & 1 \\ 0 & 0 \end{pmatrix}, \qquad \hat{t}_- = \begin{pmatrix} 0 & 0 \\ 1 & 0 \end{pmatrix}. \tag{6.1.1}$$

For a many-body system of A nucleons, the total isospin operators are simply

$$\hat{T}_z = \sum_{i=1}^{A} \hat{t}_z^i, \qquad \hat{T}_+ = \sum_{i=1}^{A} \hat{t}_+^i, \qquad \hat{T}_- = \sum_{i=1}^{A} \hat{t}_-^i. \tag{6.1.2}$$

It is useful to express these operators in the language of second quantisation, where we have

$$\hat{T}_z = \frac{1}{2} \sum_{\alpha} \left(a_{\alpha n}^\dagger a_{\alpha n} - a_{\alpha p}^\dagger a_{\alpha p} \right) = \frac{1}{2} (\hat{N}_n - \hat{N}_p); \tag{6.1.3}$$

$$\hat{T}_\pm = \hat{T}_x \pm i\hat{T}_y \quad \Rightarrow \quad \hat{T}_+ = \sum_{\alpha} a_{\alpha n}^\dagger a_{\alpha p}, \qquad \hat{T}_- = \sum_{\alpha} a_{\alpha p}^\dagger a_{\alpha n}. \tag{6.1.4}$$

[*]Note that under the convention employed by particle physics, the proton (uud) would have isospin z–projection $+\frac{1}{2}$ and the neutron (ddu) $-\frac{1}{2}$, due to the isospin projection of the up (down) quark being $\pm\frac{1}{2}$. This can lead to confusion, as I experienced first-hand when comparing numerical results of Chapter 7 with those coming from *ab initio* nuclear theory, which borrows the particle physics convention. My (totally unbiased) opinion is that the better convention (the nuclear physics one) agrees with the original one proposed by Heisenberg 1932.

[†]There is also a freedom in defining these operators with an arbitrary phase instead of 1. Our choice corresponds to the Condon-Shortley phase convention, which fixes the phase between proton and neutron single-particle states (Robson 1966). These phases have important consequences under time-reversal, an anti-linear operator (Perlińska et al. 2004).

Note that these operators satisfy the SU(2) algebra, just as spin, and we have $\left[\hat{T}_+, \hat{T}_-\right] = 2\hat{T}_z$ and $\left[\hat{T}_z, \hat{T}_\pm\right] = \pm\hat{T}_\pm$. It should become clear from these expressions that the isospin ladder operators $\hat{T}_\pm$ simply perform a rotation in isospin space, with a sum over all particle states on which a proton/neutron on a state α can be rotated into a neutron/proton.

In a system of N neutrons and Z protons, the total isospin is the vector sum of all the particles' isospin, and the total z-component is well-defined

$$T_z = \frac{(N-Z)}{2}, \qquad |T_z| \leq T \leq \frac{(N+Z)}{2}. \tag{6.1.5}$$

The total value T can only occur in nuclei with $T_z = -T, ..., T$ and it is not an observable, although it can usually be assigned to different states. The easiest illustration of this is that of two-nucleon systems: np, nn, and pp. The projection T_z of these systems is 0 and ±1, respectively. If the nuclear Hamiltonian commutes with the isospin operator, there should be a correspondence between the states in these systems with the same total isospin T. A state with aligned spins—such as the ground state of the deuteron with $J^\pi = 1^+$—cannot be assigned to the nn and pp systems, as it would violate the Pauli principle, and thus its assigned isospin is $T = 0$ and it is called an *isosinglet*. On the other hand, there are states with $T = 1$ which are present in all three systems, and form an *isotriplet*. In the two-nucleon systems, the lowest $J^\pi = 0^+$ state is a triplet, and is unbound.

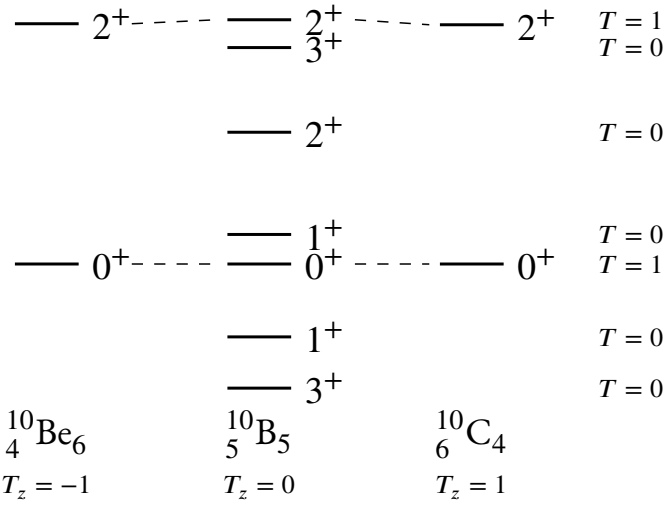


Figure 6.2: Isospin triplets and singlets in the spectra of $A = 10$ isobars, aligning the first $T = 1$ states, i.e., 0^+ (ENSDF 2023). Figure based on Ring and Schuck 1980.

Similar arguments can be made to assign a total isospin to many-body systems, keeping in mind that in general, the states with lowest energy will also have the lowest available isospin, $T = |T_z|$ (Lenzi and Bentley 2009). The only known exceptions to this rule are $N = Z$ odd-odd nuclei with a $T = 1$ ground state, such as ^{34}Cl. A practical example is illustrated in Figure 6.2, where

we see the low-lying spectra for the isobar nuclei of ${}^{10}_{4}\mathrm{Be}_6$, ${}^{10}_{5}\mathrm{B}_5$, and ${}^{10}_{6}\mathrm{C}_4$. The odd-odd $N = Z$ nucleus is the only one with singlet $T = 0$ states, while $T = 1$ states with very similar energies are present in all three nuclei, forming a triplet. If isospin is a good quantum number, it can be used to identify *isobaric analog states* (IAS), where a near identical behavior can be observed in systems with the same number of nucleons. Naturally, small differences are still observed due to isospin non-conserving forces (e.g. Coulomb).

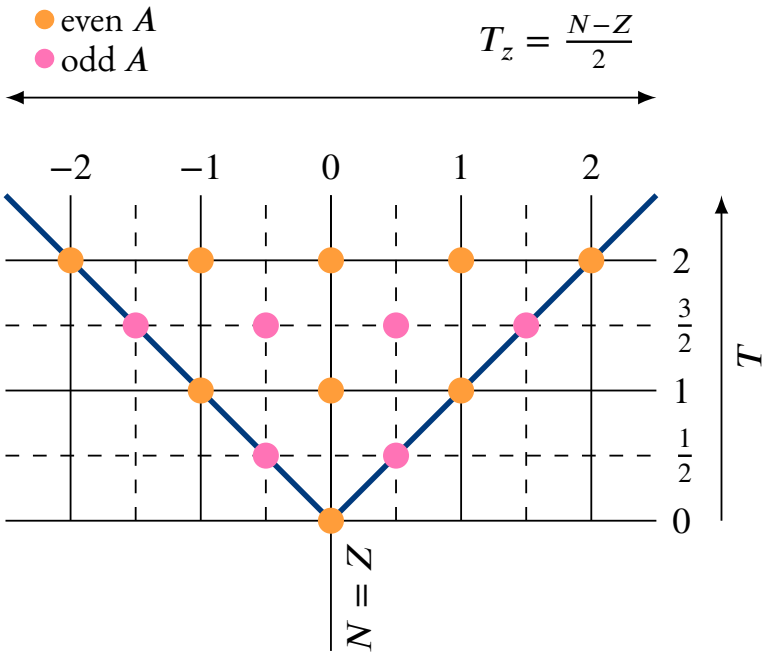


Figure 6.3: Representation of isospin multiplets.

Beyond $T = 0$ and $T = 1$, we can define isospin multiplets as states with the same total isospin and different T_z projection. These are represented in Figure 6.3, where we can see that for even masses the total isospin is an integer, and for odd masses it is a semi-integer, and $T < |T_z|$ is forbidden. Exact isospin symmetry implies correspondence between the isobaric analog states, represented by the horizontal lines. Henceforth, tests of isospin symmetry are performed on states along those lines, as we shall see in the next section. In particular, a *mirror pair* or *mirror nuclei*—with the same mass number, but exchanged numbers of protons and neutrons—should have an identical structure from the point of view of an isospin-symmetric interaction. And indeed, this property of mirror pairs has successfully been used by experimentalists to help identify level schemes. Although the concept works best in light nuclei, where the Coulomb energy is nearly negligible, studies of isospin symmetry have been extended to medium-heavy nuclei, and from low-lying states to high-spin yrast states (Lenzi and Bentley 2009).

6.2 Isospin symmetry-breaking

As just exposed, isospin symmetry is a powerful tool for theory and experiment alike. However, just as important as its concept is the understanding of when it is *broken* instead. To begin with, it is simply not an exact symmetry. The strong interaction is not charge-symmetric, which manifests at the quark level via the different masses of the up and down quarks (Miller, Opper and Stephenson 2006). Likewise, the masses of the neutron and the proton also differ. Exact charge symmetry would require the proton-proton and neutron-neutron interactions to be the same, which can be probed via nucleon-nucleon scattering. Notably, there is a small shift between the scattering length in both measurements (Machleidt and Müther 2001). An even more strict condition is that of charge independence, requiring the np interaction to be $V_{np} = (V_{pp} + V_{nn})/2$, and it is also not fulfilled exactly (González Trotter et al. 1999)*. A more general criterion for charge independence is that the nuclear Hamiltonian commutes with T_z and T^2, i.e., is invariant under rotations in charge and isospin space

$$[H, T_z] = 0, \tag{6.2.1}$$

$$[H, T^2] = 0. \tag{6.2.2}$$

Apart from the criteria on the nuclear interaction itself, the effect of the Coulomb interaction becomes relevant in heavy nuclei, further breaking isospin symmetry. Henceforth, although extremely useful, isospin cannot be considered a "perfect" quantum number, in contrast to, e.g., angular momentum.

From the point of view of the interaction, so long as there are no charge-dependent terms in the nuclear Hamiltonian, isospin should be conserved apart from Coulomb. It is worth noting that an excess of either N or Z is known to introduce isospin impurities in mean-field Hartree-Fock results, known in the literature as *spurious isospin symmetry-breaking* (Brink and Svenne 1970; Engelbrecht and Lemmer 1970; Satuła, Dobaczewski et al. 2009). However, by comparing DFT results with experimental measurements on IAS, we should then be able to gauge whether or not charge-independent functional generators suffice to describe the properties seen in experiment†. We shall now list tests relevant to assessing the limits of isospin symmetry, and delve into detail for the test of greater interest to this work.

6.2.1 Tests of isospin symmetry

As isospin conservation is directly linked to charge dependence, it is natural that electromagnetic transitions are used to test isospin symmetry-breaking. As an example, some $E\lambda$ and $M\lambda$ transitions

*These properties refer to the bare nucleon-nucleon interaction, which is not necessarily the same as an effective in-medium interaction.

†This view is both "correct" *and* naive, as we shall see by the end of this chapter.

are forbidden if isospin is a good quantum number. Differences in excitation energies between IAS also probe isospin symmetry-breaking, an analysis of what is typically called Coulomb energy differences. Other tests of isospin symmetry are the isobaric multiplet mass equation, which assesses how the binding energy splitting is described in a multiplet when charge-violating interactions are present. None of these techniques is the focus of the experimental data confronted with the present theoretical work, and they are mentioned here for the sake of completeness. A reader interested in the topic can find comprehensive information on both the background and experimental results on all these techniques in the review paper and lecture notes by Bentley and Lenzi 2007 and Lenzi and Bentley 2009. The next Section delves deeper into the so-called *linearity rule*, which we examine in more detail over the course of this chapter.

6.2.2 The linearity rule

The proton matrix elements (M_p) are the matrix elements of the electric multipole moment of order λ, Q^λ, between states of the same T and T_z, and initial and final angular momenta J_i and J_f, respectively

$$M_p(T_z) = \left\langle J_f T T_z \left| \hat{Q}^\lambda \right| J_i T T_z \right\rangle . \tag{6.2.3}$$

Within strict isospin symmetry, there are exact predictions for how the transition matrix elements of IAS vary with respect to T_z. These predictions originate from the separation of the nuclear current density between isoscalar and isovector components (Warburton and Wessner 1969). Strictly speaking, the $E2$ transitions, which are of main interest in this study, depend on the distribution of the nuclear charge density ρ_{ch} rather than the proton density ρ_p. As discussed by Reinhard and Nazarewicz 2021, ρ_{ch} is obtained by folding ρ_p with the nucleonic charge distributions. Additional corrections come from the effect of center-of-mass projection. We estimated these corrections to have practically no effect on the quadrupole moments and $B(E2)$ rates, considering the typical experimental uncertainties. Therefore, in the following, we base our discussion on the proton density. Note that the decomposition we utilise is different from that of proton and neutron operators. An operator that depends linearly on the isospin z-projection operator, $\hat{t}_z$, is called isovector. An operator that is independent of $\hat{t}_z$ is called isoscalar. Extending the isoscalar and isovector decomposition of the current density to the quadrupole moment

$$\hat{Q}^\lambda = \hat{Q}^{\lambda(0)} + \hat{Q}^{\lambda(1)}, \tag{6.2.4}$$

we can rewrite the proton matrix elements. Note that M_p is a proton operator, as only protons have electric charge, but due to the isoscalar and isovector separation, it can be written as

$$M_p = \left\langle J_f T T_z \left| \sum_{k=0}^{1} \hat{Q}^{\lambda(k)} \right| J_i T T_z \right\rangle \tag{6.2.5}$$

Via the Wigner-Eckart theorem, we can write it as a sum over the Wigner $3-j$ symbols and the *reduced* matrix elements, which depend only on T, but not T_z

$$M_p(T_z) = \sum_{k=0}^{1} (-1)^{T-T_z} \begin{pmatrix} T & k & T \\ -T_z & 0 & T_z \end{pmatrix} \left\langle J_f T \left|\left| \hat{Q}^{\lambda(k)} \right|\right| J_i T \right\rangle . \tag{6.2.6}$$

Explicitly, the isoscalar and isovector components can be written as

$$(-1)^{T-T_z} \begin{pmatrix} T & 0 & T \\ -T_z & 0 & T_z \end{pmatrix} \left\langle J_f T \left|\left| \hat{Q}^{\lambda(0)} \right|\right| J_i T \right\rangle = \frac{1}{\sqrt{2T+1}} M^{(0)}, \tag{6.2.7}$$

$$(-1)^{T-T_z} \begin{pmatrix} T & 1 & T \\ -T_z & 0 & T_z \end{pmatrix} \left\langle J_f T \left|\left| \hat{Q}^{\lambda(1)} \right|\right| J_i T \right\rangle = \frac{T_z}{\sqrt{T(T+1)(2T+1)}} M^{(1)}, \tag{6.2.8}$$

leading to the proton matrix element

$$M_p(T_z) = \frac{1}{\sqrt{2T+1}} \left[M^{(0)} + \frac{T_z}{\sqrt{T(T+1)}} M^{(1)} \right] = a + bT_z, \tag{6.2.9}$$

which is the so-called linearity rule, where $M^{(0)}$ and $M^{(1)}$ represent the reduced matrix elements for the isoscalar and isovector components, respectively, which depend only on T and the angular momenta of each state. The reduced transition probabilities are then given by

$$B(E\lambda; J_i \to J_f) = \frac{\left| M_p(E\lambda; J_i \to J_f) \right|^2}{2J_i + 1}. \tag{6.2.10}$$

It is worth noting that for an operator with an isotensor component, terms such as

$$(-1)^{T-T_z} \begin{pmatrix} T & 2 & T \\ -T_z & 0 & T_z \end{pmatrix} \left\langle J_f T \left|\left| \hat{O}^{\lambda(2)} \right|\right| J_i T \right\rangle = \frac{3T_z^2 - T(T+1)}{\sqrt{T(T+1)(2T+1)(2T+3)(2T-1)}} M^{(2)}, \tag{6.2.11}$$

appear, which contribute with a quadratic term in T_z. The Coulomb interaction, for example, is predominantly a combination of isoscalar and isovector terms, but it also includes a small isotensor component that induces departures from a linear trend.

6.3 Is isospin broken at all?

To assess isospin purity via the linearity rule, we need three high-precision transition-rate measurements. This experimental data has been collected below $A = 50$, but becomes challenging as we

approach the proton drip line in heavier isospin triplets. A previous exploration on lighter triplets showed that although not perfect, the linear trend of eq. (6.2.9) works fairly well (Boso et al. 2019). The most recent measurements for isotriplets, however, tell a different story. For the $A = 70$ triplet (^{70}Kr, ^{70}Br, ^{70}Se) the $B(E2)$ transition rates of ^{70}Br and ^{70}Se were already known, with the value of the odd-odd being significantly reduced from the $T_z = +1$ nucleus. Wimmer et al. 2021 performed the first measurement of $B(E2)$ in ^{70}Kr, obtaining a value 60% larger than that of its mirror partner. This result led them to suggest that shape variation across the triplet would be necessary to interpret the results, which would be a clear breaking of isospin symmetry. Their analysis is shown in Figure 6.4, where the line showcases the trend set from ^{70}Br and ^{70}Se. The $A = 70$ triplet is the heaviest for which all $B(E2)$s are known, but the available experimental data for $A = 78$ follow a similar pattern. The $B(E2)$ of ^{78}Y (odd-odd, $T_z = 0$) is significantly reduced when compared to the one of ^{78}Sr ($T_z = +1$) (Llewellyn et al. 2020), and if the linearity trend would be set by these two values, the $B(E2)$ of the proton-rich ^{78}Zr would be highly asymmetrical with respect to its mirror.

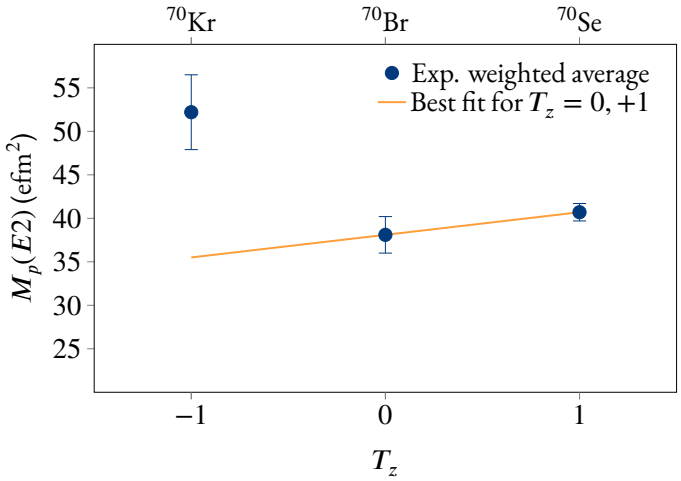


Figure 6.4: Data presented by Wimmer et al. 2021 and the linear trend set by ^{70}Br and ^{70}Se.

Isospin is explicitly broken in experimental data due to electromagnetic interactions, so a quantitative interpretation of results can be misleading. Therefore, a better question than the one posed in the title of this section is "*how* is isospin broken?" instead. The detailed experimental information in transition-rates can be used in conjunction with theoretical calculations to shed light on the mechanisms behind isospin symmetry-breaking beyond the Coulomb interaction. This requires a theoretical description of nuclei in the vicinity of the $N = Z$ line, including odd-odd nuclei, where large overlaps of neutron and proton wavefunctions enhance the $T = 0$ part of the neutron-proton (np) interaction, a driver of nuclear collectivity. Only from this point are we able to actually understand if the current theoretical description of electromagnetic effects close to the $N = Z$ line is sufficiently precise.

To address these issues, we shall first focus on which states actually represent an IAS in the odd-odd system, showcasing that the blocking technique (introduced in Chapter 2, also utilised in the results of Chapter 5) does not suffice. We then introduce two different theoretical approaches utilised to compute $B(E2)$. The first is Angular Momentum Projection (AMP), which allows us to extract the transition probabilities from a symmetry-restored wavefunction. The second, which we shall only briefly discuss, is the Generalised Bohr Hamiltonian, which accounts for collective excitations, relevant to the description of nuclei in this region of the nuclear chart. These two approaches are then applied to the description of even-even mirror nuclei with $42 \leq A \leq 98$, and AMP is used to describe $A = 70, 78$ odd-odd nuclei in multiple doubly-blocked configurations.

6.4 The odd-odd isobaric analog state

The standard approach for describing paired odd nuclei is with the blocking approximation, where a single quasiparticle is created on top of the even-even quasiparticle vacuum. Within quasiparticle pairing theory, this corresponds to the occupation probability of one single-particle state becoming equal to one and that of its canonical partner becoming equal to zero. This concept was also introduced in Chapter 2. The corresponding independent-quasiparticle wavefunction in a canonical-HFB representation (i.e., where the quasiparticle wave-functions are eigenstates of the density matrix, see chapter 3) corresponds to

$$|\Psi_{\alpha_0\tau_0}\rangle = a^\dagger_{\alpha_0\tau_0} \prod_{\alpha\tau\neq\alpha_0\tau_0}{}' (u_{\alpha\tau} + v_{\alpha\tau} a^\dagger_{\alpha\tau} a^\dagger_{\bar{\alpha}\tau})|0\rangle, \tag{6.4.1}$$

where α_0 represents the space-spin quantum numbers of a blocked state (e.g. its Nilsson labels) and τ_0 represents its isospin projection of n or p, $u_{\alpha\tau}$ and $v_{\alpha\tau}$ are the canonical occupation coefficients, $\bar{\alpha}$ represents a canonical partner state, and $|0\rangle$ is the single-particle vacuum. The prime symbol indicates that the product runs over half of the states, one for each canonical pair, usually denoted by $\alpha > 0$. Evidently, for $\tau_0 = n$ or p, state (6.4.1) represents the state of an odd-N or odd-Z nucleus, respectively.

Now let us think about describing an odd-odd nucleus. One may assume that it could be described by blocking simultaneously a proton quasiparticle in a state $\alpha_0 p$ and a neutron quasiparticle in a state $\bar{\alpha}_0 n$, such that its wave-function corresponds to

$$|\Psi_{\alpha_0 p,\bar{\alpha}_0 n}\rangle = a^\dagger_{\alpha_0 p} a^\dagger_{\bar{\alpha}_0 n} \prod_{\alpha\tau\neq\alpha_0 p,\alpha_0 n}{}' (u_{\alpha\tau} + v_{\alpha\tau} a^\dagger_{\alpha\tau} a^\dagger_{\bar{\alpha}\tau})|0\rangle, \tag{6.4.2}$$

where we may select the angular momentum of the blocked configurations to couple it to a desired final J_z. In the study of IAS, e.g., we could naively assume that this would be done by selecting a state $\alpha_0 p$ close to the Fermi surface, and the partner $\bar{\alpha}_0 n$ with opposite projection of angular-momentum

on the axial-symmetry axis, which would then select a final state with $J_z = 0$. Due to the high level density, experimental data for neighbouring nuclei can help to identify the best candidates for the Fermi surface. In Figure 6.5, we exemplify this approach for ^{78}Y. As all neighbouring nuclei have $J^\pi = 5/2^+$, we can select a proton and a neutron state of that angular momentum and anti-aligned projections, thus building an odd-odd state as in eq. (6.4.2).

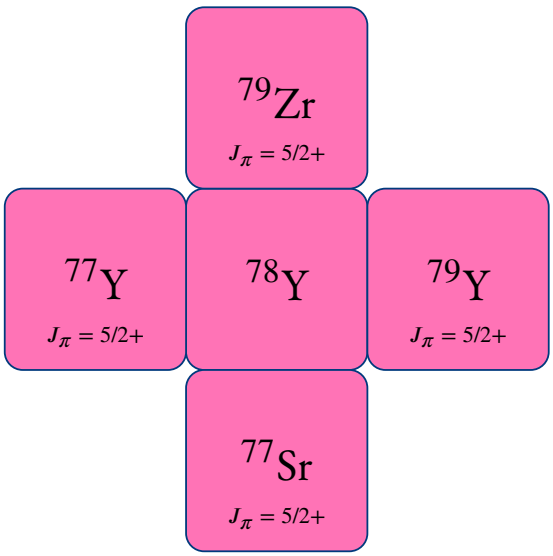


Figure 6.5: A helpful representation of how to identify the states closest to the Fermi surface in odd-odd nuclei. Here we display ^{78}Y, and its neighbouring odd nuclei with their respective experimental ground states.

However, would such state be suitable to the description of odd-odd IAS? We can verify this assumption by obtaining the IAS via isospin ladder operators, which are guaranteed to give us a wavefunction of the same multiplet and different T_z. Extending the definition of eq. (6.1.4) to the canonical basis, remembering that the primed sum covers only half of the single-particle spectra, we have

$$\hat{T}_+^\dagger = \hat{T}_- = {\sum_\alpha}' \left(a_{\alpha p}^\dagger a_{\alpha n} + a_{\bar{\alpha} p}^\dagger a_{\bar{\alpha} n} \right), \tag{6.4.3}$$

which gives the wavefunction of the IAS in odd-odd nuclei by acting on the ground state of even-even $T = 1$ states

$$|\Psi_{\mathrm{IAS}}(T = 1, T_z = 0)\rangle = \frac{1}{\sqrt{2}} \hat{T}_\pm |\Psi_{\mathrm{e-e}}(T = 1, T_z = \mp 1)\rangle. \tag{6.4.4}$$

Approximating $|\Psi_{\mathrm{e-e}}(T = 1, T_z = \mp 1)\rangle$ by the quasiparticle vacuum

$$|\Psi_{\mathrm{vac}}^\mp\rangle = {\prod_{\alpha\tau}}' (u_{\alpha\tau}^\mp + v_{\alpha\tau}^\mp a_{\alpha\tau}^\dagger a_{\bar{\alpha}\tau}^\dagger)|0\rangle, \tag{6.4.5}$$

we obtain

$$
\begin{aligned}
|\Psi_{\rm IAS}\rangle &= \frac{1}{\sqrt{2}}\hat{T}_-|\Psi^+_{\rm vac}\rangle \\
&= \frac{1}{\sqrt{2}}\sum_\alpha{}' \left(a^\dagger_{\alpha p}a_{\alpha n} + a^\dagger_{\bar{\alpha} p}a_{\bar{\alpha} n}\right)\prod_{\alpha\tau}{}'(u^+_{\alpha\tau} + v^+_{\alpha\tau}a^\dagger_{\alpha\tau}a^\dagger_{\bar{\alpha}\tau})|0\rangle. \qquad (6.4.6)
\end{aligned}
$$

We can explicitly separate the terms with αp and αn from the right-hand side of eq. (6.4.6), which gives

$$
|\Psi_{\rm IAS}\rangle = \frac{1}{\sqrt{2}}\sum_\alpha{}' \left(a^\dagger_{\alpha p}a_{\alpha n} + a^\dagger_{\bar{\alpha} p}a_{\bar{\alpha} n}\right)\left(u^+_{\alpha p} + v^+_{\alpha p}a^\dagger_{\alpha p}a^\dagger_{\bar{\alpha} p}\right)\left(u^+_{\alpha n} + v^+_{\alpha n}a^\dagger_{\alpha n}a^\dagger_{\bar{\alpha} n}\right)\prod_{\alpha\tau\neq\alpha p,\alpha n}{}'(u^+_{\alpha\tau} + v^+_{\alpha\tau}a^\dagger_{\alpha\tau}a^\dagger_{\bar{\alpha}\tau})|0\rangle. \qquad (6.4.7)
$$

The terms with α can be rewritten as

$$
\begin{aligned}
\left(a^\dagger_{\alpha p}a_{\alpha n} + a^\dagger_{\bar{\alpha} p}a_{\bar{\alpha} n}\right)\left(u^+_{\alpha p} + v^+_{\alpha p}a^\dagger_{\alpha p}a^\dagger_{\bar{\alpha} p}\right)\left(u^+_{\alpha n} + v^+_{\alpha n}a^\dagger_{\alpha n}a^\dagger_{\bar{\alpha} n}\right) &= \left(u^+_{\alpha p}a^\dagger_{\alpha p}a_{\alpha n} + u^+_{\alpha p}a^\dagger_{\bar{\alpha} p}a_{\bar{\alpha} n}\right)\left(u^+_{\alpha n} + v^+_{\alpha n}a^\dagger_{\alpha n}a^\dagger_{\bar{\alpha} n}\right) \\
&= u^+_{\alpha p}u^+_{\alpha n}\left(a^\dagger_{\alpha p}a_{\alpha n} + a^\dagger_{\bar{\alpha} p}a_{\bar{\alpha} n}\right) \\
&\quad + u^+_{\alpha p}v^+_{\alpha n}\left(a^\dagger_{\alpha p}a_{\alpha n}a^\dagger_{\alpha n}a^\dagger_{\bar{\alpha} n} + a^\dagger_{\bar{\alpha} p}a_{\bar{\alpha} n}a^\dagger_{\alpha n}a^\dagger_{\bar{\alpha} n}\right),
\end{aligned}
$$

where terms with more than one creation operator on the same state vanish, and we can neglect the terms with an extra annihilation operator, as they would vanish when acting on the state of eq. (6.4.7). Doing the same, but acting with $\hat{T}_+$ on the $T_z = -1$ state, we have the following IAS wavefunction

$$
\begin{aligned}
|\Psi_{\rm IAS}\rangle &= \frac{1}{\sqrt{2}}\hat{T}_+|\Psi^-_{\rm vac}\rangle \qquad (6.4.8) \\
&= \frac{1}{\sqrt{2}}\sum_\alpha{}' \left(a^\dagger_{\alpha n}a_{\alpha p} + a^\dagger_{\bar{\alpha} n}a_{\bar{\alpha} p}\right)\prod_{\alpha\tau}{}'(u^-_{\alpha\tau} + v^-_{\alpha\tau}a^\dagger_{\alpha\tau}a^\dagger_{\bar{\alpha}\tau})|0\rangle, \qquad (6.4.9)
\end{aligned}
$$

which also can be written, after separating and simplifying the terms with αp and αn

$$
\begin{aligned}
\left(a^\dagger_{\alpha n}a_{\alpha p} + a^\dagger_{\bar{\alpha} n}a_{\bar{\alpha} p}\right)\left(u^-_{\alpha p} + v^-_{\alpha p}a^\dagger_{\alpha p}a^\dagger_{\bar{\alpha} p}\right)\left(u^-_{\alpha n} + v^-_{\alpha n}a^\dagger_{\alpha n}a^\dagger_{\bar{\alpha} n}\right) &= v^-_{\alpha p}\left(a^\dagger_{\alpha n}a_{\alpha p}a^\dagger_{\alpha p}a^\dagger_{\bar{\alpha} p} + a^\dagger_{\bar{\alpha} n}a_{\bar{\alpha} p}a^\dagger_{\alpha p}a^\dagger_{\bar{\alpha} p}\right)\left(u^-_{\alpha n} + v^-_{\alpha n}a^\dagger_{\alpha n}a^\dagger_{\bar{\alpha} n}\right) \\
&= u^-_{\alpha n}v^-_{\alpha p}\left(a^\dagger_{\alpha n}a_{\alpha p}a^\dagger_{\alpha p}a^\dagger_{\bar{\alpha} p} + a^\dagger_{\bar{\alpha} n}a_{\bar{\alpha} p}a^\dagger_{\alpha p}a^\dagger_{\bar{\alpha} p}\right),
\end{aligned}
$$

and has a very similar form to the previous expression. Noting that we can write a time-even proton-neutron pair with $T = 1$ as

$$
\mathcal{S}^{T=1}_\alpha = \frac{1}{\sqrt{2}}\left(a^\dagger_{\alpha p}a^\dagger_{\bar{\alpha} n} + a^\dagger_{\alpha n}a^\dagger_{\bar{\alpha} p}\right), \qquad (6.4.10)
$$

we get the wavefunction of the IAS

$$
\begin{aligned}
|\Psi_{\mathrm{IAS}}\rangle &= \sum_{\alpha}{}' u^{+}_{\alpha p} v^{+}_{\alpha n} \mathcal{S}^{T=1}_{\alpha} \prod_{\alpha\tau\neq\alpha n,\alpha p}{}' (u^{+}_{\alpha\tau} + v^{+}_{\alpha\tau} a^{\dagger}_{\alpha\tau} a^{\dagger}_{\bar{\alpha}\tau})|0\rangle \\
&= \sum_{\alpha}{}' u^{-}_{\alpha n} v^{-}_{\alpha p} \mathcal{S}^{T=1}_{\alpha} \prod_{\alpha\tau\neq\alpha n,\alpha p}{}' (u^{-}_{\alpha\tau} + v^{-}_{\alpha\tau} a^{\dagger}_{\alpha\tau} a^{\dagger}_{\bar{\alpha}\tau})|0\rangle. \qquad (6.4.11)
\end{aligned}
$$

We note the equality of two forms of $|\Psi_{\mathrm{IAS}}\rangle$ given in eq. (6.4.11), which reflects the analogous equality in eq. (6.4.4), and is based on symmetry of the occupation factors $v^{-}_{\alpha p} = v^{+}_{\alpha n}$ and $v^{-}_{\alpha n} = v^{+}_{\alpha p}$ in the $T_z = \pm 1$ mirror nuclei. By inspecting eq. (6.4.11), we explicitly see that the IAS wavefunction *is not* a product state associated with a doubly blocked even-even vacuum as eq. (6.4.2). Instead, it corresponds to a coherent superposition of the blocked $T = 1$ proton-neutron pairs atop the even-even quasiparticle vacua. The contributions from individual components are weighted by factors $u^{+}_{\alpha p} v^{+}_{\alpha n} = u^{-}_{\alpha n} v^{-}_{\alpha p}$, i.e., they peak for states around the corresponding neutron and proton Fermi surface. It is now clear that by taking a symmetrised combination of the double-blocked states at the Fermi levels, as we previously exemplified, we obtain not a complete IAS (6.4.11), but only its dominating components. In the absence of pairing, the sum in (6.4.11) will be reduced to only one term associated with the valence neutron level α occupied in the $T_z = 1$ nucleus ($v^{+}_{\alpha n}$=1) with the proton level α being empty ($u^{+}_{\alpha p} = 1$) (the opposite holds for the $T_z = -1$ system).

Lastly, iso-cranking offers a similar interpretation of $T = 1$ IAS states in odd-odd $N = Z$ nuclei (Głowacz, Satuła and Wyss 2004; Satuła and Wyss 2001), based on a false vacuum situated midway between the vacua of even-even $T_z = \pm 1$ nuclei. Moreover, charge-exchange Quasiparticle Random-Phase Approximation (QRPA), which builds states via charge-exchange quasiparticle superpositions, is a very good representation of odd-odd $T = 1$ IAS. Notably, spherical QRPA calculations do not see changes in the energy between IAS apart from Coulomb (Fracasso and Colò 2005), and have been used to investigate isovector and isoscalar pairing correlations (Fracasso and Colò 2007).

6.5 Angular momentum projected DFT

As we now understand what is necessary to assess the linearity rule in isospin triplets, we shall focus on the theoretical techniques we utilised. To perform systematic nuclear DFT calculations of $B(E2; 2^{+} \rightarrow 0^{+})$ for all even-even $T = 1$ mirror nuclei with $42 \leq A \leq 98$, we utilised the code HFODD, version (3.28o) (Dobaczewski, Bączyk et al. 2021; Dobaczewski et al. 2026; Dobaczewski, Satuła et al. 2009b). We enforced axial symmetry, followed by the exact angular momentum projection (Sheikh, Dobaczewski et al. 2021). As a first step, we performed a series of HFB calculations constraining the quadrupole moment Q_{20} on a grid with a step size of 0.5b, illustrated in Figure 6.6. This allows us to identify all local minima on the grid, and then carry out unconstrained

calculations to find prolate, oblate, or spherical HFB solutions by starting the self-consistent loop from a point near each minima.

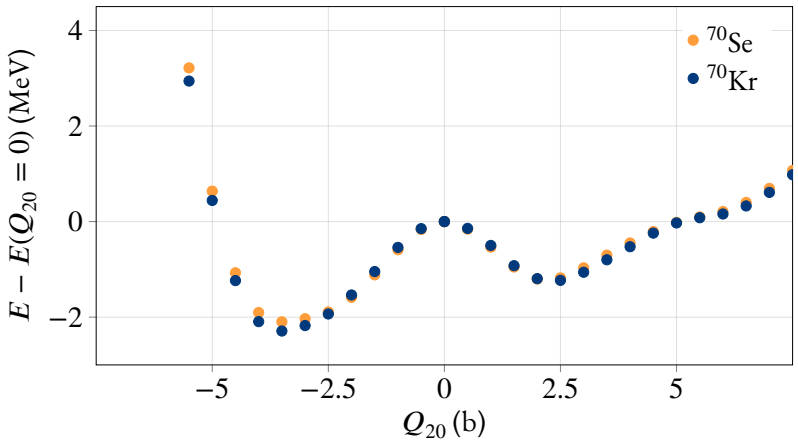


Figure 6.6: Potential energy curves, obtained with UNEDF1, with constrained quadrupole moments Q_{20} for the mirror pair of $A = 70$ (^{70}Kr,^{70}Se). The energies are normalised to the energy at the spherical shape.

The minima can be characterized using either the dimensionless Bohr deformation parameter β or the proton intrinsic quadrupole moments $Q_{20}(p)$, which are conventionally linked as follows,

$$\beta = 4\pi \frac{\langle r^2 Y_{20} \rangle_p}{3ZR^2} = \frac{\sqrt{5\pi}}{3ZR^2} Q_{20}(p), \tag{6.5.1}$$

where $R = 1.2A^{1/2}$ fm. We then used AMP to project each solution onto good angular momentum I, following the procedure introduced in Chapter 2. From the symmetry-restored wave-functions, we can determine the electromagnetic transition rates from the initial and final projected states via

$$B(E\lambda; I_i \to I_f) = \frac{1}{2I_i + 1} \left| \left\langle f, I_f \left| \left| \hat{Q}_\lambda \right| \right| i, I_i \right\rangle \right|^2. \tag{6.5.2}$$

This allows us to extract the $B(E2; 2^+ \to 0^+)$ and the respective $\mathcal{M}_p$ necessary for the analysis of the linearity rule.

Beyond the global analysis of even-even mirror nuclei, our goal is to assess the isotriplets with $A = 70$ and $A = 78$. To calculate odd-odd $N = Z$ nuclei, we first constrained the particle numbers without blocking to obtain an axial false quasiparticle vacuum. This yields an even state with an odd average particle number. Then, we break the time-reversal, signature, and simplex symmetries, using the z-component of the isoscalar angular frequency vector of $\hbar\omega_z = 0.001$ MeV to quantize the single-particle angular momenta along the axial symmetry axis. For these calculations, we increased the proton and neutron pairing strengths by 20% relative to the original UNEDF1 parametrization to account for the effects of not using the Lipkin-Nogami approximate particle number projection (Sheikh, Dobaczewski et al. 2021). The impact of pairing strengths is also discussed in Chapter 5.

As we previously showed, the IAS is a coherent superposition of blocked $T = 1$ proton-neutron pairs, with contributions from different states peaking around the Fermi surface. To identify the states at the Fermi surface, we examined the ground states of the closest isotopes (isotones) to the odd-odd nuclei, as highlighted in the previous section. We connected them to the Nilsson labels of the single-particle neutron (proton) states to be blocked. For neutrons (protons), we then selected z-aligned states with positive (negative) z-projections Ω_z of angular momentum, ensuring that the total angular momentum projections summed to zero.

We note that the doubly blocked states obtained in this way break the signature symmetry, allowing both even and odd angular momenta to be projected from the intrinsic states. However, since the signature operator simply exchanges the blocked neutron and proton quasiparticles, the even and odd angular momenta form the $T = 1$ and $T = 0$ rotational bands, respectively. Finally, the doubly blocked HFB solutions were converged and projected onto good $J = 0$ and $J = 2$ angular momenta. This allowed for the determination of the $B(E2 : 2^+ \rightarrow 0^+)$ values for individual two-quasiparticle (qp) states (6.4.2) of odd-odd $N = Z$ nuclei (Llewellyn et al. 2020), which shall be discussed later in contrast to the expected behaviour of the IAS.

6.6 The Generalised Bohr Hamiltonian

A pitfall of single-reference AMP calculations is that we can only compute the $B(E2)$s for one given PES minimum (i.e. deformation) at a time. This is troublesome in medium-mass $N \sim Z$ nuclei—like the ones we aim to describe here—as they are known to exhibit configurations of different shapes competing energetically at very low energies (Eberth, Meyer and Sistemich 1988; Nazarewicz et al. 1985). This leads to coexistence effects of prolate, oblate, and spherical shapes, which cannot be described purely with single-reference AMP calculations.

To describe quadrupole collective excitations and determine the values of $B(E2 : 2^+ \rightarrow 0^+)$, we utilized the Generalized Bohr Hamiltonian (GBH) (Klüpfel et al. 2008; Próchniak and Rohoziński 2009; Rowe and Wood 2010), which encompasses the rotational and vibrational motion associated with quadrupole deformations (β, γ). The GBH results presented here were performed by David Muir, a collaborator on this work. The summary below follows the description included on our publication (Backes, Dobaczewski et al. 2025), which also offers technical details of the calculations. The analysis of the data, which led to the results presented, was performed by me.

The general form of the GBH is given by:

$$\hat{H}_{coll} = \hat{T}_{vib} + \hat{T}_{rot} + \hat{V}\left(\beta, \gamma\right) \ , \tag{6.6.1}$$

where

$$\hat{T}_{\text{vib}} = -\frac{1}{2\sqrt{wr}}\left\{\frac{1}{\beta^4}\left[\partial_\beta\left(\beta^4\sqrt{\frac{r}{w}}B_{\gamma\gamma}\right)\partial_\beta - \partial_\beta\left(\beta^3\sqrt{\frac{r}{w}}B_{\beta\gamma}\right)\partial_\gamma\right]\right.$$
$$\left. + \frac{1}{\beta\sin(3\gamma)}\left[-\partial_\gamma\left(\sqrt{\frac{r}{w}}\sin(3\gamma)\,B_{\beta\gamma}\right)\partial_\beta + \frac{1}{\beta}\partial_\gamma\left(\sqrt{\frac{r}{w}}\sin(3\gamma)\,B_{\beta\beta}\right)\partial_\gamma\right]\right\}, \tag{6.6.2}$$

$$\hat{T}_{\text{rot}} = \frac{1}{2}\sum_{k=1}^{3}\frac{I_k^2(\Omega)}{4B_k(\beta,\gamma)\beta^2\sin^2(\gamma - 2\pi k/3)}, \tag{6.6.3}$$

where $\hat{V}(\beta,\gamma)$ is the potential energy of the nucleus, B_k $(k = 1,2,3)$ are 3 components of the rotational moment of inertia, $B_{\beta\beta}, B_{\beta\gamma}, B_{\beta\gamma}$ are components of the quadrupole vibrational inertia tensor, and I_k denotes the k-component of the angular momentum in the nuclear body-fixed frame. All inertia (mass parameters) are parametrised in terms of the Bohr deformations β and γ. In eq. (6.6.2), we used the shorthand notation: $w = B_{\beta\beta}B_{\gamma\gamma} - B_{\beta\gamma}^2$ and $r = B_xB_yB_z$. The 6 mass parameters used in the GBH have been systematically obtained via the cranking approximation (Baran et al. 2011; Girod and Grammaticos 1979) from constrained HFB calculations for each nucleus under consideration following the procedure of Muir et al. 2020; Prochniak 2015. It is worth noting that the rotational and vibrational inertia strongly depend on pairing (Brack et al. 1972; Próchniak and Rohoziński 2009). The reader can find a didactic explanation of the model in the thesis of Muir 2021.

6.7 Global analysis of $T = 1$ mirror nuclei

We shall now review the results obtained following the approaches of sections 6.6 and 6.5. Figure 6.7 shows the HFB potential energy curves for even-even mirror nuclei with $42 \le A \le 98$ obtained using the UNEDF1 EDF (Kortelainen, McDonnell et al. 2012), projected onto angular momentum $I = 0$. The calculations predict shape-coexisting minima for many mid-shell nuclei, while the systems closest to shell closures exhibit only a spherical minimum. The largest oblate ($\beta < 0$) deformations are expected for the $A = 66$ and $A = 70$ systems, while the largest prolate ($\beta > 0$) deformations are calculated for the $A = 74$ and $A = 78$ nuclei.

The potential energy curves of $T_z = \pm 1$ mirror nuclei are generally very similar when normalised to the spherical energy. However, it is worth noting that slight shape deviations are still observed in mirror pairs. These small shifts arise due to the Coulomb interaction, which explicitly breaks isospin symmetry, and they are particularly evident at large deformations. As a result, the energy of the $T_z = -1$ (proton-rich) system falls slightly below that of the $T_z = 1$ partner, which has a smaller atomic number and Coulomb energy. This difference in total energy leads to slightly larger values of $|\beta|$ in the $T_z = -1$ nuclei. This is particularly noticeable in minima with higher deformations, e.g. mirror pairs with $A = 70$ and 78. Despite these shifts in β, shape changes between mirror

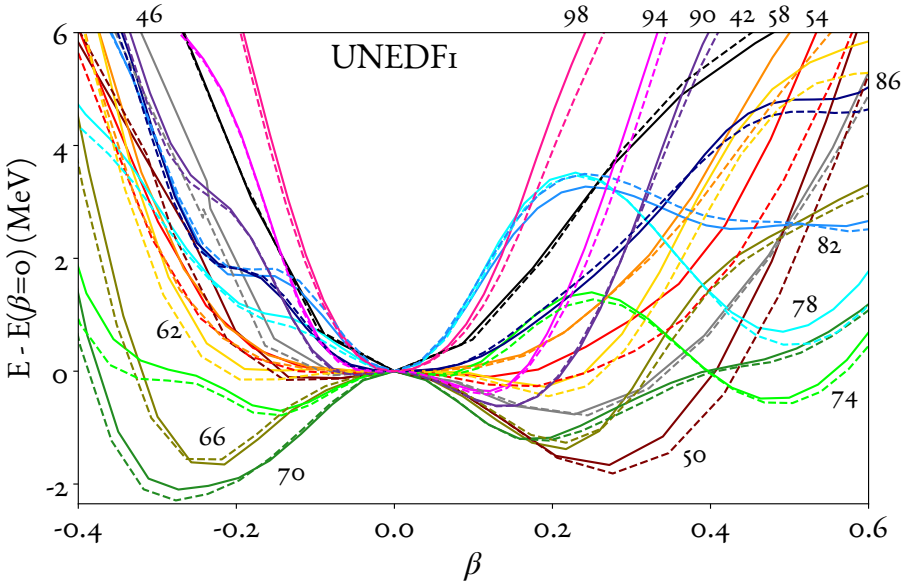


Figure 6.7: Hartree-Fock-Bogoliubov (HFB) potential energy curves, obtained with UNEDF1, projected on $I = 0$ as functions of quadrupole deformation β (6.5.1) for the even-even $T = 1$ mirror nuclei considered in this study. Solid lines denote $T_z = 1$, and dashed lines $T_z = -1$. The mass numbers are marked explicitly, close to curves of different colours. The energies are normalized to the energy at the spherical shape.

pairs are unlikely, given the overall similarity between the potential energy curves. Notably, in the $A = 70$ mirror pair, the oblate and prolate minima are separated by ≈ 1 MeV. This contradicts the suggestion of Wimmer et al. 2021 that ^{70}Kr would be prolate and ^{70}Se oblate. An important aspect of this discussion is that deformations are not explicitly measured, but rather they are inferred from experimental $B(E2)$ data, linked via eq. (6.5.2). As the quadrupole moment carries information about the shape of the nucleus, a larger $B(E2)$ indicates enhanced collective effects and deformation. The specific shape, however—determined by the *sign* of the quadrupole moment—cannot be determined from the transition probabilities.

In this scenario, the GBH and AMP frameworks allow us to understand the connection between shapes and $B(E2)$ data in different ways. The first—and most complete—framework is capable of describing shape coexistence, and obtains meaningful $B(E2)$s even for spherical nuclei. Meanwhile, the AMP framework allows us to examine data for individual configurations and investigate whether a specific deformation can describe the experimental data. Our results for both frameworks are presented in Figure 6.8, with prolate and oblate configurations shown separately for the AMP calculations. Spherical and nearly spherical solutions around shell closures are omitted, as the projection of a spherical state is not meaningful. As expected in a region with enhanced collectivity, the GBH calculations yield better results and demonstrate an overall satisfactory

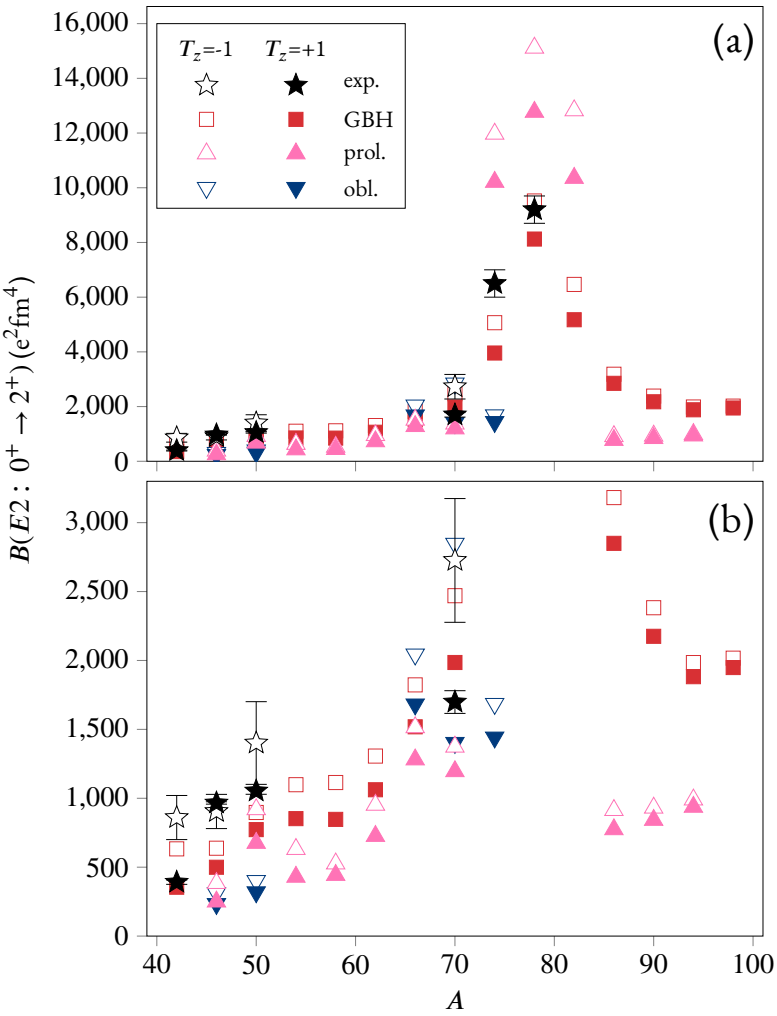


Figure 6.8: $B(E2)$ values of even-even $T = 1$ mirror nuclei with $42 \leq A \leq 98$ and the available experimental data (Boso et al. 2019; Giles et al. 2019, 2021; Hadyńska-Klęk et al. 2016; Llewellyn et al. 2020; Morse et al. 2018; Pritychenko et al. 2016; Wimmer et al. 2021), in (a) full scale and (b) reduced scale. $T_z = 1$ ($T_z = -1$) nuclei are represented with open (filled) symbols. Stars show experimental values, squares mark the GBH UNEDF1 predictions, and the prolate (oblate) AMP UNEDF1 predictions are shown with up-pointing (down-pointing) triangles.

agreement with experimental data across the entire range of interest. The AMP results fall short in comparison, indicating the importance of shape mixing to these results. This is also seen in the mass region of $74 \leq A \leq 82$, where AMP overestimates the experimental B(E2)s. The HFB calculations predict a nearly spherical and a deformed minimum for these nuclei, and considering only the prolate-deformed one yields $B(E2)$ values well in excess of experimental data. This indicates that shape mixing with the spherical-deformed minima plays an important role, and accounting for the distribution of shapes with the GBH provides a better description. The two frameworks agree when clear prolate and oblate minima can be identified in the AMP potential energy curves, such as for A =50, 66, and 70. In all cases, the difference

$$\Delta B(E2) \equiv B(E2, T_Z = -1) - B(E2, T_Z = +1) \tag{6.7.1}$$

is positive. This is to be expected, as the $T_z = -1$ nuclei have larger electric charges, while their equilibrium deformation is very similar and slightly larger also in the proton-rich nuclei. The $\Delta B(E2)$ also frequently varies between the two approaches. This can, once again, be attributed to shape coexistence in systems around $A = 78$. Meanwhile, for the lighter mirror nuclei, such as $A = 62$, this is attributed to closely lying weakly deformed prolate and oblate minima.

6.8 The $A = 70$ and $A = 78$ isobaric triplets

We will specifically focus on the $A = 70$ and $A = 78$ triplets, where deviations from the linearity rule are anticipated. For the analysis of $M_p(T_z)$ of eq. (6.2.9), it is imperative to address the physics of the odd-odd $N = Z$ ($T_z = 0$) nuclei*. From our analysis of the $B(E2)$s near the $N = Z$ line, it is clear that the collective degrees of freedom are crucial in accurately describing the quadrupole strength. Henceforth, the GBH is the preferred formalism for describing nuclei in this region, but the extension of the GBH model to odd-odd nuclei, including decoupled proton-neutron pairs, still needs to be developed. Doubly-blocked calculations, on the other hand, provide a simpler method for the description of odd-odd nuclei, and open the opportunity to gain insights into the $B(E2)$ strengths of the $T_z = 0$ isotriplet partners. Moreover, AMP is well-suited for the description of deformed nuclei such as ^{70}Br and ^{78}Y, and allows for a quantitative assessment of how the puzzling experimental results could be interpreted from a nuclear theory perspective.

As we have established in Section 6.4, the IAS in odd-odd $N = Z$ nuclei is represented by a superposition of blocked $T = 1$ proton-neutron pair excitations. We attempted to perform such calculations; however, the resulting energy mixing matrix elements were strongly perturbed by the self-interaction terms and singularities of the UNEDF1 functional (Sheikh, Dobaczewski et al. 2021). For our analysis of the odd-odd nuclei in isotriplets, we chose to compute the $B(E2)$ matrix

*Famously, the trend set from only two data points will always be a line.

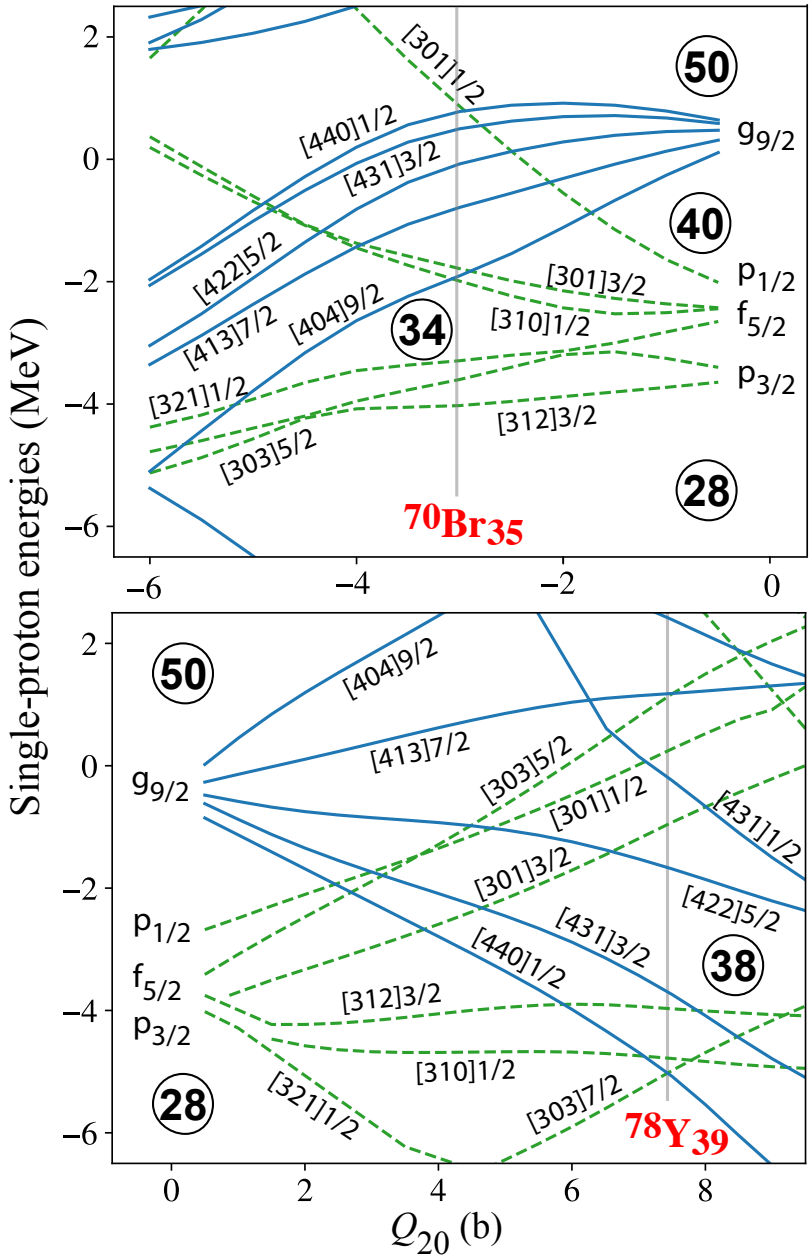


Figure 6.9: The Nilsson proton diagrams for ^{70}Br (top) and ^{78}Y (bottom) obtained using the UNEDF1 EDF and plotted as a function of the total intrinsic quadrupole moment Q_{20}. (The neutron diagrams are quite similar; therefore, they are not shown.) Although the wavefunctions are strongly mixed in many cases, the asymptotic quantum numbers $[Nn_z\Lambda]\Omega$ provided match those of Nazarewicz et al. 1985 to simplify the identification of individual levels. The vertical lines mark the false-vacuum equilibrium quadrupole moments of $A = 70$ ($Q_{20}^{\min} \approx -3.2$ b) and $A = 78$ ($Q_{20}^{\min} \approx 7.5$ b) isotriplets. Figure is the same as the one included in Backes, Dobaczewski et al. 2025.

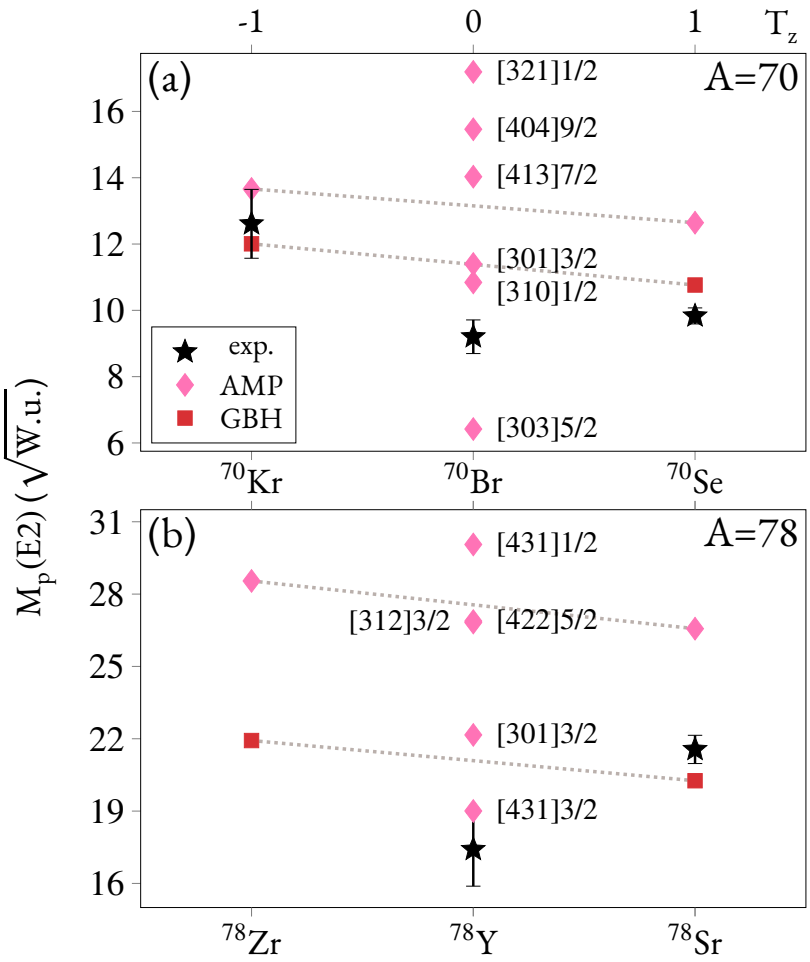


Figure 6.10: $M_p(E2)$ values computed with HFB+AMP and UNEDF1 for (a) $A = 70$ and (b) $A = 78$ triplets, and the available experimental data (Wimmer et al. 2021). We selected the oblate solutions for the $A = 70$ triplet and the prolate ones for the $A = 78$ triplet. The different points shown for the odd-odd $T_Z = 0$ nuclei correspond to different 2-qp states near the Fermi level. Even-even results from GBH calculations are shown as squares.

elements for several 2-qp states near the Fermi level in the oblate configuration of ^{70}Br and the prolate configuration of ^{78}Y, knowing that none of them would represent the IAS exactly. The known or extrapolated ground-state spins and parities of the odd neighbours of ^{70}Br and ^{78}Y are $5/2^-$ and $5/2^+$, respectively, and this guides the identification of which states should be used for 2-qp (two-quasiparticle) blocking. Figure 6.9 shows the corresponding Nilsson diagrams, which support the extrapolated ground-states, as the Nilsson levels [303]5/2 and [422]5/2 are located near the Fermi levels of N or $Z = 35$ and N or $Z = 39$, respectively. The figure also indicates that the main contributions to the IAS wavefunction (6.4.11) are expected to arise from [310]1/2, [301]3/2, and [404]9/2 states in ^{70}Br, and from [422]5/2, [301]3/2, and [431]1/2 states in ^{78}Y.

Finally, Figure 6.10 shows the values of M_p for the $A = 70$ and $A = 78$ isotriplets, considering the same shape for the even-even mirrors (oblate for $A = 70$ and prolate for $A = 78$). Once again, the difference between the GBH and AMP results in even-even mirror nuclei stems from shape mixing, as the same functional was employed in both calculations. The discussion on shapes, including the competing low-lying spherical and prolate configurations in $A = 78$ is discussed in the previous section. The M_p are shown in square root of Weisskopf units (W.u.), which correspond to the estimate of the number of nucleons contributing to radiation, given by

$$B(E\lambda; I_i \to I_f) = \frac{1.2^{2\lambda}}{4\pi}\left(\frac{3}{\lambda+3}\right)^2 A^{2\lambda/3} e^2 \mathrm{fm}^{2\lambda}. \tag{6.8.1}$$

There is a significant spread in the M_p values for 2-qp states of $T_z = 0$ isotriplet members. This is due to the different intrinsic quadrupole moments of associated Nilsson levels, which give rise to different quadrupole polarisations. Notably, blocking influences the occupation numbers. As a result, we may drive the deformation towards prolate or oblate configurations depending on the slope of the blocked orbitals and on whether we are blocking a particle or a hole. We also highlight in Figure 6.10 the linear trend set by the two even-even $T = 1, T_z = \pm 1$ nuclei. The extrapolated ground-state orbitals of [303]5/2 and [422]5/2 do not correspond to the linearity rule; and in fact, as none of the 2-qp states uniquely correspond to the IAS, deviations from the linearity rule (6.2.9) are expected. The different quadrupole polarisations cause the spread of predictions for the odd-odd $N = Z$ nucleus relative to the linear trend, and states contributing to the IAS show M_p both under and over the extrapolated line.

As eq. (6.4.11) suggests, a multi-reference mixing of several doubly blocked states should be performed to test whether the IAS hypothesis better aligns with the data. While our attempt failed, the search for well-adjusted, spectroscopic-quality, and self-interaction-free functionals is actively pursued (Bennaceur, Dobaczewski and Raimondi 2014; Raimondi, Bennaceur and Dobaczewski 2014; Sadoudi et al. 2013). However, the existing infrastructure is insufficient to address the $B(E2)$ rates in the IAS of odd-odd nuclei, and the detailed assessment of potential deviations from (6.2.9) must wait.

6.9 Conclusions

Our theoretical work shows that nuclear DFT, with the UNEDF1 Skyrme parametrisation, describes the reduced transition probabilities of $T = 1$ even-even mirrors. This can be achieved without resorting to beyond-Coulomb charge-dependent functionals. However, close to the $N = Z$ line, only collective models such as the Generalised Bohr Hamiltonian are capable of describing data due to the enhanced quadrupole collectivity and shape coexistence. Angular momentum projection—with the UNEDF1 Skyrme parametrisation—is sufficient only when the potential

energy curves have well-defined deformed minima, but it fails to address shape coexistence and small deformations close to shell closures. Overall, the AMP potential energy surfaces are similar between mirror nuclei, but small differences in deformation are still observed.

In the context of isospin-symmetry studies, the DFT results come with a caveat. No explicit beyond-Coulomb symmetry breaking may exist in the interaction, but this does not indicate that all isospin symmetry-breaking effects arise from Coulomb. Collective effects depend on the effective pairing strengths, which differ between protons and neutrons due to the asymmetry between corresponding shell structures across the nuclear chart. As a result, differences will always exist between mirror nuclei in DFT, aside from a different Coulomb repulsion.

Beyond the differences in pairing strengths and the spurious symmetry-breaking related to many-body methods, it is important to note that the nuclear Hamiltonian itself is *not* isospin-symmetric. Differences in the masses of protons and neutrons—as well as of the constituent u and d quarks—exemplify this symmetry-breaking. There is an ongoing effort in the community to introduce charge symmetry-breaking terms to energy density functionals (Naito et al. 2024). So far, no complete analysis of the linearity rule within triplets with a charge symmetry-breaking functional has been performed. Hence, further calculations are necessary to quantify the influence of isospin symmetry-breaking coming from the nuclear Hamiltonian.

We have derived and discussed which state of the odd-odd nucleus is most suitable for isospin physics studies of isobaric triplets, corresponding to a rotation of an even-even $T = 1$ state in isospin space. The true IAS consists of a superposition of doubly blocked $T = 1$ proton-neutron pairs atop the even-even quasiparticle vacuum. Our numerical results indicate that double quasiparticle blocking close to the Fermi surface, without mixing, does not lead to the "linearity rule," and the corresponding $B(E2)$ values vary significantly depending on the deformations and slopes of the Nilsson orbitals. Furthermore, the same previous remark is valid: even for a mixed solution, small deviations from the linear trend are expected, as the protons and neutrons have different pairing strengths.

Regarding the linearity rule, we want to emphasise what follows.

- While shell model calculations, commonly used to interpret $B(E2)$ data in isobaric triplets, produce results within the exact isospin symmetry regime, they lack a non-perturbative description of the Coulomb and shape polarisations, which are integral parts of the nuclear DFT;

- No shape change is expected between $T = 1$ even-even mirrors with $42 \leq A \leq 98$, but shape and configuration mixing is a crucial aspect that future DFT implementations need to address;

- Analysing isospin symmetry-breaking from the linear trend set by the $T_z = 0, +1$ members of the triplet can be misleading;
- Currently, no DFT studies accurately describe the $N = Z, T = 1$ IAS. The existing infrastructure is not sufficient to capture the complex physics of odd-odd nuclei. Specifically, there is a need for multi-reference calculations using self-interaction-free functionals.

Another challenge to nuclear theory, which was not addressed in this work, is that the overlap between the proton and neutron wavefunctions in $N \sim Z$ leads to *pn*-pairing correlations, which are also relevant to the study of IAS. Indeed, the competition between isovector $T = 1$ and isoscalar $T = 0$ *np*-pairing modes remains a key question in nuclear structure physics. Some references on the topic are works of Engel et al. 1997; Frauendorf and Macchiavelli 2014; Martínez-Pinedo, Langanke and Vogel 1999; Romero, Dobaczewski and Pastore 2019; Satuła and Wyss 1997 and references therein. Within the (quasi)local density approximation to nuclear DFT with pairing, principles of the approach have been laid down by Perlińska et al. 2004 but have never been implemented or tested so far. The main challenge is that such pairing implies the proton-neutron mixing (Sato et al. 2013; Sheikh, Hinohara et al. 2014) in the particle-hole channel. Indeed, for any quasiparticle vacuum, the density matrix ρ and the pairing tensor κ are linked to one another by the expression $\rho - \rho^2 = \kappa\kappa^+$ (Ring and Schuck 1980). Therefore, the presence of the three types of pairing, κ_{nn}, κ_{pp}, and κ_{np}, implies, in general, a non-zero proton-neutron mixing ρ_{np} in the density matrix. For nuclear matter, this aspect was fully covered in the work presented in Chapter 4.

Lastly, all AMP results are available online (Backes 2025). Further details on the GBH results, and zero-point energy corrections for $A = 70$ and $A = 78$ mirror nuclei are available in the published manuscript (Backes, Dobaczewski et al. 2025).

Part III

Other research questions

Seven

Relativistic two-body currents

In this chapter, we briefly introduce the motivation behind studying two-body magnetic dipole moments. We introduce the two-body magnetic dipole operator, coming from meson-exchange corrections, and underline the work necessary to describe it within nuclear density functional theory (DFT).

The notion that nuclear DFT struggles to describe magnetic dipole moments of heavy nuclei was introduced in Chapter 5. However, this challenge is not unique to DFT. Historically, an accurate description of magnetic dipole moments of medium and heavy nuclei relies on effective charges or g-factors. Recent *ab initio* studies suggest that one-body contributions to the magnetic dipole moment may not suffice to accurately describe the system. Specifically, electromagnetic interactions are probed through photon-nucleus interactions. One-body terms contain a sum of photon interactions with individual nucleons and do not account for the interaction between nucleons mediated by pions. Seutin et al. 2023 suggested that higher-order contributions are necessary for an accurate description of electromagnetic properties, and Miyagi et al. 2024 investigated the effect of two-body currents, coming from next-to-leading-order two-body terms of Chiral Effective Field Theory (χEFT), on magnetic dipole moments. This work aims to test the aforementioned conjecture within the framework of nuclear DFT.

The brief introduction that follows is based on Section 5 of Dobaczewski, Backes et al. 2026. The publication on the methods and results is in preparation (Wibowo, Han et al. 2026). Up to two-body contributions, we can write the magnetic dipole moment as

$$\hat{\mu} = \sum_{k}^{A} \hat{\mu}_{1\mathrm{b},k} + \sum_{k<\ell}^{A} \hat{\mu}_{2\mathrm{b},k\ell}, \tag{7.0.1}$$

where the one-body part of the magnetic dipole operator is given by

$$\hat{\mu}_{1\mathrm{b}} = \sqrt{\tfrac{4\pi}{3}}\hat{M}_{10} = \mu_{\mathrm{N}} \sum_{\tau=n,p} \left[g_s^{(\tau)} \hat{S}_z^{(\tau)} + g_l^{(\tau)} \hat{L}_z^{(\tau)} \right], \tag{7.0.2}$$

where $\hat{S}_z^{(\tau)} = \frac{1}{2}\hat{\sigma}_z$ and $\hat{L}_z^{(\tau)} = -i\mathbf{r}_x \times \nabla_y$ (with units of $\hbar$ omitted), the gyromagnetic factors (i.e.

g-factors) and nuclear magneton μ_N are equal to

$$g_l^{(p)} = 1, \quad g_l^{(n)} = 0, \quad g_s^{(p)} = 2(1+\kappa_p) = 5.587, \quad g_s^{(n)} = 2\kappa_n = -3.826, \quad \mu_N = \frac{e\hbar}{2m_p c}, \tag{7.0.3}$$

and the two-body term comes from meson-exchange corrections due to the interactions between nucleons

$$\hat{\mu}_{2b}(\mathbf{r}_1, \mathbf{r}_2) = \frac{1}{2}\int d\mathbf{x}^3 \mathbf{x} \times \hat{j}_{2b}(\mathbf{x}, \mathbf{r}_1, \mathbf{r}_2). \tag{7.0.4}$$

The two-body current, $\hat{j}_{2b}$, arises from two distinct Feynman diagrams, commonly referred to as the seagull and pion-in-flight diagrams (Castel and Towner 1990). They are responsible for accounting for next-to-leading order (NLO) pion-exchange contributions from χEFT (Miyagi et al. 2024; Seutin et al. 2023). We note that for full two-body contributions, formally, heavier meson exchanges are also possible, and the chiral expansion also includes contact terms. Our work is restricted to the two aforementioned diagrams accounting for NLO pion-exchange contributions in the chiral expansion.

The two-body operator (7.0.1) has two terms, called the intrinsic

$$\hat{\mu}_{2b}^{\text{int}}(\mathbf{r}_1, \mathbf{r}_2) = -\frac{g_A^2 m_\pi}{32\pi F_\pi^2}(\hat{\tau}_1 \times \hat{\tau}_2)_z \left\{\left(1+\frac{1}{u}\right)\left[(\hat{\sigma}_1 \times \hat{\sigma}_2)\cdot \hat{\mathbf{r}}\right]\hat{\mathbf{r}} - (\hat{\sigma}_1 \times \hat{\sigma}_2)\right\} e^{-u}, \tag{7.0.5}$$

and the Sachs term

$$\hat{\mu}_{2b}^{\text{Sachs}}(\mathbf{r}_1, \mathbf{r}_2) = -\frac{m_\pi^3 g_A^2}{96\pi F_\pi^2}(\hat{\tau}_1 \times \hat{\tau}_2)_z (\mathbf{R} \times \mathbf{r})\left[\hat{S}_{12}\left(1+\frac{3}{u}+\frac{3}{u^2}\right) + \hat{\sigma}_1 \cdot \hat{\sigma}_2\right]\frac{e^{-u}}{u}, \tag{7.0.6}$$

where $\mathbf{r}$ is the relative coordinate and $\mathbf{R}$ is the centre-of-mass coordinate between the two interacting nucleons. $\hat{\sigma}$ and $\hat{\tau}$ are the spin and isospin Pauli matrices, and the tensor operator $\hat{S}_{12}$ is defined as $\hat{S}_{12} = 3(\hat{\mathbf{r}}\cdot\hat{\sigma}_1)(\hat{\mathbf{r}}\cdot\hat{\sigma}_2) - \hat{\sigma}_1\cdot\hat{\sigma}_2$. The remaining constants and the values we utilised are the axial coupling constant $g_A = 1.27$, the pion decay constant $F_\pi = 92.3$ MeV, $m_\pi = 0.7045$ fm^{-1} is the average pion mass, and we use the scaled distance $u = m_\pi r$. To analyse the contribution of (7.0.1) to the magnetic dipole moments, we must compute the expectation value

$$\langle \hat{\mu}_{2b}(\mathbf{r}_1, \mathbf{r}_2)\rangle = \frac{1}{2}\sum_{ij}\langle ij|\hat{\mu}_{2b}(\mathbf{r}_1, \mathbf{r}_2)|ij\rangle - \frac{1}{2}\sum_{ij}\langle ij|\hat{\mu}_{2b}(\mathbf{r}_1, \mathbf{r}_2)\hat{P}^M\hat{P}^\sigma\hat{P}^\tau|ij\rangle, \tag{7.0.7}$$

where the first term is the direct contribution, and the second is the exchange, which includes the spatial-, spin-, and isospin-exchange operators. To compute these values numerically, it is useful to analyse eqs. (7.0.5) and (7.0.6). Both include the same isospin term

$$\begin{aligned}\left(\hat{\tau}_{(1)} \times \hat{\tau}_{(2)}\right)_3 &= \varepsilon_{3jk}\hat{\tau}_j^{(1)}\hat{\tau}_k^{(2)} \\ &= \left(\hat{\tau}_1^{(1)}\hat{\tau}_2^{(2)} - \hat{\tau}_2^{(1)}\hat{\tau}_1^{(2)}\right),\end{aligned}$$

where we denote the different directions in the conventional way of $x \equiv 1$, $y \equiv 2$, and $z \equiv 3$, and we denote the operators from the first and second nucleon between parentheses, for clarity. These operators mix the proton and neutron wave-functions in the direct channel, such that for mean-field DFT calculations there will be no contribution from (7.0.7) in the direct channel. To compute the contribution of the exchange channel, we first write the isospin exchange operator

$$\hat{P}^{\tau} = \frac{1}{2}\left[\hat{\tau}_0^{(1)}\hat{\tau}_0^{(2)} + \hat{\tau}_n^{(1)}\hat{\tau}_n^{(2)}\right] \tag{7.0.8}$$

and compute the isospin exchange term

$$\begin{aligned}
\hat{\mu}^{\text{exc}}_{2\text{b},\tau} &= \varepsilon_{3kl}\hat{\tau}_k^{(1)}\hat{\tau}_l^{(2)}\hat{P}^{\tau} \\
&= \frac{1}{2}\varepsilon_{3kl}\hat{\tau}_k^{(1)}\hat{\tau}_l^{(2)} + \frac{1}{2}\varepsilon_{3kl}(\hat{\tau}_k^{(1)}\hat{\tau}_n^{(1)})(\hat{\tau}_l^{(2)}\hat{\tau}_n^{(2)}) \\
&\qquad \leftarrow \hat{\tau}_i\hat{\tau}_k = i\varepsilon_{ikm}\hat{\tau}_m + \delta_{ik}\hat{\tau}_0 \\
&= \frac{1}{2}\varepsilon_{3kl}\hat{\tau}_k^{(1)}\hat{\tau}_l^{(2)} + \frac{1}{2}\varepsilon_{3kl}\left[(i\varepsilon_{knp}\hat{\tau}_p^{(1)} + \delta_{kn}\hat{\tau}_0^{(1)})(i\varepsilon_{lnq}\hat{\tau}_q^{(2)} + \delta_{ln}\hat{\tau}_0^{(2)})\right] \\
&\qquad \leftarrow \varepsilon_{knp}\varepsilon_{lnq} = \delta_{kl}\delta_{pq} - \delta_{kq}\delta_{pl} \\
&= \frac{1}{2}\varepsilon_{3kl}\hat{\tau}_k^{(1)}\hat{\tau}_l^{(2)} + \frac{1}{2}\varepsilon_{3kl}\left[-\delta_{kl}\hat{\tau}_p^{(1)}\hat{\tau}_p^{(2)} + \hat{\tau}_l^{(1)}\hat{\tau}_k^{(2)} + i\varepsilon_{klp}\hat{\tau}_p^{(1)}\hat{\tau}_0^{(2)} + \varepsilon_{lkq}\hat{\tau}_0^{(1)}\hat{\tau}_q^{(2)}\right] \\
&= \frac{1}{2}\varepsilon_{3kl}\left[\hat{\tau}_k^{(1)}\hat{\tau}_l^{(2)} + \hat{\tau}_l^{(1)}\hat{\tau}_k^{(2)} + i\hat{\tau}_0^{(1)}\varepsilon_{lkq}\hat{\tau}_q^{(2)} + i\varepsilon_{klp}\hat{\tau}_p^{(1)}\hat{\tau}_0^{(2)}\right] \\
&= \frac{1}{2}\left[i\varepsilon_{3kl}\varepsilon_{lkq}\hat{\tau}_0^{(1)}\hat{\tau}_q^{(2)} + i\varepsilon_{3kl}\varepsilon_{klp}\hat{\tau}_p^{(1)}\hat{\tau}_0^{(2)}\right] \\
&= \frac{1}{2}\left[i(\delta_{3l}\delta_{lq} - \delta_{3q}\delta_{ll})\hat{\tau}_0^{(1)}\hat{\tau}_q^{(2)} + i(\delta_{3p}\delta_{ll} - \delta_{3l}\delta_{lp})\hat{\tau}_p^{(1)}\hat{\tau}_0^{(2)}\right] \\
&= \frac{i}{2}\left[\hat{\tau}_0^{(1)}\hat{\tau}_3^{(2)} - 3\hat{\tau}_0^{(1)}\hat{\tau}_3^{(2)} + 3\hat{\tau}_3^{(1)}\hat{\tau}_0^{(2)} - \hat{\tau}_3^{(1)}\hat{\tau}_0^{(2)}\right] \\
&= \frac{i}{2}\left[2\hat{\tau}_3^{(1)}\hat{\tau}_0^{(2)} - 2\hat{\tau}_0^{(1)}\hat{\tau}_3^{(2)}\right] \\
&= i\left[\hat{\tau}_3^{(1)}\hat{\tau}_0^{(2)} - \hat{\tau}_0^{(1)}\hat{\tau}_3^{(2)}\right].
\end{aligned}$$

For the spin part, (7.0.6) has scalar, vector, and tensor contributions. The scalar terms are

$$\begin{aligned}
\hat{\mu}^{\text{exc}}_{2\text{b},\sigma,\text{scalar}} &= \hat{\sigma}_\nu^{(1)}\hat{\sigma}_\nu^{(2)}\hat{P}^{\sigma} \\
&= (2\hat{P}^{\sigma} - \hat{\sigma}_0^{(1)}\hat{\sigma}_0^{(2)})\hat{P}^{\sigma} \\
&= \hat{\sigma}_\nu^{(1)}\hat{\sigma}_\nu^{(2)} \cdot \frac{1}{2}\left(\hat{\sigma}_0^{(1)}\hat{\sigma}_0^{(2)} + \hat{\sigma}_\mu^{(1)}\hat{\sigma}_\mu^{(2)}\right) \\
&= 2\hat{\sigma}_0^{(1)}\hat{\sigma}_0^{(2)} - \frac{1}{2}\left(\hat{\sigma}_0^{(1)}\hat{\sigma}_0^{(2)} + \hat{\sigma}_\mu^{(1)}\hat{\sigma}_\mu^{(2)}\right) \\
&= \frac{1}{2}\left[3\hat{\sigma}_0^{(1)}\hat{\sigma}_0^{(2)} - \hat{\sigma}_\mu^{(1)}\hat{\sigma}_\mu^{(2)}\right],
\end{aligned}$$

and the vector spin terms are analogous to those derived for isospin, i.e.,

$$\begin{aligned}
\hat{\mu}^{\text{exc}}_{2\text{b},\sigma,\text{vector}} &= (\hat{\sigma}^{(1)} \times \hat{\sigma}^{(2)})_\lambda \hat{P}^{\sigma} \\
&= i\left[\hat{\sigma}_\lambda^{(1)}\hat{\sigma}_0^{(2)} - \hat{\sigma}_0^{(1)}\hat{\sigma}_\lambda^{(2)}\right].
\end{aligned}$$

For the tensor operator, we can use the property

$$\hat{S}_{12}\hat{P}^{\sigma} = \hat{S}_{12} \tag{7.0.9}$$

directly when writing the tensor exchange terms. For the pairing channel, the derivation is more intricate. It requires utilising the coupling scheme from Perlińska et al. 2004, such that lastly, one obtains that the contributions from 7.0.1 vanish in the pairing channel.

This chapter expands on the summary of Dobaczewski, Backes et al. 2026, focusing on aspects crucial to the numerical development. It is worth noting that the radial terms are separated into five different form factors, $F(u)$,

$$F_1(u) = e^{-u}, \tag{7.0.10}$$

$$F_2(u) = \left(1 + \frac{1}{u}\right)\frac{e^{-u}}{u^2}, \tag{7.0.11}$$

$$F_3(u) = \frac{e^{-u}}{u}, \tag{7.0.12}$$

$$F_4(u) = \left(1 + \frac{3}{u} + \frac{3}{u^2}\right)\frac{e^{-u}}{u^3}, \tag{7.0.13}$$

$$F_5(u) = \left(1 + \frac{3}{u} + \frac{3}{u^2}\right)\frac{e^{-u}}{u}, \tag{7.0.14}$$

that can be rewritten as a Gaussian expansion (Wibowo, Han et al. 2026). The computation of Gaussian matrix elements in nuclear DFT is the theme of the next chapter, where it shall become clear that new computational techniques are crucial for the advancement of nuclear theory. Lastly, some of the numerical results coming from this work are available (Bissell et al. 2026), while the main publication is in preparation.

Eight

The Gaussian Separalisation Method

In this chapter, we briefly discuss some of the computational challenges of modern nuclear DFT and introduce a new algorithm to accelerate the computation for finite-range functional generators. We shall present the specific properties of Gaussian-type interactions that enable the new approach, discuss the findings of our implementation, and consider its limitations.

The efficiency of high-performance computing in physics depends not only on the computers' ever-growing speed but also crucially relies on the algorithms used to solve fundamental equations. This is particularly important when solving equations that describe quantum systems of many particles and fields. Examples thereof are ubiquitous. From the Lüscher's algorithm (Lüscher and Weisz 2001) to solve the QCD equations on the lattice to the Lanczos algorithm (Caurier et al. 2005) to diagonalize the shell-model Hamiltonian of 10^{10} dimensions, progress has been driven by advanced ideas in constructing powerful numerical algorithms.

Within nuclear theory, *ab initio* methods are more severely impacted by this issue, since the Hamiltonian scales exponentially with the system size (see Chapter 1). While less costly, progress in Nuclear density functional theory (DFT) also becomes constrained by computational resources as the community tackles increasingly difficult problems. Notoriously, the use of finite-range functionals requires an order of magnitude more resources over local functionals (Dobaczewski, Satuła et al. 2009a). Furthermore, modern approaches to fission require an exact computation of the Coulomb exchange interaction (Sánchez-Fernández et al. 2025), and obtaining two-body meson-exchange contributions to magnetic moments (Wibowo, Han et al. 2026, also briefly introduced in Chapter 7) requires the expensive computation of two-body operators. Uniting these problems is the approach of utilising Gaussian expansions to describe finite-range interactions. Due to the property (Girod and Grammaticos 1983)

$$\frac{1}{|\mathbf{r}-\mathbf{r}'|} = \frac{2}{\sqrt{\pi}} \int_0^\infty \exp\{-(\mathbf{r}-\mathbf{r}')^2/\mu^2\} \frac{d\mu}{\mu^2}, \tag{8.0.1}$$

it is usual to approximate potentials such as Coulomb and Yukawa by a sum of Gaussian potentials

with different ranges and scales (Dobaczewski, Satuła et al. 2009a)

$$\hat{G}(\mathbf{r}_1, \mathbf{r}_2) = \sum_{\omega=1}^{N} \alpha_\omega \exp\{-\beta_\omega(\mathbf{r}_1 - \mathbf{r}_2)^2\}, \tag{8.0.2}$$

especially when dealing with the Harmonic Oscillator (HO) basis (Schunck 2019). This is the approach of choice for our aforementioned examples, which require exact contributions to finite-range interactions. As shown in section 2.3.1, this also applies to the class of finite-range energy density functionals (EDFs): the Gogny pseudopotential (Dechargé and Gogny 1980) uses a sum of two Gaussians with different ranges, or the regularised pseudopotentials which employ a Gaussian form factor for the regularisation (Dobaczewski, Bennaceur and Raimondi 2012). This showcases the vital importance of developing new and more efficient algorithms for Gaussian-type functional generators for nuclear DFT.

To further illustrate the challenges of computing matrix elements from these functional generators, let us consider the special case of Cartesian coordinates. Since the Gaussian potential is separable, we can write the matrix elements of the 1-dimensional component of the potential, $\hat{G} \equiv \hat{G}(u_1, u_2)$, with $u = x, y, z$,

$$\begin{aligned} G_{m'm,n'n} &= \left\langle m'm \middle| \hat{G} \middle| n'n \right\rangle, \\ &= \int \mathrm{d}u_1 \int \mathrm{d}u_2 \psi_{m'}(u_1)\psi_m(u_2)\hat{G}(u_1, u_2)\psi^*_{n'}(u_1)\psi^*_n(u_2). \end{aligned} \tag{8.0.3}$$

The mean field is then obtained by the contraction

$$\Gamma_{\mathbf{nm}} = \sum_{\mathbf{n'm'}} G^x_{m'_x m_x, n'_x n_x} G^y_{m'_y m_y, n'_y n_y} G^z_{m'_z m_z, n'_z n_z} \rho_{\mathbf{n'm'}}, \tag{8.0.4}$$

where $\rho_{\mathbf{n'm'}}$ is the density matrix, and $\mathbf{m} = m_x, m_y, m_z$. It is clear that the main challenge at hand is the large number of nested loops. Being N_0 the number of harmonic oscillator (HO) shells, naively computing the mean field would require 12 independent nested loops, and an order of N_0^{12} operations. With the introduction of partial summations, the scaling of computing matrix elements can be reduced to N_0^8 operations (Dobaczewski, Satuła et al. 2009a; Schunck 2019), which is treatable, albeit expensive. The next section offers a primer on computational efficiency and on partial summations for tensor contractions, which should further elucidate these concepts.

It is in this context that we developed the Gaussian Separalisation Method (GSM), improving the efficiency of computing Gaussian-type finite-range functional generators and aiming to enable new directions and possibilities for nuclear DFT. The core idea of this approach is diagonalising the 1-dimensional Gaussian matrix elements $G^\mu_{m'_\mu m_\mu, n'_\mu n_\mu}$ and manipulating the indices in the *separalisation* scheme

$$G^\mu_{m'_\mu m_\mu, n'_\mu n_\mu} = A^\mu_{\ell, m'_\mu n'_\mu} \lambda_\ell A^\mu_{\ell, m_\mu n_\mu}, \tag{8.0.5}$$

which allows us to exploit features of both its eigenvectors and eigenvalue spectra. From this initial setup, we can introduce intermediates such that the complexity of computing matrix elements is kept to an order of N_0^8 operations. As the spectra of eigenvalues λ_ℓ rapidly go to zero, with only a few being of numerical significance, cut-offs are allowed without sacrificing precision. The concept of truncating an eigendecomposition is not new. It is prominent for applications such as Principal Component Analysis and Singular Value Decomposition (Dongarra et al. 2018; Greenacre et al. 2022). Despite the similarities, in our case, the eigendecomposition is arguably the easiest step in computing the energy. Instead, the most delicate part of our algorithm is exploiting the separability of the problem and optimising the indices coupling scheme. This new approach also allows us to exploit symmetry properties of the eigenvectors post-diagonalisation, so that sums over Cartesian HO indices can also be optimised. In this chapter, we first introduce aspects of computational complexity in Section 8.1, and then establish the foundation of the method by showing key properties of the Gaussian matrix elements, eigenvectors, and eigenvalues in Section 8.2. A simplified algorithmic structure of the GSM is shown in Section 8.3. The number of operations cut from the symmetries of eigenvectors, and from the eigenvalue spectra are shown respectively in Sections 8.4 and 8.5. Finally, the precision of the method is analysed in Section 8.6, and the timing results are discussed in Section 8.7. Further technical details of the implementation, as well as the exact algorithm developed are discussed in Appendix E.

8.1 Computational efficiency

An extremely useful notion to evaluate when writing scientific code is the *cost* of an algorithm. The same mathematical expression can be computed in many different ways. Typically, the cost we evaluate is the time, or how long it takes to execute, and space, or how much memory space it requires[*]. Evaluating the cost of an algorithm, or its complexity, constitutes an active area of research in computer science (Arora and Barak 2009; Watson 2026), of which we shall only loosely discuss the most common notions. An intuitive way of quantifying the time complexity of an algorithm is to evaluate the number of basic floating-point operations it executes. We are often interested not in the number of operations required for a specific problem, but in how an algorithm *scales* as a function of its input (e.g., system size). To this end, it is common to use *big-O notation*, defined as follows: for two functions $f(n)$ and $g(n)$, $f(n)$ is said to be $\mathcal{O}\big(g(n)\big)$ if there exists a constant c such that $f(n) \leq cg(n)$. Thus, we can think of it as the asymptotic behaviour of function f, and as how our algorithm scales for large inputs[†].

[*]Often neglected, but also important, is the cost to the sanity of the developer or user of an algorithm.

[†]The big-O notation is equivalent to the very loose comments in the introduction of this chapter, where I mentioned that "computing x requires *an order of* y operations". Hopefully, this small section helps elucidate the concept to readers who are unfamiliar with the topic.

A simple illustrative example of different algorithms with different time complexities is the multiplication of three $N \times N$ matrices, $D = ABC$. The element D_{ij} of such multiplication is given by

$$D_{ij} = \sum_{kl} A_{ik} B_{kl} C_{lj}. \tag{8.1.1}$$

Algorithm 1: Computing all D_{ij} without intermediate steps.

```
1 forall i do
2     forall j do
3         forall k do
4             forall l do
5                 D_ij = Σ_kl A_ik B_kl C_lj
```

Algorithm 2: Computing all D_{ij} with intermediate steps.

```
1 forall j do
2     forall i do
3         forall k do
4             E_ij = Σ_k B_ik C_kj
5     forall i do
6         forall l do
7             D_ij = Σ_l A_il E_lj
```

To compute all D_{ij}, Algorithm 1 computes all the matrix elements directly, in the most intuitive way, which is $\mathcal{O}(N^4)$, going over four N nested loops. On the other hand, Algorithm 2, which is $\mathcal{O}(N^3)$, utilises an intermediate matrix, E, to store the multiplication of matrices B and C before finally computing all D_{ij}. This entails three N-sized nested loops, being a much more time-efficient algorithm for bigger matrices. Figure 8.1 shows, in doubly logarithmic scale, the execution time for both algorithms as a function of N, explicitly demonstrating that the time scales according to the number of operations performed. This is a rather straightforward example, but with complex implementations, evaluating the scaling may be more subtle. It is also important to note that Algorithm 2 requires more memory than Algorithm 1, as the intermediate must be stored. Keeping this simple introduction in mind, we shall delve into the problem of computing the energy of Gaussian-type finite-range functional generators.

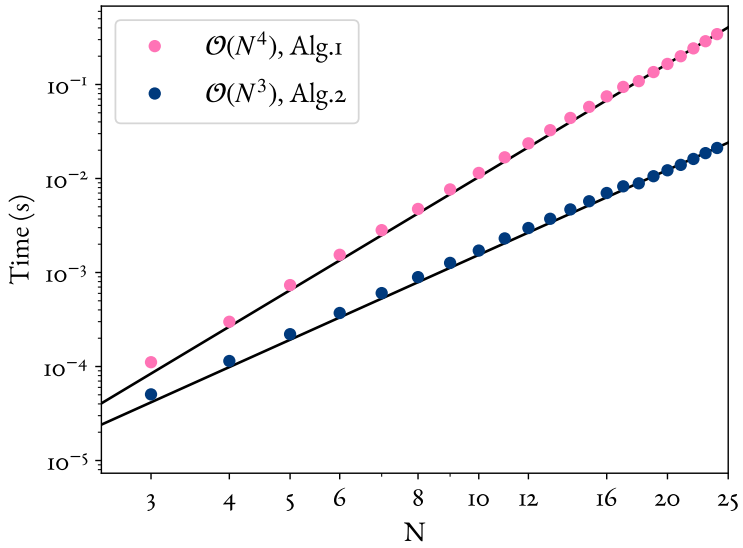


Figure 8.1: Execution times obtained for Algorithms 1 and 2 shown as a function of N, for a square matrix of dimension $N \times N$. The lines show that the times scale, respectively, as N^4 and N^3.

8.2 Properties of the Gaussian matrix elements and their eigenvalue decomposition

The key element of the new algorithm is the analysis of the one-dimensional Gaussian matrix elements in the HO basis, which follow from eq. (8.0.3) as

$$G^{\mu}_{m'm,n'n} = \frac{a}{\sqrt{\pi}} \int \mathrm{d}u_1 \int \mathrm{d}u_2 \, H^{(0)}_{m'}(u_1) H^{(0)}_{m}(u_2) e^{-a^2(u_1-u_2)^2} e^{-b^2_\mu(u_1^2+u_2^2)} H^{(0)}_{n'}(u_1) H^{(0)}_{n}(u_2), \tag{8.2.1}$$

where $H^{(0)}_m(u)$ are the normalized Hermite polynomials, $\int \mathrm{d}u \, H^{(0)}_{m'}(u) H^{(0)}_{m}(u) e^{-b^2_\mu u^2} = \delta_{m'm}$, generic integration variables u represent the Cartesian position variables r_μ for $\mu = x, y, z$, and $1/a$ and $1/b_\mu$ stand for the Gaussian width and HO length, respectively.

The total DFT energy E_{tot} is composed of the standard direct, exchange, and pairing terms, each depending on the Gaussian matrix elements (8.0.3)

$$E_{\mathrm{tot}} = \sum_{\tau' k' \tau k} C^{\tau' k' \tau k}_{\mathrm{dir}} E^{\tau' k' \tau k}_{\mathrm{dir}} + C^{\tau' k' \tau k}_{\mathrm{exc}} E^{\tau' k' \tau k}_{\mathrm{exc}} + C^{\tau' k' \tau k}_{\mathrm{pair}} E^{\tau' k' \tau k}_{\mathrm{pair}}, \tag{8.2.2}$$

where $C^{\tau' k' \tau k}_{\mathrm{dir}}$, $C^{\tau' k' \tau k}_{\mathrm{exc}}$, and $C^{\tau' k' \tau k}_{\mathrm{pair}}$ are the corresponding coupling constants (Dobaczewski, Satuła et al. 2009a),

$$E^{\tau' k' \tau k}_{\mathrm{dir}} = \sum_{\mathbf{m'n'mn}} D^{\tau' k'}_{\mathbf{m'n'}} D^{\tau k}_{\mathbf{nm}} G^{x}_{m'_x m_x, n'_x n_x} G^{y}_{m'_y m_y, n'_y n_y} G^{z}_{m'_z m_z, n'_z n_z}, \tag{8.2.3}$$

$$E^{\tau' k' \tau k}_{\text{exc}} = \sum_{\mathbf{m'n'mn}} D^{\tau' k'}_{\mathbf{m'n'}} D^{\tau k}_{\mathbf{nm}} G^{x}_{m'_x m_x, n_x n'_x} G^{y}_{m'_y m_y, n_y n'_y} G^{z}_{m'_z m_z, n_z n'_z}, \tag{8.2.4}$$

$$E^{\tau' k' \tau k}_{\text{pair}} = \sum_{\mathbf{m'n'mn}} P^{\tau' k' *}_{\mathbf{m'n'}} P^{\tau k}_{\mathbf{nm}} G^{x}_{m'_x n'_x, m_x n_x} G^{y}_{m'_y n'_y, m_y n_y} G^{z}_{m'_z n'_z, m_z n_z}. \tag{8.2.5}$$

In these expressions, $D^{\tau k}_{\mathbf{nm}}$ and $P^{\tau k}_{\mathbf{nm}}$ represent the density matrix $\rho^{\tau}_{\mathbf{n}s,\mathbf{m}u}$ and pairing tensor $\kappa^{\tau}_{\mathbf{n}s,\mathbf{m}u}$ (Ring and Schuck 1980), respectively, conveniently expanded on the harmonic-oscillator (HO) simplex basis (Dobaczewski and Dudek 1997), that is,

$$\begin{aligned} D^{\tau k}_{\mathbf{nm}} &= \sum_{su} \rho^{\tau}_{\mathbf{n}s,\mathbf{m}u} \sigma^{k}_{us}\left(m_y n_y\right), \\ P^{\tau k}_{\mathbf{nm}} &= \sum_{su} \kappa^{\tau}_{\mathbf{n}s,\mathbf{m}u} \sigma^{k}_{us}\left(m_y n_y\right), \end{aligned} \tag{8.2.6}$$

where the Cartesian HO quantum numbers are represented by vectors $\mathbf{n} = (n_x n_y n_z)$ or $\mathbf{m} = (m_x m_y m_z)$, the y-simplex quantum numbers are denoted by s or u, $\sigma^{k}_{us}(m_y n_y)$ for $k = 0, x, y$ or z are the identity and Pauli matrices in the simplex basis (Dobaczewski and Dudek 1997) (which depend on the numbers of the HO quanta in the y direction), and $\tau = \text{p, n}$ stands for protons and neutrons.

As briefly introduced in the previous section, the new method relies on diagonalising the Gaussian matrix elements. As contractions should be performed first on the indices $\{mn\}$ of the first density matrix, the key aspect is separating the indices in a way that allows summations of the primed and unprimed indices separately. To do so, we define new indices of combined pairs of the HO indices

$$i \equiv \{m'n'\} \quad j \equiv \{mn\}, \tag{8.2.7}$$

so that the generic Gaussian matrix elements are combined into square symmetric arrays that can be diagonalized and expressed via their eigenvalues λ_ℓ and eigenvectors A^{ℓ}_{i} as

$$G_{ij} = \sum_{\ell} A^{\ell}_{i} \lambda_\ell A^{\ell}_{j}. \tag{8.2.8}$$

We see that for the HO basis composed of the lowest N_0 shells, $m, n = 0 \ldots N_0$, arrays G_{ij} have small dimensions of $(N_0+1)^2 \times (N_0+1)^2$.

Since in the direct, exchange, and pairing terms of Eqs. (8.2.3)–(8.2.5), the pairs of indices $\{m'n'\}$ and $\{mn\}$ are positioned differently, the index separation in the three channels has to be performed independently, that is,

$$G^{\mu}_{m'm,n'n} = \sum_{\ell_\mu} A^{\mu,\ell_\mu,\text{dir}}_{m'n'} \lambda_{\mu,\ell_\mu,\text{dir}} A^{\mu,\ell_\mu,\text{dir}}_{mn}, \tag{8.2.9}$$

$$G^{\mu}_{m'm,nn'} = \sum_{\ell_\mu} A^{\mu,\ell_\mu,\text{exc}}_{m'n'} \lambda_{\mu,\ell_\mu,\text{exc}} A^{\mu,\ell_\mu,\text{exc}}_{mn}, \tag{8.2.10}$$

$$G^{\mu}_{m'n',mn} = \sum_{\ell_\mu} A^{\mu,\ell_\mu,\text{pair}}_{m'n'} \lambda_{\mu,\ell_\mu,\text{pair}} A^{\mu,\ell_\mu,\text{pair}}_{mn}. \tag{8.2.11}$$

This gives us the final generic separalized expression for energies (8.2.3)–(8.2.5) as

$$E^{\tau' k' \tau k}_{\text{chan}} = \sum_{\ell_x \ell_y \ell_z} \left(\prod_{\mu=x,y,z} \lambda_{\mu,\ell_\mu,\text{chan}} \right) E^{\tau' k' *}_{\boldsymbol{\ell},\text{chan}} E^{\tau k}_{\boldsymbol{\ell},\text{chan}}, \tag{8.2.12}$$

where "chan" stands for "dir", "exc", or "pair" and $\boldsymbol{\ell} = (\ell_x \ell_y \ell_z)$ represents the vector of eigenvalue indices, and where

$$E^{\tau k}_{\boldsymbol{\ell},\text{chan}} = \sum_{\mathbf{mn}} D^{\tau k}_{\mathbf{nm}} A^{x,\ell_x,\text{chan}}_{m_x n_x} A^{y,\ell_y,\text{chan}}_{m_y n_y} A^{z,\ell_z,\text{chan}}_{m_z n_z}. \tag{8.2.13}$$

In the numerical implementations, expressions (8.2.3)–(8.2.5) and (8.2.13) are always evaluated by considering one Cartesian direction after another, which leads to the numbers of the nested loops that are much smaller than those appearing in those equations explicitly. In appendix E, we present details of the implementations and show that both the standard (8.2.3)–(8.2.5) and new (8.2.13) algorithms lead to the nested loops and numerical effort of the order of $\mathcal{O}(N_0^8)$. Therefore, a naive implementation of the separalised algorithm is not expected to bring any major improvement. However, a primary difference between the two is that the latter involves summations of terms multiplied by the products of the eigenvalues (8.2.12). This reduces the sums to those multiplied by large products, which has the potential to reduce the computational burden significantly. We now proceed with discussing this aspect of the new algorithm.

First, let us analyze the properties of eigenvalues and eigenvectors in the pairing channel. Directly from the definition of the Gaussian matrix elements (8.2.1), we see that for an arbitrary array X_{mn}, the average energy in this channel $\sum_{m'n'mn} X_{m'n'} G^{\mu}_{m'n',mn} X_{mn}$ is equal to the integral of the product of the square of the polynomial $\Phi(u_1, u_2) = \sum_{mn} X_{mn} H^{(0)}_m(u_1) H^{(0)}_n(u_2)$ and Gaussian factors and, therefore, is strictly positive. As a result the corresponding array G_{ij} is positive definite and thus all its eigenvalues are positive, $\lambda_{\mu,\ell_\mu,\text{pair}} > 0$. Second, since in this channel, the Gaussian matrix elements are invariant to exchanging indices related to variables $u_1 \leftrightarrow u_2$, the arrays of the corresponding eigenvectors must be either symmetric or antisymmetric

$$A^{\mu,\ell_\mu\pm,\text{pair}}_{mn} = \pm A^{\mu,\ell_\mu\pm,\text{pair}}_{nm}. \tag{8.2.14}$$

Further, we can employ the locality of the Gaussian functional generator in eq. (8.2.1), which entails the symmetry of the Gaussian matrix elements under exchanging either the two indices related to variable u_1 or those related to u_2. Then, acting with the matrix elements in the exchange channel, eq. (8.2.10), on the eigenvectors in the pairing channel, we obtain

$$\begin{aligned} \sum_{mn} G^{\mu}_{m'm,nn'} A^{\mu,\ell_\mu\pm,\text{pair}}_{mn} &= \sum_{mn} G^{\mu}_{m'n',nm} A^{\mu,\ell_\mu\pm,\text{pair}}_{mn} = \\ \pm \sum_{mn} G^{\mu}_{m'n',nm} A^{\mu,\ell_\mu\pm,\text{pair}}_{nm} &= \pm \lambda_{\mu,\ell_\mu\pm,\text{pair}} A^{\mu,\ell_\mu\pm,\text{pair}}_{m'n'}. \end{aligned} \tag{8.2.15}$$

This interesting property means that the eigenvectors in the exchange channel are identical to those in the pairing channel and the eigenvalues in the exchange channel corresponding to the symmetric (antisymmetric) eigenvectors are equal (have opposite signs) to those in the pairing channel. Consequently, an efficient algorithm can treat the exchange and pairing channels simultaneously.

Finally, we can discuss the separalised Gaussian matrix elements in the direct channel. For that, we use the simple fact that a product of polynomials is a polynomial, and thus we can express it as a linear combination of orthogonal Hermite polynomials (see, e.g., Dobaczewski and Dudek 1997),

$$H^{(0)}_m(u)H^{(0)}_n(u) = \sum_p C^p_{mn} H^{(0)}_p(u), \tag{8.2.16}$$

where C^p_{mn} is a symmetric matrix of coefficients and for $0 \le m,n \le N_0$ we have $0 \le p \le m+n \le 2N_0$. Equation (8.2.16) tells us that the Gaussian matrix elements in the direct channel (8.2.9) are given by a much smaller $(2N_0+1)\times(2N_0+1)$ symmetric matrix $\bar{G}^{\mu}_{p'p}$ or its eigenvectors $\bar{A}^{\mu,\bar{\ell}_\mu}_p$ and eigenvalues $\bar{\lambda}_{\mu,\bar{\ell}_\mu}$,

$$\bar{G}^{\mu}_{p'p} = \tfrac{a}{\sqrt{\pi}} \int \mathrm{d}u_1 \int \mathrm{d}u_2 \, H^{(0)}_{p'}(u_1) e^{-a^2(u_1-u_2)^2} e^{-b^2_\mu(u_1^2+u_2^2)} H^{(0)}_p(u_2) = \sum_{\bar{\ell}_\mu} \bar{A}^{\mu,\bar{\ell}_\mu}_{p'} \bar{\lambda}_{\mu,\bar{\ell}_\mu} \bar{A}^{\mu,\bar{\ell}_\mu}_{p}, \tag{8.2.17}$$

and are zero otherwise, that is,

$$G^{\mu}_{m'm,n'n} = \sum_{p'p} C^{p'}_{m'n'} \bar{G}^{\mu}_{p'p} C^{p}_{mn}. \tag{8.2.18}$$

In this way, we obtain that the eigenvectors and eigenvalues in the direct channel (8.2.9) are given by $\ell_\mu \equiv \bar{\ell}_\mu$,

$$A^{\mu,\ell_\mu,\mathrm{dir}}_{mn} \equiv \sum_p C^p_{mn} \bar{A}^{\mu,\bar{\ell}_\mu}_p, \tag{8.2.19}$$

$$\lambda_{\mu,\ell_\mu,\mathrm{dir}} \equiv \bar{\lambda}_{\mu,\bar{\ell}_\mu}, \tag{8.2.20}$$

and thus in this channel, the spectrum extends to a much smaller number of non-zero eigenvalues, $(2N_0+1)$ instead of $(N_0+1)^2$. As a result, the evaluation of energies (8.2.12) in the direct channel becomes computationally insignificant and thus contributes a factor of 1/3 to the overall acceleration of the algorithm.

8.3 Simplified structure of the algorithm

To exemplify the method, we implemented GSM to the nuclear DFT code HFODD (Dobaczewski, Bączyk et al. 2021), specifically to the case of Gogny DS1 functional generator. The energy of the direct, exchange, and pairing channel is given, respectively, by eqs. (8.2.3), (8.2.4), and (8.2.5).

In practice, computing the energy with $\mathcal{O}(N_0^8)$ requires the introduction of intermediary arrays (similar to the simple example of section 8.1). To showcase this method, we first introduce the traditional procedure as given by Dobaczewski, Satuła et al. 2009a and Schunck 2019, and then compare it to a simplified version of the GSM.

8.3.1 Traditional approach

The traditional algorithm starts with storing auxiliary arrays for the y and z-directions, obtained by the product of the density matrix by the respective Gaussian matrix, contracting the "unprimed" m, n indices. This procedure is $\mathcal{O}(N_0^8)$ in both directions

$$\begin{aligned} Y^{\tau k}_{n_x m'_y n_z, m_x n'_y m_z} &= \sum_{n_y m_y} D^{\tau k}_{n_x n_y n_z, m_x m_y m_z} G^{y}_{m'_y, m_y, n'_y n_y}, \\ Z^{\tau k}_{n_x m'_y m'_z, m_x n'_y n'_z} &= \sum_{n_z m_z} Y^{\tau k}_{n_x m'_y n_z, m_x n'_y m_z} G^{z}_{m'_z m_z, n'_z n_z}. \end{aligned} \tag{8.3.1}$$

Then, we contract the "primed" indices of the z-direction intermediate with the second density matrix, which is $\mathcal{O}(N_0^8)$ once more

$$X^{\tau', \tau k}_{n'_x n_x, m'_x m_x} = \sum_{n'_y n'_z m'_y m'_z} D^{\tau'}_{n'_x n'_y n'_z, m'_x m'_y m'_z} Z^{\tau k}_{n_x m'_y m'_z, m_x n'_y n'_z}. \tag{8.3.2}$$

Finally, we sum over the x-direction "primed" and "unprimed" indices, which is $\mathcal{O}(N_0^4)$

$$E^{\tau' k' \tau k}_{\text{dir}} = \sum_{n'_x n_x, m'_x m_x} X^{\tau', \tau k}_{n'_x n_x, m'_x m_x} G^{x}_{m'_x m_x, n'_x n_x}. \tag{8.3.3}$$

8.3.2 Simplified GSM intermediates

One big difference between the old and new approach is that the "primed" and "unprimed" indices are now computed completely separately. Any loop over an eigenvalue index ℓ_μ corresponds to $(N_0 + 1)^2$ operations. We start with the y-direction, contracting the "primed" indices

$$Y^{\tau' k'}_{n'_x n'_z m'_x m'_z \ell_y} = \sum_{m'_y n'_y} D^{\tau' k'}_{n'_x n'_y n'_z, m'_x m'_y m'_z} A^{y}_{m'_y, n'_y, \ell_y} \lambda_{\ell_y}, \tag{8.3.4}$$

which is $\mathcal{O}(N_0^8)$. Now, the same is done for the z-direction

$$Z^{\tau' k'}_{n'_x m'_x \ell_y \ell_z} = \sum_{m'_z n'_z} Y^{\tau' k'}_{n'_x n'_z m'_x m'_z \ell_y} A^{z}_{m'_z, n'_z, \ell_z} \lambda_{\ell_z} \tag{8.3.5}$$

and the x-direction

$$X^{\tau' k'}_{\ell_x \ell_y \ell_z} = \sum_{m'_x n'_x} Z^{\tau' k'}_{n'_x m'_x \ell_y \ell_z} A^{x}_{m'_x, n'_x, \ell_x} \lambda_{\ell_x}, \tag{8.3.6}$$

both $\mathcal{O}(N_0^8)$. After summing over the "primed" indices, we then sum over the eigenvalue indices ℓ_μ to recover the HO indices and compute the field:

$$\tilde{X}^{\tau' k'}_{\ell_y \ell_z m_x n_x} = \sum_{\ell_x} X^{\tau' k'}_{\ell_x \ell_y \ell_z} A^{x}_{\ell_x, n_x m_x}, \tag{8.3.7}$$

$$\tilde{Z}^{\tau' k'}_{\ell_y m_x n_x m_z n_z} = \sum_{\ell_z} \tilde{X}^{\tau' k'}_{\ell_y \ell_z m_x n_x} A^{z}_{\ell_z, n_z m_z}, \tag{8.3.8}$$

$$\tilde{Y}^{\tau' k'}_{m_x n_x m_z n_z m_y n_y} = \sum_{\ell_y} \tilde{Z}^{\tau' k'}_{\ell_y m_x n_x m_z n_z} A^{y}_{\ell_y, n_y m_y}. \tag{8.3.9}$$

Each of the steps above is $\mathcal{O}(N_0^8)$. Lastly, we contract the "unprimed" indices with those of the second density matrix, which is $\mathcal{O}(N_0^6)$

$$E^{\tau' k' \tau k}_{\text{dir}} = \sum_{\mathbf{mn}} D^{\tau k}_{n_x n_y n_z m_x m_y m_z} \tilde{Y}^{\tau' k'}_{m_x n_x m_z n_z m_y n_y}. \tag{8.3.10}$$

An exact computation of the energy following this procedure would naively not yield any numerical acceleration, as both algorithms have the same asymptotic behaviour. The next sections are dedicated to showing how the properties of the Gaussian eigenvalues and eigenvectors make it possible to accelerate finite-range calculations via the separalisation. More detailed notes and schematics of the algorithm are provided in Appendix E, which is useful guidance for implementing the method.

8.4 Acceleration due to symmetry of the eigenvectors

An important property of the eigenvectors is their symmetry or anti-symmetry on exchange of Harmonic Oscillator (HO) indices, $A^{\mu,\ell_\mu \pm}_{mn} = \pm A^{\mu,\ell_\mu \pm}_{nm}$. Using this property, we can avoid exchanged HO indices when contracting the eigenvectors with the density matrix, provided that ρ is also separated into its symmetric and antisymmetric parts. In practice, the code has loops over the HO indices in a nested loop structure, which always respects $n_x + n_y + n_z \leq N_0$ and $m_x + m_y + m_z \leq N_0$. In HFODD (Dobaczewski et al. 2026), the limits of nested loops obey the following structure: The first loops correspond to indices in the x direction, where both the m_x and n_x quanta go from 0 to N_0. For the second direction (z), the limits of the HO quanta loops become $m_z \leq N_0 - m_x$ and $n_z \leq N_0 - n_x$. Lastly, in the last direction (y), the limits are $m_y \leq N_0 - m_z - m_x$ and $n_y \leq N_0 - n_z - n_x$. This mapping is illustrated in Figure 8.2.

In each iteration, we always perform the same basic floating-point operations, consisting of one multiplication and one addition. Strictly speaking, actions such as array accesses also contribute to the CPU time. However, for both the GSM and the traditional approach, the number of operations for each set of $\{m, n\}$ is equivalent. Thus, the length of the loops is a direct indicator of the number of operations performed, and a good source of comparison between the two algorithms. We can

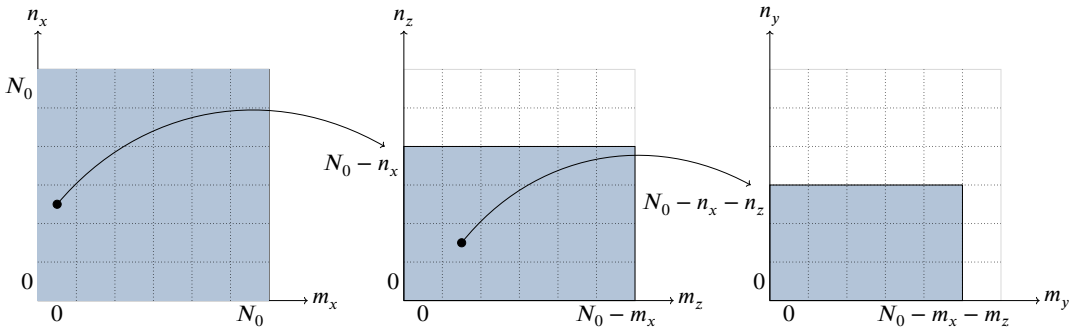


Figure 8.2: Schematic representation of the loops for the HO indices for $N_0 = 5$ shells.

compute the total number of iterations exactly. It depends solely on the basis size, and is equivalent to

$$
\begin{aligned}
O^{3D}_{\text{original}} &= \sum_{n_x=0}^{N_0} \sum_{m_x=0}^{N_0} \sum_{n_z=0}^{N_0-n_x} \sum_{m_z=0}^{N_0-m_x} \sum_{n_y=0}^{N_0-n_x-n_z} \sum_{m_y=0}^{N_0-m_x-m_z} 1 \\
&= \sum_{n_x=0}^{N_0} \sum_{m_x=0}^{N_0} \sum_{n_z=0}^{N_0-n_x} \sum_{m_z=0}^{N_0-m_x} (N_0 - m_x - m_z + 1)(N_0 - n_x - n_z + 1) \\
&\qquad \Longrightarrow \sum_{m_z=0}^{N_0-mx} (N_0 - m_x - m_z + 1) = \sum_{m_z=0}^{N_0-mx} (N_0 - m_x + 1) - \sum_{m_z=0}^{N_0-mx} m_z \\
&\qquad\quad = (N_0 - m_x + 1)(N_0 - m_x + 1) - \frac{1}{2}(N_0 - m_x + 1)(N_0 - m_x) \\
&\qquad\quad = \frac{1}{2}(N_0 - m_x + 1)(N_0 - m_x + 2) \\
O^{3D}_{\text{original}} &= \sum_{n_x=0}^{N_0} \sum_{m_x=0}^{N_0} \left[\frac{1}{2}(N_0 - m_x + 1)(N_0 - m_x + 2)\right]\left[\frac{1}{2}(N_0 - n_x + 1)(N_0 - n_x + 2)\right] \\
&= \frac{1}{4}\left[\frac{1}{3}(N_0 + 1)(N_0^2 + 5N_0 + 6)\right]^2 \\
&= \left[\frac{1}{6}(N_0 + 1)(N_0 + 2)(N_0 + 3)\right]^2 . \qquad (8.4.1)
\end{aligned}
$$

Naturally, at some stages of the contractions between the Gaussian matrix elements and ρ/κ, not all Cartesian directions are present in the same iteration. If only one Cartesian direction is present, the number of iterations is

$$
\begin{aligned}
O^{1D}_{\text{original}} &= \sum_{n_x=0}^{N_0} \sum_{m_x=0}^{N_0} 1 \\
&= (N_0 + 1)^2, \qquad (8.4.2)
\end{aligned}
$$

and two Cartesian directions

$$
\begin{aligned}
O^{2D}_{\text{original}} &= \sum_{n_x=0}^{N_0} \sum_{m_x=0}^{N_0} \sum_{n_z=0}^{N_0-n_x} \sum_{m_z=0}^{N_0-m_x} 1 \\
&= \sum_{n_x=0}^{N_0} \sum_{m_x=0}^{N_0} (N_0 - n_x + 1)(N_0 - m_x + 1) \\
&= \left[\frac{1}{2}(N_0 + 1)(N_0 + 2)\right]^2 . \qquad (8.4.3)
\end{aligned}
$$

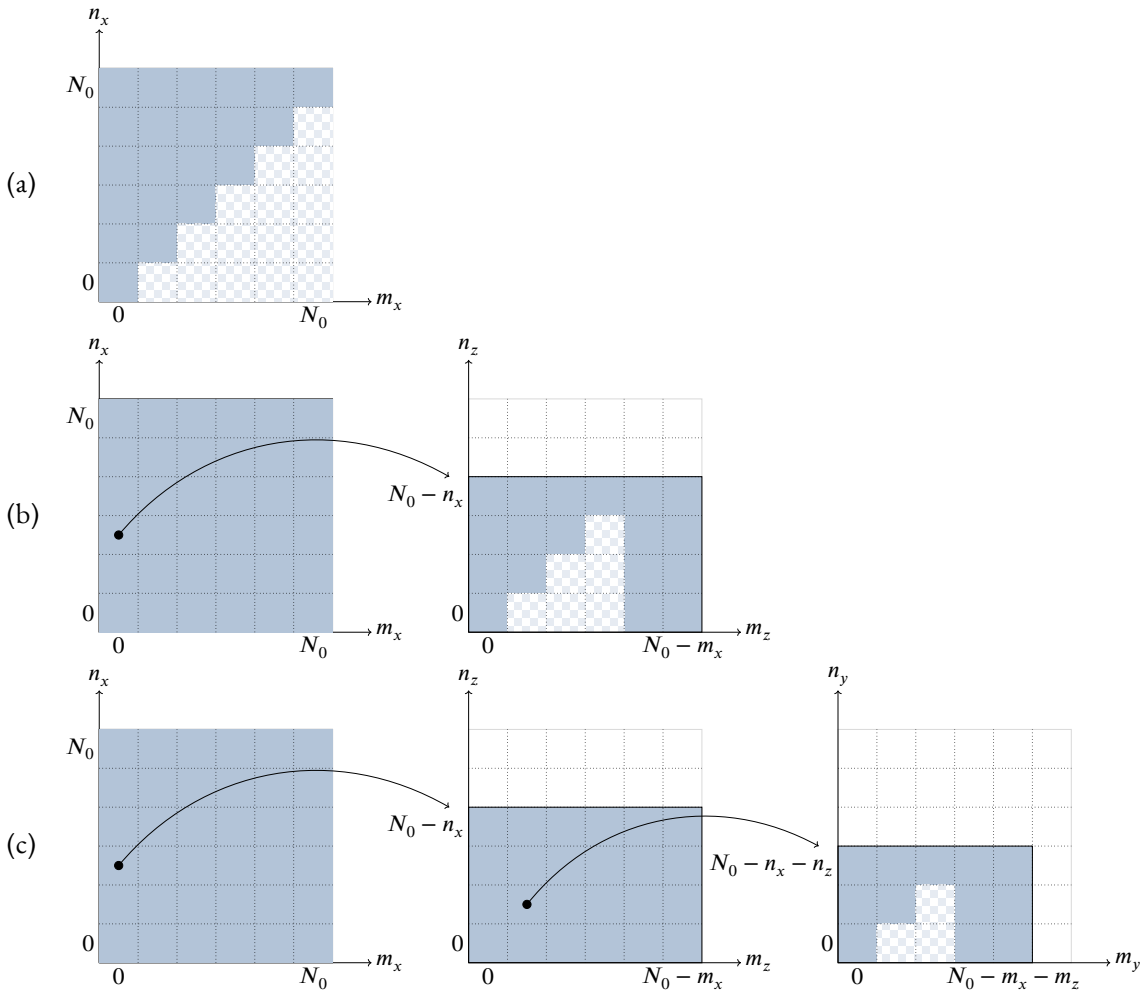


Figure 8.3: Schematic representation of the loops for the HO indices in the new scheme for $N_0 = 5$ shells. Panels (a), (b), and (c) correspond to the innermost loop with HO indices in the x, z, and y direction, respectively. The lighter and patterned indices, always highlighted in the innermost loops, can be omitted in the GSM algorithm.

As we have introduced, the length of loops over HO indices can be reduced by considering the property of eq. (8.2.14). This entails: (i) separating the symmetric and antisymmetric eigenvectors;

(ii) symmetrising the arrays which multiply the eigenvectors, over the same pair of indices which will then be contracted (in our case, the first example of this is symmetrising the density matrix of eq. (8.2.6) over m_y, n_y). With this, we can skip over indices which are symmetric, $m \leftrightarrow n$. This procedure can be repeated for the following directions by symmetrising the intermediate arrays that follow. The number of iterations performed with this procedure varies according to the number of Cartesian directions with HO indices in the current nested loop. For one Cartesian direction, the total number of iterations then becomes

$$\begin{aligned} O^{1D}_{\text{sym-skip}} &= \sum_{n_x=0}^{N_0} \sum_{m_x=0}^{n_x} 1 \\ &= \frac{1}{2}(N_0+1)(N_0+2). \end{aligned} \tag{8.4.4}$$

The exact analytic expressions for two and three sets of HO indices in different Cartesian directions are less illustrative, but can be computed exactly. The *skipped* $\{mn\}$ index pairs in one, two, and three Cartesian directions satisfy the following criteria, respectively

$$\begin{aligned} m_x &> n_x, \\ m_z &> n_z, \qquad m_z \leq \min(N_0 - n_x, N_0 - m_x), \\ m_y &> n_y, \qquad m_y \leq \min(N_0 - n_x - n_z, N_0 - m_x - m_z). \end{aligned} \tag{8.4.5}$$

This is illustrated in Figure 8.3, where the lighter and patterned indices have a symmetric $m \leftrightarrow n$ counterpart included, and thus can be omitted.

The number of iterations after skipping the indices under the conditions 8.4.5, which we denote $O_{\text{sym-skip}}$, can be compared to the number of iterations including all indices, indicated by eqs. (8.4.1)-(8.4.3). Figure 8.4 shows the ratio between the two approaches, separating this ratio for one to three Cartesian directions with HO quanta indices. Throughout the GSM algorithm, there is always at least one set of HO indices included in the nested loops, such that the acceleration due to the symmetries of the eigenvectors is carried in the performance of the entire algorithm. Note that, e.g., for loops with the HO quanta in the three Cartesian directions, both algorithms are $\mathcal{O}(N_0^6)$. However, the factors hidden under big-O notation are relevant in the use case of typical nuclear DFT bases. Our results shall focus more significantly on $N_0 = 16$ and 20, but across a wide range of basis sizes, this property corresponds to performing $\approx 50 - 60\%$ fewer operations than with the full loops.

8.5 Acceleration due to eigenvalue cutoffs

The second source of acceleration to the GSM is the eigenvalue spectra of the diagonalised Gaussian matrix elements of eq. (8.2.8). The arrays containing the Gaussian matrix elements have dimensions

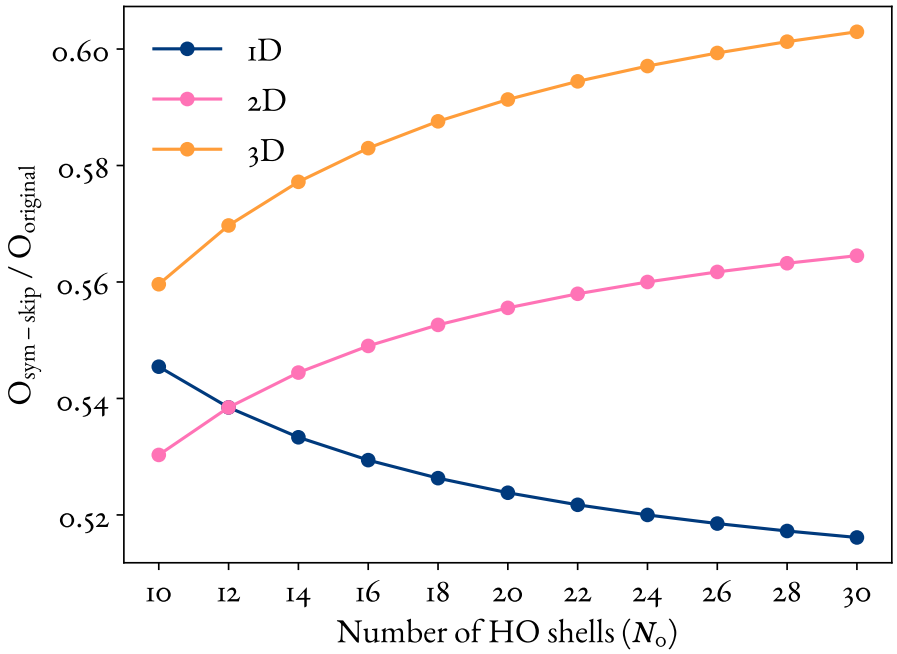


Figure 8.4: Ratio between the number of iterations when skipping the symmetric $m \leftrightarrow n$ indices ($O_{\text{sym-skip}}$) and accounting for all HO indices (O_{original}).

of $(N_0 + 1)^2 \times (N_0 + 1)^2$, and thus, each Cartesian direction has $(N_0 + 1)^2$ eigenvalues. There are, therefore, $(N_0 + 1)^4$ and $(N_0 + 1)^6$ products of eigenvalues in two and three Cartesian directions, respectively. These quantities, which we shall denote n_{max}, can be directly compared with the number of operations performed on loops over HO indices, which correspond to O_{original} given in eqs. (8.4.1)—(8.4.3). It is important to note that, due to the constraints $n_x + n_y + n_z \leq N_0$ and $m_x + m_y + m_z \leq N_0$, the loops over the HO quanta will always be shorter than those of a product of eigenvalues without cutoffs. Figure 8.5 shows the spectra coming from the separalisation of Gaussian matrix elements in the direct, exchange/pairing channels, for Gaussians with different widths (1.2 and 0.7 corresponding to the widths of the Gaussians in the Gogny DS1 potential), and different basis sizes. The ratio between the number of operations in HO-indexed loops, introduced as $O^{1D,2D,3D}_{\text{original}}$, and the number of products of eigenvalues, represents the vertical separation between the shaded and unshaded region. Thus, the interpretation of the shaded region is that it contains the largest eigenvalues (or product of eigenvalues) before the size of loops over λs surpasses the size of equivalent loops with HO quanta indices.

When performing cutoffs, we wish to select only the normalised eigenvalues which are bigger than a cutoff value, which we shall denote λ_c*. This process directly dictates the numerical precision

*In principle, one could also define the cutoff as a percentage n_c of eigenvalues to be kept. The freedom in choosing how many eigenvalues to keep makes it so that the *timing* is easily controlled. However, unlike choosing the cutoff on λ,

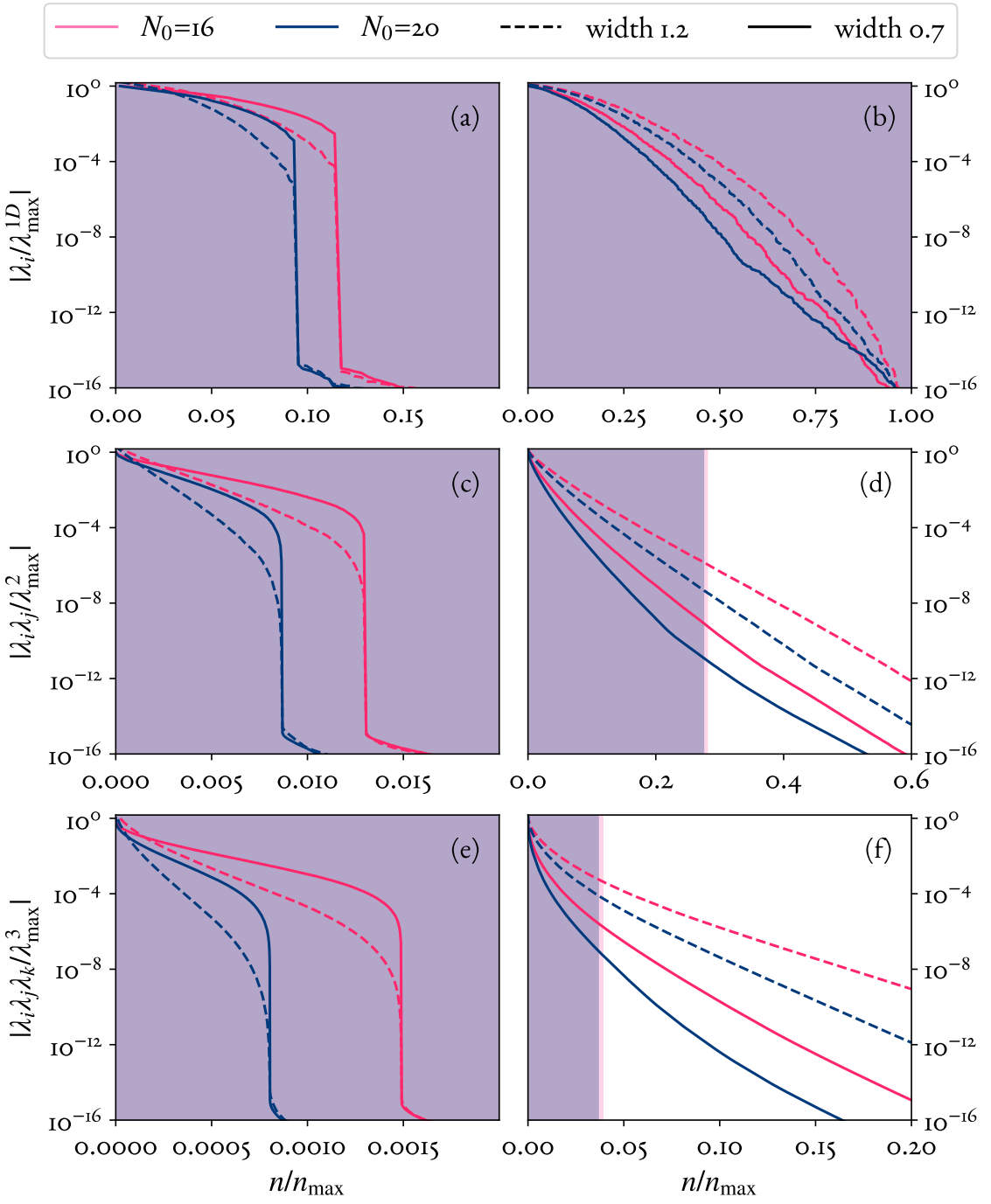


Figure 8.5: Normalised eigenvalue spectra for a product of eigenvalues in one (a,b), two (c,d), and three (e,f) Cartesian directions, for the direct (left) and exchange/pairing (right) channels. Different colors denote the spectra for different basis sizes, and different lines denote the different Gaussian widths for the Gogny DS1 potential.

it has no direct connection to the numerical precision.

of our algorithm. Moreover, as the spectra is shown in decreasing value, the ratio $n/n_{\max}$ for any specific $|\lambda/\lambda_{\max}|$ corresponds to the percentage of eigenvalues larger than $|\lambda/\lambda_{\max}|$. The left-side panels in Figure 8.5 explicitly show that, as discussed in section 8.2, very few eigenvalues are non-zero in the direct channel. The scale of these panels showcases how rapidly the direct channel spectra decays before the eigenvalues become numerically insignificant (analytically, of course, they would be exactly zero). The right-side panels, which contain the spectra for the exchange/pairing channel (which have the same absolute value $|\lambda_i|$), require a more careful analysis. The change in scale between the direct and exchange/pairing is very noticeable. For a single eigenvalue, any cutoff would represent an acceleration when compared to two loops over m, n. However, the spectra do not decay quickly enough to clearly offset the reduced number of operations coming from the pyramidal structure of the HO quanta in two and three Cartesian coordinates (in contrast to what is observed in the direct channel). To be inside the shaded region—i.e., the region of numerical advantage—one needs to keep less than ~ 28% of the eigenvalues for two Cartesian directions, or ~ 3.9% in three directions. The eigenvalue cutoff in these scenarios would depend on the basis size and Gaussian width. In the pairing/exchange channel, this would roughly correspond to keeping $|\lambda/\lambda_{\max}| < 10^{-10}$ and $|\lambda/\lambda_{\max}| < 10^{-5}$ for products of two (panel (d)) and three eigenvalues (panel (f)), respectively. We later show how these cutoffs relate to the numerical precision of our calculations in section 8.6. Lastly, an important feature of these spectra is that they decay faster for larger basis sizes, which could enable finite-range calculations to be performed in a larger basis.

8.6 Precision

The previous section helps us stipulate which λ cutoffs are numerically advantageous in comparison to the iterations with HO indices (especially in the pairing/exchange channels), but we must still analyse which ones are *reasonable* without sacrificing accuracy in our description of nuclear systems. To this end, we performed Hartree-Fock-Bogoliubov calculations for the nucleus of ^{160}Gd, with the Gogny D1S EDF. The absolute difference in the energies between the full calculation and the GSM as a function of the cutoff, λ_c, is shown in Figures 8.6 and 8.7 for bases of 16 and 20 HO shells, respectively. The range of $10^{-8} \leq \lambda_c \leq 10^{-3}$ gives us absolute energy differences between a few eV and a few MeV, respectively. The non-smooth behaviour of these curves comes from the fact that we perform cutoffs on the absolute value $|\lambda_c|$, but the sign of the remaining ℓs and remaining arrays matters, which may lead to oscillations in the precision. This is the case for both basis sizes, which can be seen in Figure 8.8, where the lines indicate the product between the energy on each channel, E_0, and the eigenvalue cutoff. This relation serves as a rough estimation of the numerical uncertainty of the method. Figure 8.9 shows the absolute energy difference for Hartree-Fock (HF) calculations of ^{208}Pb, where we can verify that this uncertainty is independent of the system and is

also valid without pairing.

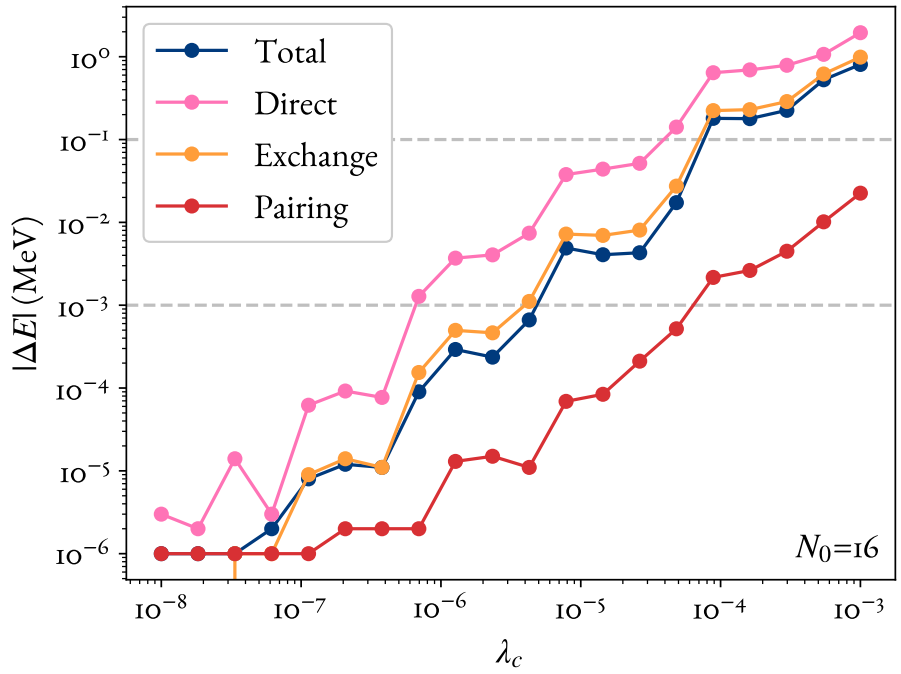


Figure 8.6: Precision of the total, direct, exchange, and pairing energies with different eigenvalue cutoffs in 16 HO shells for ^{160}Gd.

When choosing a cutoff based on precision, it is useful to analyse which range of energy precision is *useful* in a theoretical calculation. Naturally, this will vary with the user's objective. Although modern experimental mass measurements are determined to a precision of a few keV in medium-heavy nuclei, or down to eV for light and stable nuclei (Mukherjee et al. 2008; Wang et al. 2021a), theoretical calculations are usually less accurate. Fittings of EDFs are performed across the entire nuclear chart, and typical root mean square error sits at around 1.5 MeV (Bennaceur, Dobaczewski, Haverinen et al. 2020; Bertsch, Sabbey and Uusnäkki 2005). More than the residuals of EDF fittings, it is important to acknowledge the uncertainties associated with theoretical calculations, which come not only from parameter error propagation, but also from model uncertainty (McDonnell et al. 2015; Schunck et al. 2014). Of course, that is a current feature of the theory—as the form of the *real* nuclear EDF is not known—and not an imprecision of the calculations. A technical limitation of numerical calculations, on the other hand, is the constraint on basis size. Due to the nature of quantum mechanics and Hilbert spaces, the real description of quantum systems would require an infinite basis size. Numerical implementations deal with this constraint by utilising a basis which is, hopefully, large enough to capture the behaviour of a system without being computationally prohibitive. Nuclear DFT calculations typically utilise basis sizes of 16 HO

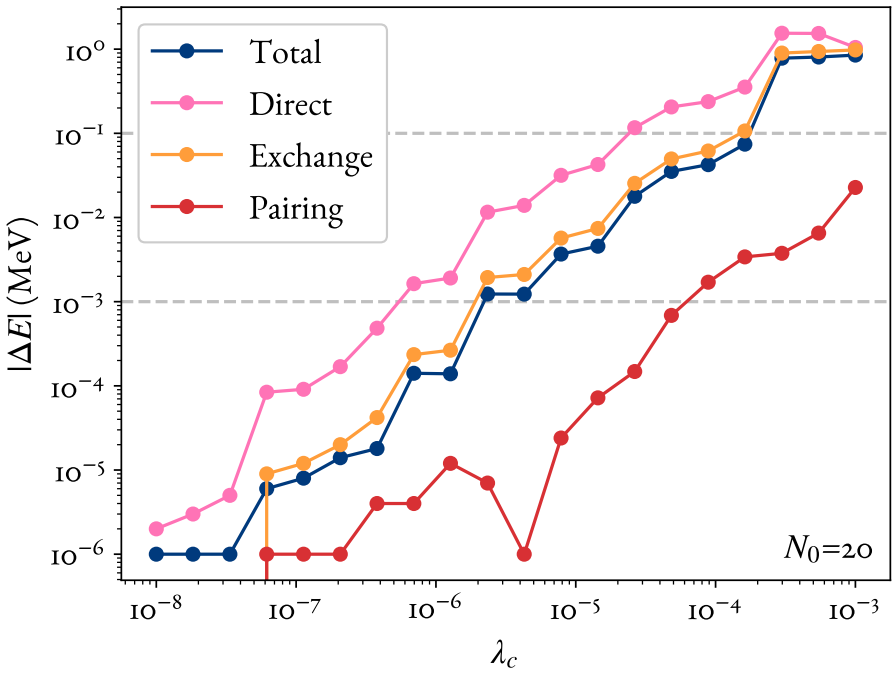


Figure 8.7: Precision of the total, direct, exchange, and pairing energies with different eigenvalue cutoffs in 20 HO shells for ^{160}Gd.

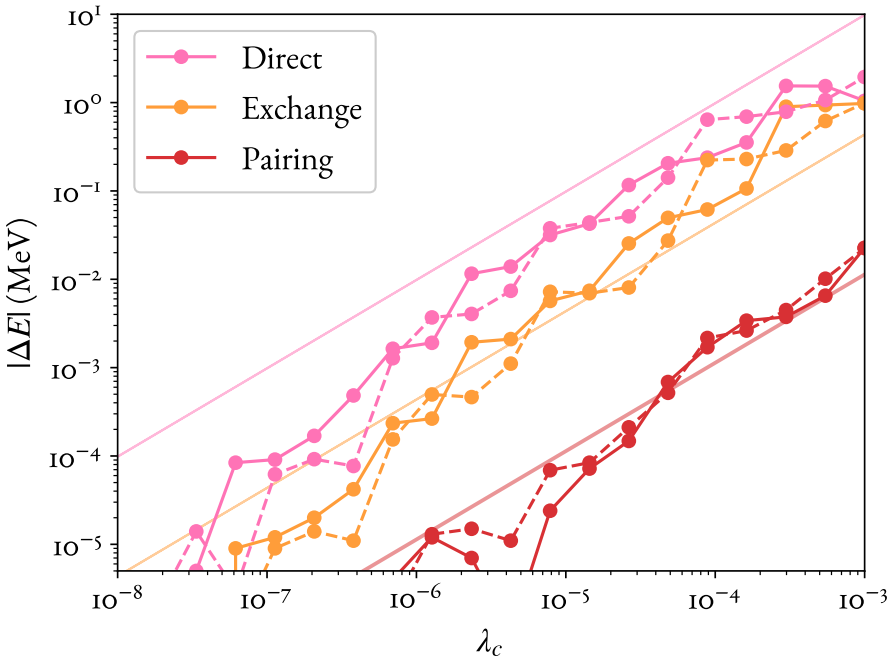


Figure 8.8: The absolute error as a function of eigenvalue cutoff for 16 (dashed lines) and 20 (full lines) HO shells, for ^{160}Gd. The lines indicate the product between the cutoff and the energy on each channel, $E\lambda_c$.

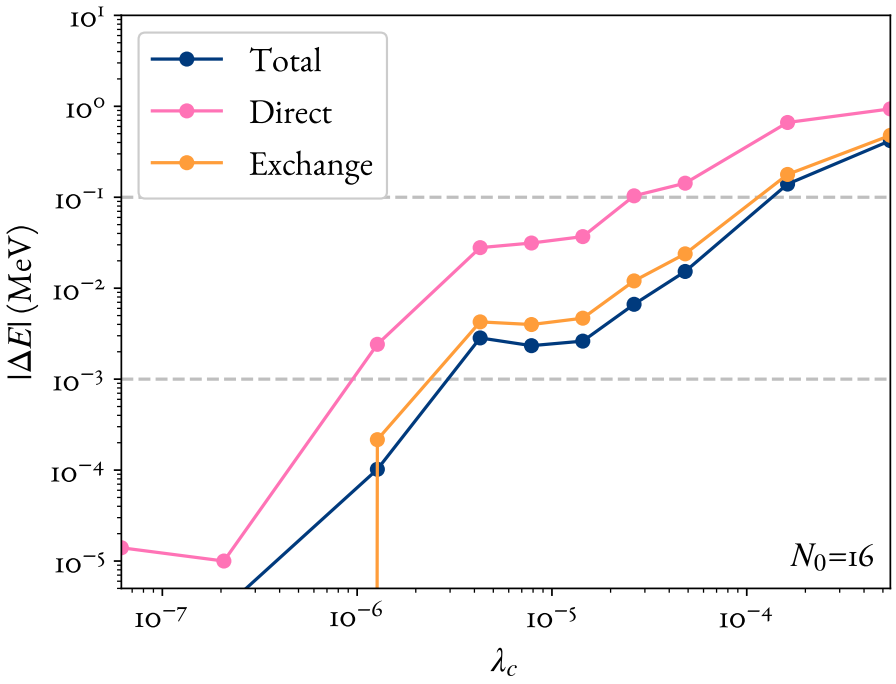


Figure 8.9: Precision of the total, direct, and exchange energies with different eigenvalue cutoffs. Results come from HF calculations in 16 HO shells for ^{208}Pb.

shells, but we highlight that for our example of ^{160}Gd, there is a difference of ~0.63 MeV between the ground state energy obtained in 20 and 16 HO shells. These remarks serve as guidelines for someone willing to utilise the method. In our precision plots, we highlighted the range between 0.1 MeV and 1 keV with a horizontal line, as we perceive them as a sweet spot for various applications of the method. Another important remark is that electromagnetic moments are not sensitive to changes in the basis parameters (Wibowo, Backes et al. 2025). Therefore, when interested in observables other than the energy, one may wish to adopt another strategy of choosing the cutoffs, which is a subject for future research.

8.7 Timing results

Lastly, we shall analyse how the same range of cutoff parameters performs numerically when compared to the traditional algorithm. The ratio between the CPU time of the GSM algorithm (T) and the traditional algorithm (T_0), per iteration of the self-consistent loop, is shown in Figures 8.10 and 8.11 for HFB calculations of ^{160}Gd in 16 and 20 HO shells, respectively. Collecting timing results is delicate, as they are sensitive to many external factors. To ensure the quality of our results, we submitted all calculations to the Viking 2 high-performance computing facility at the same

time. This helps avoid fluctuations due to different levels of activity in the cluster nodes. We also collected the time spent specifically on the GSM subroutine in HFODD, separating it by the calls for each different channel. Due to the noisy nature of timing data, we have collected the timing for 20 distinct calculations with each cutoff parameter, and averaged the results.

As the original algorithm computes the direct, exchange, and pairing energy with the same procedure, traditionally each channel is responsible for 1/3 of the total CPU time. The 1/3 threshold is marked with a horizontal line in Figures 8.10 and 8.11, and should be compared with the time for *each channel* instead of the total. In the range of cutoffs analysed, all channels show some degree of acceleration when compared to the original implementation, as they are below the threshold. Notably, the GSM time gain improves for larger bases. As the pairing and exchange channels have the same spectra, they also have the same execution time. For the range of cutoffs highlighted in the energy precision plots, computing the Gogny energy takes only ≈20%-30% of the original time in both 16 and 20 HO shells. This significantly speeds up calculations in both cases, and roughly allows for calculations in 20 HO shells within the same CPU time as the traditional algorithm executed for 16 HO shells. As we previously established, this change significantly improves the feasibility of large-scale nuclear DFT calculations.

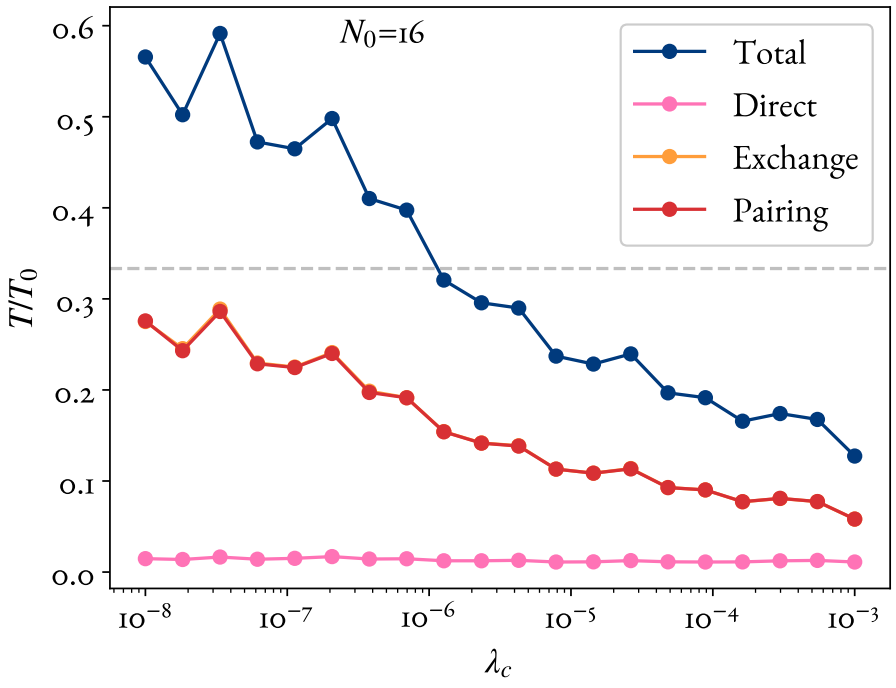


Figure 8.10: Ratio of the time per iteration with and without use of the GSM, separated between all channels and the total time for 16 HO shells in ^{160}Gd.

Finally, we also computed the execution time for HF calculations of ^{208}Pb, shown in Figure

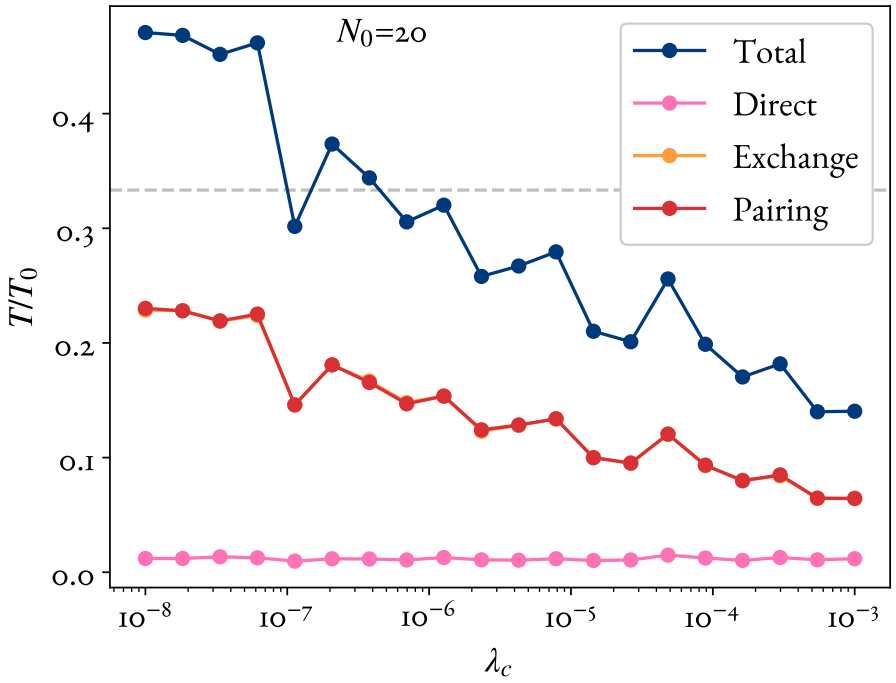


Figure 8.11: Ratio of the time per iteration with and without use of the GSM, separated between all channels and the total time for 20 HO shells in ^{160}Gd.

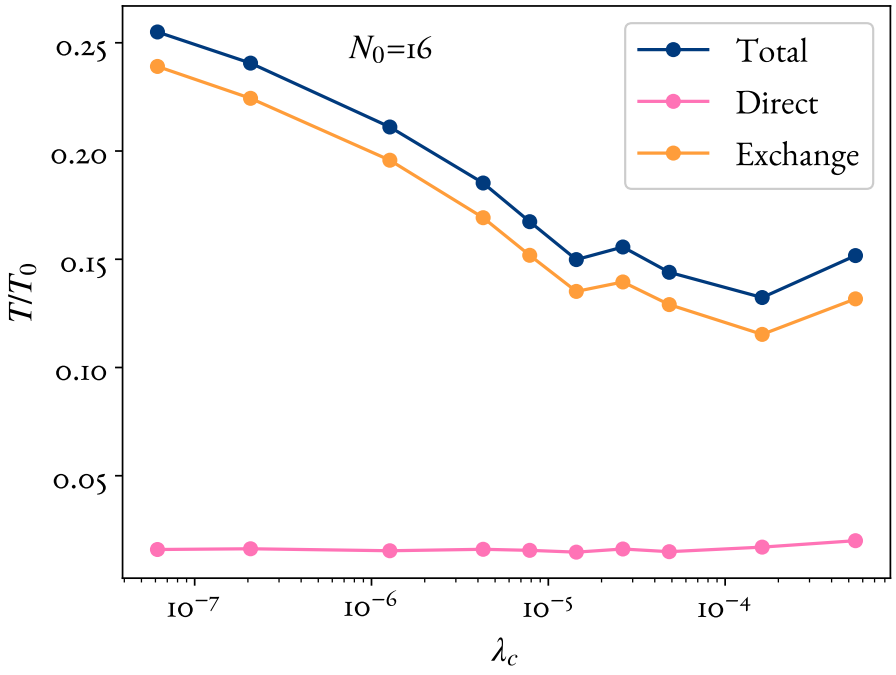


Figure 8.12: Ratio of the time per iteration with and without use of the GSM, separated between channels, and the total time, for HF calculations in 16 HO shells for ^{208}Pb.

8.12. Without any contribution from the pairing channel, the total CPU time is roughly equivalent to the time required to compute the exchange energy.

8.8 Final remarks

In this chapter, we have introduced a new algorithm for Gaussian-type finite-range functional generators in DFT. With the method introduced here, we exploit properties exclusive to Gaussian functional generators (such as their separability) and properties arising from their diagonalisation.

A technical aspect which has not yet been discussed is that of space complexity. The GSM does require more memory than the usual implementation. Technical comments on how to optimally allocate memory are included in Appendix E. However, it is worth noting that the largest arrays necessary for the method have three $(N_0 + 1)^2$ indices. This corresponds to ≈ 193 or 386MB for double- or quadruple-precision calculations in 16 HO shells, or ≈0.68 or 1.37GB for double- or quadruple-precision calculations in 20 HO shells. These are far from the most memory-expensive arrays necessary in a nuclear DFT calculation. As the constraint we are trying to mitigate is the *time* cost of finite-range calculations, this is a fair trade-off.

The new algorithm has the potential to be crucial for applications in nuclear DFT, including fission, many-body moments, and new finite-range functionals. All tests were performed with the code HFODD (Dobaczewski et al. 2026), version 333u. The version of the code and numerical results discussed in this chapter are available online (Backes 2026).

Nine

Hybrid neutron stars: equation of state, phase transition, and radial oscillations

This chapter provides a brief introduction to the research on determining the composition of neutron stars, some of the most extreme objects in the universe. We shall understand how microscopic nuclear physics is combined with general relativity to obtain macroscopic properties of stars. We shall understand how nuclear and hadronic effective models can be used to determine the Quantum Chromodynamics (QCD) phase transition at high densities, and how those can be used to describe hybrid stars composed of hadronic external layers followed by a quark matter core. We will briefly introduce the findings of a study on the radial oscillation of hybrid stars using this methodology.

> Toto, I have a feeling we're not in Kansas anymore.
>
> Dorothy (Judy Garland) in *The Wizard of Oz*.

> "[...] when the density of matter becomes so great that atomic nuclei come in close contact, forming one gigantic nucleus."
>
> Landau 1932

Throughout this thesis, I have explored various facets of nuclear physics: from how pairing manifests in infinite nuclear matter, to its effects on magnetic moments of nuclei and on isospin symmetry studies, and to computational aspects of high-fidelity nuclear DFT calculations. This chapter takes the subject of nuclear physics in yet another direction*. As demonstrated in Chapter 4, the connection between finite and infinite systems is not always straightforward. Nevertheless, we know that an "infinite" nucleus-like system exists in nature, in the form of a stellar remnant: the neutron star (NS). As NSs are composed mostly of strongly-interacting matter, they have been a crucial part of high-energy nuclear and hadron astrophysics research (Glendenning 1997; Menezes

*Although some would contest the use of the word "nuclear" in this sentence.

2021). Despite having the same basic constituents as other nuclear systems (at least in principle), NSs are extreme objects whose magnetic and gravitational fields are stronger than those of any other systems, aside from black holes, and whose interior may be an order of magnitude more dense than the nuclear saturation density* (n_0). A rigorous description of their properties covers a plethora of areas of physics: electromagnetism, general relativity, nuclear and hadron physics, quantum mechanics, statistical mechanics, thermodynamics, condensed matter, and others. Beyond the technical challenges, however, stands a unique opportunity to explore what happens to strongly interacting matter under extreme conditions.

From the side of nuclear and hadron physics, one can start from a model for the equation of state (EoS)—a relationship between state variables, which determines how a system behaves for different conditions, typically a pressure and energy density curve for this context—and obtain different macroscopic properties of stars, such as their masses and radii. Due to the difficulties of solving QCD, however, very little is known about the actual constitution of neutron stars, especially at higher densities closer to the core of the star. Effective models have then established themselves as a crucial part of investigating dense nuclear matter, from which the masses and radii can be compared to astrophysical data (Glendenning 1997). These models can vary from including merely protons and neutrons, to many other hadrons—i.e., composite objects made of two or more quarks, and confined due to the strong interaction—, and even a deconfined quark phase. A step further from masses and radii, the breakthrough of the LIGO and Virgo collaborations in detecting gravitational waves from a binary neutron star merger (Abbott, Abbott et al. 2017, 2018) started a new era for multimessenger astronomy data. Specifically, gravitational wave data from binary NS mergers can help constrain the EoS of dense nuclear matter, giving insight into the actual composition of these objects (Piekarewicz, Jorge 2024).

Such a hadron-physics-focused topic may appear unrelated to that of the previous chapters, apart from the direct connections to the topic of nuclear matter (NM). However, this "bonus chapter" is a work that I developed during the last years independently from my core PhD research, and that has been both published (see Rather, Marquez, Backes et al. 2024) and holds a strong emotional value to me. Kau Marquez was a master's degree student when I started my first undergraduate internship in the Nuclear and Hadron physics group in Brazil, and was one of the reasons I chose this area of research. With her sharp physics instinct and unmatched sense of humour, she became not only one of my favourite people to work with and discuss physics, but also a very close friend. In 2023 she contacted me to continue our collaboration, and I was thrilled. This chapter is about the work we developed together that year, describing hybrid stars with density-dependent

*The nuclear saturation density corresponds to the density at which the energy density curve of infinite nuclear matter is minimised, which is ~ 0.16 fm^{-3} (Roca-Maza and Paar 2018). This is similar to the average density of heavy nuclei.

equation of state models and observing how the deconfinement phase transition impacts the radial oscillations of colliding stars. We planned many collaborations and encounters for the future, so it never crossed my mind that this work would be our last one. Kau prematurely passed away at the beginning of 2025, at the early age of 30, but I will always carry a part of her with me. With much love and a broken heart, I hope this chapter can honour the last time we adventured together through hadron physics, and above anything, share with the readers a part of the fascination we both had for this area of research.

9.1 A very brief introduction to NS EoS physics

From the point of view of the standard model, QCD is the quantum field theory responsible for explaining the interaction between quarks through gluons. The Lagrangian density that describes the dynamics of strongly-interacting particles is

$$\mathscr{L}_{\mathrm{QCD}} = \sum_f \bar{\Psi}_f \left[i\gamma^\mu \left(\partial_\mu + igA^\alpha_\mu t_\alpha \right) - m_f \right] \Psi_f - \frac{1}{4} G^\alpha_{\mu\nu} G^{\mu\nu}_\alpha, \tag{9.1.1}$$

where f are the six quark flavours (u, d, s, t, b, c), A is the gluon vector field with $\alpha = 1, ..., 8$, μ and ν are the four-coordinates, Ψ_f are the quarks' Dirac spinors, G is the field tensor, which couples the vector fields as

$$G^{\mu\nu}_\alpha = \partial^\mu A^\nu_\alpha - \partial^\nu A^\mu_\alpha - g f^{\alpha\beta\gamma} A^\mu_\beta A^\nu_\gamma, \tag{9.1.2}$$

t_α are the Gell-Mann matrices, $f^{\alpha\beta\gamma}$ are the structure constants, and g is the colour charge (Greiner, Schramm and Stein 2007; Schunck 2019). The last term of eq. (9.1.2) shows that gluons interact with each other, as they carry colour. In contrast to the simpler quantum field theory of quantum electrodynamics, where photons *do not* directly interact with each other (as they are charge-neutral), the self-interaction between gluons is what makes QCD—and thus nuclear physics—so complicated.

Due to the analytical challenges of QCD, there is no unified way of describing strongly interacting matter. As a consequence, different energy regimes take different theoretical approaches, and are accessible through different experiments or observations. Figure 9.1 depicts a conjectured QCD phase diagram in terms of isospin asymmetry, density, and temperature. At low densities and temperatures (green-shaded region of the diagram), we have nuclei as described in the previous chapters of this thesis. These "terrestrial" conditions allow information—such as nuclear shapes and energies—to be drawn from experiments, which fuel the advancement of theoretical approaches such as density functional theory and *ab initio* nuclear theory. At low densities and high temperatures, results from lattice quantum chromodynamics (LQCD), a non-perturbative

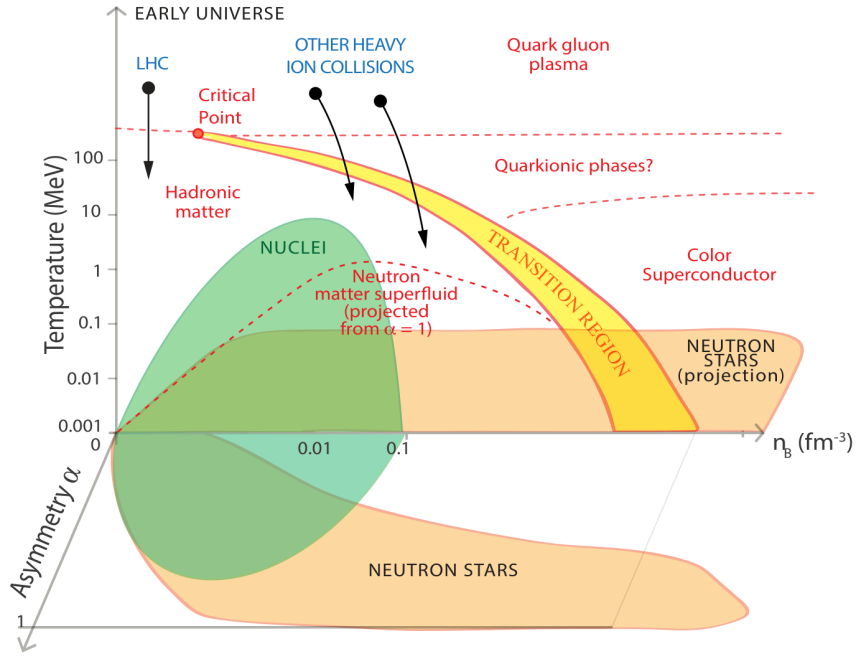


Figure 9.1: Conjectured QCD phase diagram. Reproduced from Watts et al. 2014.

approach which solves the dynamics for quarks and gluons on a grid, offer a true *ab initio* perspective on nuclear matter. This region of the diagram is also accessible to particle colliders, such as the Large Hadron Collider. What is observed in this region is that there is a phase transition between confined hadrons and the quark gluon plasma, which LQCD predicts to be a crossover* (Aoki et al. 2009; Bazavov et al. 2012). In the regime of very dense QCD, perturbative approaches also tell us about how matter should behave asymptotically. In the remaining parts of the diagram, we heavily rely on hadron and quark effective models for a theoretical description. These models often come attached to coupling constants that are not easily fixed, and extracting precise information from dense and hot heavy-ion collisions or astrophysical data is not always straightforward. This generates somewhat of a *terra incognita* on the diagram, where some phases are still only speculated, and it is not trivial to draw a line on where there should be a phase transition between confined and deconfined nuclear matter. The phase transition at high densities is predicted to be of first order—in contrast to the crossover at lower densities—which would indicate the existence of a critical end point, which is an active area of research (Du, Sorensen and Stephanov 2024; Pandav, Mallick and Mohanty 2022; Stephanov 2024). Notoriously, neutron stars live in the regime of cold and dense matter (orange-shaded region of the diagram), which coincides with this uncertainty. This has

*A type of transition on which the properties of the system change smoothly rather than sharply.

been a strong driver of NSs as a tool to understand nuclear matter under extreme conditions.

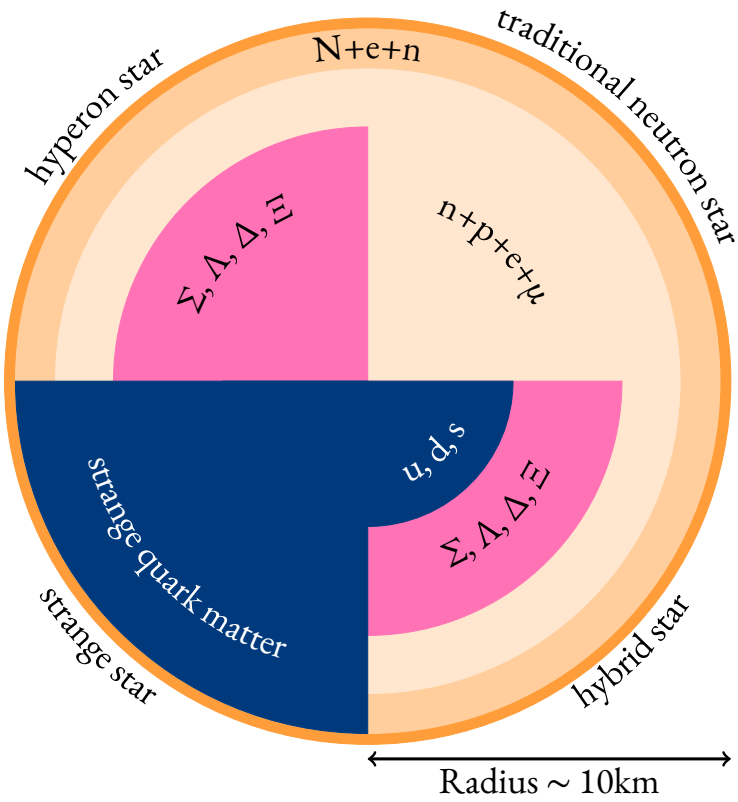


Figure 9.2: Illustration of different possible neutron star compositions.

Historically, discoveries in nuclear—and hadron—physics have been directly linked to our understanding of compact stars: the proposition of a compact object composed of NM predates the discovery of the neutron (Landau 1932), and only gained traction after Chadwick 1932 discovered the neutron, as a nucleon with neutral charge made the idea ever more possible (Baade and Zwicky 1934). Over the decades, the discovery of new hadrons led to new suggestions about the composition of compact stars (Glendenning 1997), such that despite the misleading name of "neutron star", what these dense stellar remnants are *actually* made of is an active area of nuclear astrophysics research (Burgio et al. 2021; Menezes 2021). Figure 9.2 shows some of the different hypotheses for the constitution of NSs, where we highlight the possibility of a *hybrid* star, i.e., a star composed of hadrons on its most external layers, but that undergoes a phase transition into a deconfined quark core. A model-independent analysis—which interpolates equations of state between the limits of Chiral Effective Field Theory (χEFT) and perturbative QCD—suggests that a quark core should be the standard when describing massive NSs, not an exotic alternative (Annala, Gorda, Kurkela et al. 2020). The theoretical framework we introduce in the next section serves the

purpose of describing such hybrid stars.

As previously mentioned, these stars exist around a region of uncertainty in the QCD phase diagram. The most common theoretical approach for hadron matter is that of relativistic mean-field (RMF) models, which typically emulate the strong interaction among hadrons through virtual meson exchanges[*]. One has the freedom to account for different interacting hadrons and virtual mesons, each described by different Lagrangian densities. This type of approach is generally referred to as Walecka-type models due to the prominent work of Walecka 1974. Some of the "exotic" degrees of freedom included in the EoS are hyperons (hadrons which include at least one strange quark), kaons, and delta baryons (Δ). Although one would expect the formation of hyperons from energy-related considerations, they soften the hadronic EoS[†], which reduces the maximum mass predicted for NSs. This contradicts astronomical observations, leading to the so-called *hyperon puzzle* (Bombaci 2017). Sections 9.2 and 9.3 explicitly discuss aspects of the hybrid EoS, and the next subsection provides a brief overview of the bridge between nuclear theory and observational astrophysics.

9.1.1 Uniting the micro- and macro-physics

Due to the intense gravitational field, Newtonian gravity does not suffice to describe NSs, and one must use general relativity. Expressions for relativistic hydrostatic equilibrium of a static and spherically symmetric star come from solving the Einstein field equation, and are known as the Tolman-Oppenheimer-Volkoff (TOV) equations (Oppenheimer and Volkoff 1939; Tolman 1939)

$$\frac{dP(r)}{dr} = -\frac{[\mathscr{E}(r) + P(r)][m(r) + 4\pi r^3 P(r)]}{r^2(1 - 2m(r)/r)}, \tag{9.1.3}$$

$$\frac{dm(r)}{dr} = 4\pi r^2 \mathscr{E}(r), \tag{9.1.4}$$

where $\mathscr{E}$ is the energy density, and P is the pressure. For a given EoS—i.e., $P(\mathscr{E})$—the TOV equations can be solved for the initial conditions $m(r = 0) = 0$ and $P(r = 0) = P_c$, where P_c is the central pressure. The radius of the star is determined by requiring that the pressure vanishes at the surface, $P(R) = 0$, and the mass of the star is then given by $M = m(R)$. This gives a *mass-radius* curve for each EoS, which can be used as comparison with observational data. Beyond the TOV results, this new and upcoming era of multi-messenger astronomy allows for detailed information about the composition to be drawn from binary NS mergers. Derivations about radial oscillations of colliding stars can be found in the original publication of this work (Rather, Marquez, Backes et al. 2024) and references therein. The general relativity aspects of our calculations were led by Ishfaq Rather, the leading author.

[*]These phenomenological models are also said to be in the *relativistic Hartree* approximation, where the meson fields are taken to have a constant average value, without fluctuations.

[†]"Softening" the EoS means decreasing the pressure of the system for the same energy density.

9.2 The density-dependent equation of state

The intrinsic mathematical difficulties of QCD are behind all models which ignore the quark structure of hadrons, utilising composite particles as the primary degrees of freedom in the system*. We previously mentioned the flexibility of RMF models. Not only is there freedom to choose which hadrons to include in a model, but also freedom on how many mesons would be responsible for the interaction. All of these possibilities come with a set of coupling constants, which should then be adjusted to empirical data. This gives rise to an incredibly vast collection of possible adjustments (i.e., models). An analysis of 263 RMF models available in the literature has shown that less than 40 accurately describe nuclear bulk properties (Dutra et al. 2014). Notably, density-dependent RMF models are some of the most successful. This is interesting, as three-body forces are proposed as a potential solution to the hyperon puzzle (Gerstung, Kaiser and Weise 2020; Lonardoni et al. 2015), and effective density-dependence can be interpreted as a three-body interaction (Haidenbauer et al. 2017). We shall now briefly review the density-dependent quark and hadron models we utilised in this work.

9.2.1 Deconfined quark matter

We chose the density-dependent quark mass (DDQM) model to describe quark matter, which is a simple and versatile model Kau and I previously utilised to study the deconfinement phase transition (Backes, Marquezb and Menezes 2021), making it a good fit for our investigation of hybrid stars. For a complete overview of this model, see Backes, Hafemann et al. 2021. Within this model, we emulate confinement by the density dependence introduced in the quark masses as

$$m_i = m_{i0} + \frac{D}{n_B^{1/3}} + C n_B^{1/3} = m_{i0} + m_I, \tag{9.2.1}$$

where m_{i0} ($i = u, d, s$) is the current mass of the ith quark, n_B is the baryon number density, and m_I is the density-dependent term responsible for the interaction between quarks. The model has two free parameters: D, which dictates linear confinement; and C, which is responsible for leading-order perturbative interactions. Introducing a new dependence on the state variables—such as density, temperature, or magnetic field—notoriously breaks thermodynamic consistency, i.e., your EoS becomes incompatible with the laws of thermodynamics. One way of circumventing this problem is to introduce effective variables, which return the model to a thermodynamically consistent EoS (Xia et al. 2014). To this end, at zero temperature, we start from the differential fundamental relation

$$\mathrm{d}\mathscr{E} = \sum_i \mu_i \mathrm{d}n_i, \tag{9.2.2}$$

*Notably, we followed this prescription throughout this thesis.

where $\mathscr{E}$ is the energy density of the system, μ_i are the particles' chemical potentials, and n_i are the particle densities. We can then introduce effective chemical potentials to the model, such that the energy density can be viewed as the one for a free system with particle masses $m_i(n_B)$ and effective chemical potentials μ_i^*

$$\mathscr{E} = \Omega_0(\{\mu_i^*\}, \{m_i\}) + \sum_i \mu_i^* n_i, \tag{9.2.3}$$

where Ω_0 is the thermodynamic potential of a free system. The differential form of eq. (9.2.3) is

$$\mathrm{d}\mathscr{E} = \mathrm{d}\Omega_0 + \sum_i \mu_i^* \mathrm{d}n_i + \sum_i n_i \mathrm{d}\mu_i^*. \tag{9.2.4}$$

Explicitly, we can write $\mathrm{d}\Omega_0$ as

$$\mathrm{d}\Omega_0 = \sum_i \frac{\partial \Omega_0}{\partial \mu_i^*} \mathrm{d}\mu_i^* + \sum_i \frac{\partial \Omega_0}{\partial m_i} \mathrm{d}m_i \tag{9.2.5}$$

with

$$\mathrm{d}m_i = \sum_j \frac{\partial m_i}{\partial n_j} \mathrm{d}n_j, \tag{9.2.6}$$

where the densities are connected to the effective chemical potentials by

$$n_i = -\frac{\partial \Omega_0}{\partial \mu_i^*}. \tag{9.2.7}$$

Equation (9.2.4) can then be rewritten as

$$\mathrm{d}\mathscr{E} = \sum_i \left(\mu_i^* + \sum_j \frac{\partial \Omega_0}{\partial m_j} \frac{\partial m_j}{\partial n_i} \right) \mathrm{d}n_i, \tag{9.2.8}$$

which should be consistent with the fundamental equation. Finally, comparing eqs. (9.2.2) and (9.2.8) gives the relation between the real and effective chemical potentials

$$\mu_i = \mu_i^* + \sum_j \frac{\partial \Omega_0}{\partial m_j} \frac{\partial m_j}{\partial n_i}. \tag{9.2.9}$$

It immediately follows that the pressure, P, is then given by

$$\begin{aligned} P &= -\mathscr{E} + \sum_i \mu_i n_i && (9.2.10) \\ &= -\Omega_0 + \sum_i (\mu_i - \mu_i^*) n_i \\ &= -\Omega_0 + \sum_{i,j} \frac{\partial \Omega_0}{\partial m_j} n_i \frac{\partial m_j}{\partial n_i}, && (9.2.11) \end{aligned}$$

which is the thermodynamically consistent EoS, that is determined for different densities and chemical potentials. For the case of quark matter in stars, these are constrained to fulfill β-equilibrium

and charge neutrality. During the cooling of a NS following a supernova, the initial energy is lost via neutrino emission, which is called the Urca process

$$d, s \leftrightarrow u + e + \bar{\nu}_e, \tag{9.2.12}$$

such that after the cooling, the chemical potentials must satisfy

$$\mu_d = \mu_s = \mu_u + \mu_e. \tag{9.2.13}$$

Charge neutrality, on the other hand, requires that

$$\frac{2}{3}n_u - \frac{1}{3}n_d - \frac{1}{3}n_s - n_e = 0. \tag{9.2.14}$$

From these conditions, one must define the densities and chemical potentials for each baryonic density, $n_b = \sum_q n_q$. This allows us to determine the curve $P(\mathscr{E})$ necessary for the TOV equations.

9.2.2 Hadronic matter

The RMF model of choice introduces the density dependence in the meson-nucleon coupling constants. For this study, we chose to investigate different constituents for the EoS. Specifically, we evaluated the phase transition to quark matter following from a hadronic phase composed of only nucleons (N), nucleons and delta baryons (N+Δ), nucleons and hyperons (N+H), and nucleons, hyperons, and deltas (N+H+Δ). Recent experimental effort to constrain the coupling constants between Δ baryons and nucleons indicates that Δs may be present in neutron stars (Li, Sedrakian and Weber 2018; Lopes, Marquez and Menezes 2023; Malfatti et al. 2020; Marquez et al. 2022; Raduta 2021; Xiang and Hua 2003). Furthermore, Δ baryons are only ≈30% heavier than nucleons (m_Δ = 1232 MeV and m_n = 939 MeV), and are lighter than some hyperons included in the octet (the mass of Ξ hyperons is m_Ξ = 1315 MeV). Therefore, they could appear in NSs at densities around 2-3n_0, similar to where hyperons are predicted to appear. The interplay between Δ baryons and hyperons is, therefore, a very interesting aspect of neutron star EoS studies, as both are expected to be a substantial portion of the constituents and have a significant impact on the stars' properties.

The EoS for RMF models is typically obtained from a Lagrangian density. Specifically, one obtains the energy-momentum tensor from the Lagrangian, and different components of this tensor give the pressure and energy density. The Lagrangian density and all expressions for the EoS for the model employed are listed in Rather, Marquez, Panotopoulos et al. 2023, and a more pedagogical review can be found in the PhD thesis of Marquez 2022.

9.3 Deconfinement phase transition

As previously mentioned, the hadron-quark phase transition at high densities is assumed to be of first-order. For such transitions, we obtain a coexistence point for the two phases by matching the

EoS of both phases according to the Gibbs criteria,

$$\begin{aligned} P^{(i)} &= P^{(f)} = P_0, \\ \mu^{(i)}(P_0) &= \mu^{(f)}(P_0) = \mu_0, \end{aligned} \tag{9.3.1}$$

which determines the transition between the initial (i) and final (f) homogeneous phases, both at $T = 0$ MeV, with

$$\mu^{(i,f)} = \frac{\mathscr{E}^{(i,f)} + P^{(i,f)}}{n_B^{(i,f)}}, \tag{9.3.2}$$

where $\mathscr{E}^{(i,f)}$, $P^{(i,f)}$ and $n_B^{(i,f)}$ are the total energy density, pressure and baryon number density, obtained from the effective models of each phase. Note that the transition occurs at a constant pressure. This causes a discontinuity in the density of the system, which goes from the hadronic phase to a denser quark phase, with the interface of both being at the same pressure. From the criteria above, P_0 and μ_0 are determined from the equations of state of both phases. This formulation for the phase transition is commonly referred to as a *Maxwell* phase transition (Glendenning 1997). Other formulations, such as the Gibbs phase transition, impose charge neutrality and β-equilibrium in the coexistence point, leading to a finite density transition instead of a discontinuity.

9.4 Some results

The results coming from this work are extensive, especially those coming from the analysis of radial oscillations. Although I did partake in the analysis of all results, this topic is rather different from that of all other chapters in this thesis. Therefore, readers are referred to the manuscript of Rather, Marquez, Backes et al. 2024 for the complete set of results, including oscillation modes, tidal deformability, and the speed of sound. We shall present here merely simple analyses coming from the EoS.

Figure 9.3 shows the charge-neutral EoS in β-equilibrium, consisting of the variation of pressure with the energy density of the system. Different hadron compositions were utilised, as well as two different sets of density-dependent quark mass (DDQM) parameters. The horizontal lines—zones of constant pressure—correspond to the first-order phase transition. The most important things to note are that the presence of Δ baryons (red and blue curves) corresponds to the two softest EoS—i.e., the system is at lower pressures for the same energy density—while the pure nucleonic and N+H curves are harder. The different compositions impact the coexistence pressure dramatically. As the Δs soften the EoS, the coexistence point then happens at higher pressures. This is an important aspect, should quark matter indeed be required to exist in massive stars as suggested by Annala, Gorda, Kurkela et al. 2020. After the phase transition, the EoS becomes that of deconfined quark matter. As we considered two sets of DDQM parameters, this corresponds to

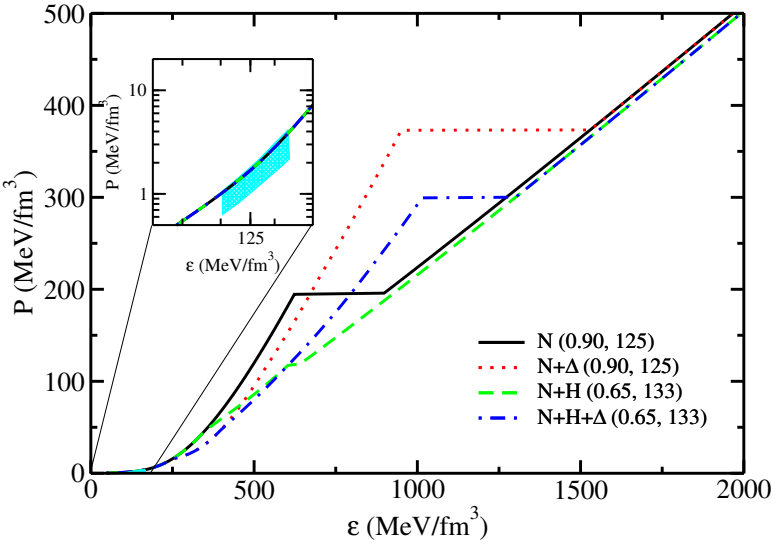


Figure 9.3: Energy density and pressure variation for the N (solid lines), N+Δ (dotted lines), N+H (dashed lines), and N+H+Δ (dot-dashed lines) DD-RMF EoS for α_v = 1.0 with a phase transition to the quark matter at parameter values $(C, D^{1/2})$ = (0.90, 125 MeV) for N and N+Δ EoS and $(C, D^{1/2})$ = (0.65, 133 MeV) for N+H and N+H+Δ EoS. The inset represents the EoS at low density with constraints from chiral effective field theory (Hebeler et al. 2013). Reproduced from Rather, Marquez, Backes et al. 2024.

the two lines observed at high energies. The light blue shaded region of the inset corresponds to constraints from χEFT, which are satisfied for all EoS considered (Hebeler et al. 2013).

Figure 9.4 shows the particle populations for all hybrid EoS. The shaded region corresponds to the aforementioned density discontinuity, where the Δs are included in the right panels, and the hyperons in the bottom panels. By comparing the left and right panels, we can observe how Δ baryons move the coexistence point towards higher densities. The bottom two panels also show that Δs suppress some of the hyperons, as Σ^- are not present in the bottom right panel. One can also observe that the presence of Δ baryons increases the difference between the densities of the two phases.

Lastly, Figure 9.5 shows the mass-radius profile obtained when integrating the TOV equations with the four hybrid EoS we considered in this work, compared to the available observational measurements. As the EoS with Δ baryons are much softer, the maximum stellar masses obtained with N+Δ and N+H+Δ are smaller than those of the other two cases. Specifically, for an N-only hybrid star, the maximum mass is 2.30 $M_\odot$ with a radius of 13.03 km. For N+Δ, this shifts to 2.25 $M_\odot$ and 11.80 km. For N+H, the maximum mass is 1.97 $M_\odot$ with a radius of 12.47 km. Lastly, the N+H+Δ EoS gives a maximum mass of 1.98 $M_\odot$ with an 11.57 km radius. This illustrates the hyperon puzzle to those unfamiliar with it, as recent NS observations point towards masses larger than $\approx 2M_\odot$. Despite that, the hybrid EoS were still in agreement with many of the constraints.

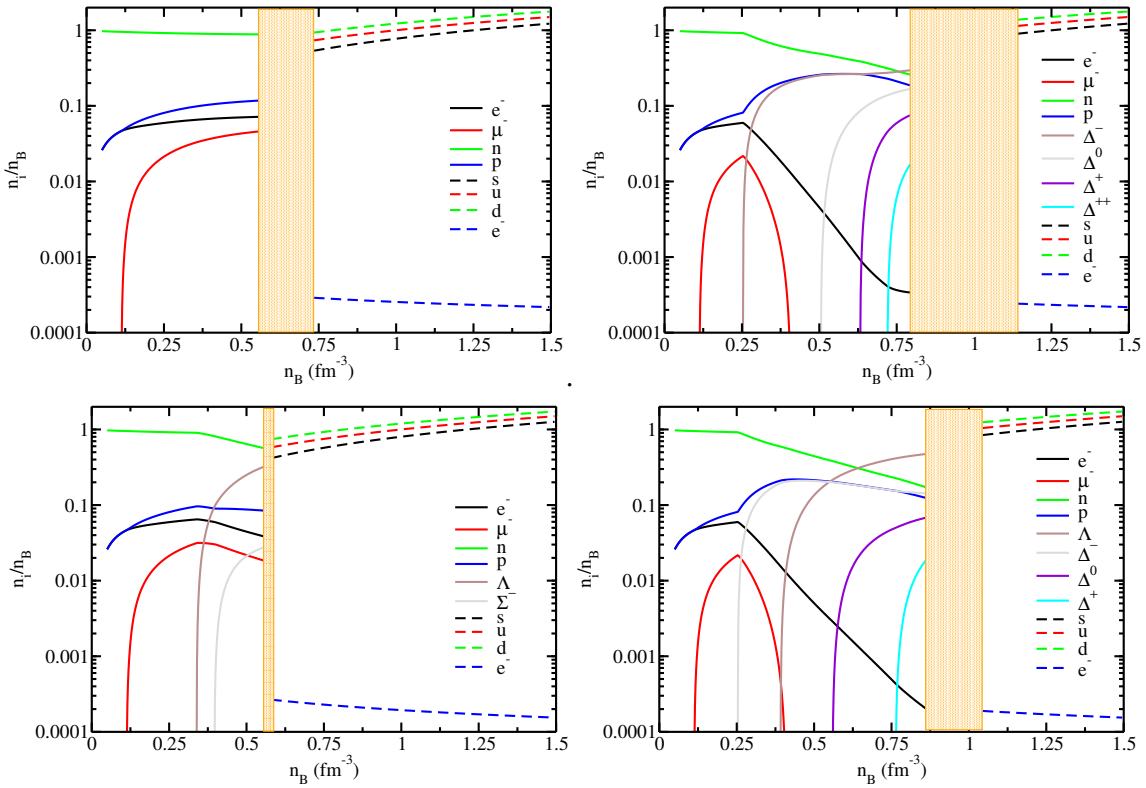


Figure 9.4: Particle population for different hybrid EoS: N (top left), N+Δ (top right), N+H (bottom left), N+H+Δ (bottom right). The solid lines represent baryons while the dashed lines represent the quark fractions. The shaded region (orange) represents the density discontinuity gap between both parts of the EoS. Reproduced from Rather, Marquez, Backes et al. 2024.

9.5 Final remarks

In this chapter, I have introduced basic aspects of hadron theory research towards understanding the neutron star equation of state. This branch of nuclear astrophysics is a rich area of study, with many unique opportunities for detailed information to be accessible from gravitational waves in the coming years. Until then, the different theoretical models are key to understanding how the different compositions impact each observable. This work serves as an example of how properties of stars are heavily impacted by what happens to strongly interacting matter at high densities, one of the most uncertain regions of the QCD phase diagram. Lastly, nuclear theory and experiment are directly fed into RMF models, connected by the fact that all systems we study are under the umbrella of the strong interaction.

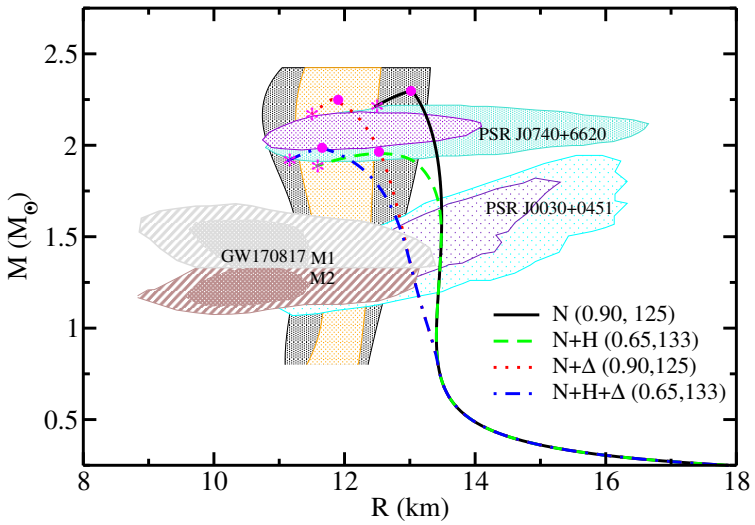


Figure 9.5: Mass-radius profile for DD-RMF parameter set with different compositions of Δ baryons and hyperons along with a phase transition to the quark matter at parameter values $(C, D^{1/2})$ = (0.90, 125 MeV) for N and N+Δ EoS and $(C, D^{1/2})$ = (0.65, 133 MeV) for N+H and N+H+Δ EoS. The 68% (violet) and 95% (turquoise) credible regions for mass and radius are inferred from the analysis of PSR J0740+6620 (Miller et al. 2021; Riley et al. 2021). For PSR J0030+0451, the indigo dotted region is for 68% credibility while the green dotted region is for 95% credibility (Miller *et al.* 2019). The grey upper (brown lower) shaded region corresponds to the higher (smaller) component of the GW170817 event (Abbott, Abbott et al. 2018). The joint constraints from HIC experiments and multimessenger astrophysics with 68% (orange) and 95% (black) credible ranges are also shown (Huth et al. 2022). Reproduced from Rather, Marquez, Backes et al. 2024.

Ten

Conclusions and perspectives

In this thesis, we utilised the versatile framework of nuclear density functional theory (DFT) to assess different questions in nuclear theory.

- We derived the most general pairing tensor for infinite nuclear matter, starting from the general wavefunction of a pairing condensate. We have explicitly shown that proton-neutron channels are mixed in the pairing tensor and density matrix of infinite nuclear matter, and that the relationship between the pairing tensor and the wavefunction cannot be taken for granted in the nuclear infinite system.

- We scrutinised the adequacy of adjusted pairing strengths in the region of Sn-Gd. Even though the magnetic dipole moment is heavily influenced by single-particle properties, discrepancies between nuclear DFT calculations and experimental data cannot be attributed to a poor adjustment of pairing. We also introduced contributions from two-body magnetic dipole moments for DFT calculations, a work in progress.

- The vicinity of the $N = Z$ line offers unique opportunities to test nuclear models and the degree of isospin symmetry breaking in nuclei, especially as experiments are able to access progressively heavier nuclei close to the proton drip line. We have explicitly shown that when isospin-symmetry tests are concerned, the $T_z = 0, T = 1$ nuclei do not correspond to the doubly blocked wave-function, but rather a coherent superposition of the blocked $T = 1$ proton-neutron pairs atop the even-even quasiparticle vacua. We employed a mean-field approach with symmetry restoration to show that $B(E2\downarrow)$ values for the odd-odd $T_z = 0$ nuclei of ^{70}Br and ^{78}Y in doubly-blocked configurations do not align with the expectation for isospin symmetry. We also showed that collective effects are crucial for describing experimental data near the $N = Z$ line. Lastly, our results challenge experimental analysis, showing that it is possible to interpret the available $B(E2)$ data without invoking explicit beyond-Coulomb isospin symmetry-breaking corrections.

- We introduced the Gaussian Separalisation Method (GSM), an algorithm which exploits properties specific to Gaussian matrix elements to accelerate DFT calculations of finite-range interactions. The implementation reduces the CPU time by $\approx 60 - 90\%$ without sacrificing numerical precision. The GSM has the potential to be crucial for many applications of nuclear DFT, including calculations of fission, many-body moments, and new finite-range functional generators.
- Lastly, we also briefly introduced a work on the equation of state of neutron stars, an area of vibrant progress in the era of multi-messenger astronomy.

The works introduced in this thesis also opened many new research questions. Crucial aspects are:

- What is the quantitative impact of proton-neutron mixing in adjusting new energy density functionals, and in bulk properties of nuclear matter?
- Do nuclear structure calculations including proton-neutron pairing accurately follow the expected trend for the conservation of isospin symmetry in $T = 1$ triplets?
- What are the consequences of the GSM to other observables? How much does the timing improve in problems of many Gaussian matrix elements?

These remaining questions shall be addressed over time. Notably, addressing proton-neutron pairing in the nuclear structure code HFODD would require a careful implementation, especially towards the mixing of protons and neutrons.

Part IV

Appendices

A

The coupled ST representation

The ST basis has four quantum numbers SS_zTT_z:

$$|SS_zTT_z\rangle = \sum_{s's t't=\pm 1/2} C^{SS_z}_{\frac{1}{2}s'\frac{1}{2}s} C^{TT_z}_{\frac{1}{2}t'\frac{1}{2}t} |\tfrac{1}{2}s'\tfrac{1}{2}t'\rangle|\tfrac{1}{2}s\tfrac{1}{2}t\rangle, \tag{A.0.1}$$

$$|\tfrac{1}{2}s'\tfrac{1}{2}t'\rangle|\tfrac{1}{2}s\tfrac{1}{2}t\rangle = \sum_{SS_zTT_z} C^{SS_z}_{\frac{1}{2}s'\frac{1}{2}s} C^{TT_z}_{\frac{1}{2}t'\frac{1}{2}t} |SS_zTT_z\rangle. \tag{A.0.2}$$

We wish to map the s.p. basis of four spin-isospin states, $|n\uparrow\rangle$, $|n\downarrow\rangle$, $|p\uparrow\rangle$, $|p\downarrow\rangle$, into the basis of coupled spin and isospin $|SS_zTT_z\rangle$. Naturally, we should always have $T_z = t' + t$ and $S_z = s' + s$. We list below all the different states in the ST basis.

$$\begin{aligned}
|0000\rangle &= C^{00}_{\frac{1}{2}+\frac{1}{2}\frac{1}{2}-\frac{1}{2}} C^{00}_{\frac{1}{2}+\frac{1}{2}\frac{1}{2}-\frac{1}{2}} |\tfrac{1}{2}+\tfrac{1}{2}\tfrac{1}{2}+\tfrac{1}{2}\rangle|\tfrac{1}{2}-\tfrac{1}{2}\tfrac{1}{2}-\tfrac{1}{2}\rangle + C^{00}_{\frac{1}{2}-\frac{1}{2}\frac{1}{2}+\frac{1}{2}} C^{00}_{\frac{1}{2}+\frac{1}{2}\frac{1}{2}-\frac{1}{2}} |\tfrac{1}{2}-\tfrac{1}{2}\tfrac{1}{2}+\tfrac{1}{2}\rangle|\tfrac{1}{2}+\tfrac{1}{2}\tfrac{1}{2}-\tfrac{1}{2}\rangle + \\
&\quad C^{00}_{\frac{1}{2}-\frac{1}{2}\frac{1}{2}+\frac{1}{2}} C^{00}_{\frac{1}{2}-\frac{1}{2}\frac{1}{2}+\frac{1}{2}} |\tfrac{1}{2}-\tfrac{1}{2}\tfrac{1}{2}-\tfrac{1}{2}\rangle|\tfrac{1}{2}+\tfrac{1}{2}\tfrac{1}{2}+\tfrac{1}{2}\rangle + C^{00}_{\frac{1}{2}+\frac{1}{2}\frac{1}{2}-\frac{1}{2}} C^{00}_{\frac{1}{2}-\frac{1}{2}\frac{1}{2}+\frac{1}{2}} |\tfrac{1}{2}+\tfrac{1}{2}\tfrac{1}{2}-\tfrac{1}{2}\rangle|\tfrac{1}{2}-\tfrac{1}{2}\tfrac{1}{2}+\tfrac{1}{2}\rangle \\
&= \tfrac{1}{\sqrt{2}}\tfrac{1}{\sqrt{2}}|\tfrac{1}{2}+\tfrac{1}{2}\tfrac{1}{2}+\tfrac{1}{2}\rangle|\tfrac{1}{2}-\tfrac{1}{2}\tfrac{1}{2}-\tfrac{1}{2}\rangle + \left(-\tfrac{1}{\sqrt{2}}\right)\tfrac{1}{\sqrt{2}}|\tfrac{1}{2}-\tfrac{1}{2}\tfrac{1}{2}+\tfrac{1}{2}\rangle|\tfrac{1}{2}+\tfrac{1}{2}\tfrac{1}{2}-\tfrac{1}{2}\rangle + \\
&\quad \left(-\tfrac{1}{\sqrt{2}}\right)\left(-\tfrac{1}{\sqrt{2}}\right)|\tfrac{1}{2}-\tfrac{1}{2}\tfrac{1}{2}-\tfrac{1}{2}\rangle|\tfrac{1}{2}+\tfrac{1}{2}\tfrac{1}{2}+\tfrac{1}{2}\rangle + \tfrac{1}{\sqrt{2}}\left(-\tfrac{1}{\sqrt{2}}\right)|\tfrac{1}{2}+\tfrac{1}{2}\tfrac{1}{2}-\tfrac{1}{2}\rangle|\tfrac{1}{2}-\tfrac{1}{2}\tfrac{1}{2}+\tfrac{1}{2}\rangle \\
&= \tfrac{1}{2}(|n\uparrow\rangle|p\downarrow\rangle - |n\downarrow\rangle|p\uparrow\rangle + |p\downarrow\rangle|n\uparrow\rangle - |p\uparrow\rangle|n\downarrow\rangle);
\end{aligned}$$

$$\begin{aligned}
|001\text{-}1\rangle &= C^{00}_{\frac{1}{2}+\frac{1}{2}\frac{1}{2}-\frac{1}{2}} C^{1-1}_{\frac{1}{2}-\frac{1}{2}\frac{1}{2}-\frac{1}{2}} |\tfrac{1}{2}+\tfrac{1}{2}\tfrac{1}{2}-\tfrac{1}{2}\rangle|\tfrac{1}{2}-\tfrac{1}{2}\tfrac{1}{2}-\tfrac{1}{2}\rangle + C^{00}_{\frac{1}{2}-\frac{1}{2}\frac{1}{2}+\frac{1}{2}} C^{1-1}_{\frac{1}{2}-\frac{1}{2}\frac{1}{2}-\frac{1}{2}} |\tfrac{1}{2}-\tfrac{1}{2}\tfrac{1}{2}-\tfrac{1}{2}\rangle|\tfrac{1}{2}+\tfrac{1}{2}\tfrac{1}{2}-\tfrac{1}{2}\rangle \\
&= \tfrac{1}{\sqrt{2}}|\tfrac{1}{2}+\tfrac{1}{2}\tfrac{1}{2}-\tfrac{1}{2}\rangle|\tfrac{1}{2}-\tfrac{1}{2}\tfrac{1}{2}-\tfrac{1}{2}\rangle - \tfrac{1}{\sqrt{2}}|\tfrac{1}{2}-\tfrac{1}{2}\tfrac{1}{2}-\tfrac{1}{2}\rangle|\tfrac{1}{2}+\tfrac{1}{2}\tfrac{1}{2}-\tfrac{1}{2}\rangle \\
&= \tfrac{1}{\sqrt{2}}(|p\uparrow\rangle|p\downarrow\rangle - |p\downarrow\rangle|p\uparrow\rangle);
\end{aligned}$$

$$
\begin{aligned}
|0010\rangle &= C^{00}_{\frac{1}{2}+\frac{1}{2}\frac{1}{2}-\frac{1}{2}} C^{10}_{\frac{1}{2}+\frac{1}{2}\frac{1}{2}-\frac{1}{2}} |\tfrac{1}{2}+\tfrac{1}{2}\tfrac{1}{2}+\tfrac{1}{2}\rangle|\tfrac{1}{2}-\tfrac{1}{2}\tfrac{1}{2}-\tfrac{1}{2}\rangle + C^{00}_{\frac{1}{2}-\frac{1}{2}\frac{1}{2}+\frac{1}{2}} C^{10}_{\frac{1}{2}+\frac{1}{2}\frac{1}{2}-\frac{1}{2}} |\tfrac{1}{2}-\tfrac{1}{2}\tfrac{1}{2}+\tfrac{1}{2}\rangle|\tfrac{1}{2}+\tfrac{1}{2}\tfrac{1}{2}-\tfrac{1}{2}\rangle + \\
&\quad C^{00}_{\frac{1}{2}-\frac{1}{2}\frac{1}{2}+\frac{1}{2}} C^{10}_{\frac{1}{2}-\frac{1}{2}\frac{1}{2}+\frac{1}{2}} |\tfrac{1}{2}-\tfrac{1}{2}\tfrac{1}{2}-\tfrac{1}{2}\rangle|\tfrac{1}{2}+\tfrac{1}{2}\tfrac{1}{2}+\tfrac{1}{2}\rangle + C^{00}_{\frac{1}{2}+\frac{1}{2}\frac{1}{2}-\frac{1}{2}} C^{10}_{\frac{1}{2}-\frac{1}{2}\frac{1}{2}+\frac{1}{2}} |\tfrac{1}{2}+\tfrac{1}{2}\tfrac{1}{2}-\tfrac{1}{2}\rangle|\tfrac{1}{2}-\tfrac{1}{2}\tfrac{1}{2}+\tfrac{1}{2}\rangle \\
&= \tfrac{1}{\sqrt{2}}\tfrac{1}{\sqrt{2}}|\tfrac{1}{2}+\tfrac{1}{2}\tfrac{1}{2}+\tfrac{1}{2}\rangle|\tfrac{1}{2}-\tfrac{1}{2}\tfrac{1}{2}-\tfrac{1}{2}\rangle + \left(-\tfrac{1}{\sqrt{2}}\right)\tfrac{1}{\sqrt{2}}|\tfrac{1}{2}-\tfrac{1}{2}\tfrac{1}{2}+\tfrac{1}{2}\rangle|\tfrac{1}{2}+\tfrac{1}{2}\tfrac{1}{2}-\tfrac{1}{2}\rangle \\
&\quad \left(-\tfrac{1}{\sqrt{2}}\right)\tfrac{1}{\sqrt{2}}|\tfrac{1}{2}-\tfrac{1}{2}\tfrac{1}{2}-\tfrac{1}{2}\rangle|\tfrac{1}{2}+\tfrac{1}{2}\tfrac{1}{2}+\tfrac{1}{2}\rangle + \tfrac{1}{\sqrt{2}}\tfrac{1}{\sqrt{2}}|\tfrac{1}{2}+\tfrac{1}{2}\tfrac{1}{2}-\tfrac{1}{2}\rangle|\tfrac{1}{2}-\tfrac{1}{2}\tfrac{1}{2}+\tfrac{1}{2}\rangle \\
&= \tfrac{1}{2}(|n\uparrow\rangle|p\downarrow\rangle - |n\downarrow\rangle|p\uparrow\rangle - |p\downarrow\rangle|n\uparrow\rangle + |p\uparrow\rangle|n\downarrow\rangle);
\end{aligned}
$$

$$
\begin{aligned}
|0011\rangle &= C^{00}_{\frac{1}{2}+\frac{1}{2}\frac{1}{2}-\frac{1}{2}} C^{11}_{\frac{1}{2}+\frac{1}{2}\frac{1}{2}+\frac{1}{2}} |\tfrac{1}{2}+\tfrac{1}{2}\tfrac{1}{2}+\tfrac{1}{2}\rangle|\tfrac{1}{2}-\tfrac{1}{2}\tfrac{1}{2}+\tfrac{1}{2}\rangle + C^{00}_{\frac{1}{2}-\frac{1}{2}\frac{1}{2}+\frac{1}{2}} C^{11}_{\frac{1}{2}+\frac{1}{2}\frac{1}{2}+\frac{1}{2}} |\tfrac{1}{2}-\tfrac{1}{2}\tfrac{1}{2}+\tfrac{1}{2}\rangle|\tfrac{1}{2}+\tfrac{1}{2}\tfrac{1}{2}+\tfrac{1}{2}\rangle \\
&= \tfrac{1}{\sqrt{2}}|\tfrac{1}{2}+\tfrac{1}{2}\tfrac{1}{2}+\tfrac{1}{2}\rangle|\tfrac{1}{2}-\tfrac{1}{2}\tfrac{1}{2}+\tfrac{1}{2}\rangle - \tfrac{1}{\sqrt{2}}|\tfrac{1}{2}-\tfrac{1}{2}\tfrac{1}{2}+\tfrac{1}{2}\rangle|\tfrac{1}{2}+\tfrac{1}{2}\tfrac{1}{2}+\tfrac{1}{2}\rangle \\
&= \tfrac{1}{\sqrt{2}}(|n\uparrow\rangle|n\downarrow\rangle - |n\downarrow\rangle|n\uparrow\rangle);
\end{aligned}
$$

$$
\begin{aligned}
|1\text{-}100\rangle &= C^{1-1}_{\frac{1}{2}-\frac{1}{2}\frac{1}{2}-\frac{1}{2}} C^{00}_{\frac{1}{2}+\frac{1}{2}\frac{1}{2}-\frac{1}{2}} |\tfrac{1}{2}-\tfrac{1}{2}\tfrac{1}{2}+\tfrac{1}{2}\rangle|\tfrac{1}{2}-\tfrac{1}{2}\tfrac{1}{2}-\tfrac{1}{2}\rangle + C^{1-1}_{\frac{1}{2}-\frac{1}{2}\frac{1}{2}-\frac{1}{2}} C^{00}_{\frac{1}{2}-\frac{1}{2}\frac{1}{2}+\frac{1}{2}} |\tfrac{1}{2}-\tfrac{1}{2}\tfrac{1}{2}-\tfrac{1}{2}\rangle|\tfrac{1}{2}-\tfrac{1}{2}\tfrac{1}{2}+\tfrac{1}{2}\rangle \\
&= \tfrac{1}{\sqrt{2}}|\tfrac{1}{2}-\tfrac{1}{2}\tfrac{1}{2}+\tfrac{1}{2}\rangle|\tfrac{1}{2}-\tfrac{1}{2}\tfrac{1}{2}-\tfrac{1}{2}\rangle - \tfrac{1}{\sqrt{2}}|\tfrac{1}{2}-\tfrac{1}{2}\tfrac{1}{2}-\tfrac{1}{2}\rangle|\tfrac{1}{2}-\tfrac{1}{2}\tfrac{1}{2}+\tfrac{1}{2}\rangle \\
&= \tfrac{1}{\sqrt{2}}(|n\downarrow\rangle|p\downarrow\rangle - |p\downarrow\rangle|n\downarrow\rangle);
\end{aligned}
$$

$$
\begin{aligned}
|1000\rangle &= C^{10}_{\frac{1}{2}+\frac{1}{2}\frac{1}{2}-\frac{1}{2}} C^{00}_{\frac{1}{2}+\frac{1}{2}\frac{1}{2}-\frac{1}{2}} |\tfrac{1}{2}+\tfrac{1}{2}\tfrac{1}{2}+\tfrac{1}{2}\rangle|\tfrac{1}{2}-\tfrac{1}{2}\tfrac{1}{2}-\tfrac{1}{2}\rangle + C^{10}_{\frac{1}{2}-\frac{1}{2}\frac{1}{2}+\frac{1}{2}} C^{00}_{\frac{1}{2}+\frac{1}{2}\frac{1}{2}-\frac{1}{2}} |\tfrac{1}{2}-\tfrac{1}{2}\tfrac{1}{2}+\tfrac{1}{2}\rangle|\tfrac{1}{2}+\tfrac{1}{2}\tfrac{1}{2}-\tfrac{1}{2}\rangle + \\
&\quad C^{10}_{\frac{1}{2}-\frac{1}{2}\frac{1}{2}+\frac{1}{2}} C^{00}_{\frac{1}{2}-\frac{1}{2}\frac{1}{2}+\frac{1}{2}} |\tfrac{1}{2}-\tfrac{1}{2}\tfrac{1}{2}-\tfrac{1}{2}\rangle|\tfrac{1}{2}+\tfrac{1}{2}\tfrac{1}{2}+\tfrac{1}{2}\rangle + C^{10}_{\frac{1}{2}+\frac{1}{2}\frac{1}{2}-\frac{1}{2}} C^{00}_{\frac{1}{2}-\frac{1}{2}\frac{1}{2}+\frac{1}{2}} |\tfrac{1}{2}+\tfrac{1}{2}\tfrac{1}{2}-\tfrac{1}{2}\rangle|\tfrac{1}{2}-\tfrac{1}{2}\tfrac{1}{2}+\tfrac{1}{2}\rangle \\
&= \tfrac{1}{\sqrt{2}}\tfrac{1}{\sqrt{2}}|\tfrac{1}{2}+\tfrac{1}{2}\tfrac{1}{2}+\tfrac{1}{2}\rangle|\tfrac{1}{2}-\tfrac{1}{2}\tfrac{1}{2}-\tfrac{1}{2}\rangle + \tfrac{1}{\sqrt{2}}\tfrac{1}{\sqrt{2}}|\tfrac{1}{2}-\tfrac{1}{2}\tfrac{1}{2}+\tfrac{1}{2}\rangle|\tfrac{1}{2}+\tfrac{1}{2}\tfrac{1}{2}-\tfrac{1}{2}\rangle + \\
&\quad \tfrac{1}{\sqrt{2}}\left(-\tfrac{1}{\sqrt{2}}\right)|\tfrac{1}{2}-\tfrac{1}{2}\tfrac{1}{2}-\tfrac{1}{2}\rangle|\tfrac{1}{2}+\tfrac{1}{2}\tfrac{1}{2}+\tfrac{1}{2}\rangle + \tfrac{1}{\sqrt{2}}\left(-\tfrac{1}{\sqrt{2}}\right)|\tfrac{1}{2}+\tfrac{1}{2}\tfrac{1}{2}-\tfrac{1}{2}\rangle|\tfrac{1}{2}-\tfrac{1}{2}\tfrac{1}{2}+\tfrac{1}{2}\rangle \\
&= \tfrac{1}{2}(|n\uparrow\rangle|p\downarrow\rangle + |n\downarrow\rangle|p\uparrow\rangle - |p\downarrow\rangle|n\uparrow\rangle - |p\uparrow\rangle|n\downarrow\rangle);
\end{aligned}
$$

$$
\begin{aligned}
|1100\rangle &= C^{11}_{\frac{1}{2}+\frac{1}{2}\frac{1}{2}+\frac{1}{2}} C^{00}_{\frac{1}{2}+\frac{1}{2}\frac{1}{2}-\frac{1}{2}} |\tfrac{1}{2}+\tfrac{1}{2}\tfrac{1}{2}+\tfrac{1}{2}\rangle|\tfrac{1}{2}+\tfrac{1}{2}\tfrac{1}{2}-\tfrac{1}{2}\rangle + C^{11}_{\frac{1}{2}+\frac{1}{2}\frac{1}{2}+\frac{1}{2}} C^{00}_{\frac{1}{2}-\frac{1}{2}\frac{1}{2}+\frac{1}{2}} |\tfrac{1}{2}+\tfrac{1}{2}\tfrac{1}{2}-\tfrac{1}{2}\rangle|\tfrac{1}{2}+\tfrac{1}{2}\tfrac{1}{2}-\tfrac{1}{2}\rangle \\
&= \tfrac{1}{\sqrt{2}}|\tfrac{1}{2}+\tfrac{1}{2}\tfrac{1}{2}+\tfrac{1}{2}\rangle|\tfrac{1}{2}+\tfrac{1}{2}\tfrac{1}{2}-\tfrac{1}{2}\rangle - \tfrac{1}{\sqrt{2}}|\tfrac{1}{2}+\tfrac{1}{2}\tfrac{1}{2}-\tfrac{1}{2}\rangle|\tfrac{1}{2}+\tfrac{1}{2}\tfrac{1}{2}+\tfrac{1}{2}\rangle \\
&= \tfrac{1}{\sqrt{2}}(|n\uparrow\rangle|p\uparrow\rangle - |p\uparrow\rangle|n\uparrow\rangle);
\end{aligned}
$$

$$
\begin{aligned}
|1\text{-}11\text{-}1\rangle &= C^{1-1}_{\frac{1}{2}-\frac{1}{2}\frac{1}{2}-\frac{1}{2}} C^{1-1}_{\frac{1}{2}-\frac{1}{2}\frac{1}{2}-\frac{1}{2}} |\tfrac{1}{2}-\tfrac{1}{2}\tfrac{1}{2}-\tfrac{1}{2}\rangle|\tfrac{1}{2}-\tfrac{1}{2}\tfrac{1}{2}-\tfrac{1}{2}\rangle \\
&= |p\downarrow\rangle|p\downarrow\rangle;
\end{aligned}
$$

$$
\begin{aligned}
|111\text{-}1\rangle &= C^{11}_{\frac{1}{2}+\frac{1}{2}\,\frac{1}{2}+\frac{1}{2}} C^{1-1}_{\frac{1}{2}-\frac{1}{2}\,\frac{1}{2}-\frac{1}{2}} |\tfrac{1}{2}+\tfrac{1}{2}\,\tfrac{1}{2}-\tfrac{1}{2}\rangle |\tfrac{1}{2}+\tfrac{1}{2}\,\tfrac{1}{2}-\tfrac{1}{2}\rangle \\
&= \left|p\uparrow\right\rangle \left|p\uparrow\right\rangle;
\end{aligned}
$$

$$
\begin{aligned}
|1\text{-}111\rangle &= C^{1-1}_{\frac{1}{2}-\frac{1}{2}\,\frac{1}{2}-\frac{1}{2}} C^{11}_{\frac{1}{2}+\frac{1}{2}\,\frac{1}{2}+\frac{1}{2}} |\tfrac{1}{2}-\tfrac{1}{2}\,\tfrac{1}{2}+\tfrac{1}{2}\rangle |\tfrac{1}{2}-\tfrac{1}{2}\,\tfrac{1}{2}+\tfrac{1}{2}\rangle \\
&= |n\downarrow\rangle |n\downarrow\rangle;
\end{aligned}
$$

$$
\begin{aligned}
|1111\rangle &= C^{11}_{\frac{1}{2}+\frac{1}{2}\,\frac{1}{2}+\frac{1}{2}} C^{11}_{\frac{1}{2}+\frac{1}{2}\,\frac{1}{2}+\frac{1}{2}} |\tfrac{1}{2}+\tfrac{1}{2}\,\tfrac{1}{2}+\tfrac{1}{2}\rangle |\tfrac{1}{2}+\tfrac{1}{2}\,\tfrac{1}{2}+\tfrac{1}{2}\rangle \\
&= |n\uparrow\rangle |n\uparrow\rangle;
\end{aligned}
$$

$$
\begin{aligned}
|101\text{-}1\rangle &= C^{10}_{\frac{1}{2}+\frac{1}{2}\,\frac{1}{2}-\frac{1}{2}} C^{1-1}_{\frac{1}{2}-\frac{1}{2}\,\frac{1}{2}-\frac{1}{2}} |\tfrac{1}{2}+\tfrac{1}{2}\,\tfrac{1}{2}-\tfrac{1}{2}\rangle |\tfrac{1}{2}-\tfrac{1}{2}\,\tfrac{1}{2}-\tfrac{1}{2}\rangle + C^{10}_{\frac{1}{2}-\frac{1}{2}\,\frac{1}{2}+\frac{1}{2}} C^{1-1}_{\frac{1}{2}-\frac{1}{2}\,\frac{1}{2}-\frac{1}{2}} |\tfrac{1}{2}-\tfrac{1}{2}\,\tfrac{1}{2}-\tfrac{1}{2}\rangle |\tfrac{1}{2}+\tfrac{1}{2}\,\tfrac{1}{2}-\tfrac{1}{2}\rangle \\
&= \tfrac{1}{\sqrt{2}}(\left|p\uparrow\right\rangle \left|p\downarrow\right\rangle + \left|p\downarrow\right\rangle \left|p\uparrow\right\rangle);
\end{aligned}
$$

$$
\begin{aligned}
|1011\rangle &= C^{10}_{\frac{1}{2}+\frac{1}{2}\,\frac{1}{2}-\frac{1}{2}} C^{11}_{\frac{1}{2}+\frac{1}{2}\,\frac{1}{2}+\frac{1}{2}} |\tfrac{1}{2}+\tfrac{1}{2}\,\tfrac{1}{2}+\tfrac{1}{2}\rangle |\tfrac{1}{2}-\tfrac{1}{2}\,\tfrac{1}{2}+\tfrac{1}{2}\rangle + C^{10}_{\frac{1}{2}-\frac{1}{2}\,\frac{1}{2}+\frac{1}{2}} C^{11}_{\frac{1}{2}+\frac{1}{2}\,\frac{1}{2}+\frac{1}{2}} |\tfrac{1}{2}-\tfrac{1}{2}\,\tfrac{1}{2}+\tfrac{1}{2}\rangle |\tfrac{1}{2}+\tfrac{1}{2}\,\tfrac{1}{2}+\tfrac{1}{2}\rangle \\
&= \tfrac{1}{\sqrt{2}}(|n\uparrow\rangle |n\downarrow\rangle + |n\downarrow\rangle |n\uparrow\rangle);
\end{aligned}
$$

$$
\begin{aligned}
|1\text{-}110\rangle &= C^{1-1}_{\frac{1}{2}-\frac{1}{2}\,\frac{1}{2}-\frac{1}{2}} C^{10}_{\frac{1}{2}+\frac{1}{2}\,\frac{1}{2}-\frac{1}{2}} |\tfrac{1}{2}-\tfrac{1}{2}\,\tfrac{1}{2}+\tfrac{1}{2}\rangle |\tfrac{1}{2}-\tfrac{1}{2}\,\tfrac{1}{2}-\tfrac{1}{2}\rangle + C^{1-1}_{\frac{1}{2}-\frac{1}{2}\,\frac{1}{2}-\frac{1}{2}} C^{10}_{\frac{1}{2}-\frac{1}{2}\,\frac{1}{2}+\frac{1}{2}} |\tfrac{1}{2}-\tfrac{1}{2}\,\tfrac{1}{2}-\tfrac{1}{2}\rangle |\tfrac{1}{2}-\tfrac{1}{2}\,\tfrac{1}{2}+\tfrac{1}{2}\rangle; \\
&= \tfrac{1}{\sqrt{2}}(|n\downarrow\rangle \left|p\downarrow\right\rangle + \left|p\downarrow\right\rangle |n\downarrow\rangle);
\end{aligned}
$$

$$
\begin{aligned}
|1110\rangle &= C^{11}_{\frac{1}{2}+\frac{1}{2}\,\frac{1}{2}+\frac{1}{2}} C^{10}_{\frac{1}{2}+\frac{1}{2}\,\frac{1}{2}-\frac{1}{2}} |\tfrac{1}{2}+\tfrac{1}{2}\,\tfrac{1}{2}+\tfrac{1}{2}\rangle |\tfrac{1}{2}+\tfrac{1}{2}\,\tfrac{1}{2}-\tfrac{1}{2}\rangle + C^{11}_{\frac{1}{2}+\frac{1}{2}\,\frac{1}{2}+\frac{1}{2}} C^{10}_{\frac{1}{2}-\frac{1}{2}\,\frac{1}{2}+\frac{1}{2}} |\tfrac{1}{2}+\tfrac{1}{2}\,\tfrac{1}{2}-\tfrac{1}{2}\rangle |\tfrac{1}{2}+\tfrac{1}{2}\,\tfrac{1}{2}+\tfrac{1}{2}\rangle; \\
&= \tfrac{1}{\sqrt{2}}(|n\uparrow\rangle \left|p\uparrow\right\rangle + \left|p\uparrow\right\rangle |n\uparrow\rangle);
\end{aligned}
$$

$$
\begin{aligned}
|1010\rangle &= C^{10}_{\frac{1}{2}+\frac{1}{2}\,\frac{1}{2}-\frac{1}{2}} C^{10}_{\frac{1}{2}+\frac{1}{2}\,\frac{1}{2}-\frac{1}{2}} |\tfrac{1}{2}+\tfrac{1}{2}\,\tfrac{1}{2}+\tfrac{1}{2}\rangle |\tfrac{1}{2}-\tfrac{1}{2}\,\tfrac{1}{2}-\tfrac{1}{2}\rangle + C^{10}_{\frac{1}{2}-\frac{1}{2}\,\frac{1}{2}+\frac{1}{2}} C^{10}_{\frac{1}{2}+\frac{1}{2}\,\frac{1}{2}-\frac{1}{2}} |\tfrac{1}{2}-\tfrac{1}{2}\,\tfrac{1}{2}+\tfrac{1}{2}\rangle |\tfrac{1}{2}+\tfrac{1}{2}\,\tfrac{1}{2}-\tfrac{1}{2}\rangle + \\
&\quad C^{10}_{\frac{1}{2}-\frac{1}{2}\,\frac{1}{2}+\frac{1}{2}} C^{10}_{\frac{1}{2}-\frac{1}{2}\,\frac{1}{2}+\frac{1}{2}} |\tfrac{1}{2}-\tfrac{1}{2}\,\tfrac{1}{2}-\tfrac{1}{2}\rangle |\tfrac{1}{2}+\tfrac{1}{2}\,\tfrac{1}{2}+\tfrac{1}{2}\rangle + C^{10}_{\frac{1}{2}+\frac{1}{2}\,\frac{1}{2}-\frac{1}{2}} C^{10}_{\frac{1}{2}-\frac{1}{2}\,\frac{1}{2}+\frac{1}{2}} |\tfrac{1}{2}+\tfrac{1}{2}\,\tfrac{1}{2}-\tfrac{1}{2}\rangle |\tfrac{1}{2}-\tfrac{1}{2}\,\tfrac{1}{2}+\tfrac{1}{2}\rangle \\
&= \tfrac{1}{\sqrt{2}}\tfrac{1}{\sqrt{2}} |\tfrac{1}{2}+\tfrac{1}{2}\,\tfrac{1}{2}+\tfrac{1}{2}\rangle |\tfrac{1}{2}-\tfrac{1}{2}\,\tfrac{1}{2}-\tfrac{1}{2}\rangle + \tfrac{1}{\sqrt{2}}\tfrac{1}{\sqrt{2}} |\tfrac{1}{2}-\tfrac{1}{2}\,\tfrac{1}{2}+\tfrac{1}{2}\rangle |\tfrac{1}{2}+\tfrac{1}{2}\,\tfrac{1}{2}-\tfrac{1}{2}\rangle + \\
&\quad \tfrac{1}{\sqrt{2}}\tfrac{1}{\sqrt{2}} |\tfrac{1}{2}-\tfrac{1}{2}\,\tfrac{1}{2}-\tfrac{1}{2}\rangle |\tfrac{1}{2}+\tfrac{1}{2}\,\tfrac{1}{2}+\tfrac{1}{2}\rangle + \tfrac{1}{\sqrt{2}}\tfrac{1}{\sqrt{2}} |\tfrac{1}{2}+\tfrac{1}{2}\,\tfrac{1}{2}-\tfrac{1}{2}\rangle |\tfrac{1}{2}-\tfrac{1}{2}\,\tfrac{1}{2}+\tfrac{1}{2}\rangle \\
&= \tfrac{1}{2}(|n\uparrow\rangle \left|p\downarrow\right\rangle + |n\downarrow\rangle \left|p\uparrow\right\rangle + \left|p\downarrow\right\rangle |n\uparrow\rangle + \left|p\uparrow\right\rangle |n\downarrow\rangle).
\end{aligned}
$$



B

Rotated *ST* states

With the expressions from subsection 4.5.1, we can explicitly write the rotated states. Starting with the vector isoscalar pairs, we have

$$
\begin{aligned}
\left|1S'_z(\Omega_S)00\right\rangle &= z^*_{10} \sum_{s's=\pm 1/2} C^{1S_z}_{\frac{1}{2}s'\frac{1}{2}s} D^1_{S_z 0} \sum_{t't=\pm 1/2} C^{00}_{\frac{1}{2}t'\frac{1}{2}t} |\tfrac{1}{2}s'\tfrac{1}{2}t'\rangle |\tfrac{1}{2}s\tfrac{1}{2}t\rangle \\
&= z^*_{10} \sum_{s's=\pm 1/2} C^{1S_z}_{\frac{1}{2}s'\frac{1}{2}s} D^1_{S_z 0} \left(C^{00}_{\frac{1}{2}+\frac{1}{2}\frac{1}{2}-\frac{1}{2}} \left|s'n\right\rangle \left|sp\right\rangle + C^{00}_{\frac{1}{2}-\frac{1}{2}\frac{1}{2}+\frac{1}{2}} \left|s'p\right\rangle \left|sn\right\rangle \right) \\
&= \frac{z^*_{10}}{\sqrt{2}} \sum_{s's=\pm 1/2} C^{1S_z}_{\frac{1}{2}s'\frac{1}{2}s} D^1_{S_z 0} \left(+ \left|s'n\right\rangle \left|sp\right\rangle - \left|s'p\right\rangle \left|sn\right\rangle \right) \\
&= \frac{z^*_{10}}{\sqrt{2}} \Big[C^{10}_{\frac{1}{2}+\frac{1}{2}\frac{1}{2}-\frac{1}{2}} D^1_{00} (|n\uparrow\rangle |p\downarrow\rangle - |p\uparrow\rangle |n\downarrow\rangle) + C^{10}_{\frac{1}{2}-\frac{1}{2}\frac{1}{2}+\frac{1}{2}} D^1_{00} (|n\downarrow\rangle |p\uparrow\rangle - |p\downarrow\rangle |n\uparrow\rangle) \\
&\quad + C^{11}_{\frac{1}{2}+\frac{1}{2}\frac{1}{2}+\frac{1}{2}} D^1_{10} (|n\uparrow\rangle |p\uparrow\rangle - |p\uparrow\rangle |n\uparrow\rangle) + C^{1-1}_{\frac{1}{2}-\frac{1}{2}\frac{1}{2}-\frac{1}{2}} D^1_{-10} (|n\downarrow\rangle |p\downarrow\rangle - |p\downarrow\rangle |n\downarrow\rangle) \Big] \\
&= \frac{z^*_{10}}{\sqrt{2}} \Big[\frac{\cos\beta_S}{\sqrt{2}} (|n\uparrow\rangle |p\downarrow\rangle - |p\uparrow\rangle |n\downarrow\rangle) + \frac{\cos\beta_S}{\sqrt{2}} (|n\downarrow\rangle |p\uparrow\rangle - |p\downarrow\rangle |n\uparrow\rangle) \\
&\quad - \frac{\sin\beta_S}{\sqrt{2}} e^{-i\alpha_S} (|n\uparrow\rangle |p\uparrow\rangle - |p\uparrow\rangle |n\uparrow\rangle) + \frac{\sin\beta_S}{\sqrt{2}} e^{+i\alpha_S} (|n\downarrow\rangle |p\downarrow\rangle - |p\downarrow\rangle |n\downarrow\rangle) \Big].
\end{aligned}
$$

Similarly for the scalar isovector pairs we obtain

$$
\begin{aligned}
\left|001T_z'(\Omega_T)\right\rangle &= z_{01}^* \sum_{s's=\pm1/2} C^{00}_{\frac{1}{2}s'\frac{1}{2}s} \sum_{t't=\pm1/2} C^{1T_z}_{\frac{1}{2}t'\frac{1}{2}t} D^1_{T_z'0} |\tfrac{1}{2}s'\tfrac{1}{2}t'\rangle |\tfrac{1}{2}s\tfrac{1}{2}t\rangle \\
&= z_{01}^* \sum_{t't=\pm1/2} C^{1T_z}_{\frac{1}{2}t'\frac{1}{2}t} D^1_{T_z'0} \left(C^{00}_{\frac{1}{2}+\frac{1}{2}\frac{1}{2}-\frac{1}{2}} \left|t'\uparrow\right\rangle |t\downarrow\rangle + C^{00}_{\frac{1}{2}-\frac{1}{2}\frac{1}{2}+\frac{1}{2}} \left|t'\downarrow\right\rangle |t\uparrow\rangle \right) \\
&= \frac{z_{01}^*}{\sqrt{2}} \sum_{t't=\pm1/2} C^{1T_z}_{\frac{1}{2}t'\frac{1}{2}t} D^1_{T_z'0} \left(+ \left|t'\uparrow\right\rangle |t\downarrow\rangle - \left|t'\downarrow\right\rangle |t\uparrow\rangle \right) \\
&= \frac{z_{01}^*}{\sqrt{2}} \Big[C^{10}_{\frac{1}{2}+\frac{1}{2}\frac{1}{2}-\frac{1}{2}} D^1_{00}(|n\uparrow\rangle \left|p\downarrow\right\rangle - |n\downarrow\rangle \left|p\uparrow\right\rangle) + C^{10}_{\frac{1}{2}-\frac{1}{2}\frac{1}{2}+\frac{1}{2}} D^1_{00}(\left|p\uparrow\right\rangle |n\downarrow\rangle - \left|p\downarrow\right\rangle |n\uparrow\rangle) \\
&\quad + C^{11}_{\frac{1}{2}+\frac{1}{2}\frac{1}{2}+\frac{1}{2}} D^1_{10}(|n\uparrow\rangle |n\downarrow\rangle - |n\downarrow\rangle |n\uparrow\rangle) + C^{1-1}_{\frac{1}{2}-\frac{1}{2}\frac{1}{2}-\frac{1}{2}} D^1_{-10}(\left|p\uparrow\right\rangle \left|p\downarrow\right\rangle - \left|p\downarrow\right\rangle \left|p\uparrow\right\rangle) \Big] \\
&= \frac{z_{01}^*}{2} \left[\cos\beta_T (|n\uparrow\rangle \left|p\downarrow\right\rangle - |n\downarrow\rangle \left|p\uparrow\right\rangle) + \cos\beta_T (\left|p\uparrow\right\rangle |n\downarrow\rangle - \left|p\downarrow\right\rangle |n\uparrow\rangle) \right. \\
&\quad \left. - \sin\beta_T e^{-i\alpha_T} (|n\uparrow\rangle |n\downarrow\rangle - |n\downarrow\rangle |n\uparrow\rangle) + \sin\beta_T e^{+i\alpha_T} (\left|p\uparrow\right\rangle \left|p\downarrow\right\rangle - \left|p\downarrow\right\rangle \left|p\uparrow\right\rangle) \right].
\end{aligned}
$$

Lastly, rotating the z-aligned vector-isovector pairs yields components in all 16 possible pn pairs

$$
\begin{aligned}
\left|1S_z'(\Omega_S)1T_z'(\Omega_T)\right\rangle &= z_{11}^{*}\sum_{t't=\pm1/2} C^{1T_z}_{\frac{1}{2}t'\frac{1}{2}t} D^{1}_{T_z0}\Big(C^{10}_{\frac{1}{2}+\frac{1}{2}\frac{1}{2}-\frac{1}{2}} D^{1}_{00}\left|t'\uparrow\right\rangle|t\downarrow\rangle + C^{10}_{\frac{1}{2}-\frac{1}{2}\frac{1}{2}+\frac{1}{2}} D^{1}_{00}\left|t'\downarrow\right\rangle|t\uparrow\rangle \\
&\qquad + C^{11}_{\frac{1}{2}+\frac{1}{2}\frac{1}{2}+\frac{1}{2}} D^{1}_{10}\left|t'\uparrow\right\rangle|t\uparrow\rangle + C^{1-1}_{\frac{1}{2}-\frac{1}{2}\frac{1}{2}-\frac{1}{2}} D^{1}_{-10}\left|t'\downarrow\right\rangle|t\downarrow\rangle\Big) \\
&= \frac{z_{11}^{*}}{\sqrt{2}}\sum_{t't=\pm1/2} C^{1T_z}_{\frac{1}{2}t'\frac{1}{2}t} D^{1}_{T_z0}\left(\cos\beta_S\left|t'\uparrow\right\rangle|t\downarrow\rangle + \cos\beta_S\left|t'\downarrow\right\rangle|t\uparrow\rangle\right. \\
&\qquad \left. - \sin\beta_S e^{-i\alpha_S}\left|t'\uparrow\right\rangle|t\uparrow\rangle + \sin\beta_S e^{+i\alpha_S}\left|t'\downarrow\right\rangle|t\downarrow\rangle\right) \\
&= \frac{z_{11}^{*}}{\sqrt{2}}\Big[C^{10}_{\frac{1}{2}+\frac{1}{2}\frac{1}{2}-\frac{1}{2}} D^{1}_{00}\left(\cos\beta_S|n\uparrow\rangle\left|p\downarrow\right\rangle + \cos\beta_S|n\downarrow\rangle\left|p\uparrow\right\rangle - \sin\beta_S e^{-i\alpha_S}|n\uparrow\rangle\left|p\uparrow\right\rangle\right. \\
&\quad \left. + \sin\beta_S e^{+i\alpha_S}|n\downarrow\rangle\left|p\downarrow\right\rangle\right) + C^{10}_{\frac{1}{2}-\frac{1}{2}\frac{1}{2}+\frac{1}{2}} D^{1}_{00}\left(\cos\beta_S\left|p\uparrow\right\rangle|n\downarrow\rangle + \cos\beta_S\left|p\downarrow\right\rangle|n\uparrow\rangle\right. \\
&\quad \left. - \sin\beta_S e^{-i\alpha_S}\left|p\uparrow\right\rangle|n\uparrow\rangle + \sin\beta_S e^{+i\alpha_S}\left|p\downarrow\right\rangle|n\downarrow\rangle\right) + C^{11}_{\frac{1}{2}+\frac{1}{2}\frac{1}{2}+\frac{1}{2}} D^{1}_{10}\left(\cos\beta_S|n\uparrow\rangle|n\downarrow\rangle\right. \\
&\quad \left. + \cos\beta_S|n\downarrow\rangle|n\uparrow\rangle - \sin\beta_S e^{-i\alpha_S}|n\uparrow\rangle|n\uparrow\rangle + \sin\beta_S e^{+i\alpha_S}|n\downarrow\rangle|n\downarrow\rangle\right) \\
&\quad + C^{1-1}_{\frac{1}{2}-\frac{1}{2}\frac{1}{2}-\frac{1}{2}} D^{1}_{-10}\left(\cos\beta_S\left|p\uparrow\right\rangle\left|p\downarrow\right\rangle + \cos\beta_S\left|p\downarrow\right\rangle\left|p\uparrow\right\rangle - \sin\beta_S e^{-i\alpha_S}\left|p\uparrow\right\rangle\left|p\uparrow\right\rangle\right. \\
&\quad \left. + \sin\beta_S e^{+i\alpha_S}\left|p\downarrow\right\rangle\left|p\downarrow\right\rangle\right)\Big] \\
&= \frac{z_{11}^{*}}{2}\Big[\cos\beta_T\left(\cos\beta_S|n\uparrow\rangle\left|p\downarrow\right\rangle + \cos\beta_S|n\downarrow\rangle\left|p\uparrow\right\rangle - \sin\beta_S e^{-i\alpha_S}|n\uparrow\rangle\left|p\uparrow\right\rangle\right. \\
&\quad \left. + \sin\beta_S e^{+i\alpha_S}|n\downarrow\rangle\left|p\downarrow\right\rangle\right) + \cos\beta_T\left(\cos\beta_S\left|p\uparrow\right\rangle|n\downarrow\rangle + \cos\beta_S\left|p\downarrow\right\rangle|n\uparrow\rangle\right. \\
&\quad \left. - \sin\beta_S e^{-i\alpha_S}\left|p\uparrow\right\rangle|n\uparrow\rangle + \sin\beta_S e^{+i\alpha_S}\left|p\downarrow\right\rangle|n\downarrow\rangle\right) - \sin\beta_T e^{-i\alpha_T}\left(\cos\beta_S|n\uparrow\rangle|n\downarrow\rangle\right. \\
&\quad \left. + \cos\beta_S|n\downarrow\rangle|n\uparrow\rangle - \sin\beta_S e^{-i\alpha_S}|n\uparrow\rangle|n\uparrow\rangle + \sin\beta_S e^{+i\alpha_S}|n\downarrow\rangle|n\downarrow\rangle\right) \\
&\quad + \sin\beta_T e^{+i\alpha_T}\left(\cos\beta_S\left|p\uparrow\right\rangle\left|p\downarrow\right\rangle + \cos\beta_S\left|p\downarrow\right\rangle\left|p\uparrow\right\rangle - \sin\beta_S e^{-i\alpha_S}\left|p\uparrow\right\rangle\left|p\uparrow\right\rangle\right. \\
&\quad \left. + \sin\beta_S e^{+i\alpha_S}\left|p\downarrow\right\rangle\left|p\downarrow\right\rangle\right)\Big].
\end{aligned}
$$

C

Rotated Thouless matrix

We shall list the elements of the rotates Thouless matrix, following subsection 4.5.2. Starting with the diagonal

$$
\begin{aligned}
(\mathcal{Z}^{+}_{\mathrm{rot}})_{11} &= \frac{z^{*}_{11}}{2}\sin\beta_T e^{-i\alpha_T}\sin\beta_S e^{-i\alpha_S},\\
(\mathcal{Z}^{+}_{\mathrm{rot}})_{22} &= -\frac{z^{*}_{11}}{2}\sin\beta_T e^{-i\alpha_T}\sin\beta_S e^{+i\alpha_S},\\
(\mathcal{Z}^{+}_{\mathrm{rot}})_{33} &= -\frac{z^{*}_{11}}{2}\sin\beta_T e^{+i\alpha_T}\sin\beta_S e^{-i\alpha_S},\\
(\mathcal{Z}^{+}_{\mathrm{rot}})_{44} &= \frac{z^{*}_{11}}{2}\sin\beta_T e^{+i\alpha_T}\sin\beta_S e^{+i\alpha_S},
\end{aligned}
$$

the anti-diagonal

$$
\begin{aligned}
(\mathcal{Z}^{+}_{\mathrm{rot}})_{14} &= \frac{z^{*}_{00}}{2}+\frac{z^{*}_{10}}{2}\cos\beta_S+\frac{z^{*}_{01}}{2}\cos\beta_T+\frac{z^{*}_{11}}{2}\cos\beta_T\cos\beta_S,\\
(\mathcal{Z}^{+}_{\mathrm{rot}})_{23} &= -\frac{z^{*}_{00}}{2}+\frac{z^{*}_{10}}{2}\cos\beta_S-\frac{z^{*}_{01}}{2}\cos\beta_T+\frac{z^{*}_{11}}{2}\cos\beta_T\cos\beta_S,\\
(\mathcal{Z}^{+}_{\mathrm{rot}})_{32} &= -\frac{z^{*}_{00}}{2}-\frac{z^{*}_{10}}{2}\cos\beta_S+\frac{z^{*}_{01}}{2}\cos\beta_T+\frac{z^{*}_{11}}{2}\cos\beta_T\cos\beta_S,\\
(\mathcal{Z}^{+}_{\mathrm{rot}})_{41} &= \frac{z^{*}_{00}}{2}-\frac{z^{*}_{10}}{2}\cos\beta_S-\frac{z^{*}_{01}}{2}\cos\beta_T+\frac{z^{*}_{11}}{2}\cos\beta_T\cos\beta_S,
\end{aligned}
$$

and lastly the off-diagonal

$$
\begin{aligned}
(\mathcal{Z}^{+}_{\mathrm{rot}})_{12} &= -\frac{z^{*}_{01}}{2}\sin\beta_T e^{-i\alpha_T} - \frac{z^{*}_{11}}{2}\sin\beta_T e^{-i\alpha_T}\cos\beta_S = \sin\beta_T e^{-i\alpha_T}\left(-\frac{z^{*}_{01}}{2} - \frac{z^{*}_{11}}{2}\cos\beta_S\right),\\
(\mathcal{Z}^{+}_{\mathrm{rot}})_{13} &= -\frac{z^{*}_{10}}{2}\sin\beta_S e^{-i\alpha_S} - \frac{z^{*}_{11}}{2}\cos\beta_T\sin\beta_S e^{-i\alpha_S} = \sin\beta_S e^{-i\alpha_S}\left(-\frac{z^{*}_{10}}{2} - \frac{z^{*}_{11}}{2}\cos\beta_T\right),\\
(\mathcal{Z}^{+}_{\mathrm{rot}})_{21} &= +\frac{z^{*}_{01}}{2}\sin\beta_T e^{-i\alpha_T} - \frac{z^{*}_{11}}{2}\sin\beta_T e^{-i\alpha_T}\cos\beta_S = \sin\beta_T e^{-i\alpha_T}\left(+\frac{z^{*}_{01}}{2} - \frac{z^{*}_{11}}{2}\cos\beta_S\right),\\
(\mathcal{Z}^{+}_{\mathrm{rot}})_{24} &= +\frac{z^{*}_{10}}{2}\sin\beta_S e^{+i\alpha_S} + \frac{z^{*}_{11}}{2}\cos\beta_T\sin\beta_S e^{+i\alpha_S} = \sin\beta_S e^{+i\alpha_S}\left(+\frac{z^{*}_{10}}{2} + \frac{z^{*}_{11}}{2}\cos\beta_T\right),\\
(\mathcal{Z}^{+}_{\mathrm{rot}})_{31} &= +\frac{z^{*}_{10}}{2}\sin\beta_S e^{-i\alpha_S} - \frac{z^{*}_{11}}{2}\cos\beta_T\sin\beta_S e^{-i\alpha_S} = \sin\beta_S e^{-i\alpha_S}\left(+\frac{z^{*}_{10}}{2} - \frac{z^{*}_{11}}{2}\cos\beta_T\right),\\
(\mathcal{Z}^{+}_{\mathrm{rot}})_{34} &= +\frac{z^{*}_{01}}{2}\sin\beta_T e^{+i\alpha_T} + \frac{z^{*}_{11}}{2}\cos\beta_S\sin\beta_T e^{+i\alpha_T} = \sin\beta_T e^{+i\alpha_T}\left(+\frac{z^{*}_{01}}{2} + \frac{z^{*}_{11}}{2}\cos\beta_S\right),\\
(\mathcal{Z}^{+}_{\mathrm{rot}})_{42} &= -\frac{z^{*}_{10}}{2}\sin\beta_S e^{+i\alpha_S} + \frac{z^{*}_{11}}{2}\cos\beta_T\sin\beta_S e^{+i\alpha_S} = \sin\beta_S e^{+i\alpha_S}\left(-\frac{z^{*}_{10}}{2} + \frac{z^{*}_{11}}{2}\cos\beta_T\right),\\
(\mathcal{Z}^{+}_{\mathrm{rot}})_{43} &= -\frac{z^{*}_{01}}{2}\sin\beta_T e^{+i\alpha_T} + \frac{z^{*}_{01}}{2}\sin\beta_T e^{+i\alpha_T}\cos\beta_S = \sin\beta_T e^{+i\alpha_T}\left(-\frac{z^{*}_{01}}{2} + \frac{z^{*}_{11}}{2}\cos\beta_S\right).
\end{aligned}
$$

We can easily verify that, as we started from a state that was aligned to the z axis, if $\beta_S = \beta_T = 0$ (i.e., if we also do not rotate over the y axis), all matrix elements outside of the anti-diagonal vanish and we recover the z-aligned matrix. Although redundant, we also write the matrix elements of $\mathcal{Z}_{\mathrm{rot}}$ explicitly, as those will be used to obtain the pairing tensor. Again, for the diagonal

$$
\begin{aligned}
(\mathcal{Z}_{\mathrm{rot}})_{11} &= \frac{z_{11}}{2}\sin\beta_T e^{+i\alpha_T}\sin\beta_S e^{+i\alpha_S}, &\text{(C.0.1)}\\
(\mathcal{Z}_{\mathrm{rot}})_{22} &= -\frac{z_{11}}{2}\sin\beta_T e^{+i\alpha_T}\sin\beta_S e^{-i\alpha_S}, &\text{(C.0.2)}\\
(\mathcal{Z}_{\mathrm{rot}})_{33} &= -\frac{z_{11}}{2}\sin\beta_T e^{-i\alpha_T}\sin\beta_S e^{+i\alpha_S}, &\text{(C.0.3)}\\
(\mathcal{Z}_{\mathrm{rot}})_{44} &= \frac{z_{11}}{2}\sin\beta_T e^{-i\alpha_T}\sin\beta_S e^{-i\alpha_S}, &\text{(C.0.4)}
\end{aligned}
$$

the anti-diagonal

$$
\begin{aligned}
(\mathcal{Z}_{\mathrm{rot}})_{41} &= \frac{z_{00}}{2} + \frac{z_{10}}{2}\cos\beta_S + \frac{z_{01}}{2}\cos\beta_T + \frac{z_{11}}{2}\cos\beta_T\cos\beta_S,\\
(\mathcal{Z}_{\mathrm{rot}})_{32} &= -\frac{z_{00}}{2} + \frac{z_{10}}{2}\cos\beta_S - \frac{z_{01}}{2}\cos\beta_T + \frac{z_{11}}{2}\cos\beta_T\cos\beta_S,\\
(\mathcal{Z}_{\mathrm{rot}})_{23} &= -\frac{z_{00}}{2} - \frac{z_{10}}{2}\cos\beta_S + \frac{z_{01}}{2}\cos\beta_T + \frac{z_{11}}{2}\cos\beta_T\cos\beta_S,\\
(\mathcal{Z}_{\mathrm{rot}})_{14} &= \frac{z_{00}}{2} - \frac{z_{10}}{2}\cos\beta_S - \frac{z_{01}}{2}\cos\beta_T + \frac{z_{11}}{2}\cos\beta_T\cos\beta_S,
\end{aligned}
$$

and lastly the off-diagonal

$$
\begin{aligned}
(\mathcal{Z}_{\mathrm{rot}})_{21} &= \sin\beta_T e^{+i\alpha_T}\left(-\frac{z_{01}}{2}-\frac{z_{11}}{2}\cos\beta_S\right),\\
(\mathcal{Z}_{\mathrm{rot}})_{31} &= \sin\beta_S e^{+i\alpha_S}\left(-\frac{z_{10}}{2}-\frac{z_{11}}{2}\cos\beta_T\right),\\
(\mathcal{Z}_{\mathrm{rot}})_{12} &= \sin\beta_T e^{+i\alpha_T}\left(+\frac{z_{01}}{2}-\frac{z_{11}}{2}\cos\beta_S\right),\\
(\mathcal{Z}_{\mathrm{rot}})_{42} &= \sin\beta_S e^{-i\alpha_S}\left(+\frac{z_{10}}{2}+\frac{z_{11}}{2}\cos\beta_T\right),\\
(\mathcal{Z}_{\mathrm{rot}})_{13} &= \sin\beta_S e^{+i\alpha_S}\left(+\frac{z_{10}}{2}-\frac{z_{11}}{2}\cos\beta_T\right),\\
(\mathcal{Z}_{\mathrm{rot}})_{43} &= \sin\beta_T e^{-i\alpha_T}\left(+\frac{z_{01}}{2}+\frac{z_{11}}{2}\cos\beta_S\right),\\
(\mathcal{Z}_{\mathrm{rot}})_{24} &= \sin\beta_S e^{-i\alpha_S}\left(-\frac{z_{10}}{2}+\frac{z_{11}}{2}\cos\beta_T\right),\\
(\mathcal{Z}_{\mathrm{rot}})_{34} &= \sin\beta_T e^{-i\alpha_T}\left(-\frac{z_{01}}{2}+\frac{z_{11}}{2}\cos\beta_S\right).
\end{aligned}
$$

D

Partial derivatives of the rotated Thouless matrix

Here we include the partial derivatives of the Thouless submatrix with respect to the anti-diagonal and off-diagonal elements. These expressions are listed for completeness, but should not overload the message of Chapter 4. They follow the notation and remarks of section 4.5.3. For the anti-diagonal, the partial derivatives will be similar, but have exchanged signs due to derivatives with respect to different z_i. Explicitly, they read

$$\begin{aligned}
\frac{\partial}{\partial(\mathscr{T}_{\text{rot}})_{41}} &= 1/\frac{\partial(\mathscr{T}_{\text{rot}})_{41}}{\partial z_{00}}\frac{\partial}{\partial z_{00}} + 1/\frac{\partial(\mathscr{T}_{\text{rot}})_{41}}{\partial z_{10}}\frac{\partial}{\partial z_{10}} + 1/\frac{\partial(\mathscr{T}_{\text{rot}})_{41}}{\partial z_{01}}\frac{\partial}{\partial z_{01}} + 1/\frac{\partial(\mathscr{T}_{\text{rot}})_{41}}{\partial z_{11}}\frac{\partial}{\partial z_{11}} + \partial(\alpha\beta)_{41} \\
&= \frac{\partial}{\partial z_{00}} + \frac{2}{\cos\beta_S}\frac{\partial}{\partial z_{10}} + \frac{2}{\cos\beta_T}\frac{\partial}{\partial z_{01}} + \frac{2}{\cos\beta_S\cos\beta_T}\frac{\partial}{\partial z_{11}} + \partial(\alpha\beta)_{41} \\
&= \frac{1}{4}\left[\left(1 + \frac{2}{\cos\beta_S} + \frac{2}{\cos\beta_T} + \frac{2}{\cos\beta_S\beta_T}\right)\frac{\partial}{\partial z_+} + \left(1 - \frac{2}{\cos\beta_S} - \frac{2}{\cos\beta_T} + \frac{2}{\cos\beta_S\beta_T}\right)\frac{\partial}{\partial \bar{z}_+}\right. \\
&\quad \left. + \left(-1 + \frac{2}{\cos\beta_S} - \frac{2}{\cos\beta_T} + \frac{2}{\cos\beta_S\beta_T}\right)\frac{\partial}{\partial z_-} + \left(-1 - \frac{2}{\cos\beta_S} + \frac{2}{\cos\beta_T} + \frac{2}{\cos\beta_S\beta_T}\right)\frac{\partial}{\partial \bar{z}_-}\right] \\
&\quad + \partial(\alpha\beta)_{41},
\end{aligned}$$

$$\begin{aligned}
\frac{\partial}{\partial(\mathscr{T}_{\text{rot}})_{32}} &= -\frac{\partial}{\partial z_{00}} + \frac{2}{\cos\beta_S}\frac{\partial}{\partial z_{10}} - \frac{2}{\cos\beta_T}\frac{\partial}{\partial z_{01}} + \frac{2}{\cos\beta_S\cos\beta_T}\frac{\partial}{\partial z_{11}} + \partial(\alpha\beta)_{32} \\
&= \frac{1}{4}\left[\left(-1 + \frac{2}{\cos\beta_S} - \frac{2}{\cos\beta_T} + \frac{2}{\cos\beta_S\beta_T}\right)\frac{\partial}{\partial z_+} + \left(-1 - \frac{2}{\cos\beta_S} + \frac{2}{\cos\beta_T} + \frac{2}{\cos\beta_S\beta_T}\right)\frac{\partial}{\partial \bar{z}_+}\right. \\
&\quad \left. + \left(1 + \frac{2}{\cos\beta_S} + \frac{2}{\cos\beta_T} + \frac{2}{\cos\beta_S\beta_T}\right)\frac{\partial}{\partial z_-} + \left(1 - \frac{2}{\cos\beta_S} - \frac{2}{\cos\beta_T} + \frac{2}{\cos\beta_S\beta_T}\right)\frac{\partial}{\partial \bar{z}_-}\right] \\
&\quad + \partial(\alpha\beta)_{32},
\end{aligned}$$

$$\begin{aligned}\frac{\partial}{\partial(\mathscr{Z}_{\mathrm{rot}})_{23}} &= -\frac{\partial}{\partial z_{00}} - \frac{2}{\cos\beta_S}\frac{\partial}{\partial z_{10}} + \frac{2}{\cos\beta_T}\frac{\partial}{\partial z_{01}} + \frac{2}{\cos\beta_S\cos\beta_T}\frac{\partial}{\partial z_{11}} + \partial(\alpha\beta)_{23} \\ &= \frac{1}{4}\left[\left(-1 - \frac{2}{\cos\beta_S} + \frac{2}{\cos\beta_T} + \frac{2}{\cos\beta_S\beta_T}\right)\frac{\partial}{\partial z_+} + \left(-1 + \frac{2}{\cos\beta_S} - \frac{2}{\cos\beta_T} + \frac{2}{\cos\beta_S\beta_T}\right)\frac{\partial}{\partial \bar{z}_+}\right. \\ &\quad \left. + \left(1 - \frac{2}{\cos\beta_S} - \frac{2}{\cos\beta_T} + \frac{2}{\cos\beta_S\beta_T}\right)\frac{\partial}{\partial z_-} + \left(1 + \frac{2}{\cos\beta_S} + \frac{2}{\cos\beta_T} + \frac{2}{\cos\beta_S\beta_T}\right)\frac{\partial}{\partial \bar{z}_-}\right] \\ &\quad + \partial(\alpha\beta)_{23},\end{aligned}$$

and

$$\begin{aligned}\frac{\partial}{\partial(\mathscr{Z}_{\mathrm{rot}})_{14}} &= \frac{\partial}{\partial z_{00}} - \frac{2}{\cos\beta_S}\frac{\partial}{\partial z_{10}} - \frac{2}{\cos\beta_T}\frac{\partial}{\partial z_{01}} + \frac{2}{\cos\beta_S\cos\beta_T}\frac{\partial}{\partial z_{11}} + \partial(\alpha\beta)_{14} \\ &= \frac{1}{4}\left[\left(1 - \frac{2}{\cos\beta_S} - \frac{2}{\cos\beta_T} + \frac{2}{\cos\beta_S\beta_T}\right)\frac{\partial}{\partial z_+} + \left(1 + \frac{2}{\cos\beta_S} + \frac{2}{\cos\beta_T} + \frac{2}{\cos\beta_S\beta_T}\right)\frac{\partial}{\partial \bar{z}_+}\right. \\ &\quad \left. + \left(-1 - \frac{2}{\cos\beta_S} + \frac{2}{\cos\beta_T} + \frac{2}{\cos\beta_S\beta_T}\right)\frac{\partial}{\partial z_-} + \left(-1 + \frac{2}{\cos\beta_S} - \frac{2}{\cos\beta_T} + \frac{2}{\cos\beta_S\beta_T}\right)\frac{\partial}{\partial \bar{z}_-}\right] \\ &\quad + \partial(\alpha\beta)_{14}.\end{aligned}$$

Finally, the off-diagonal terms will have the following structure

$$\begin{aligned}\frac{\partial}{\partial(\mathscr{Z}_{\mathrm{rot}})_{21}} &= 1/\frac{\partial(\mathscr{Z}_{\mathrm{rot}})_{21}}{\partial z_{01}}\frac{\partial}{\partial z_{01}} + 1/\frac{\partial(\mathscr{Z}_{\mathrm{rot}})_{21}}{\partial z_{11}}\frac{\partial}{\partial z_{11}} + \partial(\alpha\beta)_{21} \\ &= -\frac{2}{\sin\beta_T e^{+i\alpha_T}}\left(\frac{\partial}{\partial z_{01}} + \frac{1}{\cos\beta_S}\frac{\partial}{\partial z_{11}}\right) + \partial(\alpha\beta)_{21} \\ &= -\frac{1}{2\sin\beta_T e^{+i\alpha_T}}\left[\left(1 + \frac{1}{\cos\beta_S}\right)\frac{\partial}{\partial z_+} + \left(-1 + \frac{1}{\cos\beta_S}\right)\frac{\partial}{\partial \bar{z}_+} + \left(-1 + \frac{1}{\cos\beta_S}\right)\frac{\partial}{\partial z_-}\right. \\ &\quad \left. + \left(1 + \frac{1}{\cos\beta_S}\right)\frac{\partial}{\partial \bar{z}_-}\right] + \partial(\alpha\beta)_{21},\end{aligned}$$

$$\begin{aligned}\frac{\partial}{\partial(\mathscr{Z}_{\mathrm{rot}})_{12}} &= -\frac{2}{\sin\beta_T e^{+i\alpha_T}}\left(-\frac{\partial}{\partial z_{01}} + \frac{1}{\cos\beta_S}\frac{\partial}{\partial z_{11}}\right) + \partial(\alpha\beta)_{12} \\ &= -\frac{1}{2\sin\beta_T e^{+i\alpha_T}}\left[\left(-1 + \frac{1}{\cos\beta_S}\right)\frac{\partial}{\partial z_+} + \left(1 + \frac{1}{\cos\beta_S}\right)\frac{\partial}{\partial \bar{z}_+} + \left(1 + \frac{1}{\cos\beta_S}\right)\frac{\partial}{\partial z_-}\right. \\ &\quad \left. + \left(-1 + \frac{1}{\cos\beta_S}\right)\frac{\partial}{\partial \bar{z}_-}\right] + \partial(\alpha\beta)_{12},\end{aligned}$$

$$\begin{aligned}\frac{\partial}{\partial(\mathscr{Z}_{\mathrm{rot}})_{43}} &= -\frac{2}{\sin\beta_T e^{-i\alpha_T}}\left(-\frac{\partial}{\partial z_{01}} - \frac{1}{\cos\beta_S}\frac{\partial}{\partial z_{11}}\right) + \partial(\alpha\beta)_{43} \\ &= -\frac{1}{2\sin\beta_T e^{-i\alpha_T}}\left[\left(-1 - \frac{1}{\cos\beta_S}\right)\frac{\partial}{\partial z_+} + \left(1 - \frac{1}{\cos\beta_S}\right)\frac{\partial}{\partial \bar{z}_+} + \left(1 - \frac{1}{\cos\beta_S}\right)\frac{\partial}{\partial z_-}\right. \\ &\quad \left. + \left(-1 - \frac{1}{\cos\beta_S}\right)\frac{\partial}{\partial \bar{z}_-}\right] + \partial(\alpha\beta)_{43},\end{aligned}$$

$$\begin{aligned}\frac{\partial}{\partial(\mathscr{Z}_{\rm rot})_{34}} &= -\frac{2}{\sin\beta_T e^{-i\alpha_T}}\left(\frac{\partial}{\partial z_{01}}-\frac{1}{\cos\beta_S}\frac{\partial}{\partial z_{11}}\right)+\partial(\alpha\beta)_{34}\\ &= -\frac{1}{2\sin\beta_T e^{-i\alpha_T}}\left[\left(1-\frac{1}{\cos\beta_S}\right)\frac{\partial}{\partial z_+}+\left(-1-\frac{1}{\cos\beta_S}\right)\frac{\partial}{\partial\bar z_+}+\left(-1-\frac{1}{\cos\beta_S}\right)\frac{\partial}{\partial z_-}\right.\\ &\quad\left.+\left(1-\frac{1}{\cos\beta_S}\right)\frac{\partial}{\partial\bar z_-}\right]+\partial(\alpha\beta)_{34},\end{aligned}$$

$$\begin{aligned}\frac{\partial}{\partial(\mathscr{Z}_{\rm rot})_{31}} &= -\frac{2}{\sin\beta_S e^{+i\alpha_S}}\left(\frac{\partial}{\partial z_{10}}+\frac{1}{\cos\beta_T}\frac{\partial}{\partial z_{11}}\right)+\partial(\alpha\beta)_{31}\\ &= -\frac{1}{2\sin\beta_S e^{+i\alpha_S}}\left[\left(1+\frac{1}{\cos\beta_T}\right)\frac{\partial}{\partial z_+}+\left(-1+\frac{1}{\cos\beta_T}\right)\frac{\partial}{\partial\bar z_+}+\left(1+\frac{1}{\cos\beta_T}\right)\frac{\partial}{\partial z_-}\right.\\ &\quad\left.+\left(-1+\frac{1}{\cos\beta_T}\right)\frac{\partial}{\partial\bar z_-}\right]+\partial(\alpha\beta)_{31},\end{aligned}$$

$$\begin{aligned}\frac{\partial}{\partial(\mathscr{Z}_{\rm rot})_{13}} &= -\frac{2}{\sin\beta_S e^{+i\alpha_S}}\left(-\frac{\partial}{\partial z_{10}}+\frac{1}{\cos\beta_T}\frac{\partial}{\partial z_{11}}\right)+\partial(\alpha\beta)_{13}\\ &= -\frac{1}{2\sin\beta_S e^{+i\alpha_S}}\left[\left(-1+\frac{1}{\cos\beta_T}\right)\frac{\partial}{\partial z_+}+\left(1+\frac{1}{\cos\beta_T}\right)\frac{\partial}{\partial\bar z_+}+\left(-1+\frac{1}{\cos\beta_T}\right)\frac{\partial}{\partial z_-}\right.\\ &\quad\left.+\left(1+\frac{1}{\cos\beta_T}\right)\frac{\partial}{\partial\bar z_-}\right]+\partial(\alpha\beta)_{13},\end{aligned}$$

$$\begin{aligned}\frac{\partial}{\partial(\mathscr{Z}_{\rm rot})_{24}} &= -\frac{2}{\sin\beta_S e^{-i\alpha_S}}\left(\frac{\partial}{\partial z_{10}}-\frac{1}{\cos\beta_T}\frac{\partial}{\partial z_{11}}\right)+\partial(\alpha\beta)_{24}\\ &= -\frac{1}{2\sin\beta_S e^{-i\alpha_S}}\left[\left(1-\frac{1}{\cos\beta_T}\right)\frac{\partial}{\partial z_+}+\left(-1-\frac{1}{\cos\beta_T}\right)\frac{\partial}{\partial\bar z_+}+\left(1-\frac{1}{\cos\beta_T}\right)\frac{\partial}{\partial z_-}\right.\\ &\quad\left.+\left(-1-\frac{1}{\cos\beta_T}\right)\frac{\partial}{\partial\bar z_-}\right]+\partial(\alpha\beta)_{24},\end{aligned}$$

and

$$\begin{aligned}\frac{\partial}{\partial(\mathscr{Z}_{\rm rot})_{42}} &= -\frac{2}{\sin\beta_S e^{-i\alpha_S}}\left(-\frac{\partial}{\partial z_{10}}-\frac{1}{\cos\beta_T}\frac{\partial}{\partial z_{11}}\right)+\partial(\alpha\beta)_{42}\\ &= -\frac{1}{2\sin\beta_S e^{-i\alpha_S}}\left[\left(-1-\frac{1}{\cos\beta_T}\right)\frac{\partial}{\partial z_+}+\left(1-\frac{1}{\cos\beta_T}\right)\frac{\partial}{\partial\bar z_+}+\left(-1-\frac{1}{\cos\beta_T}\right)\frac{\partial}{\partial z_-}\right.\\ &\quad\left.+\left(1-\frac{1}{\cos\beta_T}\right)\frac{\partial}{\partial\bar z_-}\right]+\partial(\alpha\beta)_{42}.\end{aligned}$$

E

Details of the Gaussian Separalisation Method (GSM) implementation

This appendix serves as a guideline to those wishing to adapt the GSM to their own density functional theory code. As such, it will focus solely on computational details not discussed in Chapter 8. For rendering purposes, the graphic algorithmic structure is hosted alongside the GSM database (Backes 2026), under the name loop-structure.pdf, and consists of a companion document to this appendix*.

The algorithm is a one-to-one correspondence to the implementation in HFODD. Before entering the loops for contractions, one should:

- Diagonalise the Gaussian matrix elements, grouping the indices according to the notes on chapter 8, eqs. (8.2.9), (8.2.10), and (8.2.11);
- Separate the symmetric/antisymmetric eigenvectors, and sum/subtract the pairs of indices outside the diagonal, as they will be counted twice in the main algorithm;
- Establish the limits of the eigenvalue loops by first comparing the product of the eigenvalues with the cutoff value. This process should be done separately for each different product of symmetric/antisymmetric eigenvalues, and the cutoff should be compared to the product $|\lambda_i| \leq \lambda_c$, $|\lambda_i \lambda_j| \leq \lambda_c$, $|\lambda_i \lambda_j \lambda_l| \leq \lambda_c$

In terms of notation, in the file loop-structure.pdf, we utilise the following conventions:

- Eigenvalues linked to symmetric eigenvectors are denoted as $\lambda_{i,j,l+}$;
- Eigenvalues linked to antisymmetric eigenvectors are denoted as $\lambda_{i,j,l-}$;

*Those curious enough to open the document should find it very clear that the graphic representation is not very printable or A4-friendly.

- When a pair of indices is symmetrised, it is denoted between parentheses, (n, m);
- When a pair of indices is antisymmetrised, it is denoted between square brackets, $[n, m]$.

All loops over symmetrised/antisymmetrised indices skip the redundant HO quanta indices. It is important to note that the document serves as guidance with respect to:

- Where each array should be initialised and set to zero;
- Which indices should be kept, and which indices can be omitted to save memory (the latter are marked in red);
- How the limits of the loops should be written to avoid symmetric m, n pairs in the current index contraction;
- Where to symmetryse/antisymmetrise arrays;
- List the ideal index order to minimise cache misses.

Abiding by these rules is fundamental; apparently minor things, such as index order, can have a big impact on the timing.

A technical aspect to note is that the GSM does require more memory than the usual implementation. This can be remedied by allocating the intermediate arrays to the precise size, determined after counting which eigenvalues will be kept, as well as keeping track of indices that do not need to be stored.

Bibliography

Abbott, B. P., R. Abbott et al. (2017). *Phys. Rev. Lett.* 119 (16), p. 161101. DOI: 10.1103/PhysRevLett.119.161101. URL: https://link.aps.org/doi/10.1103/PhysRevLett.119.161101 (cit. on p. 110).

——— (2018). *Phys. Rev. Lett.* 121 (16), p. 161101. DOI: 10.1103/PhysRevLett.121.161101. URL: https://link.aps.org/doi/10.1103/PhysRevLett.121.161101 (cit. on pp. 110, 121).

Anderson, P. W. (1972). 'More Is Different'. *Science* 177.4047, pp. 393–396. DOI: 10.1126/science.177.4047.393. eprint: https://www.science.org/doi/pdf/10.1126/science.177.4047.393. URL: https://www.science.org/doi/abs/10.1126/science.177.4047.393 (cit. on p. 2).

Annala, E., T. Gorda, A. Kurkela et al. (2020). 'Evidence for quark-matter cores in massive neutron stars'. *Nature Physics* 16.9, pp. 907–910. DOI: 10.1038/s41567-020-0914-9. URL: https://doi.org/10.1038/s41567-020-0914-9 (cit. on pp. 113, 118).

Aoki, Y. et al. (2009). 'The QCD transition temperature: results with physical masses in the continuum limit II.' *JHEP* 06, p. 088. DOI: 10.1088/1126-6708/2009/06/088. arXiv: 0903.4155 [hep-lat] (cit. on p. 112).

Arora, Sanjeev and Boaz Barak (2009). *Computational Complexity: A Modern Approach*. Cambridge University Press. ISBN: 9780521424264. URL: https://theory.cs.princeton.edu/complexity/ (cit. on p. 89).

Baade, W. and F. Zwicky (1934). 'On Super-Novae'. *Proceedings of the National Academy of Sciences* 20.5, pp. 254–259. DOI: 10.1073/pnas.20.5.254. eprint: https://www.pnas.org/doi/pdf/10.1073/pnas.20.5.254. URL: https://www.pnas.org/doi/abs/10.1073/pnas.20.5.254 (cit. on p. 113).

Backes, B. C. (2025). *Database for Quadrupole Strength in Isobaric Triplets*. Online available at: https://webfiles.york.ac.uk/HFODD/Projects/Isobaric_Triplets/ (cit. on p. 81).

——— (2026). *Database for the Gaussian Separalisation Method*. Online available at: https://github.com/b-backes/gsm and https://webfiles.york.ac.uk/HFODD/Projects/Gaussian_Separalisation_Method/ (cit. on pp. 108, 138).

Backes, B. C., J. Dobaczewski et al. (2025). 'Quadrupole strength in isobaric triplets'. *Phys. Rev. C* 112 (6), p. 064311. DOI: 10.1103/5wkc-7gmf. URL: https://link.aps.org/doi/10.1103/5wkc-7gmf (cit. on pp. 72, 77, 81).

Backes, Betânia C, Eduardo Hafemann et al. (2021). 'Density-dependent quark mass model revisited: thermodynamic consistency, stability windows and stellar properties'. *Journal of Physics G: Nuclear and Particle Physics* 48.5, p. 055104. DOI: 10.1088/1361-6471/abc6e9. URL: https://doi.org/10.1088/1361-6471/abc6e9 (cit. on p. 115).

Backes, Betânia C. T., Kauan D. Marquezb and Débora P. Menezes (2021). 'Effects of strong magnetic fields on the hadron-quark deconfinement transition'. *The European Physical Journal A* 57.7. ISSN: 1434-601X. DOI: 10.1140/epja/s10050-021-00544-2. URL: http://dx.doi.org/10.1140/epja/s10050-021-00544-2 (cit. on p. 115).

Baran, A et al. (2011). 'Quadrupole collective inertia in nuclear fission: Cranking approximation'. *Physical Review C* 84.5, p. 054321 (cit. on p. 73).

Bardeen, J., L. N. Cooper and J. R. Schrieffer (1957). 'Theory of Superconductivity'. *Phys. Rev.* 108 (5), pp. 1175–1204. DOI: 10.1103/PhysRev.108.1175. URL: https://link.aps.org/doi/10.1103/PhysRev.108.1175 (cit. on pp. 6, 24).

Bartlett, Rodney J. (2010). 'Ab initio DFT and its role in electronic structure theory'. *Molecular Physics* 108.21-23, pp. 3299–3311. DOI: 10.1080/00268976.2010.532818. eprint: https://doi.org/10.1080/00268976.2010.532818. URL: https://doi.org/10.1080/00268976.2010.532818 (cit. on p. 4).

Bazavov, A. et al. (2012). 'Chiral and deconfinement aspects of the QCD transition'. *Phys. Rev. D* 85 (5), p. 054503. DOI: 10.1103/PhysRevD.85.054503. URL: https://link.aps.org/doi/10.1103/PhysRevD.85.054503 (cit. on p. 112).

Bender, M., K. Rutz et al. (2000). 'Pairing gaps from nuclear mean-field models'. *The European Physical Journal A* 8, pp. 59–75. DOI: 10.1007/s10050-000-4504-z. arXiv: nucl-th/0005028 [nucl-th] (cit. on p. 50).

Bender, Michael, Karim Bennaceur and Valentin Guillon (2026). *Parameter adjustment of nuclear leading-order local pairing energy density functionals*. arXiv: 2603.13164 [nucl-th]. URL: https://arxiv.org/abs/2603.13164 (cit. on p. 25).

Bender, Michael, Paul-Henri Heenen and Paul-Gerhard Reinhard (2003). 'Self-consistent mean-field models for nuclear structure'. *Rev. Mod. Phys.* 75 (1), pp. 121–180. DOI: 10.1103/RevModPhys.75.121. URL: https://link.aps.org/doi/10.1103/RevModPhys.75.121 (cit. on p. 4).

Bennaceur, K, J Dobaczewski, T Haverinen et al. (2020). 'Regularized pseudopotential for mean-field calculations'. *Journal of Physics: Conference Series* 1643.1, p. 012112. ISSN: 1742-6596. DOI: 10.1088/1742-6596/1643/1/012112. URL: http://dx.doi.org/10.1088/1742-6596/1643/1/012112 (cit. on p. 103).

Bennaceur, K., J. Dobaczewski and F. Raimondi (2014). 'New density-independent interactions for nuclear structure calculations'. *EPJ Web of Conferences* 66, p. 02031. DOI: 10.1051/epjconf/20146602031. URL: http://dx.doi.org/10.1051/epjconf/20146602031 (cit. on p. 79).

Bentley, M.A. and S.M. Lenzi (2007). 'Coulomb energy differences between high-spin states in isobaric multiplets'. *Progress in Particle and Nuclear Physics* 59.2, pp. 497–561. ISSN: 0146-6410. DOI: https://doi.org/10.1016/j.ppnp.2006.10.001. URL: https://www.sciencedirect.com/science/article/pii/S0146641006000743 (cit. on p. 64).

Bertsch, G. F., B. Sabbey and M. Uusnäkki (2005). 'Fitting theories of nuclear binding energies'. *Physical Review C* 71.5. ISSN: 1089-490X. DOI: 10.1103/physrevc.71.054311. URL: http://dx.doi.org/10.1103/PhysRevC.71.054311 (cit. on p. 103).

Bethe, H. A. and R. F. Bacher (1936). 'Nuclear Physics. A. Stationary States of Nuclei'. *Reviews of Modern Physics* 8.2. DOI: 10.1103/RevModPhys.8.82. URL: https://doi.org/10.1103/RevModPhys.8.82 (cit. on p. 5).

Bissell, M. L. et al. (2026). *Interrogating the composition and distribution of nuclear magnetization via the hyperfine anomaly: experiment meets nuclear and atomic theory for short-lived* ^{47}K. arXiv: 2603.20090 [nucl-ex]. URL: https://arxiv.org/abs/2603.20090 (cit. on p. 86).

Bogoliubov, N. N. (1958). 'On a Variational Principle in the Many-Body Problem'. *Soviet Physics Doklady* 3, p. 292 (cit. on p. 6).

Bohr, Aage and Ben R Mottelson (1998). *Nuclear Structure*. World Scientific Publishing Company. DOI: 10.1142/3530. eprint: https://www.worldscientific.com/doi/pdf/10.1142/3530. URL: https://www.worldscientific.com/doi/abs/10.1142/3530 (cit. on p. 25).

Bohr, Aage, Ben R. Mottelson and David Pines (1958). 'Possible Analogy between the Excitation Spectra of Nuclei and Those of the Superconducting Metallic State'. *Physical Review* 110, pp. 936–938. DOI: 10.1103/PhysRev.110.936 (cit. on p. 6).

Bombaci, Ignazio (2017). 'The Hyperon Puzzle in Neutron Stars'. In: *Proceedings of the 12th International Conference on Hypernuclear and Strange Particle Physics (HYP2015*, 101002, p. 101002. DOI: 10.7566/JPSCP.17.101002 (cit. on p. 114).

Bonnard, J. et al. (2023). 'Nuclear DFT electromagnetic moments in heavy deformed open-shell odd nuclei'. *Physics Letters B* 843, p. 138014. ISSN: 0370-2693. DOI: 10.1016/j.physletb.2023.138014. URL: http://dx.doi.org/10.1016/j.physletb.2023.138014 (cit. on pp. 48, 50).

Boso, A. et al. (2019). 'Isospin dependence of electromagnetic transition strengths among an isobaric triplet'. *Physics Letters B* 797, p. 134835. ISSN: 0370-2693. DOI: https://doi.org/10.1016/j.physletb.2019.134835. URL: https://www.sciencedirect.com/science/article/pii/S0370269319305490 (cit. on pp. 66, 75).

Brack, M. et al. (1972). 'Funny Hills: The Shell-Correction Approach to Nuclear Shell Effects and Its Applications to the Fission Process'. *Rev. Mod. Phys.* 44 (2), pp. 320–405. DOI: 10.1103/RevModPhys.44.320. URL: https://link.aps.org/doi/10.1103/RevModPhys.44.320 (cit. on p. 73).

Brink, D.M. and J.P. Svenne (1970). 'Isospin mixing of hartree-fock solutions'. *Nuclear Physics A* 154.3, pp. 449–457. ISSN: 0375-9474. DOI: https://doi.org/10.1016/0375-9474(70)90117-X. URL: https://www.sciencedirect.com/science/article/pii/037594747090117X (cit. on p. 63).

Brink, David M. and Ricardo A. Broglia (2005). *Nuclear Superfluidity: Pairing in Finite Systems*. Vol. 24. Cambridge Monographs on Particle Physics, Nuclear Physics and Cosmology. Cambridge University Press. ISBN: 978-1139443074. DOI: 10.1017/CBO9780511534911 (cit. on p. 5).

Burgio, G.F. et al. (2021). 'Neutron stars and the nuclear equation of state'. *Progress in Particle and Nuclear Physics* 120, p. 103879. ISSN: 0146-6410. DOI: https://doi.org/10.1016/j.ppnp.2021.103879. URL: https://www.sciencedirect.com/science/article/pii/S0146641021000338 (cit. on p. 113).

Castel, B. and I. S. Towner (1990). *Modern Theories of Nuclear Moments*. Clarendon Press (cit. on pp. 48, 84).

Caurier, E. et al. (2005). 'The shell model as a unified view of nuclear structure'. *Reviews of Modern Physics* 77 (2), p. 427. DOI: 10.1103/RevModPhys.77.427. URL: https://doi-org.libproxy.york.ac.uk/10.1103/RevModPhys.77.427 (cit. on p. 87).

Chadwick, J. (1932). 'Possible Existence of a Neutron'. *Nature* 129.312. DOI: https://doi.org/10.1038/129312a0 (cit. on pp. 59, 113).

Colò, G. (2018). *Density Functional Theory (DFT) for atomic nuclei: a simple introduction*. arXiv: 1807.02643 [nucl-th]. URL: https://arxiv.org/abs/1807.02643 (cit. on p. 9).

Cooper, L. N., R. L. Mills and A. M. Sessler (1959). 'Possible Superfluidity of a System of Strongly Interacting Fermions'. *Phys. Rev.* 114 (6), pp. 1377–1382. DOI: 10.1103/PhysRev.114.1377. URL: https://link.aps.org/doi/10.1103/PhysRev.114.1377 (cit. on pp. 6, 24).

Da Costa, Philippe et al. (2024). 'Impact of choices for center-of-mass correction energy on the surface energy of Skyrme energy density functionals'. *Phys. Rev. C* 109 (3), p. 034316. DOI: 10.1103/PhysRevC.109.034316. URL: https://link.aps.org/doi/10.1103/PhysRevC.109.034316 (cit. on p. 25).

Dean, D. J. and M. Hjorth-Jensen (2003). 'Pairing in nuclear systems: from neutron stars to finite nuclei'. *Rev. Mod. Phys.* 75 (2), pp. 607–656. DOI: 10.1103/RevModPhys.75.607. URL: https://link.aps.org/doi/10.1103/RevModPhys.75.607 (cit. on pp. 6, 25).

Dechargé, J. and D. Gogny (1980). 'Hartree-Fock-Bogolyubov calculations with the $D1$ effective interaction on spherical nuclei'. *Phys. Rev. C* 21 (4), pp. 1568–1593. DOI: 10.1103/PhysRevC.21.1568. URL: https://link.aps.org/doi/10.1103/PhysRevC.21.1568 (cit. on pp. 13, 88).

Dobaczewski, J, P Bączyk et al. (2021). 'Solution of universal nonrelativistic nuclear DFT equations in the Cartesian deformed harmonic-oscillator basis. (IX) HFODD (v3.06h): a new version of the program'. *Journal of Physics G: Nuclear and Particle Physics* 48.10, p. 102001. ISSN: 1361-6471. DOI: 10.1088/1361-6471/ac0a82. URL: http://dx.doi.org/10.1088/1361-6471/ac0a82 (cit. on pp. 70, 94).

Dobaczewski, J, K Bennaceur and F Raimondi (2012). 'Effective theory for low-energy nuclear energy density functionals'. *Journal of Physics G: Nuclear and Particle Physics* 39.12, p. 125103. DOI: 10.1088/0954-3899/39/12/125103. URL: https://doi.org/10.1088/0954-3899/39/12/125103 (cit. on p. 88).

Dobaczewski, J. et al. (2026). *Code HFODD, version to be published* (cit. on pp. 70, 96, 108).

Dobaczewski, J., B. C. Backes et al. (2026). *Electromagnetic and Exotic Moments in Nuclear DFT*. arXiv: 2511.04632 [nucl-th]. URL: https://arxiv.org/abs/2511.04632 (cit. on pp. 14, 83, 86).

Dobaczewski, J. and J. Dudek (1997). 'Solution of the Skyrme-Hartree-Fock equations in the Cartesian deformed harmonic oscillator basis I. The method'. *Comput. Phys. Comm.* 102.1, pp. 166–182. ISSN: 0010-4655. DOI: https://doi.org/10.1016/S0010-4655(97)00004-0. URL: http://www.sciencedirect.com/science/article/pii/S0010465597000040 (cit. on pp. 92, 94).

Dobaczewski, J. and W. Nazarewicz (1993). 'Comment on "Pairing correlations studied in the two-level model"'. *Phys. Rev. C* 47 (5), pp. 2418–2421. DOI: 10.1103/PhysRevC.47.2418. URL: https://link.aps.org/doi/10.1103/PhysRevC.47.2418 (cit. on p. 50).

Dobaczewski, J., W. Nazarewicz and M. V. Stoitsov (2002). 'Nuclear ground-state properties from mean-field calculations'. *The European Physical Journal A* 15, pp. 21–26. DOI: 10.1140/epja/i2001-10218-8. arXiv: nucl-th/0203060 [nucl-th] (cit. on p. 50).

Dobaczewski, J., W. Satuła et al. (2009a). 'Solution of the Skyrme–Hartree–Fock–Bogolyubov equations in the Cartesian deformed harmonic-oscillator basis.' *Computer Physics Communications* 180.11, pp. 2361–2391. ISSN: 0010-4655. DOI: 10.1016/j.cpc.2009.08.009. URL: http://dx.doi.org/10.1016/j.cpc.2009.08.009 (cit. on pp. 87, 88, 91, 95).

——— (2009b). 'Solution of the Skyrme–Hartree–Fock–Bogolyubov equations in the Cartesian deformed harmonic-oscillator basis.: (VI) hfodd (v2.40h): A new version of the program'. *Computer Physics Communications* 180.11, pp. 2361–2391. ISSN: 0010-4655. DOI: https://doi.org/10.1016/j.cpc.2009.08.009. URL: https://www.sciencedirect.com/science/article/pii/S0010465509002598 (cit. on pp. 12, 70).

Dobaczewski, Jacek (2009). 'Lipkin translational-symmetry restoration in the mean-field and energy–density-functional methods'. *Journal of Physics G: Nuclear and Particle Physics* 36.10, p. 105105. ISSN: 1361-6471. DOI: 10.1088/0954-3899/36/10/105105. URL: http://dx.doi.org/10.1088/0954-3899/36/10/105105 (cit. on p. 50).

Dongarra, Jack et al. (2018). 'The Singular Value Decomposition: Anatomy of Optimizing an Algorithm for Extreme Scale'. *SIAM Review* 60. DOI: 10.1137/17M1117732 (cit. on p. 89).

Dreizler, Reiner M. and E. K. U. Gross (1990). *Density Functional Theory: An Approach to the Quantum Many-Body Problem*. Berlin: Springer. ISBN: 978-3-540-51993-7. DOI: 10.1007/978-3-642-86105-5 (cit. on p. 9).

Du, Lipei, Agnieszka Sorensen and Mikhail Stephanov (2024). 'The QCD phase diagram and Beam Energy Scan physics: A theory overview'. *International Journal of Modern Physics E* 33.07. ISSN: 1793-6608. DOI: 10.1142/s021830132430008x. URL: http://dx.doi.org/10.1142/S021830132430008X (cit. on p. 112).

Dutra, M. et al. (2014). *Phys. Rev. C* **90** (5), p. 055203. DOI: 10.1103/PhysRevC.90.055203. URL: https://link.aps.org/doi/10.1103/PhysRevC.90.055203 (cit. on p. 115).

Eberth, Jürgen, Richard A. Meyer and Kornelius Sistemich, eds. (1988). *Nuclear Structure of the Zirconium Region*. Berlin, Heidelberg: Springer Berlin Heidelberg. ISBN: 978-3-642-73958-3. URL: https://link.springer.com/book/10.1007/978-3-642-73958-3 (cit. on p. 72).

Ekström, A. et al. (2023). 'What is ab initio in nuclear theory?' *Frontiers in Physics* 11. DOI: 10.3389/fphy.2023.1129094. URL: https://www.frontiersin.org/articles/10.3389/fphy.2023.1129094 (cit. on p. 4).

Elgaroy, O. and M. Hjorth-Jensen (1997). *Properties of Pairing Correlations in Infinite Nuclear Matter*. arXiv: nucl-th/9710058 [nucl-th]. URL: https://arxiv.org/abs/nucl-th/9710058 (cit. on p. 25).

Elgarøy, Ø. et al. (1998). 'Minimal relativity and $^3S_1$-$^3D_1$ pairing in symmetric nuclear matter'. *Phys. Rev. C* 57 (3), R1069–R1072. DOI: 10.1103/PhysRevC.57.R1069. URL: https://link.aps.org/doi/10.1103/PhysRevC.57.R1069 (cit. on p. 25).

Emery, V. J. and A. M. Sessler (1960). 'Energy Gap in Nuclear Matter'. *Phys. Rev.* 119 (1), pp. 248–250. DOI: 10.1103/PhysRev.119.248. URL: https://link.aps.org/doi/10.1103/PhysRev.119.248 (cit. on p. 24).

Engel, J. et al. (1997). *Phys. Rev. C* 55 (4), pp. 1781–1788. DOI: 10.1103/PhysRevC.55.1781. URL: https://link.aps.org/doi/10.1103/PhysRevC.55.1781 (cit. on p. 81).

Engelbrecht, C. A. and R. H. Lemmer (1970). 'Isospin Polarization in the Nuclear Many-Body Problem'. *Phys. Rev. Lett.* 24 (11), pp. 607–611. DOI: 10.1103/PhysRevLett.24.607. URL: https://link.aps.org/doi/10.1103/PhysRevLett.24.607 (cit. on p. 63).

ENSDF (2023). Evaluated Nuclear Structure Data File. URL: http://www.nndc.bnl.gov/ensdf/, visited on 18th Sept. 2023 (cit. on pp. 52, 54, 55, 61).

Fracasso, S. and G. Colò (2005). 'Fully self-consistent charge-exchange quasiparticle random-phase approximation and its application to isobaric analog resonances'. *Physical Review C* 72.6. ISSN: 1089-490X. DOI: 10.1103/physrevc.72.064310. URL: http://dx.doi.org/10.1103/PhysRevC.72.064310 (cit. on p. 70).

——— (2007). 'Spin-isospin nuclear response using the existing microscopic Skyrme functionals'. *Physical Review C* 76.4. ISSN: 1089-490X. DOI: 10.1103/physrevc.76.044307. URL: http://dx.doi.org/10.1103/PhysRevC.76.044307 (cit. on p. 70).

Frauendorf, Stefan and Augusto O Macchiavelli (2014). 'Overview of neutron–proton pairing'. *Progress in Particle and Nuclear Physics* 78, pp. 24–90 (cit. on pp. 6, 81).

Gerstung, Dominik, Norbert Kaiser and Wolfram Weise (2020). 'Hyperon–nucleon three-body forces and strangeness in neutron stars'. *The European Physical Journal A* 56.6. ISSN: 1434-601X. DOI: 10.1140/epja/s10050-020-00180-2. URL: http://dx.doi.org/10.1140/epja/s10050-020-00180-2 (cit. on p. 115).

Giles, M. M. et al. (2019). 'Probing isospin symmetry in the (^{50}Fe,^{50} Mn,^{50} Cr) isobaric triplet via electromagnetic transition rates'. *Phys. Rev. C* 99 (4), p. 044317. DOI: 10.1103/PhysRevC.99.044317. URL: https://link.aps.org/doi/10.1103/PhysRevC.99.044317 (cit. on p. 75).

——— (2021). 'Erratum: Probing isospin symmetry in the (^{50}Fe, ^{50}Mn, ^{50}Cr) isobaric triplet via electromagnetic transition rates [Phys. Rev. C 99, 044317 (2019)]'. *Phys. Rev. C* 104 (2), p. 029901. DOI: 10.1103/PhysRevC.104.029901. URL: https://link.aps.org/doi/10.1103/PhysRevC.104.029901 (cit. on p. 75).

Girod, M and B Grammaticos (1979). 'The zero-point energy correction and its effect on nuclear dynamics'. *Nuclear Physics A* 330.1, pp. 40–52 (cit. on p. 73).

——— (1983). 'Triaxial Hartree-Fock-Bogolyubov calculations with $D1$ effective interaction'. *Phys. Rev. C* 27 (5), pp. 2317–2339. DOI: 10.1103/PhysRevC.27.2317. URL: https://link.aps.org/doi/10.1103/PhysRevC.27.2317 (cit. on p. 87).

Glendenning, Norman K. (1997). *Compact Stars: Nuclear Physics, Particle Physics and General Relativity*. Springer. DOI: https://doi.org/10.1007/978-1-4684-0491-3 (cit. on pp. 109, 110, 113, 118).

Głowacz, S., W. Satuła and R. A. Wyss (2004). 'Cranking in isospace'. *Eur. Phys. J. A* 19.1, pp. 33–44. DOI: 10.1140/epja/i2003-10111-6. URL: https://doi.org/10.1140/epja/i2003-10111-6 (cit. on p. 70).

Goeppert-Mayer, Maria (1949). 'On Closed Shells in Nuclei. II'. *Physical Review* 75.12, pp. 1969–1970. DOI: 10.1103/PhysRev.75.1969 (cit. on p. 4).

——— (1950). 'Nuclear Configurations in the Spin-Orbit Coupling Model. II. Theoretical Considerations'. *Physical Review* 78.1, pp. 22–27. DOI: 10.1103/PhysRev.78.22 (cit. on p. 6).

González Trotter, D. E. et al. (1999). 'New Measurement of the $^1S_0$ Neutron-Neutron Scattering Length Using the Neutron-Proton Scattering Length as a Standard'. *Phys. Rev. Lett.* 83 (19), pp. 3788–3791. DOI: 10.1103/PhysRevLett.83.3788. URL: https://link.aps.org/doi/10.1103/PhysRevLett.83.3788 (cit. on p. 63).

Grams, Guilherme et al. (2025). 'Skyrme–Hartree–Fock–Bogoliubov mass models on a 3D mesh: IV. Improved description of the isospin dependence of pairing'. *The European Physical Journal A* 61 (2). DOI: 10.1140/epja/s10050-025-01503-x. URL: https://doi.org/10.1140/epja/s10050-025-01503-x (cit. on p. 25).

Greenacre, Michael et al. (2022). 'Principal component analysis'. *Nature Reviews Methods Primers* 2, p. 100. DOI: 10.1038/s43586-022-00184-w (cit. on p. 89).

Greiner, Walter, Stefan Schramm and Eckart Stein (2007). *Quantum Chromodynamics*. 3rd ed. Springer-Verlag Berlin Heidelberg. ISBN: 978-3-540-48535-3. DOI: 10.1007/978-3-540-48535-3 (cit. on pp. 2, 111).

Hadyńska-Klęk, K. et al. (2016). 'Superdeformed and Triaxial States in ^{42}Ca'. *Phys. Rev. Lett.* 117 (6), p. 062501. DOI: 10.1103/PhysRevLett.117.062501. URL: https://link.aps.org/doi/10.1103/PhysRevLett.117.062501 (cit. on p. 75).

Haidenbauer, J. et al. (2017). 'Lambda-nuclear interactions and hyperon puzzle in neutron stars'. *The European Physical Journal A* 53.6. ISSN: 1434-601X. DOI: 10.1140/epja/i2017-12316-4. URL: http://dx.doi.org/10.1140/epja/i2017-12316-4 (cit. on p. 115).

Hebeler, K. et al. (2013). 'Equation of state and neutron star properties constrained by nuclear physics and observation'. *Astrophys. J.* 773, p. 11. DOI: 10.1088/0004-637X/773/1/11. arXiv: 1303.4662 [astro-ph.SR] (cit. on p. 119).

Heisenberg, W. (1932). 'On the Structure of Atomic Nuclei, I'. *Zeits. f. Physik* 77.1. Online available at: https://archive.org/details/nuclearforces0000unse/page/144/ (cit. on pp. 59, 60).

Henderson, J. et al. (2018). 'Testing microscopically derived descriptions of nuclear collectivity: Coulomb excitation of 22Mg'. *Physics Letters B* 782, pp. 468–473. ISSN: 0370-2693. DOI: https://doi.org/10.1016/j.physletb.2018.05.064. URL: https://www.sciencedirect.com/science/article/pii/S0370269318304283 (cit. on p. 48).

Hergert, Heiko (2020). 'A Guided Tour of ab initio Nuclear Many-Body Theory'. *Frontiers in Physics* Volume 8 - 2020. ISSN: 2296-424X. DOI: 10.3389/fphy.2020.00379. URL: https://www.frontiersin.org/journals/physics/articles/10.3389/fphy.2020.00379 (cit. on p. 4).

Hohenberg, P. and W. Kohn (1964). 'Inhomogeneous Electron Gas'. *Physical Review* 136, B864–B871. DOI: 10.1103/PhysRev.136.B864 (cit. on p. 4).

Huth, S. et al. (2022). 'Constraining Neutron-Star Matter with Microscopic and Macroscopic Collisions'. *Nature* 606, pp. 276–280. DOI: 10.1038/s41586-022-04750-w. eprint: 2107.06229 (cit. on p. 121).

Karthein, Jonas (2024). *nuclear-chart-plotter*. Python script for producing publication-ready nuclear chart plots, based on the Atomic Mass Evaluation 2020. URL: https://github.com/jonas-ka/nuclear-chart-plotter (cit. on pp. 3, 6).

Klose, A. et al. (2019). 'Ground-state electromagnetic moments of ^{37}Ca'. *Phys. Rev. C* 99 (6), p. 061301. DOI: 10.1103/PhysRevC.99.061301. URL: https://link.aps.org/doi/10.1103/PhysRevC.99.061301 (cit. on p. 48).

Klüpfel, P. et al. (2008). 'Systematics of collective correlation energies from self-consistent mean-field calculations'. *Eur. Phys. J A* 37. http://www.arxiv.org/abs/0804.340, p. 343. URL: http://dx.doi.org/10.1140/epja/i2008-10633-3 (cit. on p. 72).

Kohn, W. and L. J. Sham (1965). 'Self-Consistent Equations Including Exchange and Correlation Effects'. *Physical Review* 140, A1133–A1138. DOI: 10.1103/PhysRev.140.A1133 (cit. on p. 4).

Kopfermann, Hans (1958). *Nuclear Moments*. 2nd ed. Vol. 2. Pure and Applied Physics. New York: Academic Press, p. 505 (cit. on p. 48).

Kortelainen, M., T. Lesinski et al. (2010). 'Nuclear energy density optimization'. *Phys. Rev. C* 82 (2), p. 024313. DOI: 10.1103/PhysRevC.82.024313. URL: https://link.aps.org/doi/10.1103/PhysRevC.82.024313 (cit. on p. 52).

Kortelainen, M., J. McDonnell et al. (2012). 'Nuclear energy density optimization: Large deformations'. *Phys. Rev. C* 85 (2), p. 024304. DOI: 10.1103/PhysRevC.85.024304. URL: https://link.aps.org/doi/10.1103/PhysRevC.85.024304 (cit. on pp. 50–52, 54, 55, 73).

Landau, L. (1932). 'On the theory of stars'. *Phys. Z. Sowjetunion* 1, pp. 285–288 (cit. on pp. 109, 113).

Lenzi, S.M. and M.A. Bentley (2009). 'Test of Isospin Symmetryisospin symmetry Along the N=Z Line'. In: *The Euroschool Lectures on Physics with Exotic Beams, Vol. III*. Ed. by J.S. Al-Khalili and E. Roeckl. Berlin, Heidelberg: Springer Berlin Heidelberg, pp. 57–98. ISBN: 978-3-540-85839-3. DOI: 10.1007/978-3-540-85839-3_3. URL: https://doi.org/10.1007/978-3-540-85839-3_3 (cit. on pp. 7, 61, 62, 64).

Li, Jia Jie, Armen Sedrakian and Fridolin Weber (2018). 'Competition between delta isobars and hyperons and properties of compact stars'. *Physics Letters B* 783, pp. 234–240. ISSN: 0370-2693. DOI: https://doi.org/10.1016/j.physletb.2018.06.051. URL: https://www.sciencedirect.com/science/article/pii/S0370269318305070 (cit. on p. 117).

Lipkin, Harry J (1960). 'Collective motion in many-particle systems: Part 1. The violation of conservation laws'. *Annals of Physics* 9.2, pp. 272–291. ISSN: 0003-4916. DOI: https://doi.org/10.1016/0003-4916(60)90032-4. URL: https://www.sciencedirect.com/science/article/pii/0003491660900324 (cit. on p. 50).

Liu, Menglan and Cenxi Yuan (2023). 'Recent progress in configuration–interaction shell model'. *International Journal of Modern Physics E* 32.12. ISSN: 1793-6608. DOI: 10.1142/s0218301323300035. URL: http://dx.doi.org/10.1142/S0218301323300035 (cit. on p. 4).

Llewellyn, R. D. O. et al. (2020). 'Establishing the Maximum Collectivity in Highly Deformed [$N = Z$] Nuclei'. *Phys. Rev. Lett.* 124 (15), p. 152501. DOI: 10.1103/PhysRevLett.124.152501. URL: https://link.aps.org/doi/10.1103/PhysRevLett.124.152501 (cit. on pp. 66, 72, 75).

Lonardoni, Diego et al. (2015). 'Hyperon Puzzle: Hints from Quantum Monte Carlo Calculations'. *Phys. Rev. Lett.* 114 (9), p. 092301. DOI: 10.1103/PhysRevLett.114.092301. URL: https://link.aps.org/doi/10.1103/PhysRevLett.114.092301 (cit. on p. 115).

Lopes, Luiz L., Kauan D. Marquez and Débora P. Menezes (2023). 'Baryon coupling scheme in a unified SU(3) and SU(6) symmetry formalism'. *Phys. Rev. D* 107 (3), p. 036011. DOI: 10.1103/PhysRevD.107.036011. URL: https://link.aps.org/doi/10.1103/PhysRevD.107.036011 (cit. on p. 117).

Lüscher, Martin and Peter Weisz (2001). 'Locality and exponential error reduction in numerical lattice gauge theory'. *Journal of High Energy Physics* 2001.09, p. 010. DOI: 10.1088/1126-6708/2001/09/010. URL: https://dx.doi.org/10.1088/1126-6708/2001/09/010 (cit. on p. 87).

Machleidt, R. and H. Müther (2001). 'Charge symmetry breaking of the nucleon-nucleon interaction: ρ-ω mixing versus nucleon mass splitting'. *Phys. Rev. C* 63 (3), p. 034005. DOI: 10.1103/PhysRevC.63.034005. URL: https://link.aps.org/doi/10.1103/PhysRevC.63.034005 (cit. on p. 63).

Machleidt, Ruprecht and Francesca Sammarruca (2024). *Recent advances in chiral EFT based nuclear forces and their applications*. arXiv: 2402.14032 [nucl-th]. URL: https://arxiv.org/abs/2402.14032 (cit. on p. 4).

Malfatti, Germán et al. (2020). 'Delta baryons and diquark formation in the cores of neutron stars'. *Phys. Rev. D* 102 (6), p. 063008. DOI: 10.1103/PhysRevD.102.063008. URL: https://link.aps.org/doi/10.1103/PhysRevD.102.063008 (cit. on p. 117).

Marquez, Kauan D. et al. (2022). ' baryons in neutron stars'. *Phys. Rev. C* 106 (5), p. 055801. DOI: 10.1103/PhysRevC.106.055801. URL: https://link.aps.org/doi/10.1103/PhysRevC.106.055801 (cit. on p. 117).

Marquez, Kauan Dalfovo (2022). 'Astrophysical implications of exotic particles and magnetic fields in neutron stars'. PhD thesis. Florianópolis, Brazil: Universidade Federal de Santa Catarina. URL: https://repositorio.ufsc.br/handle/123456789/240907 (cit. on p. 117).

Marshalek, Eugene R. (1965). 'Self-Consistent Perturbation of Hartree-Fock-Bogoliubov Equations and Nuclear Rotational Spectra. I'. *Physical Review* 139, B770–B780. DOI: 10.1103/PhysRev.139.B770 (cit. on p. 6).

Martínez-Pinedo, G., K. Langanke and P. Vogel (1999). 'Competition of isoscalar and isovector proton-neutron pairing in nuclei'. *Nucl. Phys. A* 651.4, pp. 379–393. ISSN: 0375-9474. DOI: 10.1016/S0375-9474(99)00141-4. URL: http://www.sciencedirect.com/science/article/pii/S0375947499001414 (cit. on p. 81).

McDonnell, J. D. et al. (2015). 'Uncertainty Quantification for Nuclear Density Functional Theory and Information Content of New Measurements'. *Phys. Rev. Lett.* 114 (12), p. 122501. DOI: 10.1103/PhysRevLett.114.122501. URL: https://link.aps.org/doi/10.1103/PhysRevLett.114.122501 (cit. on p. 103).

Menezes, Débora Peres (2021). 'A Neutron Star Is Born'. *Universe* 7.8. ISSN: 2218-1997. URL: https://www.mdpi.com/2218-1997/7/8/267 (cit. on pp. 109, 113).

Miller, Gerald A., Allena K. Opper and Edward J. Stephenson (2006). 'Charge Symmetry Breaking and QCD'. *Annual Review Nuclear and Particle Science.* 56, pp. 253–292. DOI: 10.1146/annurev.nucl.56.080805.140446. URL: https://doi.org/10.1146/annurev.nucl.56.080805.140446 (cit. on p. 63).

Miller, M. C. et al. (2021). 'The Radius of PSR J0740+6620 from NICER and XMM-Newton Data'. *The Astrophysical Journal Letters* 918.2, p. L28. DOI: 10.3847/2041-8213/ac089b. URL: https://dx.doi.org/10.3847/2041-8213/ac089b (cit. on p. 121).

Miller *et al.*, M. C. (2019). 'PSR J0030+0451 Mass and Radius from NICER Data and Implications for the Properties of Neutron Star Matter'. *Astrophys. J.* 887.1, p. L24. DOI: 10.3847/2041-8213/ab50c5. URL: https://doi.org/10.3847/2041-8213/ab50c5 (cit. on p. 121).

Mills, R. L. et al. (1959). 'Superfluidity of Nuclear Matter'. *Phys. Rev. Lett.* 3 (8), pp. 381–383. DOI: 10.1103/PhysRevLett.3.381. URL: https://link.aps.org/doi/10.1103/PhysRevLett.3.381 (cit. on pp. 6, 24).

Miyagi, T. et al. (2024). 'Impact of Two-Body Currents on Magnetic Dipole Moments of Nuclei'. *Phys. Rev. Lett.* 132 (23), p. 232503. DOI: 10.1103/PhysRevLett.132.232503. URL: https://link.aps.org/doi/10.1103/PhysRevLett.132.232503 (cit. on pp. 83, 84).

Morse, C. et al. (2018). 'Lifetime measurement of the 21^+ state in ^{74}Rb and isospin properties of quadrupole transition strengths at $N = Z$'. *Physics Letters B* 787, pp. 198–203. ISSN: 0370-2693. DOI: https://doi.org/10.1016/j.physletb.2018.10.064. URL: https://www.sciencedirect.com/science/article/pii/S037026931830844X (cit. on p. 75).

Muir, D. (2021). 'Microscopic Modelling of Collective Quadrupole Excitations of Nuclei'. Online available at: https://etheses.whiterose.ac.uk/id/eprint/29823/1/Muir_203027525_Thesis.pdf. PhD thesis. Physics (cit. on p. 73).

Muir, David et al. (2020). 'Structure of Krypton Isotopes using the Generalised Bohr Hamiltonian Method'. In: *27th International Nuclear Physics Conference*. DOI: 10.1088/1742-6596/1643/1/012147. arXiv: 2004.10835 [nucl-th] (cit. on p. 73).

Mukherjee, M. et al. (2008). 'ISOLTRAP: An on-line Penning trap for mass spectrometry on short-lived nuclides'. *The European Physical Journal A* 35.1, pp. 1–29. DOI: 10.1140/epja/i2007-10528-9 (cit. on p. 103).

Naito, Tomoya et al. (2024). 'Possible inconsistency between phenomenological and theoretical determinations of charge symmetry breaking in nuclear energy density functionals'. *Il Nuovo Cimento C* 47.2, pp. 1–6. ISSN: 03905551, 03905551. DOI: 10.1393/ncc/i2024-24052-9. URL: https://doi.org/10.1393/ncc/i2024-24052-9 (cit. on p. 80).

Nazarewicz, W. et al. (1985). 'Microscopic study of the high-spin behaviour in selected $A \simeq 80$ nuclei'. *Nucl. Phys. A* 435.2, pp. 397–447. ISSN: 0375-9474. DOI: 10.1016/0375-9474(85)90471-3. URL: http://www.sciencedirect.com/science/article/pii/0375947485904713 (cit. on pp. 72, 77).

Neyens, Gerda (2003). 'Nuclear magnetic and quadrupole moments for nuclear structure research on exotic nuclei'. *Reports on Progress in Physics* 66.4, p. 633. DOI: 10.1088/0034-4885/66/4/205. URL: https://dx.doi.org/10.1088/0034-4885/66/4/205 (cit. on p. 48).

Nogami, Yukihisa (1964). 'Improved Superconductivity Approximation for the Pairing Interaction in Nuclei'. *Physical Review* 134.2B, B313–B321. DOI: 10.1103/PhysRev.134.B313 (cit. on p. 50).

Onishi, Naoki and Shiro Yoshida (1966). 'Generator coordinate method applied to nuclei in the transition region'. *Nuclear Physics* 80.2, pp. 367–376. ISSN: 0029-5582. DOI: https://doi.org/10.1016/0029-5582(66)90096-4. URL: https://www.sciencedirect.com/science/article/pii/0029558266900964 (cit. on p. 31).

Oppenheimer, J. R. and G. M. Volkoff (1939). 'On Massive Neutron Cores'. *Phys. Rev.* 55 (4), pp. 374–381. DOI: 10.1103/PhysRev.55.374. URL: https://link.aps.org/doi/10.1103/PhysRev.55.374 (cit. on p. 114).

Pandav, A., D. Mallick and B. Mohanty (2022). 'Search for the QCD critical point in high energy nuclear collisions'. *Progress in Particle and Nuclear Physics* 125, p. 103960. ISSN: 0146-6410. DOI: https://doi.org/10.1016/j.ppnp.2022.103960. URL: https://www.sciencedirect.com/science/article/pii/S0146641022000217 (cit. on p. 112).

Papuga, J. et al. (2013). 'Spins and Magnetic Moments of ^{49}**K** and ^{51}**K**: Establishing the $1/2^+$ and $3/2^+$ Level Ordering Beyond N=28'. *Phys. Rev. Lett.* 110 (17), p. 172503. DOI: 10.1103/PhysRevLett.110.172503. URL: https://link.aps.org/doi/10.1103/PhysRevLett.110.172503 (cit. on p. 48).

Pelicer, M. R. et al. (2023). 'Do short range correlations inhibit the appearance of the nuclear pasta?' *The European Physical Journal A* 59.9. ISSN: 1434-601X. DOI: 10.1140/epja/s10050-023-01122-4. URL: http://dx.doi.org/10.1140/epja/s10050-023-01122-4 (cit. on pp. 24, 25).

Perlińska, E. et al. (2004). 'Local density approximation for proton-neutron pairing correlations: Formalism'. *Phys. Rev. C* 69 (1), p. 014316. DOI: 10.1103/PhysRevC.69.014316. URL: http://link.aps.org/doi/10.1103/PhysRevC.69.014316 (cit. on pp. 60, 81, 86).

Petkov, I. Zh. and M. V. Stoitsov (1991). *Nuclear Density Functional Theory*. Vol. 14. Oxford Studies in Nuclear Physics. Oxford: Clarendon Press. ISBN: 0-19-851731-9 (cit. on p. 9).

Piekarewicz, Jorge (2024). 'Heaven and Earth: Nuclear Astrophysics after GW170817'. *EPJ Web Conf.* 301, p. 01003. DOI: 10.1051/epjconf/202430101003. URL: https://doi.org/10.1051/epjconf/202430101003 (cit. on p. 110).

Pritychenko, B. et al. (2016). 'Tables of E2 transition probabilities from the first 2+ states in even–even nuclei'. *Atomic Data and Nuclear Data Tables* 107, pp. 1–139. ISSN: 0092-640X. DOI: https://doi.org/10.1016/j.adt.2015.10.001. URL: https://www.sciencedirect.com/science/article/pii/S0092640X15000406 (cit. on p. 75).

Prochniak, L (2015). 'Microscopic description of collective properties of even-even Xe isotopes'. *Physica Scripta* 90.11, p. 114005 (cit. on p. 73).

Próchniak, L and SG Rohoziński (2009). 'Quadrupole collective states within the Bohr collective Hamiltonian'. *J. Phys. G* 36.12, p. 123101 (cit. on pp. 72, 73).

Qi, Chong (2026). 'Neutron–proton pairing correlations: Theoretical foundations, open questions and confrontation of BCS and exact solutions'. *International Journal of Modern Physics E* 35. DOI: 10.1142/S021830132630002X (cit. on p. 6).

Raduta, Adriana R. (2021). 'Δ-admixed neutron stars: Spinodal instabilities and dUrca processes'. *Physics Letters B* 814, p. 136070. ISSN: 0370-2693. DOI: https://doi.org/10.1016/j.physletb.2021.136070. URL: https://www.sciencedirect.com/science/article/pii/S0370269321000101 (cit. on p. 117).

Raimondi, F, K Bennaceur and J Dobaczewski (2014). 'Nonlocal energy density functionals for low-energy nuclear structure'. *Journal of Physics G: Nuclear and Particle Physics* 41.5, p. 055112. URL: http://stacks.iop.org/0954-3899/41/i=5/a=055112 (cit. on p. 79).

Rather, Ishfaq A., Kauan D. Marquez, Betânia C. Backes et al. (2024). 'Radial oscillations of hybrid stars and neutron stars including delta baryons: the effect of a slow quark phase transition'. *Journal of Cosmology and Astroparticle Physics* 2024.05, p. 130. DOI: 10.1088/1475-7516/2024/05/130. URL: https://doi.org/10.1088/1475-7516/2024/05/130 (cit. on pp. 110, 114, 118–121).

Rather, Ishfaq A., Kauan D. Marquez, Grigoris Panotopoulos et al. (2023). 'Radial oscillations in neutron stars with delta baryons'. *Physical Review D* 107.12. ISSN: 2470-0029. DOI: 10.1103/physrevd.107.123022. URL: http://dx.doi.org/10.1103/PhysRevD.107.123022 (cit. on p. 117).

Reinhard, Paul-Gerhard and Witold Nazarewicz (2021). 'Nuclear charge densities in spherical and deformed nuclei: Toward precise calculations of charge radii'. *Phys. Rev. C* 103 (5), p. 054310. DOI: 10.1103/PhysRevC.103.054310. URL: https://link.aps.org/doi/10.1103/PhysRevC.103.054310 (cit. on p. 64).

Remmert, Reinhold (1991). *Theory of Complex Functions*. Vol. 122. Graduate Texts in Mathematics. New York: Springer. ISBN: 978-0-387-97195-7. DOI: 10.1007/978-1-4612-0939-3. URL: https://doi.org/10.1007/978-1-4612-0939-3 (cit. on p. 34).

Riley, Thomas E. et al. (2021). 'A NICER View of the Massive Pulsar PSR J0740+6620 Informed by Radio Timing and XMM-Newton Spectroscopy'. *The Astrophysical Journal Letters* 918.2, p. L27. DOI: 10.3847/2041-8213/ac0a81. URL: https://dx.doi.org/10.3847/2041-8213/ac0a81 (cit. on p. 121).

Ring, Peter and Peter Schuck (1980). *The nuclear many-body problem*. Springer-Verlag, Berlin. URL: https://www.springer.com/gp/book/9783540212065 (cit. on pp. 5, 9, 26, 31, 61, 81, 92).

Rios, Arnau, Artur Polls and W. H. Dickhoff (2017). 'Pairing and Short-Range Correlations in Nuclear Systems'. *Journal of Low Temperature Physics* 189, pp. 234–249. DOI: 10.1007/s10909-017-1818-7 (cit. on p. 6).

Robson, D (1966). 'Isobaric Spin in Nuclear Physics'. *Annual Review of Nuclear and Particle Science* 16.Volume 16, 1966, pp. 119–152. ISSN: 1545-4134. DOI: https://doi.org/10.1146/annurev.ns.16.120166.001003. URL: https://www.annualreviews.org/content/journals/10.1146/annurev.ns.16.120166.001003 (cit. on p. 60).

Roca-Maza, X. and N. Paar (2018). 'Nuclear equation of state from ground and collective excited state properties of nuclei'. *Progress in Particle and Nuclear Physics* 101, pp. 96–176. ISSN: 0146-6410. DOI: https://doi.org/10.1016/j.ppnp.2018.04.001. URL: https://www.sciencedirect.com/science/article/pii/S0146641018300334 (cit. on p. 110).

Rodríguez, L. V. et al. (2020). 'Doubly-magic character of ^{132}Sn studied via electromagnetic moments of ^{133}Sn'. *Phys. Rev. C* 102 (5), p. 051301. DOI: 10.1103/PhysRevC.102.051301. URL: https://link.aps.org/doi/10.1103/PhysRevC.102.051301 (cit. on p. 48).

Romero, A. M., J. Dobaczewski and A. Pastore (2019). 'Symmetry restoration in the mean-field description of proton-neutron pairing'. *Phys. Lett. B* 795, pp. 177–182. ISSN: 0370-2693. DOI: 10.1016/j.physletb.2019.06.032. URL: http://www.sciencedirect.com/science/article/pii/S0370269319304113 (cit. on pp. 7, 32, 81).

Rowe, David J and John L Wood (2010). *Fundamentals of nuclear models: foundational models*. World Scientific Publishing Company (cit. on p. 72).

Sadoudi, J et al. (2013). 'Skyrme pseudo-potential-based EDF parametrization for spuriousity-free MR EDF calculations'. *Physica Scripta* T154, p. 014013. DOI: 10.1088/0031-8949/2013/t154/014013. URL: https://doi.org/10.1088/0031-8949/2013/t154/014013 (cit. on p. 79).

Sagawa, H, C L Bai and G Colò (2016). 'Isovector spin-singlet (T = 1, S = 0) and isoscalar spin-triplet (T = 0, S = 1) pairing interactions and spin-isospin response'. *Physica Scripta* 91.8, p. 083011. DOI: 10.1088/0031-8949/91/8/083011. URL: https://doi.org/10.1088/0031-8949/91/8/083011 (cit. on p. 6).

Sánchez-Fernández, Adrián et al. (2025). 'Two-center harmonic oscillator basis for Skyrme-DFT calculations (I): formalism and Proof of Principle'. *The European Physical Journal A* 61.6. ISSN: 1434-601X. DOI: 10.1140/epja/s10050-025-01605-6. URL: http://dx.doi.org/10.1140/epja/s10050-025-01605-6 (cit. on p. 87).

Sassarini, P L et al. (2022). 'Nuclear DFT analysis of electromagnetic moments in odd near doubly magic nuclei'. *Journal of Physics G: Nuclear and Particle Physics* 49.11, 11LT01. DOI: 10.1088/1361-6471/ac900a. URL: https://dx.doi.org/10.1088/1361-6471/ac900a (cit. on p. 48).

Sato, Koichi et al. (2013). 'Energy-density-functional calculations including proton-neutron mixing'. *Phys. Rev. C* 88 (6), p. 061301. DOI: 10.1103/PhysRevC.88.061301. URL: https://link.aps.org/doi/10.1103/PhysRevC.88.061301 (cit. on p. 81).

Satpathy, L., D. Goss and M. K. Banerjee (1969). 'Hartree-Fock-Bogoliubov Calculations in the *sd* Shell'. *Physical Review* 183, pp. 887–891. DOI: 10.1103/PhysRev.183.887 (cit. on p. 6).

Satuła, W., J. Dobaczewski et al. (2009). 'Isospin Mixing in Nuclei within the Nuclear Density Functional Theory'. *Phys. Rev. Lett.* 103 (1), p. 012502. DOI: 10.1103/PhysRevLett.103.012502. URL: https://link.aps.org/doi/10.1103/PhysRevLett.103.012502 (cit. on p. 63).

Satuła, W. and R. Wyss (1997). 'Competition between T = 0 and T = 1 pairing in proton-rich nuclei'. *Phys. Lett. B* 393.1, pp. 1–6. ISSN: 0370-2693. DOI: 10.1016/S0370-2693(96)01603-6. URL: http://www.sciencedirect.com/science/article/pii/S0370269396016036 (cit. on p. 81).

Satuła, Wojciech and Ramon Wyss (2001). 'Microscopic Structure of Fundamental Excitations in $N = Z$ Nuclei'. *Phys. Rev. Lett.* 87 (5), p. 052504. DOI: 10.1103/PhysRevLett.87.052504. URL: https://link.aps.org/doi/10.1103/PhysRevLett.87.052504 (cit. on p. 70).

Schunck, N. et al. (2014). *Quantification of Uncertainties in Nuclear Density Functional theory*. arXiv: 1406.4374 [nucl-th]. URL: https://arxiv.org/abs/1406.4374 (cit. on p. 103).

Schunck, Nicolas, ed. (2019). *Energy Density Functional Methods for Atomic Nuclei*. 2053-2563. IOP Publishing. ISBN: 978-0-7503-1422-0. DOI: 10.1088/2053-2563/aae0ed. URL: https://dx.doi.org/10.1088/2053-2563/aae0ed (cit. on pp. 3, 9, 13, 26, 88, 95, 111).

Seutin, R. et al. (2023). 'Magnetic dipole operator from chiral effective field theory for many-body expansion methods'. *Phys. Rev. C* 108 (5), p. 054005. DOI: 10.1103/PhysRevC.108.054005. URL: https://link.aps.org/doi/10.1103/PhysRevC.108.054005 (cit. on pp. 83, 84).

Shavitt, Isaiah and Rodney J. Bartlett (2009). *Many-Body Methods in Chemistry and Physics: MBPT and Coupled-Cluster Theory*. Cambridge Molecular Science. Cambridge University Press (cit. on pp. 9, 17, 19).

Sheikh, J A, J Dobaczewski et al. (2021). 'Symmetry restoration in mean-field approaches'. *J. Phys. G* 48.12, p. 123001. DOI: 10.1088/1361-6471/ac288a. URL: https://dx.doi.org/10.1088/1361-6471/ac288a (cit. on pp. 5, 14, 70, 71, 76).

Sheikh, J. A., N. Hinohara et al. (2014). 'Isospin-invariant Skyrme energy-density-functional approach with axial symmetry'. *Phys. Rev. C* 89 (5), p. 054317. DOI: 10.1103/PhysRevC.89.054317. URL: http://link.aps.org/doi/10.1103/PhysRevC.89.054317 (cit. on p. 81).

Skyrme, T. H. R. (1959). 'The Effective Nuclear Potential'. *Nuclear Physics* 9, pp. 615–634. DOI: 10.1016/0029-5582(58)90345-6 (cit. on p. 14).

Staszczak, A. et al. (2010). 'Augmented Lagrangian method for constrained nuclear density functional theory'. *The European Physical Journal A* 46.1, pp. 85–90. ISSN: 1434-601X. DOI: 10.1140/epja/i2010-11018-9. URL: http://dx.doi.org/10.1140/epja/i2010-11018-9 (cit. on p. 13).

Stephanov, Mikhail (2024). *QCD critical point: recent developments*. arXiv: 2410.02861 [nucl-th]. URL: https://arxiv.org/abs/2410.02861 (cit. on p. 112).

Stone, N.J. (2021). *Table of nuclear electric quadrupole moments*. Tech. rep. INDC International Nuclear Data Committee (cit. on p. 49).

Stroberg, S. R. et al. (2022). 'Systematics of $E2$ strength in the *sd* shell with the valence-space in-medium similarity renormalization group'. *Phys. Rev. C* 105 (3), p. 034333. DOI: 10.1103/PhysRevC.105.034333. URL: https://link.aps.org/doi/10.1103/PhysRevC.105.034333 (cit. on p. 48).

Thouless, D.J. (1960). 'Stability conditions and nuclear rotations in the Hartree-Fock theory'. *Nuclear Physics* 21, pp. 225–232. ISSN: 0029-5582. DOI: https://doi.org/10.1016/0029-5582(60)90048-1. URL: https://www.sciencedirect.com/science/article/pii/0029558260900481 (cit. on p. 10).

Tolman, Richard C. (1939). 'Static Solutions of Einstein's Field Equations for Spheres of Fluid'. *Phys. Rev.* 55 (4), pp. 364–373. DOI: 10.1103/PhysRev.55.364. URL: https://link.aps.org/doi/10.1103/PhysRev.55.364 (cit. on p. 114).

Varshalovich, D.A., A.N. Moskalev and V.K. Khersonskii (1988). *Quantum Theory of Angular Momentum: Irreducible Tensors, Spherical Harmonics, Vector Coupling Coefficients, 3nj Symbols*. World Scientific. ISBN: 9789971509965. URL: https://books.google.co.uk/books?id=hQx_QgAACAAJ (cit. on pp. 39, 40).

Walecka, J.D (1974). 'A theory of highly condensed matter'. *Annals of Physics* 83.2, pp. 491–529. ISSN: 0003-4916. DOI: https://doi.org/10.1016/0003-4916(74)90208-5. URL: https://www.sciencedirect.com/science/article/pii/0003491674902085 (cit. on p. 114).

Wang, Meng et al. (2021a). 'The AME 2020 atomic mass evaluation (II). Tables, graphs and references'. *Chinese Physics C* 45.3, p. 030003. DOI: 10.1088/1674-1137/abddaf (cit. on pp. 3, 6, 103).

——— (2021b). 'The AME 2020 atomic mass evaluation (II). Tables, graphs and references'. *Chinese Physics C* 45.3, p. 030003. DOI: 10.1088/1674-1137/abddaf. URL: https://dx.doi.org/10.1088/1674-1137/abddaf (cit. on p. 52).

Warburton, E. K. and J. Wessner (1969). *Isospin in Nuclear Physics*. Ed. by D. H. Wilkinson. Online available at: https://archive.org/details/isospininnuclear0000unse/. North-Holland Publishing Company, Amsterdam. Chap. 5 (cit. on p. 64).

Watson, Thomas (2026). *Complexity in Computer Science*. Freely available prepublication version. Prepublication draft. URL: https://complexityincs.com/ (cit. on p. 89).

Watts, Anna et al. (2014). *Probing the neutron star interior and the Equation of State of cold dense matter with the SKA*. arXiv: 1501.00042 [astro-ph.SR]. URL: https://arxiv.org/abs/1501.00042 (cit. on p. 112).

Weizsäcker, Carl Friedrich von (1935). 'Zur Theorie der Kernmassen'. *Zeitschrift für Physik* 96, pp. 431–458. DOI: 10.1007/BF01337700 (cit. on p. 5).

Wibowo, H., B. C. Backes et al. (2025). 'Electromagnetic moments in the Sn-Gd region determined within nuclear DFT'. *Journal of Physics G: Nuclear and Particle Physics* 52.6, p. 065104. DOI: 10.1088/1361-6471/ade0dd. URL: https://doi.org/10.1088/1361-6471/ade0dd (cit. on pp. 12, 48–51, 105).

Wibowo, H., R. Han et al. (2026). 'Nuclear DFT meson-exchange contributions to magnetic dipole moments of atomic nuclei'. To be published (cit. on pp. 83, 86, 87).

Wigner, E. (1937). 'On the Consequences of the Symmetry of the Nuclear Hamiltonian on the Spectroscopy of Nuclei'. *Phys. Rev.* 51 (2), pp. 106–119. DOI: 10.1103/PhysRev.51.106. URL: https://link.aps.org/doi/10.1103/PhysRev.51.106 (cit. on p. 59).

Wimmer, K. et al. (2021). 'Shape Changes in the Mirror Nuclei ^{70}Kr and ^{70}Se'. *Phys. Rev. Lett.* 126 (7), p. 072501. DOI: 10.1103/PhysRevLett.126.072501. URL: https://link.aps.org/doi/10.1103/PhysRevLett.126.072501 (cit. on pp. 66, 74, 75, 78).

Xia, C. J. et al. (2014). 'Thermodynamic consistency, quark mass scaling, and properties of strange matter'. *Phys. Rev. D* 89 (10), p. 105027. DOI: 10.1103/PhysRevD.89.105027. URL: https://link.aps.org/doi/10.1103/PhysRevD.89.105027 (cit. on p. 115).

Xiang, Hu and Guo Hua (2003). 'Δ excitation and its influences on neutron stars in relativistic mean field theory'. *Phys. Rev. C* 67 (3), p. 038801. DOI: 10.1103/PhysRevC.67.038801. URL: https://link.aps.org/doi/10.1103/PhysRevC.67.038801 (cit. on p. 117).

Yakovlev, Dmitrii G, Kseniya P Levenfish and Yurii A Shibanov (1999). 'Cooling of neutron stars and superfluidity in their cores'. *Physics-Uspekhi* 42.8, pp. 737–778. ISSN: 1468-4780. DOI: 10.1070/pu1999v042n08abeh000556. URL: http://dx.doi.org/10.1070/PU1999v042n08ABEH000556 (cit. on p. 24).

Yin, P. et al. (2023). 'Pairing properties of semilocal coordinate- and momentum-space regularized chiral interactions'. *Physical Review C* 108.3. ISSN: 2469-9993. DOI: 10.1103/physrevc.108.034002. URL: http://dx.doi.org/10.1103/PhysRevC.108.034002 (cit. on p. 25).